IMPERIAL

Mitigation of Deep Space Two-Line Element Set Biases with Pseudo-Orbit Determination and Data-Driven Models

Max I. Hallgarten La Casta

Imperial College London
Department of Aeronautics

Supervised by
Dr Davide Amato

Submitted in partial fulfilment of the requirements for the degree of Doctor of Philosophy

April 2026

Copyright Declaration

The copyright of this thesis rests with the author. Unless otherwise indicated, its contents are licensed under a Creative Commons Attribution-NonCommercial 4.0 International Licence (CC BY-NC).

Under this licence, you may copy and redistribute the material in any medium or format. You may also create and distribute modified versions of the work. This is on the condition that: you credit the author and do not use it, or any derivative works, for a commercial purpose.

When reusing or sharing this work, ensure you make the licence terms clear to others by naming the licence and linking to the licence text. Where a work has been adapted, you should indicate that the work has been changed and describe those changes.

Please seek permission from the copyright holder for uses of this work that are not included in this licence or permitted under UK Copyright Law.

Statement of Originality

The work presented in this thesis is my own. The work of other authors has been clearly identified and referenced. No form of generative artificial intelligence was used to write this thesis.

Max I. Hallgarten La Casta

Acknowledgements

First and foremost, I would like to thank my supervisor, Davide. Thank you for your support and guidance throughout my whole PhD journey. Our weekly meetings and your insights into the complex world of astrodynamics greatly improved the results of my research.

To all of my friends from school, thank you. To all of my friends from Bristol, Delft, and UCL, thank you. To all of the friends I've made during my time here at Imperial, thank you. None of my studies would have been possible without being surrounded by such friendly, passionate, and dedicated people. To everyone in ICLR, thank you. I will cherish my time as a member of the team, particularly our adventures at Silwood and in Portugal.

Finally, I would like to thank my family. To my parents, Nieves and Daniel, thank you for everything, and for inspiring me to be curious about the world around me and encouraging me to follow my passions. To my sister, Ana, thank you for always being there for me, for supporting me through my endeavours, and for helping me to navigate the PhD with your invaluable advice. To my grandparents, Miren and Salvador, and Elaine and Peter, thank you for all of your love and support, and for the opportunities you made possible for us all.

Abstract

The past decade has seen a dramatic growth in the number of Resident Space Objects (RSOs) in near-Earth orbits, driven by the rise of the ‘New Space’ era and the increasing commercialisation of space. The growing congestion in key orbital regimes presents a threat to the continued human presence in space, due to the risk of collisions and their downstream impacts.

The limited availability of data remains a key obstacle for many Space Situational Awareness (SSA) stakeholders. This poses major challenges for ensuring safe and sustainable space operations, including safeguarding transparency of the near-Earth space environment, beyond only operators and governmental organisations. Two-Line Element Sets (TLEs) published by the United States Space Force (USSF) remain one of the few publicly available, comprehensive sources of SSA information. However, their known inaccuracy and uncertain precision limits their utility for many applications.

In this thesis, further investigation into TLE enhancement techniques was conducted, including demonstration of the continuing applicability of TLE-based Pseudo-Orbit Determination (P-OD) to extract improved state estimates from TLEs; presentation of further evidence of widespread, systematic biases affecting deep space TLEs; and modelling of TLE biases to improve TLE-derived state vectors. These techniques were demonstrated for various RSOs in Medium Earth Orbit (MEO) and Geostationary Earth Orbit (GEO), both with and without high-accuracy reference ephemerides, to pave the way for catalogue-wide TLE enhancement.

Contents

Copyright Declaration **3**

Statement of Originality **5**

Acknowledgements **7**

Abstract **9**

Contents **11**

List of Figures **15**

List of Tables **25**

List of Listings **29**

List of Acronyms **31**

1 Introduction **41**

1.1 Motivation 41

1.2 Near-Earth Environment 43

1.2.1 Space Debris 43

1.2.2 Space Debris Mitigation 45

1.3 Space Situational Awareness 48

1.4 Publicly Available Data 50

1.4.1 Two-Line Element Sets 51

1.4.2 Satellite Laser Ranging 54

1.4.3 Doppler Orbitography and Radiopositioning Integrated by Satellite 56

1.4.4 Global Navigation Satellite Systems 58

1.5 Background on Improving Two-Line Element Set Accuracy . . . 62
1.6 Thesis Objectives . . . 66
1.7 Thesis Outline . . . 67
1.8 Publications . . . 68

2 Pseudo-Orbit Determination **71**
2.1 Two-Line Element Set Propagation . . . 71
2.2 Two-Line Element Set Sampling . . . 73
2.3 Batch Least Squares State Estimation . . . 75
2.3.1 Predictor . . . 75
2.3.2 Observer . . . 76
2.3.3 Solver . . . 77
2.4 State Estimation Evaluation . . . 79
2.5 Implementation Considerations . . . 82
2.5.1 Two-Line Element Set Sampling . . . 82
2.5.2 Physical Model . . . 83
2.5.3 Non-Dimensionalisation . . . 87
2.5.4 Finite Differencing . . . 89

3 Two-Line Element Set Biases **95**
3.1 Pseudo-Orbit Determination on Two-Line Element Sets . . . 95
3.2 Error Characteristics of Deep Space Two-Line Element Sets . . . 101
3.2.1 Bias Frequency Analysis . . . 107
3.2.2 Impact of Increasing Window Size on Error Characteristics . . . 112
3.3 Data-Driven Bias Models . . . 116
3.3.1 Batch Least Squares for Bias Model Fitting . . . 120
3.3.2 Bias Model Evaluation . . . 122
3.3.3 Time-Based Bias Model . . . 123
3.3.4 Moon-Based Bias Model . . . 125
3.4 Impacts of Debiasing on Residual Bias Characteristics . . . 129
3.5 Impacts of Debiasing on Pseudo-Orbit Determination . . . 134
3.6 Large-Scale Bias Modelling . . . 142

3.6.1 Individual Time-Based Models . . . 142
3.6.2 Amplitude Model . . . 149
3.6.3 Ensemble Time- and Moon-Based Bias Models . . . 153
3.6.4 Large-Scale Bias Model Evaluation . . . 154
3.6.5 Coplanarity Amplitude Model . . . 159
3.7 Higher-Order Bias Models . . . 164

4 Pseudo-Orbit Determination in the Absence of Higher-Accuracy Ephemerides 173
4.1 Two-Line Element Sets as Reference Ephemerides . . . 174
4.2 Evaluation of Pseudo-Orbit Determination Accuracy with Two-Line Element Sets . . . 184
4.3 Pseudo-Orbit Determination for Bias Estimation . . . 196

5 Conclusions 221
5.1 Summary . . . 221
5.2 Discussion . . . 223
5.3 Key Contributions . . . 224
5.4 Future Work . . . 224

References 227

A Software 245
A.1 THALASSA . . . 245
A.2 BRENT . . . 247

List of Figures

1.1 Evolution of the number of objects in geocentric orbit by object class [1]. The rapid increase in the number of payloads in orbit over the past decade can be seen in dark blue. 41
1.2 Active ILRS stations (as of June 2025). Data from [81]. 61
1.3 Active DORIS ground beacons (as of February 2025). Data from [82]. 61
1.4 Active IGS stations (as of July 2025). Data from [83]. 61

2.1 TLE sampling strategies. 74
2.2 Position errors for calibration satellite TLEs for the first quarter of the year 2022, when using the forward, backward, and blended propagation methods. The epoch of each TLE is indicated by the grey vertical lines. 84
2.3 Position errors for calibration satellite TLEs for the first quarter of the year 2022, when using the forward, backward, and blended propagation methods. The TLEs for each satellite have been downsampled to artificially introduce 30-day gaps in availability. The epoch of each TLE is indicated by the grey vertical lines. 85
2.4 Position RMSEs, with respect to SLR, for 120-day fits with varying geopotential model degrees and orders. A 10-by-10 geopotential model provides sufficient accuracy for position RMSE to remain an order of magnitude below the expected TLE error. . . . 88
2.5 Position RMSEs, with respect to SLR, for 120-day fits with varying integrator tolerances. An integrator tolerance of 10^{-10} provides sufficient accuracy for position RMSE to remain an order of magnitude below the expected TLE error. 88
2.6 Comparison of finite differencing schemes for estimating the Jacobian matrix of the calibration satellites over a 30-day propagation. The Jacobian calculated with the central differencing scheme with a step size equivalent to a 1 mm perturbation was used as a reference solution, indicated by the dashed line. 91

2.7 Comparison of finite differencing schemes for estimating the Jacobian matrix of the calibration satellites over a 30-day propagation. The Jacobian calculated with the central differencing scheme with a step size equivalent to a 1 mm perturbation was used as a reference solution, indicated by the dashed line. 92

3.1 Position RMSE, with respect to SLR, during 30 days post-epoch for calibration satellite TLEs. New Two-Line Element Sets (TLEs) were published approximately daily, except for some multi-days gaps in availability seen with LAGEOS-1 and -2. Periodic variations in position RMSE are highly visible due to varying bias in the TLEs. The dashed lines represent the established baselines for each satellite. 97

3.2 Position RMSE during the 30 days post-fit for short-term biased fits of the calibration satellites. The red marker in the colour bar indicates the RMSE baseline derived from TLEs. Note that white regions indicate failed cases due to a lack of TLEs within the window. 98

3.3 Position RMSE during the 30 days post-fit for long-term biased fits of the calibration satellites. The red marker in the colour bar indicates the RMSE baseline derived from TLEs. Note that white regions indicate failed cases due to a lack of TLEs within the window. 99

3.4 Mean position RMSE during the 30 days post-fit for short-term and long-term biased fits of the calibration satellites. 100

3.5 Number of iterations required for the state estimator to converge for the short- and long-term biased calibration satellite fits. The average number of iterations is illustrated by the grey line. Note the change in fit window size interval between the short- and long-term fits. 102

3.6 Position errors of calibration satellite TLEs for the year 2022. 104

3.7 Angular RTN position errors of calibration satellite TLEs for the year 2022. 105

3.8 Angular RTN velocity errors of calibration satellite TLEs for the year 2022. 106

3.9 Angular along-track position error of calibration satellite TLEs for the years 2018 to 2025. 108

3.10 Angular radial velocity error of calibration satellite TLEs for the years 2018 to 2025. . 109

3.11 FFT analysis of the along-track angular position errors of the calibration satellites for the years 2018 to 2025. The orbital period of each satellite, the half period of the Moon, and the Moon's orbital period are represented by the dotted, dashed, and dash-dotted lines respectively. 110
3.12 FFT analysis of the radial angular velocity errors of the calibration satellites for the years 2018 to 2025. The orbital period of each satellite, the half period of the Moon, and the Moon's orbital period are represented by the dotted, dashed, and dash-dotted lines respectively. 111
3.13 Example of averaging a bias model (blue), illustrated by considering a line of best fit (red) for a restricted domain (black, dashed). 114
3.14 Numerically-calculated mean along-track position error for calibration satellite TLEs as a function of window midpoint and size. 117
3.15 Example along-track position error distributions for windows centred on 1st July 2022. The dashed lines indicate the mean error for each window. Densities are presented due to the different number of samples in each window. 119
3.16 Time-based along-track position error models for the calibration satellites for the years 2018 to 2025. The along-track position error of the TLEs and the models are presented in grey and colour, respectively. 124
3.17 Moon-based along-track position error models for the calibration satellites for the years 2018 to 2025. The along-track position error of the TLEs and the models are presented in grey and colour, respectively. 127
3.18 Moon-based along-track position error models, as a function of time, for the calibration satellites for the years 2018 to 2025. The along-track position error of the TLEs and the models are presented in grey and colour, respectively. 128
3.19 Residual along-track position error for the calibration satellites following debiasing with the individual time-based models for the years 2018 to 2025. 130
3.20 Residual along-track position error for the calibration satellites following debiasing with the individual Moon-based models for the years 2018 to 2025. 131

3.21 Example along-track position error distributions for windows centred on 1st July 2022, following debiasing with individual time-based bias models. The dashed lines indicate the mean error for each window. The original biased distributions from Figure 3.15 are included in grey. Densities are presented due to the different number of samples in each window. 133
3.22 Position RMSE during the 30 days post-fit for short-term debiased fits of the calibration satellites. The red marker in the colour bar indicates the RMSE baseline derived from TLEs. Note that the white regions indicate failed cases due to a lack of TLEs within the window. 135
3.23 Position RMSE during the 30 days post-fit for long-term debiased fits of the calibration satellites. The red marker in the colour bar indicates the RMSE baseline derived from TLEs. Note that the white regions indicate failed cases due to a lack of TLEs within the window. 136
3.24 Mean position RMSE during the 30 days post-fit for short-term and long-term debiased fits of the calibration satellites. 137
3.25 Position RMSE distributions during the 30 days post-fit for calibration satellite fits during the year 2022 as a function of fit window size (with and without time-based model debiasing). Note the change in fit window size interval between the short- and long-term fits. 139
3.26 Equivalent radius distributions for calibration satellite fits during the year 2022 as a function of fit window size (with and without time-based model debiasing). Note the change in fit window size interval between the short- and long-term fits, and that the y-axes has been cropped due to the presence of extreme outliers. 140
3.27 Example residual scatters in the radial-along-track plane for Etalon 1 fits, with the biased fit residuals and 3σ boundary (blue), and the debiased fit residuals and 3σ boundary (orange). 141
3.28 Examples from each GNSS constellation of along-track position error for the years 2018 to 2025. Note the larger y-axis magnitude compared to the equivalent figures for the calibration satellites. 143
3.29 Time-based model parameters for individual GNSS fits as a function of each satellite's RAAN, including GPS (blue), GLONASS (orange), Galileo (green), and BeiDou (red). 148

3.30 Time-based model amplitudes for individual GNSS fits as a function of the osculating RAAN. The dashed lines represents the fitted amplitude models for each constellation, excluding the outliers outside of the shaded regions. 152
3.31 Position RMSE distributions for GNSS satellite TLEs following debiasing with individual and ensemble time- and Moon-based models. The box plots indicate the median, upper and lower quartiles, and the IQR [137, 138]. Outliers are indicated by points. 156
3.32 Position error standard deviation distribution for GNSS satellite TLEs following debiasing with individual and ensemble time- and Moon-based models. Note that the y-axis has been cropped due to extreme outliers. 157
3.33 Position RMSE distributions for GNSS satellite TLEs, following debiasing with individual and ensemble time- and Moon-based models, for the years 2018 to 2025. . . 158
3.34 Position error standard deviation distribution for GNSS satellite TLEs, following debiasing with individual and ensemble time- and Moon-based models, for the years 2018 to 2025. 158
3.35 GNSS-derived ensemble time-based model along-track position error for the calibration satellites for the years 2018 to 2025. The along-track position error of the TLEs and the model are presented in grey and colour, respectively. 160
3.36 Residual along-track position error for the calibration satellites following debiasing with the GNSS-derived ensemble time-based model for the years 2018 to 2025. 161
3.37 Time-based model amplitudes for individual GNSS fits as a function of coplanarity with the orbit of the Moon. 163
3.38 FFT-derived time-based along-track position error models for the calibration satellites for the years 2018 to 2025. The along-track position error of the TLEs and the models are presented in grey and colour, respectively. 166
3.39 Residual along-track position error for the calibration satellites following debiasing with the individual FFT-derived time-based models for the years 2018 to 2025. 168

3.40 Example along-track position error distributions for windows centred on 1st July 2022, following debiasing with individual FFT-derived time-based bias models. The dashed lines indicate the mean error for each window. The original biased distributions from Figure 3.15 are included in grey. Densities are presented due to the different number of samples in each window. 170

4.1 TLE-based position error geometry. The three-dimensional geometry can be analysed in two dimensions as the three position vectors are coplanar. 174
4.2 Error bound models, illustrating how the simplified model does not fully capture the error behaviour and produces a physically-inconsistent lower bound for the 'inner' regime. 176
4.3 Relationship between the SLR- and TLE-based metrics for the calibration satellites. The solid line represents equal values of error, while the dashed lines represent the bounds from Table 4.1. 179
4.4 Percentage error between the SLR- and TLE-based metrics for the calibration satellites as a function of the TLE-based metric. The solid line represents equal values of error, while the dashed lines represent the bounds from Table 4.1. 180
4.5 Percentage error between the SLR- and TLE-based metrics for the calibration satellites as a function of the ratio between the intrinsic TLE error and the TLE-based metric. The solid lines represent the full error bounds from Equation (4.1). 181
4.6 Percentage error between the SLR- and TLE-based metrics for the calibration satellites as a function of the ratio between the bounds from Table 4.1 and the TLE-based metric. The solid lines represent the full error bounds from Equation (4.1). 182
4.7 A comparison of the elliptical (blue) and circular (red) error bound models. It can be seen that the difference in the TLE-based error metrics will be much larger for the minor-axis case than the major-axis case. 183
4.8 Position RMSE, relative to TLEs, during the 30 days post-fit for short-term biased fits of the calibration satellites. The red marker in the colour bar indicates the RMSE baseline derived from TLEs. Note that white regions indicate failed cases due to a lack of TLEs within the window. 186

4.9 Position RMSE, relative to TLEs, during the 30 days post-fit for long-term biased fits of the calibration satellites. The red marker in the colour bar indicates the RMSE baseline derived from TLEs. Note that white regions indicate failed cases due to a lack of TLEs within the window. 187
4.10 Position RMSE, relative to TLEs, during the 30 days post-fit for short-term debiased fits of the calibration satellites. The red marker in the colour bar indicates the RMSE baseline derived from TLEs. Note that white regions indicate failed cases due to a lack of TLEs within the window. 188
4.11 Position RMSE, relative to TLEs, during the 30 days post-fit for long-term debiased fits of the calibration satellites. The red marker in the colour bar indicates the RMSE baseline derived from TLEs. Note that white regions indicate failed cases due to a lack of TLEs within the window. 189
4.12 Difference between the TLE- and SLR-based position RMSE, during the 30 days post-fit for short-term biased fits of the calibration satellites. Positive values correspond to a larger TLE-based position RMSE. 190
4.13 Difference between the TLE- and SLR-based position RMSE, during the 30 days post-fit for long-term biased fits of the calibration satellites. Positive values correspond to a larger TLE-based position RMSE. 191
4.14 Difference between the TLE- and SLR-based position RMSE, during the 30 days post-fit for short-term debiased fits of the calibration satellites. Positive values correspond to a larger TLE-based position RMSE. 192
4.15 Difference between the TLE- and SLR-based position RMSE, during the 30 days post-fit for long-term debiased fits of the calibration satellites. Positive values correspond to a larger TLE-based position RMSE. 193
4.16 Position RMSE, with respect to TLEs, during 90 days post-epoch for test satellite TLEs. Periodic variations in position RMSE are highly visible due to varying bias in the TLEs. The dashed lines represent the established baselines for each satellite. . . 194
4.17 Position RMSE during the 90 days post-fit for long-term biased fits of the test satellites. The red marker in the colour bar indicates the RMSE baseline derived from TLEs. . . 195
4.18 SRP coefficient distributions for the test satellites fits. Note that the x-axes have been cropped due to outliers. 197

4.19 Angular RTN position errors of calibration satellite TLEs for the year 2022, estimated from with 90-day biased P-OD fits. 200
4.20 Angular RTN velocity errors of calibration satellite TLEs for the year 2022, estimated from 90-day biased P-OD fits. 201
4.21 Angular RTN position errors of test satellite TLEs for the year 2022, estimated from 90-day biased P-OD fits. 202
4.22 Angular RTN velocity errors of test satellite TLEs for the year 2022, estimated from 90-day biased P-OD fits. 203
4.23 Angular RTN position errors of calibration satellite TLEs for the year 2022, using estimated error from 90-day biased P-OD fits filtered with an hourly rolling median. . . . 204
4.24 Angular RTN velocity errors of calibration satellite TLEs for the year 2022, using estimated error from 90-day biased P-OD fits filtered with an hourly rolling median. . . . 205
4.25 Angular RTN position errors of test satellite TLEs for the year 2022, using estimated error from 90-day biased P-OD fits filtered with an hourly rolling median. 206
4.26 Angular RTN velocity errors of test satellite TLEs for the year 2022, using estimated error from 90-day biased P-OD fits filtered with an hourly rolling median. 207
4.27 Time-based along-track position error models for the calibration satellites for the year 2022, using estimated error from 90-day biased P-OD fits. The along-track position error of the TLEs and the models are presented in grey and colour, respectively. Note that the y-axis has been cropped due to extreme outliers. 210
4.28 Time-based along-track position error models for the test satellites for the year 2022, using estimated error from 90-day biased P-OD fits. The along-track position error of the TLEs and the models are presented in grey and colour, respectively. Note that the y-axis has been cropped due to extreme outliers. 211
4.29 FFT analysis of the estimated along-track angular position errors of the calibration satellites for the year 2022. The FFTs of the SLR-derived errors, as presented in Figure 3.11, are represented in grey. The orbital period of each satellite, the half period of the Moon, and the Moon's orbital period are represented by the dotted, dashed, and dash-dotted lines respectively. 212

4.30 FFT analysis of the estimated along-track angular position errors of the test satellites for the year 2022. The orbital period of each satellite, the half period of the Moon, and the Moon's orbital period are represented by the dotted, dashed, and dash-dotted lines respectively. 213
4.31 FFT-derived time-based along-track position error models for the calibration satellites for the year 2022, using estimated error from 90-day biased P-OD fits. The along-track position error of the TLEs and the models are presented in grey and colour, respectively. Note that the y-axis has been cropped due to extreme outliers. 217
4.32 FFT-derived time-based along-track position error models for the test satellites for the year 2022, using estimated error from 90-day biased P-OD fits. The along-track position error of the TLEs and the models are presented in grey and colour, respectively. Note that the y-axis has been cropped due to extreme outliers. 219

A.1 THALASSA language binding dependencies. 246

List of Tables

2.1 Summary of the perturbations considered by SGP4/SDP4. 73
2.2 Approximate orbital elements of the calibration satellites (1st January 2022). 82
2.3 Mean TLE uncertainty in the RTN frame at epoch, for 'enhanced' TLEs released after 2013. Adapted from [92]. 83
2.4 Summary of the physical model. 86
2.5 Position RMSEs, with respect to SLR, for 120-day fits with different lunisolar perturbations. 87
2.6 Comparison of calibration satellite state vectors on the 1st January 2022, before and after non-dimensionalisation. 89

3.1 Fit sweep parameters. 96
3.2 Individual calibration satellite time-based models for the years 2018 to 2025. 125
3.3 Individual calibration satellite Moon-based models for the years 2018 to 2025. 126
3.4 Approximate orbital elements of the GNSS constellations (1st January 2024). 142
3.5 RAAN-based amplitude models. 150
3.6 Ensemble bias models, each fit to all of the GNSS satellites. 154
3.7 Individual calibration satellite FFT-derived time-based models for the years 2018 to 2025. The 20 largest periodic components with a period greater than one day were included, in addition to the constant offset. The largest amplitude component is highlighted in bold. 165

4.1 Estimated error bounds for the calibration satellites for the years 2018 to 2025. 177
4.2 Approximate orbital elements of the test satellites (1st January 2022). 185
4.3 Individual calibration satellite time-based models for the year 2022, using estimated error from 90-day biased P-OD fits. 199

4.4 Individual test satellite time-based models for the year 2022, using estimated error from 90-day biased P-OD fits. 208
4.5 Individual calibration satellite FFT-derived time-based models for the year 2022, using estimated error from 90-day biased P-OD fits filtered with an hourly rolling median. The 20 largest periodic components with a period greater than one day were included, in addition to the constant offset. The largest amplitude component is highlighted in bold. 216
4.6 Individual test satellite FFT-derived time-based models for the year 2022, using estimated error from 90-day biased P-OD fits filtered with an hourly rolling median. The 20 largest periodic components with periods greater than one day, for Navstar 1 and 2, and two days, for Astra 1E and 1H, were included, in addition to the constant offset. The largest amplitude component is highlighted in bold. 218

List of Listings

1.1 Example TLE for the ISS in fixed-width format [56]. 51

1.2 Example TLE for the ISS in JSON format. The fixed-width format, presented in Listing 1.1, is included in this format in the TLE_LINE1 and TLE_LINE2 fields [56]. . . . 52

1.3 Excerpt from a SLR-derived LAGEOS-1 SP3 file [62]. 55

1.4 Excerpt from a DORIS-derived Sentinel-6A SP3 file [68]. 57

1.5 Excerpt from a GNSS-derived GPS/GLONASS/Galileo/BeiDou/QZSS SP3 file [70]. . 59

1.6 Excerpts from an ANTEX file, showing two of the assignments for the G01 SP3 identifier: NAVSTAR 28 (1992-079A) between 22th November 1992 and 17th October 2008, followed by NAVSTAR 32 (1993-032A) between 23rd October 2008 and 7th January 2009 [71]. 60

List of Acronyms

ADR	Active Debris Removal
ANTEX	Antenna Exchange
ASAT	Anti-Satellite
BDF	Backward Differentiation Formula
BMEWS	Ballistic Missile Early Warning System
CA	Conjunction Assessment
CDDIS	Crustal Dynamics Data Information System
CICLOPS	Compact Imperial College London Optical Sensor
CLI	Command Line Interface
CNES	Centre National d'Études Spatiales (National Centre for Space Studies)
CNN	Convolutional Neural Network
COSPAR	Committee on Space Research
DORIS	Doppler Orbitography and Radiopositioning Integrated by Satellite
ECEF	Earth-Centred, Earth-Fixed
ECI	Earth-Centred Inertial

EO	Earth Observation
ESA	European Space Agency
EU	European Union
EUSST	European Union Space Surveillance and Tracking
FCC	Federal Communications Commission
FFT	Fast Fourier Transform
GAM	Generalised Additive Model
GBDT	Gradient Boosting Decision Tree
GCRF	Geocentric Celestial Reference Frame
GEO	Geostationary Earth Orbit
GLONASS	Global'naya Navigatsionnaya Sputnikovaya Sistema (Global Navigation Satellite System)
GNSS	Global Navigation Satellite System
GPS	Global Positioning System
GRAVES	Grand Réseau Adapté à la Veille Spatiale (Large Network Adapted for Space Surveillance)
GRGS	Groupe de Recherche de Géodésie Spatiale (Spatial Geodesy Research Group)
GSO	Geosynchronous Earth Orbit
HEO	High Earth Orbit
IADC	Inter-Agency Space Debris Coordination Committee
ICBM	Intercontinental Ballistic Missile

IDS	International DORIS Service
IGN	Institut Géographique National (National Geographic Institute)
IGS	International GNSS Service
ILRS	International Lasing Ranging Service
IQR	Interquartile Range
IR	Infrared
ISS	International Space Station
ITRF	International Terrestrial Reference Frame
IVP	Initial Value Problem
JPL	Jet Propulsion Laboratory
JSON	JavaScript Object Notation
KF	Kalman Filter
LAGEOS	Laser Geodynamics Satellite
LEO	Low Earth Orbit
LSODAR	Livermore Solver for Ordinary Differential Equations with Automatic Method Switching for Stiff and Non-Stiff Problems and with Root-Finding
MARS	Multivariate Adaptive Regression Splines
MC	Monte Carlo
MEO	Medium Earth Orbit
MEV	Mission Extension Vehicle

ML	Machine Learning
MLP	Multilayer Perceptron
NavIC	Navigation with Indian Constellation
NEI	Non-Earth Imagery
NUFFT	Non-Uniform Fast Fourier Transform
OD	Orbit Determination
P-OD	Pseudo-Orbit Determination
PMD	Post-Mission Disposal
PNT	Position, Navigation, and Timing
POSIX	Portable Operating System Interface
PRC	People’s Republic of China
PRN	Pseudo-Random Noise
QZSS	Quasi-Zenith Satellite System
RAAN	Right Ascension of the Ascending Node
RCS	Radar Cross Section
RMSE	Root-Mean-Square Error
RSO	Resident Space Object
RTN	Radial, Transverse, Normal
SBAS	Satellite-Based Augmentation System
SDA	Space Domain Awareness

SDLR	Space Debris Laser Ranging
SGP	Simplified General Perturbations
SLR	Satellite Laser Ranging
SNR	Signal-to-Noise Ratio
SP	Special Perturbations
SP3	Standard Product 3
SRP	Solar Radiation Pressure
SSA	Space Situational Awareness
SSN	Space Surveillance Network
SST	Space Surveillance and Tracking
STM	Space Traffic Management
TEME	True Equator, Mean Equinox
TLE	Two-Line Element Set
TT	Terrestrial Time
UK	United Kingdom
USA	United States of America
USAF	United States Air Force
USN	United States Navy
USO	Ultra Stable Oscillator
USSF	United States Space Force

USSR Union of Soviet Socialist Republics

WAAS Wide Area Augmentation System

WMD Weapon of Mass Destruction

There is but one earth, tiny and fragile, and one must get 100,000 miles away from it to appreciate fully one's good fortune in living on it.

Michael Collins, Carrying the Fire: An Astronaut's Journeys

Chapter 1

Introduction

1.1 Motivation

The growth in number of objects in orbit, or Resident Space Objects (RSOs), has accelerated dramatically in the past decade with the rise of the 'New Space' era, as illustrated in Figure 1.1. Recent years have seen a large shift from primarily governmental space activities to commercial space activities, accompanied by increased launch cadences and growing popularity of small satellites. At the same time, the systems used to detect and track RSOs are improving, resulting in catalogues growing from the addition of previously untracked debris.

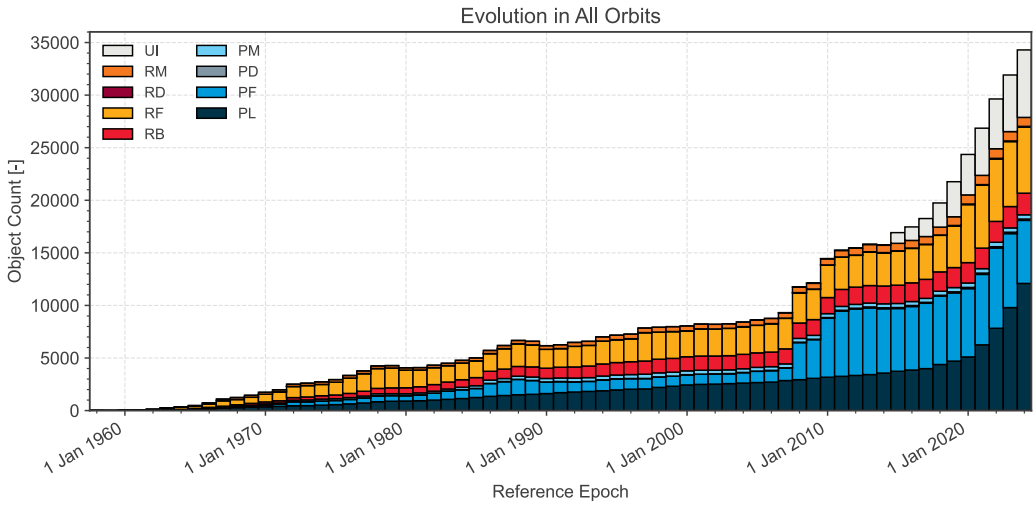


Figure 1.1: Evolution of the number of objects in geocentric orbit by object class [1]. The rapid increase in the number of payloads in orbit over the past decade can be seen in dark blue.

Currently, the main driver in the number of active payloads in orbit is the development of mega-constellations. Unlike traditional constellations, typically containing fewer than 100 satellites, mega-constellations have satellites counts in the order of thousands. For instance, to date, SpaceX have launched over 9,000 satellites for their Starlink constellation [2], with plans to add several thousand more satellites to the constellation. Starlink alone represents over half of the active payloads currently in orbit. Several other mega-constellations are currently under development, such as Project Kuiper with a planned 3,236 satellites [3] and the Guowang constellation with a planned 13,000 satellites [4]. With the deployment of these mega-constellations and others over the coming decade, congestion is expected to worsen significantly.

This growing congestion, especially in key orbital regimes such as Low Earth Orbit (LEO) and Geostationary Earth Orbit (GEO), is a threat to the continued human presence in space, due to the risk of collisions and their downstream impacts. Satellites have become particularly important for the day-to-day lives of billions of people: from Earth Observation (EO), critical for weather forecasting and climate modelling; to Position, Navigation, and Timing (PNT) services which enable safe navigation at a global scale on land, at sea, and in the air, and synchronise power grids and financial markets; to telecommunication constellations which provide connectivity anywhere on Earth, regardless of the local infrastructure. As an example of the importance of space-based services, one report estimated PNT alone as benefitting the economy of the United Kingdom (UK) by almost £14 billion per year, while the impact to the economy of losing PNT for a single day would exceed £1 billion [5].

Mega-constellations have been found to have a particularly large impact on some ground-based science, such as astronomy [6]. For example, the light reflected off Starlink satellites has been found to affect astronomy in the visual and Infrared (IR) bands by causing streaks which span across long-exposure images as satellites pass through a sensor's field of view [6]. Some mega-constellations which are under development plan to connect directly to mobile phones, requiring very large antennas to satisfy link margins. One demonstrator satellite for such a constellation, BlueWalker 3, is 'one of the brightest objects in the night sky' due to its 64 m^2 antenna array [7]. Both satellite operators and astronomers alike are working on methods for mitigating these issues, including design changes to satellite buses, operational changes, and methods for predicting and accounting for satellite passes during observations [6]. Improved satellite state estimates will be key for ensuring the effectiveness of any filtering techniques.

The limited availability of data remains a key obstacle for many Space Situational Awareness (SSA) stakeholders, particularly smaller operators and academia. Two-Line Element Sets (TLEs) published by the United States Space Force (USSF) remain one of the few publicly available, comprehensive sources of SSA information. Nevertheless, their known inaccuracy and uncertain precision limits their utility for many applications which require high quality state estimates of RSOs. Quantification and improvement of TLE accuracy is critical for a number of applications including, but not limited to, better Conjunction Assessment (CA), to prevent collisions between RSOs; better manoeuvre detection; improved transparency of the near-Earth space environment for all stakeholders, beyond only operators and governmental organisations; better safety and space sustainability; and mitigation of some of the negative effects of spacecraft on 'dark and quiet skies' for scientific research.

A significant amount of research has been conducted in the past to quantify the uncertainty in TLEs and the error propagation behaviour of SGP4, its associated analytical propagation model. This is due to their widespread use across industry and academia alike and in light of USSF not releasing any details regarding the TLE generation process. It has been demonstrated in previous literature, as will be discussed in Section 1.5, that it is possible to combine the information contained within TLEs with higher-fidelity orbital propagators to produce more accurate state vector estimates for RSOs. These previous works have focused primarily on Pseudo-Orbit Determination (P-OD) methods, where state vectors generated from the TLEs, henceforth referred to as TLE pseudo-observations, are processed with existing Orbit Determination (OD) methods. Development of improved TLE-based P-OD methods will be the core objective of this thesis.

1.2 Near-Earth Environment

1.2.1 Space Debris

Space debris poses a large threat to ongoing space operations due to the possibility of collisions. This has an impact on space operations, both directly as damage done to spacecraft hit by debris, and indirectly by the disruption caused by spacecraft having to perform collision avoidance manoeuvres. In addition to interrupting nominal operations, manoeuvres introduce additional propellant usage, reducing the overall lifetime of spacecraft.

Fragmentation events, including collisions and explosive break-ups, remain a key threat in the space environment. These are common already with current estimates suggesting a rate of approximately ten per year [8], however these are typically minor events between debris with small masses. In 1978, Kessler and Cour-Palais proposed a scenario that has since become known as the 'Kessler Syndrome' [9]. This is a scenario that suggests a runaway chain reaction whereby collisions between debris creates more debris which go on to collide with more debris in a positive feedback loop. This would result in a density of debris rendering certain orbital regimes, primarily LEO in the first instance, completely unusable. Some would suggest, including Kessler himself, that the point of instability has been reached already [8, 10, 11, 12]. Kessler Syndrome depends significantly on altitude, due to the influence of atmospheric drag on re-entry, however current predictions would suggest that, even in a scenario where there are no further launches, 'it is expected that collisions among the space debris objects already present will lead to a further growth in the space debris population' [8].

The best-known example of a major collision between an operational spacecraft and debris is the Cosmos-Iridium collision of 2009. A derelict Russian military telecommunications satellite, Cosmos 2251, collided with the active Iridium 33 telecommunications satellite with a relative velocity of over 10 km/s. This destroyed both satellites instantly and creating two large clouds of debris in LEO [13, 14, 15]. This event highlighted the threat posed by space debris and the need to improve SSA capabilities. Regrettably, it was found during subsequent analysis that the event could have been avoided with data that existed at the time, but that was not made available [15]:

> *When reflecting upon the Iridium 33 collision and future improvements to collision assessment and avoidance, the data shows policy cannot be ignored. The data existed. In one bucket, Iridium orbit estimates with covariance and a plan to maneuver for station-keeping. In the other bucket, JSpOC orbit estimates with covariance of all tracked objects. That no one could predict and stop the collision is because no one shared their bucket.*

This event was a stark reminder of the importance of collaboration and data sharing for effective SSA to take place, both in general and specifically for CA.

It cannot be understated, however, that neither collisions nor fragmentations are the only sources of space debris released into the space environment. The original source of space debris is intentional: the disposal of spacecraft and rocket bodies without any provisions for deorbiting within a small

time frame. Although international norms and regulations are being developed and implemented to mitigate the impacts of space debris, as will be discussed in Section 1.2.2, these are subject to numerous technical, financial, and geopolitical limitations. Moreover, the development of international norms and regulations cannot address existing, historical space debris.

The testing of Anti-Satellite (ASAT) weapons has been a large contributor to the space debris environment. ASAT weapons from the United States of America (USA), the Union of Soviet Socialist Republics (USSR) and Russian Federation, the People's Republic of China (PRC), and India have been tested in LEO, all producing large amounts of debris. The most infamous of these tests is the Chinese ASAT test of 2007 which destroyed Fengyun-1C, a defunct weather satellite. This remains one of the largest space debris creating events to date, producing over 2,800 trackable pieces larger than 10 cm and an estimated 150,000 untrackable particles [16, 17, 18]. The high altitude of this test further compounded the test's ongoing impact by injecting the debris into high altitudes with orbital lifetimes in the order of decades and centuries.

The core principle of the Outer Space Treaty, as it is known informally, is to promote the peaceful use of space [19]. It includes provisions against the deployment of Weapons of Mass Destruction (WMDs) in space; however, the ASAT weapons tested post-treaty were conventional and, therefore, compliant with the treaty. Recently there has been a push internationally from some states to not develop ASATs, including a commitment from the UK not to destructively test direct ascent ASATs [20], although notably this commitment specifically excludes orbital ASATs. The prevalence of dual-use technology in space remains a complication for arms control treaties, in this specific case due to the significant overlap in capabilities for some orbital ASAT concepts and benign missions, such as Active Debris Removal (ADR) and on-orbit servicing.

1.2.2 Space Debris Mitigation

Guidelines for space debris mitigation are issued by the Inter-Agency Space Debris Coordination Committee (IADC), an international governmental forum comprised of multiple space agencies from around the world [21]. These include recommendations for minimising debris released during normal operations and the potential for on-orbit explosive break-ups, two large sources of debris. Importantly, two main Post-Mission Disposal (PMD) strategies are outlined in the guidelines for LEO, and GEO and Geosynchronous Earth Orbit (GSO).

For missions in the LEO protected region, the preferred method for disposal is direct re-entry at the end of the mission. However, this is feasible only for missions with a propulsion system and sufficient remaining propellant. The more common option, therefore, is a passive decay of the orbit due to atmospheric drag. Most guidelines limit the orbital lifetime during this passive decay to a maximum of 25 years; however, several countries and organisations have started to introduce stricter requirements in light of the growing congestion in LEO. For example, both the European Space Agency (ESA) and the Federal Communications Commission (FCC) reduced the post-mission lifetime of satellites in the LEO protected region to a maximum of 5 years [22, 23].

For missions in the geosynchronous protected region, it would be impractical to deorbit spacecraft due to propulsion requirements. The guidelines recommend that '[a] manoeuvre should place such orbital stages or spacecraft in an orbit that remains outside the GEO Protected Region for at least 100 years' [24]. RSOs following this disposal strategy are placed into a higher-altitude disposal orbit satisfying the following constraints:

$$\Delta r_p \geq 235 \text{ km} + 1000\, C_R \frac{A}{m},$$

$$e \leq 0.003,$$

where Δr_p is the increase in perigee altitude from GEO; C_R is the Solar Radiation Pressure (SRP) coefficient of the spacecraft; A/m is the area-to-mass ratio of the spacecraft (in m^2/kg); and e is the eccentricity of the disposal orbit. RSOs at these altitudes will not decay and re-enter the Earth's atmosphere within any meaningful timespan, therefore this strategy represents a temporary solution to the longer-term issue of growing congestion in GEO/GSO region.

It should be emphasised that the IADC recommendations are guidelines and do not represent binding international law. Any regulations regarding space debris are enforced by individual states with their own domestic law, typically as part of the launch licensing process. This presents a challenge for ensuring effective international collaboration on space debris mitigation.

There is growing interest in the concept of ADR, both from governmental and commercial organisations. Under this concept, a spacecraft is launched to remove space debris by capturing it in orbit, followed by either actively deorbiting it in a controlled manner or otherwise reducing its orbital lifetime through, for example, augmenting its area-to-mass ratio. This would represent a significantly

accelerated timeline for some debris whose orbital lifetimes exceed decades or even centuries. One study suggested that, to stabilise the growth of the space debris population, ADR of at least five large RSOs per year was required already from the year 2020 onwards, assuming a successful PMD rate of 90 % in general for spacecraft [12].

One challenge with ADR is identifying the candidates for which removal will have the greatest positive impact on the orbital debris environment. One study combined analyses from multiple international stakeholders to produce a list of 'the 50 statistically-most-concerning objects' based on their risk of generating debris, both through collisions with operational satellites and with each other [25]. Notably, 39 of the 50 objects in the list are discarded rocket bodies which have remained in orbit. This underscores the risk posed by high-mass, high-volume RSOs, particularly those with the risk of exploding from residual propellant. An updated version of the list, released five years after the first, saw some changes in RSOs and order, however rocket bodies continue to dominate the list [26].

The first RSO on both lists, and not a rocket body, is Envisat, an EO satellite which failed in 2012. Envisat was identified as a significant risk to the orbit debris environment soon after its failure [27]:

> *Envisat is probably one of the best examples of a satellite that should have followed either NASA's 1995, or ESA's 2002 debris mitigation guidelines: Envisat is a very large target, operating at an altitude where the debris environment is the greatest and likely to increase. In the next 150 years that the satellite will remain in orbit, it will become a significant debris source and could easily become a major debris contributor from a collision with debris as small as 10 kg.*

Envisat was the target for a planned ESA ADR mission named e.Deorbit, however this was cancelled in favour of a commercial mission by Clearspace to deorbit a significantly smaller satellite [28, 29].

Closely related to ADR, from a technical perspective, is the concept of on-orbit servicing. This is where the lifetimes of operational satellites are extended by conducting repairs and replenishing consumables, such as propellant. This can greatly reduce the amount of space debris by reducing the number of launches for replacement missions. An example of a life-extension spacecraft is the Mission Extension Vehicle (MEV) which has been used twice already to extend the lifetimes of GEO telecommunications satellites by multiple years [30, 31, 32].

1.3 Space Situational Awareness

SSA encompasses a number of activities. Although many definitions exist, these typically include a combination of: Space Surveillance and Tracking (SST), which itself includes the detection, tracking, and cataloguing of RSOs, and CA and re-entry analysis; space weather monitoring; and/or planetary protection [33]. USSF and some other stakeholders, typically in defence, have started to use the term Space Domain Awareness (SDA) which includes a greater emphasis on awareness of the space domain as a whole, including attribution of events that occur in the near-Earth environment, and their impact on specific space assets and their security [34].

The origins of SSA (and later SDA) can be traced back to the beginning of the Cold War and, more specifically, the development of defences against bombers and Intercontinental Ballistic Missiles (ICBMs). For example, the USA's Ballistic Missile Early Warning System (BMEWS) provided data to Project Space Track from the 1960s onwards [35]. The importance of SSA was quickly identified, leading to the development of dedicated sensor networks for monitoring RSOs, fusing data from a variety of sources. Some examples of current major governmental SSA networks include the USA's Space Surveillance Network (SSN), Russia's Vimpel network, and the European Union Space Surveillance and Tracking (EUSST) network.

The two main types of sensor used for SST are radars and optical telescopes, the latter traditionally in the visual band but increasingly in IR. Importantly, both of these types of sensors can be used with non-cooperative RSOs, a feature which is crucial for effective surveillance of the near-Earth environment. Other systems which can be used for tracking RSOs, such as those which will be discussed in Sections 1.4.2 to 1.4.4, typically require specialised hardware. These are limited, therefore, to tracking only cooperative RSOs.

An advantage of radar-based systems is that they do not need to be tasked in the same way as traditional telescope-based systems [36]. This makes them ideal for surveillance as objects can be tracked en masse. Furthermore, radars can measure range and range-rate, unlike optical systems which remain angles-only. Nevertheless, radars are used typically only for the LEO regime as the small physical sizes of RSOs, and correspondingly small Radar Cross Sections (RCSs), result in the systems being range-limited. Nevertheless, although radars cannot reliably track small pieces of debris, they can be used for estimating debris density at various altitudes [37], providing valuable

insight into the current state of the near-Earth environment. Some examples of major radar installations include the Space Fence operated by the USA [38, 39] and the Grand Réseau Adapté à la Veille Spatiale (Large Network Adapted for Space Surveillance, GRAVES) operated by France [40].

Optical systems, on the other hand, can be used across multiple orbital regimes, including up to and beyond the cislunar regime in some cases. However, this is contingent on lighting conditions; the geometry between the observer, the RSO, and the Sun; and the weather [41]. For example, RSOs in LEO are visible typically only during twilight, restricting observations from a given location on the ground to only a few hours per day. Despite their technical limitations, optical systems are becoming increasingly popular. In addition to traditional telescope-based systems, there is growing interest in wide field of view systems which do not require tasking and can be used for surveillance. The significantly lower costs of optical systems, both initial and ongoing, when compared to traditional radar systems make them very attractive for developing and deploying large sensor networks. The low cost of these systems make them significantly more accessible outside of large governmental and commercial organisations. One example is the Compact Imperial College London Optical Sensor (CICLOPS), currently under development for research and teaching [42].

An aspect of SSA (and SDA) showing renewed interest in recent years is the issue of revisit rate, or how often a sensor network can track a given RSO. This can be critical for maintaining custody of RSOs of interest, particularly those which may manoeuvre when 'out of view', thereby delaying timely updates to their state estimates. The geographic distribution of sensors is an important factor which affects revisit rate. Historically, sensors have been concentrated within the northern hemisphere, partially due to their origins in defence, in the cases of the USA and USSR [36], and due to geopolitical constraints which may prevent the deployment of sensors in other countries. Nevertheless, the wider proliferation of more cost-effective SSA sensors has started to address this issue.

There is growing interest in space-based SSA, as an alternative to ground-based sensors, where sensors are deployed on satellites themselves to improve spatio-temporal coverage and to provide additional capabilities. One such capability is Non-Earth Imagery (NEI), where high-resolution imagery can be used for inspection and characterisation of RSOs. An example of a country investing heavily in space-based SSA is the PRC, due to a 'lack of consistent access to a worldwide network of radars and telescopes, a problem that the U.S. has not had to face' [43].

The increasing commercialisation of space has created a market for commercial SSA activities, with multiple companies developing their own sensor networks and providing Space Traffic Management (STM) services. For example, LeoLabs has a network of seven operational radars around the world with another two under development [44, 45, 46], and ExoAnalytic Solutions have a network of over 350 telescopes for monitoring Medium Earth Orbit (MEO), GEO and GSO, High Earth Orbit (HEO), and above [47]. It should be noted that many governments and their militaries, including USSF, are considering closer collaboration with commercial partners to supplement their own capabilities [48, 49].

1.4 Publicly Available Data

Many operators have high precision state estimates for their own spacecraft based on their own onboard sensors, however they remain dependent on governmental and commercial SSA organisations, and data sharing with other operators, for state estimates of other RSOs. The financial cost of these services mean that smaller operators and academia remain reliant on publicly available sources, primarily TLEs published by the USSF.

There are four main publicly available sources of data for satellite orbits, each exhibiting varying advantages and disadvantages:

- Two-Line Element Sets (TLEs);
- Satellite Laser Ranging (SLR);
- Doppler Orbitography and Radiopositioning Integrated by Satellite (DORIS); and
- Global Navigation Satellite System (GNSS).

The latter three sources are available primarily for scientific research in a variety of fields. These have the highest levels of accuracy and precision, however require dedicated hardware on spacecraft. This limits the availability of data to a small set of spacecraft in a very specific set of orbits. It should be noted that some satellites are tracked with multiple methods and have ephemerides available through multiple sources. For example, many GNSS satellites have retroreflectors for SLR [50]. This has the advantage of allowing two independent sources of data for estimating the states of the satellites and cross-validating OD methods [51, 52, 53, 54].

1.4.1 Two-Line Element Sets

SSA in the USA can be traced back to the first artificial satellite, Sputnik, launched by the USSR in October 1957 [55]. Soon thereafter, both the United States Air Force (USAF) and United States Navy (USN) started to develop their own orbit propagation models. USAF primarily used the Simplified General Perturbations (SGP) models. By 1970, the fourth version of the model, known as SGP4, was operational. This version included several simplifications to improve computational performance as 'the number of satellites in the catalog had grown to a point that computers would not be able to manage the extensive terms in the model' [55]. In 1977, the 'deep space' SDP4 model was incorporated to improve accuracy for higher-altitude satellites. It has become general practice to refer to both models jointly as SGP4. Many of the commonly used implementations of the algorithms switch between the two models automatically.

TLEs are used to distribute each RSO's particular SGP4 model parameters. TLEs are a fixed-width format with information contained within two lines, including information such as the satellite's catalogue number, epoch, orbital elements, and parameters which can be used to predict the evolution of the orbit through analytical propagation with SGP4. The age of the format is apparent when considering that the fixed-width format is a holdover from when TLEs were originally distributed as punch cards. An example of a TLE is presented in Listing 1.1, in this case one for the International Space Station (ISS).

Listing 1.1: Example TLE for the ISS in fixed-width format [56].

```
1 25544U 98067A   25182.18744301  .00005176  00000-0  97537-4 0  9990
2 25544  51.6345 237.6869 0002331 315.1210  44.9590 15.50314091517338
```

The TLE format has started to show its age for a variety of factors, namely with the limited numerical precision of the fixed-field format and a lack of metadata. USSF have started to transition to more flexible formats, such as JavaScript Object Notation (JSON), as shown in Listing 1.2. Some additional metadata is included in this format, such as the creation date of the TLE, the country of origin of the RSO and its launch date and launch site, as well as some physical data, such as an estimate of its RCS. Regardless, the actual orbital information presented in JSON format is exactly the same as that contained in the original TLE format. The original fixed-width TLE format is included still in this format, highlighting how continued backwards compatibility is needed for legacy systems.

Listing 1.2: Example TLE for the ISS in JSON format. The fixed-width format, presented in Listing 1.1, is included in this format in the TLE_LINE1 and TLE_LINE2 fields [56].


```
{
  "CCSDS_OMM_VERS": "3.0",
  "COMMENT": "GENERATED VIA SPACE-TRACK.ORG API",
  "CREATION_DATE": "2025-07-01T07:06:50",
  "ORIGINATOR": "18 SPCS",
  "OBJECT_NAME": "ISS (ZARYA)",
  "OBJECT_ID": "1998-067A",
  "CENTER_NAME": "EARTH",
  "REF_FRAME": "TEME",
  "TIME_SYSTEM": "UTC",
  "MEAN_ELEMENT_THEORY": "SGP4",
  "EPOCH": "2025-07-01T04:29:55.076064",
  "MEAN_MOTION": "15.50314091",
  "ECCENTRICITY": "0.00023310",
  "INCLINATION": "51.6345",
  "RA_OF_ASC_NODE": "237.6869",
  "ARG_OF_PERICENTER": "315.1210",
  "MEAN_ANOMALY": "44.9590",
  "EPHEMERIS_TYPE": "0",
  "CLASSIFICATION_TYPE": "U",
  "NORAD_CAT_ID": "25544",
  "ELEMENT_SET_NO": "999",
  "REV_AT_EPOCH": "51733",
  "BSTAR": "0.00009753700000",
  "MEAN_MOTION_DOT": "0.00005176",
  "MEAN_MOTION_DDOT": "0.0000000000000",
  "SEMIMAJOR_AXIS": "6793.945",
  "PERIOD": "92.884",
  "APOAPSIS": "417.394",
  "PERIAPSIS": "414.227",
  "OBJECT_TYPE": "PAYLOAD",
  "RCS_SIZE": "LARGE",
  "COUNTRY_CODE": "ISS",
  "LAUNCH_DATE": "1998-11-20",
  "SITE": "TTMTR",
  "DECAY_DATE": null,
  "FILE": "4772067",
  "GP_ID": "291295497",
  "TLE_LINE0": "0 ISS (ZARYA)",
  "TLE_LINE1": "1 25544U 98067A   25182.18744301  .00005176  00000-0  97537-4 0  9990",
  "TLE_LINE2": "2 25544  51.6345 237.6869 0002331 315.1210  44.9590 15.50314091517338"
}
```

The greatest advantage of TLEs is that the TLE catalogue is freely available and contains TLEs for a significant proportion of RSOs currently (and formerly) in near-Earth orbit. This is an unparalleled source of data for RSO state vectors. Nevertheless, TLEs are subject to a number of limitations which are difficult to overcome, primarily their limited accuracy due to the simplified perturbation models in SGP4 [55]. This is despite the fact that TLEs themselves are generated by fitting the models to higher-order predictions made by direct OD [57]. The lack of uncertainty information for TLEs means that their accuracy, even at epoch, remains effectively unknown. Rules of thumb exist for quantifying TLE accuracy and research has been conducted into TLE accuracy, as will be discussed in Section 1.5; however, TLEs remain a widely used data format with high availability across the orbital catalogue but with unknown or poor accuracy, making them unsuitable for precision applications.

The limited fidelity of the SGP4 model was identified as an issue as TLEs became more widely used, particularly when considering 'the requirements and problems in modern space mission operations' [58]. For example, the stringent requirements on accuracy for CA remain unsatisfied by traditional TLEs which are only sufficient for 'providing a first-order screening for collision alerting' [59]. The limitations of traditional TLEs and SGP4 led to the development of the SGP4-XP model, a new algorithm for propagating TLEs with greater precision, albeit with a reduction in computational performance [58]. An extension of SGP4, this updated model includes improved geopotential and resonance modelling, higher order lunisolar perturbations, a more detailed atmospheric model, and improved SRP modelling [58, 60, 61]. It should be noted that TLEs using SGP4-XP, known as Type 4 TLEs, are not compatible with the original SGP4 model, nor vice versa, because the models are based on different averaging theories and dynamical systems [58].

Binaries for SGP4-XP are available from USSF; however, mean elements compatible with SGP4-XP theory have not been publicly distributed by USSF as of the date of writing. Nevertheless, testing with synthetically generated Type 4 TLEs has demonstrated significant improvements in prediction accuracy for objects in the MEO and GEO regimes [58]. One feature, particularly critical for P-OD, is the 'more realistic dynamics coming from the SGP4-XP algorithm [yielding] a structure in the error which is more Gaussian than that of the classical SGP4' [58]. This includes a significant reduction in along-track error [60] which is the primary component of classical TLE error. Since Type 4 TLEs remain unavailable publicly, methods for reducing TLE biases remain an important area of investigation for deriving higher precision ephemerides.

1.4.2 Satellite Laser Ranging

SLR can be conducted on satellites with retroreflectors which are designed to reflect beams of light back to their point of origin. These allow ground-based laser systems to make highly precise ranging measurements, on the order of centimetres, based on the two-way time-of-flight of pulses of light.

Several institutions conduct SLR on a variety of satellites from stations distributed around the world, as illustrated in Figure 1.2. The International Lasing Ranging Service (ILRS) coordinates these efforts to combine and distribute the assorted data generated during observation campaigns 'to support programs in geodesy, geophysics, fundamental constants and lunar research, and to provide the International Earth Rotation Service with data products that are essential to the maintenance and improvement in the International Terrestrial Reference Frame (ITRF)' [50].

Orbit products derived from SLR are distributed in the Standard Product 3 (SP3) format. An example excerpt of an SP3 file is presented in Listing 1.3. These files include metadata, such as the reference frame used for the state vectors and the satellites which are included in the file, followed by a series of times and state vectors. The format is flexible, therefore additional information such as uncertainties and clock corrections can be included. Satellites are identified with alphanumeric SP3 identifiers: for example, LAGEOS-1 was assigned the identifier L51.

Geodesy satellites, the main focus of ILRS tracking campaigns, are an ideal target for the initial testing of TLE-based P-OD methods. The geodesy satellites in MEO, such as the LAGEOS and the Etalon satellites, lie outside of the atmosphere and in the 'deep space' regime where the SDP4 model is used, allowing investigation of its lunisolar modelling. Furthermore, these satellites were designed to have low area-to-mass ratios, reducing the impact of perturbations such as SRP. The passive nature of the satellites further simplifies analysis by not needing to consider the impact of manoeuvres.

Space Debris Laser Ranging (SDLR) is a related and growing field which uses laser ranging for orbit determination of non-cooperative targets. In this case, one of the challenges is the reduced Signal-to-Noise Ratio (SNR) of the reflected light, because the diffuse reflection from the whole target has to be used as opposed to the more directed reflection from a retroreflector. These techniques have been demonstrated to metre-level accuracy and during daylight, thereby presenting a promising avenue for the generation of precise orbit products for space debris [63, 64, 65].

Listing 1.3: Excerpt from a SLR-derived LAGEOS-1 SP3 file [62].

```
#cV2024 12 29  0  0  0.00000000    5041 SLR   ITR20 EST ESA
## 2347      0.00000000   120.00000000 60673 0.0000000000000
+    1   L51  0  0  0  0  0  0  0  0  0  0  0  0  0  0  0  0
+          0  0  0  0  0  0  0  0  0  0  0  0  0  0  0  0  0
+          0  0  0  0  0  0  0  0  0  0  0  0  0  0  0  0  0
+          0  0  0  0  0  0  0  0  0  0  0  0  0  0  0  0  0
+          0  0  0  0  0  0  0  0  0  0  0  0  0  0  0  0  0
++         0  0  0  0  0  0  0  0  0  0  0  0  0  0  0  0  0
++         0  0  0  0  0  0  0  0  0  0  0  0  0  0  0  0  0
++         0  0  0  0  0  0  0  0  0  0  0  0  0  0  0  0  0
++         0  0  0  0  0  0  0  0  0  0  0  0  0  0  0  0  0
++         0  0  0  0  0  0  0  0  0  0  0  0  0  0  0  0  0
%c M  cc UTC ccc cccc cccc cccc cccc ccccc ccccc ccccc ccccc
%c cc cc ccc ccc cccc cccc cccc cccc ccccc ccccc ccccc ccccc
%f  0.0000000  0.000000000  0.00000000000  0.000000000000000
%f  0.0000000  0.000000000  0.00000000000  0.000000000000000
%i    0    0    0    0      0      0      0      0         0
%i    0    0    0    0      0      0      0      0         0
/*
/*
/*
/* PCV:none       OL/AL:EOT11a   NONE     YN ORB:CoN
*  2024 12 29  0  0  0.00000000
PL51  -2021.643547 -12000.660691  -1390.309928 999999.999999
VL51 -28956.078836  -1042.399224  53351.830057 999999.999999
*  2024 12 29  0  2  0.00000000
PL51  -2365.844003 -11991.852989   -748.247802 999999.999999
VL51 -28385.654553   2508.709681  53630.658832 999999.999999
*  2024 12 29  0  4  0.00000000
PL51  -2702.303040 -11940.518083   -103.844802 999999.999999
VL51 -27666.199591   6043.214461  53741.831440 999999.999999
*  2024 12 29  0  6  0.00000000
PL51  -3029.246559 -11846.936208    540.883076 999999.999999
VL51 -26800.209234   9547.631372  53684.750506 999999.999999
*  2024 12 29  0  8  0.00000000
PL51  -3344.934600 -11711.548789   1183.915914 999999.999999
VL51 -25790.876175  13008.589020  53459.361179 999999.999999
*  2024 12 29  0 10  0.00000000
PL51  -3647.669644 -11534.956749   1823.236411 999999.999999
VL51 -24642.079674  16412.884590  53066.154256 999999.999999
*  2024 12 29  0 12  0.00000000
PL51  -3935.804777 -11317.918156   2456.836433 999999.999999
VL51 -23358.371300  19747.539673  52506.167259 999999.999999
```

1.4.3 Doppler Orbitography and Radiopositioning Integrated by Satellite

DORIS is a system that was designed jointly by the Centre National d'Études Spatiales (National Centre for Space Studies, CNES), the Institut Géographique National (National Geographic Institute, IGN), and the Groupe de Recherche de Géodésie Spatiale (Spatial Geodesy Research Group, GRGS) to be 'able to determine within a few centimetres, the location of satellites and ground beacons' [66, 67]. This system takes advantage of Doppler shift, the physical phenomenon whereby a received signal is shifted in frequency with respect to the transmitted signal due to the relative motion between the transmitter and receiver.

The DORIS system is split into two main segments: the 'flight segment', onboard a satellite, which features a radio receiver; and the 'ground segment', which can be further subdivided into the control and processing centre which manages the entire system, and a series of ground stations distributed around the world with radio transmitters, as illustrated in Figure 1.3. Both the receiver on-board the satellite and the transmitters of the ground beacons have Ultra Stable Oscillators (USOs) to provide a highly-stable frequency reference and a clock which enables the system to achieve its high level of accuracy and precision.

The 'flight segment' conducts one-way Doppler shift measurements by comparing signals received from the ground beacons against its own internal frequency reference, thereby estimating the radial velocity between the satellite and the ground beacons. DORIS measures the frequency change for two different frequencies to account for the ionosphere, a technique used also by modern GNSS constellations. By knowing the positions of the ground beacons, this information can be used in a state estimator, alongside a dynamic model of the satellite's trajectory, to estimate the state of the satellite. The orbit determination process can be executed on-board the satellite, however it is typically conducted at the control and processing centre following downlink of the receiver's telemetry.

DORIS has been used for a number of scientific satellites over the past 35 years, providing highly accurate orbit solutions which have enabled multiple scientific advances in EO. The orbit products for these satellites are publicly available, collated by the International DORIS Service (IDS) and distributed through channels such as the Crustal Dynamics Data Information System (CDDIS), providing a valuable source of precise ephemerides in the LEO regime. An example of a DORIS-derived SP3 orbit product is presented in Listing 1.4.

Listing 1.4: Excerpt from a DORIS-derived Sentinel-6A SP3 file [68].

```
#cV2025  1  2 20 24  0.00000000   14307 ORBIT ITRF  FIT CNES
## 2347 419040.00000000    60.00000000 60677 0.8500000000000
+    1   L40  0  0  0  0  0  0  0  0  0  0  0  0  0  0  0  0
+          0  0  0  0  0  0  0  0  0  0  0  0  0  0  0  0  0
+          0  0  0  0  0  0  0  0  0  0  0  0  0  0  0  0  0
+          0  0  0  0  0  0  0  0  0  0  0  0  0  0  0  0  0
+          0  0  0  0  0  0  0  0  0  0  0  0  0  0  0  0  0
++
++
++         0  0  0  0  0  0  0  0  0  0  0  0  0  0  0  0  0
++         0  0  0  0  0  0  0  0  0  0  0  0  0  0  0  0  0
++         0  0  0  0  0  0  0  0  0  0  0  0  0  0  0  0  0
%c L  cc TAI ccc cccc cccc cccc cccc ccccc ccccc ccccc ccccc
%c cc cc ccc ccc cccc cccc cccc cccc ccccc ccccc ccccc ccccc
%f  1.2500000  1.025000000  0.00000000000  0.000000000000000
%f  0.0000000  0.000000000  0.00000000000  0.000000000000000
%i    0    0    0    0      0      0      0      0         0
%i    0    0    0    0      0      0      0      0         0
/* PCV:IGS20
/* OL/AL/SS:FES2014b NONE     ITRF2020 YNY ORB:CoM CLK:CoM
/*
/*
*  2025  1  2 20 24  0.00000000
PL40  3427.9663906  -646.7559973 -6882.8796506999999.9999990
VL40-16129.1308738 66144.5226867-14239.4965694999999.9999990
*  2025  1  2 20 25  0.00000000
PL40  3327.6801768  -248.6596874 -6957.5388118999999.9999990
VL40-17290.4151171 66521.7271413-10640.4682553999999.9999990
*  2025  1  2 20 26  0.00000000
PL40  3220.5934921   151.1130474 -7010.4993864999999.9999990
VL40-18395.6638325 66703.1103834 -7008.5013792999999.9999990
*  2025  1  2 20 27  0.00000000
PL40  3107.0476001   551.3838859 -7041.5974345999999.9999990
VL40-19443.2238359 66687.6373896 -3354.8396193999999.9999990
*  2025  1  2 20 28  0.00000000
PL40  2987.3931386   950.9700343 -7050.7366836999999.9999990
VL40-20431.6234906 66474.8530336   309.2102943999999.9999990
*  2025  1  2 20 29  0.00000000
PL40  2861.9890332  1348.6877162 -7037.8888091999999.9999990
VL40-21359.5715228 66064.8851870  3972.3112939999999.9999990
*  2025  1  2 20 30  0.00000000
PL40  2731.2014206  1743.3556745 -7003.0935173999999.9999990
VL40-22225.9551385 65458.4458377  7623.1288985999999.9999990
```

1.4.4 Global Navigation Satellite Systems

Currently-operating GNSS constellations use the same basic operating principle. Each satellite generates and transmits a timing signal from an onboard atomic clock. When received, each timing signal includes a delay due to the distance between the receiver and the satellite. This is used to estimate the distance, or 'pseudo-range', between the receiver and each satellite. The pseudo-ranges from multiple satellites are used to multilaterate the receiver's position. This process can be inverted with multiple receivers on the ground multilaterating the position of a satellite.

The International GNSS Service (IGS), equivalent to the ILRS and IDS, operates a network of ground-based GNSS receivers, as illustrated in Figure 1.4, which tracks GNSS satellites to '[provide], on an openly available basis, the highest-quality GNSS data, products, services in support of the terrestrial reference frame; Earth observation and research; Position, Navigation and Timing (PNT); and other applications that benefit the scientific community and society' [69].

GNSS orbit products from the IGS use the SP3 file format, as illustrated in Listing 1.5. In this case, the orbit solutions for multiple satellites are included in a single file. Additionally, the product does not include velocity vectors which must be estimated from position information only. The SP3 identifiers for GNSS satellites are typically linked to their Pseudo-Random Noise (PRN) codes: for example, G01 refers to the Global Positioning System (GPS) satellite with PRN code 1. Importantly, these PRN codes are not statically assigned to each satellite and can change multiple times throughout a satellite's lifetime. Antenna Exchange (ANTEX) files, published by the IGS, contain a variety of information about GNSS satellites, including information which links SP3 identifiers to Committee on Space Research (COSPAR) identifiers without ambiguity, as shown in Listing 1.6.

Four different GNSS constellations were considered for this study: GPS, the Global'naya Navigatsionnaya Sputnikovaya Sistema (Global Navigation Satellite System, GLONASS), Galileo, and BeiDou. Additional GNSS constellations, such as Navigation with Indian Constellation (NavIC), the Quasi-Zenith Satellite System (QZSS), and various Satellite-Based Augmentation Systems (SBASs), are monitored by the IGS but were not considered for this study due to its focus on widespread MEO coverage. Nevertheless, these could be used in future studies to investigate other orbital regimes, such as Tundra-type MEO, as used by QZSS; and GEO and GSO, as used by some of the earlier BeiDou satellites, as well as NavIC and SBAS.

Listing 1.5: Excerpt from a GNSS-derived GPS/GLONASS/Galileo/BeiDou/QZSS SP3 file [70].

```
#dP2025  1  1  0  0  0.00000000     289 d+D   IGS20 FIT AIUB
## 2347 259200.00000000   300.00000000 60676 0.0000000000000
+  122   G01G02G03G04G05G06G07G08G09G10G11G12G13G14G15G16G17
+        G18G19G20G21G22G23G24G25G26G27G28G29G30G31G32R01R02
+        R03R04R05R07R08R09R11R12R14R15R16R17R18R19R20R21R22
+        R24R26E02E03E04E05E06E07E08E09E10E11E12E13E14E15E16
+        E18E19E21E23E24E25E26E27E29E30E31E33E34E36C06C07C08
+        C09C10C11C12C13C14C16C19C20C21C22C23C24C25C26C27C28
+        C29C30C32C33C34C35C36C37C38C39C40C41C42C43C44C45C48
+        J02J03J04  0  0  0  0  0  0  0  0  0  0  0  0  0  0
++         5  5  5  5  5  5  5  5  5  5  5  5  5  5  5  5  5
++         5  5  5  5  5  5  5  5  5  5  5  5  5  5  5  6  5
++         6  6  6  6  5  5  5  5  5  5  5  5  5  5  5  5  5
++         5  5  5  5  5  5  5  5  5  5  5  5  5  5  5  5  5
++         5  5  5  5  5  5  5  5  5  5  5  5  5  5  5  5  5
++         5  5  5  5  5  5  5  5  6  5  5  5  5  5  5  5  5
++         5 10  6  5  5  5  5  5  5  5  6  6  5  5  5  5  6
++         5  5  5  0  0  0  0  0  0  0  0  0  0  0  0  0  0
%c M  cc GPS ccc cccc cccc cccc cccc ccccc ccccc ccccc ccccc
%c cc cc ccc ccc cccc cccc cccc cccc ccccc ccccc ccccc ccccc
%f  1.2500000  1.025000000  0.00000000000  0.000000000000000
%f  0.0000000  0.000000000  0.00000000000  0.000000000000000
%i    0    0    0    0      0      0      0      0         0
%i    0    0    0    0      0      0      0      0         0
/* Center for Orbit Determination in Europe (CODE)
/* MGEX orbits and clocks for year-day 2025-0010
/* Middle day of a 3-day long-arc multi-GNSS solution
/* Systems considered: GPS/GLONASS/Galileo/BeiDou/QZSS
/* Product reference - DOI 10.48350/197028
/* PCV:IGS20      OL/AL:FES2014b NONE     YN ORB:CoN CLK:CoN
*  2025  1  1  0  0  0.00000000
PG01  15931.689356   2160.462721  21149.136212      8.650932
PG02  17192.894167   3547.033349  20509.676679   -278.712580
PG03  20188.149199  -8513.125806  14767.090134    636.907781
PG04  25319.881336   -270.110783  -8256.099511    504.888486
PG05 -14191.957003  -5880.588119 -21848.628846   -197.688078
PG06  -5062.040544 -25515.997354   5105.128052    -85.994597
PG07  10081.364971 -13723.268739 -19732.411382    -14.120527
PG08  25884.590748   6163.367635  -3410.079531    451.268304
PG09  20290.099271  -7745.556039 -15431.223106    510.533183
PG10  -7192.687905  21829.612842  13240.559699   -257.689664
PG11 -12191.685719 -22442.407838  -7359.098272   -752.547708
PG12 -20214.045976   4343.905353  16358.467882   -561.781628
```

Listing 1.6: Excerpts from an ANTEX file, showing two of the assignments for the G01 SP3 identifier: NAVSTAR 28 (1992-079A) between 22th November 1992 and 17th October 2008, followed by NAVSTAR 32 (1993-032A) between 23rd October 2008 and 7th January 2009 [71].

```
BLOCK IIA           G01                 G032      1992-079A TYPE / SERIAL NO
                                             0    29-JAN-17 METH / BY / # / DATE
    0.0                                                     DAZI
    0.0  17.0   1.0                                         ZEN1 / ZEN2 / DZEN
    2                                                       # OF FREQUENCIES
  1992    11    22     0     0    0.0000000                 VALID FROM
  2008    10    16    23    59   59.9999999                 VALID UNTIL
```

```
BLOCK IIA           G01                 G037      1993-032A TYPE / SERIAL NO
                                             0    29-JAN-17 METH / BY / # / DATE
    0.0                                                     DAZI
    0.0  17.0   1.0                                         ZEN1 / ZEN2 / DZEN
    2                                                       # OF FREQUENCIES
  2008    10    23     0     0    0.0000000                 VALID FROM
  2009     1     6    23    59   59.9999999                 VALID UNTIL
```

GPS The oldest of the currently-operating GNSS constellations, this system was developed by the USA from the 1970s onwards and reached fully operational status in 1995 [72]. Originally envisioned as a military navigation system, it was opened later to the public and has become vital to many industries, both for navigation and timing.

GLONASS The Soviet, later Russian, equivalent to GPS, this system was developed during the same time period, reaching fully operational status in 1996 [72]. The system quickly fell into disrepair but a modernisation programme over the past 20 years has restored the system to fully operational status and introduced improved interoperability with the other GNSS constellations [73, 74, 75, 76].

Galileo Currently under development by the European Union (EU) and ESA, this constellation was designed to provide an independent European PNT capability without relying on other GNSS constellations. Initial operational status was achieved in 2016 [77] with fully operational status expected within the next year.

BeiDou This constellation started as regional system for the PRC, using a series of satellites in MEO and GEO/GSO [78]. The third, and current, generation of this constellation was developed following the PRC's departure from the Galileo programme [79, 80]. Global coverage was achieved with a series of MEO satellites, reaching fully operational status in 2020 [78].

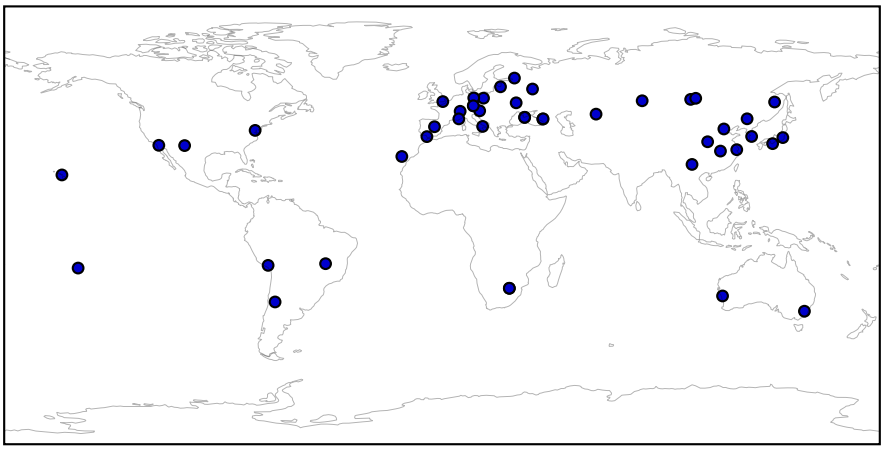


Figure 1.2: Active ILRS stations (as of June 2025). Data from [81].

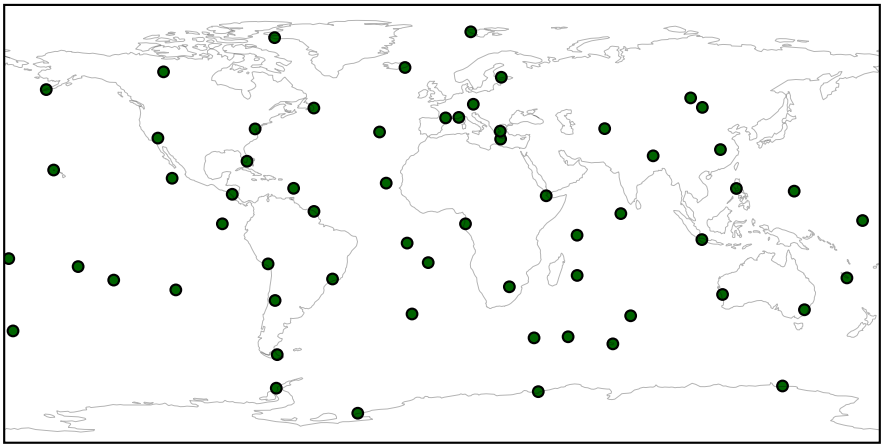


Figure 1.3: Active DORIS ground beacons (as of February 2025). Data from [82].

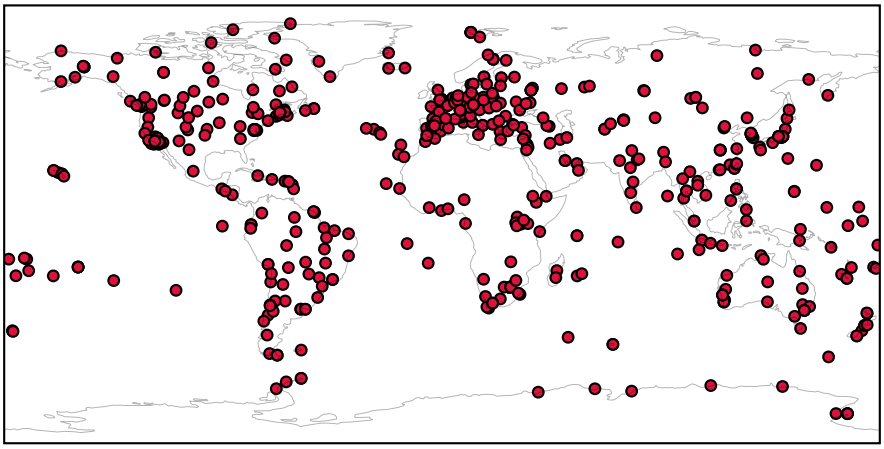


Figure 1.4: Active IGS stations (as of July 2025). Data from [83].

1.5 Background on Improving Two-Line Element Set Accuracy

Fieger used P-OD as a method of evaluating the prediction accuracy of semi-analytical propagators, specifically for highly-eccentric Molniya-type orbits [84]. This involved using batch least squares to fit a semi-analytical propagation model to the corresponding 'deep space' TLEs of the satellites, followed by propagation and comparison with future TLEs. This work demonstrated two important ideas: firstly, the use of TLEs as a source of pseudo-observations; and secondly, the use of TLEs to evaluate the quality of TLE-based P-OD fits.

Flohrer, Krag, and Klinkrad used P-OD to assess and categorise TLE uncertainty to assist with CA [85], specifically to face 'the problem that no covariance information is available for the TLE data set'. Three main methods for estimating TLE covariance were outlined: comparing subsequent TLEs through differencing; reconstructing raw observations by acquiring (or assuming) sensor data and reconstructing the TLE production process; or comparing TLEs to 'high-accuracy post-processing orbits, as they are available for some satellites to the scientific community', specifically in reference to SLR, DORIS, and GNSS orbit products.

One of the seminal works for TLE-based P-OD was presented by Levit and Marshall [86]. In this study, batch least squares methods were applied to the TLEs of several satellites in LEO and MEO to improve estimates of their state vectors. Geodesy satellites were the main focus of this work, using SLR-based orbit products for reference states. The P-OD was followed by analysis of the prediction error when propagating the estimated states into the future, compared to using the original TLEs directly with SGP4. The methods resulted in 'a predicted range error that increase[d] at a typical rate of 100 m per day, approximately a 10-fold improvement over individual TLE's [sic] propagated with their associated analytic propagator'. One limitation of the analysis conducted in this work was the number of test cases: for each satellite, 50 epoch dates were selected uniformly throughout the year 2004, limiting insight into the temporal variation in TLE quality. Nevertheless, several key contributions to the literature include successful demonstration of the technique, results on hyperparameter tuning, and the identification of TLE bias as one of the main challenges facing TLE-based P-OD.

Bennett, Sang, Smith, and Zhang investigated the use of bias models as part of the P-OD process to improve orbit predictions with SLR data [87]. They considered a combination of polynomials and sinusoidal functions to estimate biases in the along-track, across-track, and radial directions. In one

example, the maximum along-track error was reduced from 16.6 km to 4.8 km with TLE-based P-OD, further reduced to 1.7 km following bias estimation. The bias estimation was conducted over a period of 3 days as part of the OD pipeline, however it presents the question of whether more generalised models can be used to estimate the bias in a given TLE series over a longer time period.

Vallado, Virgili, and Flohrer further extended the analysis of using TLE-based P-OD for future orbit prediction by considering additional orbital regimes, hyperparameters, and force models [88]. This analysis provided several important conclusions, including that '[t]he largest uncertainty in virtually all cases was in the along-track direction' and that the fidelity of the physical model, particularly for atmospheric drag, had a limited impact on the quality of the state estimate as '[a]t the level of accuracy of the TLE, it is probably not observable'.

Oltrogge and Ramrath examined the applicability of TLEs and SGP4 from LEO through GEO/GSO by generating and analysing TLEs fitted to high-fidelity numerically-propagated 'truth' orbits [89]. The 'fit process (and by extension the underlying SGP4 theory) typically perform[ed] to better than 1 km across the entire orbit altitude range', performance which is better than that typically seen with real TLEs. Nevertheless, it was noted that '[t]his [was] not an unexpected result, when one it [sic] considers the components of error that exist in a non-cooperative tracking system'. This study highlighted that synthetically generated TLEs will typically have properties which differ from real TLEs. The lack of knowledge of tracking system performance presents a challenge when trying to reconstruct the TLE generation pipeline.

San-Juan, Pérez, San-Martín, and Vergara investigated a non-intrusive method for extending TLE validity with minimal changes to the current propagation scheme [90]. A Holt-Winters model [91] was used to model the time series of errors resulting from the TLE propagation. This model considers that a time series is composed of the combination of a secular trend with a periodic oscillation and random noise. The method was tested using TLEs and operator data for Deimos 1, an EO satellite in LEO. It was found that the proposed 'hybrid' propagator resulted in an order of magnitude improvement in prediction with respect to standard TLE propagation.

Geul, Mooij, and Noomen investigated TLE differencing techniques to quantify uncertainty in the dataset without requiring high-accuracy reference ephemerides [92]. This study made a distinction between 'classic' and 'enhanced' TLEs, where the former are estimated directly from observations,

while the latter are fitted to pseudo-observations of higher-order predictions, as discussed in Section 1.4.1. The two types of TLEs had different error behaviours with '[e]nhanced TLEs offer[ing] improved uncertainty and error-growth properties'. An asymmetry in error behaviour was noted between forward and backward propagation which varied by TLE type: 'classic' TLEs tended to be more accurate before epoch, while 'enhanced' TLEs were more accurate after epoch. Interestingly, it was observed that the minimum error for 'enhanced' TLEs did not occur at epoch but, instead, slightly after epoch. Similar to other studies, along-track position and radial velocity were identified as the main error components.

Racelis and Joerger investigated the error in TLEs for satellites in MEO and GEO [93], using precise ephemerides for GPS and Wide Area Augmentation System (WAAS)[1] satellites. This study considered data over a 20 year timespan, from 1998 to 2018, revealing that '[a]n apparent shrinkage of error spread occurs sometime after July 2012, and again after the January 2015 mark'. GPS and WAAS TLEs saw a change in error behaviour in October 2015, suggesting that some change may have been made in the TLE generation pipeline. Notably, GPS errors in MEO became smaller and more consistent, while the opposite was true for WAAS in GEO. This result presents a challenge for TLE-based P-OD as it suggests that TLE behaviour and quality can change significantly without any notice. This could potentially affect a given P-OD pipeline by changing the assumed properties of the underlying data. This study also highlighted that the '[m]agnitudes of along-track errors are significantly larger than errors in the other two directions' for MEO, however for GEO 'along-track and cross-track errors are of similar magnitude'.

Pérez, San-Martín, López, Vergara, Wittig, and San-Juan proposed an improvement on their previous work on 'hybrid' propagators [94]. The same method was used as before: a low-fidelity orbital propagator combined with a Holt-Winters model to produce more accurate state estimates. Although this method was demonstrated to be effective, the error model required control data and model tuning for each specific initial condition. The improvement made to the method in this work was to consider a grid of initial conditions, in this case generated by adjusting key Keplerian orbital parameters, and fitting the 'hybrid' propagator for each initial condition. For a given initial condition in the region of interest, the parameters of the 'hybrid' propagator can be interpolated, or even extrapolated, without requiring neither control data nor tuning of a new model. Two techniques were considered for this:

[1] WAAS is the SBAS for North America.

Generalised Additive Models (GAMs) [95] and Multivariate Adaptive Regression Splines (MARS) [96]. It was found that '[t]he former has proven to be more reliable, although the latter can lead to better results in the short term when it is applied to a dense grid'.

Ly, Lucken, and Giolito investigated the application of Machine Learning (ML) methods for correcting TLEs of the GPS constellation [97]. This study focused on making corrections to the along-track error with kernel regression techniques and polynomials which revealed significant correlation between the TLE error and both the Sun-Earth and Moon-Earth distances. For the 14 satellites considered in the study, TLE accuracy was improved 'from 5 km to 1.5 km with a 95% confidence level'. Two key takeaways from this study were that the along-track error of the TLEs had 'a periodical component that corresponds approximately to the moon cycle' and that the mean along-track error varied significantly within the analysed subset of GPS satellites.

Li, Zhang, Huang, and Sang investigated ML for estimating TLE error for LEO and MEO satellites [98]. TLE differencing was used to estimate TLE error and to produce a training dataset in the absence of high-accuracy ephemerides. The inputs were a vector containing the initial state at a given TLE, the state at a future time, the period between the two times, and the B^* term. The output was a vector of the state error at the future time. Two ML methods were tested, a Gradient Boosting Decision Tree (GBDT) and a Convolutional Neural Network (CNN), with the TLEs of five SLR satellites. Both models were highly effective with 14 day orbit predictions 'improved by more than 75% in the along-track direction and 90% in the cross-track and radial directions'.

A study by Chen and Lin focused on applications of TLE-based P-OD in LEO, specifically for SpaceX's Starlink constellation, again using batch least squares methods [99]. It was found that restricting pseudo-observations to within two orbital period of each TLE epoch improved fit prediction accuracy 'by approximately 10% compared to a uniform distribution'. This highlights the importance of sampling strategy and its impact on fit quality, and that it may be beneficial to limit the amount of propagation with SGP4 to limit the introduction of propagation errors in the pseudo-observations.

Bizalion, Guillot, Petit, and Lucken investigated the use of neural networks to correct the errors in LEO TLEs [100], building directly from the work by Ly, Lucken, and Giolito [97]. A Multilayer Perceptron (MLP) network with 8,000 neurons was used to estimate a position and velocity error vector, based on TLE elements, augmented with the argument of latitude, longitude, latitude, and the Sun-

Earth and Moon-Earth distances. The network was trained using 10 months of TLE data for 4,500 inactive RSOs in LEO. By using the neural network, 'the state vector errors are corrected by at least 40% for 70% of the TLE[s]'. Importantly, it was shown that the neural network worked for a select number of active RSOs. It is important to note that the authors of this article were given access to higher-accuracy Special Perturbations (SP) data from the USAF, a dataset which is not made available to the public.

The newer-format Type 4 TLEs have not been released publicly by USSF, as discussed in Section 1.4.1. In the meantime, COMSPOC, a commercial SSA company, have started to release their own Type 4 TLEs. These are generated by fitting the SGP4-XP model to ephemerides 'obtained from any source' [101]. This can include traditional TLEs, however there are limited details about the exact processes that are being used by COMSPOC to generate the Type 4 TLEs, and it is unclear whether and how the biases present in traditional TLEs may affect their fitting process.

1.6 Thesis Objectives

Many of the important works regarding TLE-based P-OD were published up to 15 years ago. Since then, it has been suggested that the TLE generation pipeline has changed multiple times, in some cases significantly, evidenced by changes in TLE error behaviour. An important question, therefore, is whether the previous promising outcomes of applying P-OD to improve state estimates for RSOs remain reproducible with the TLEs being published by USSF.

Previous attempts to model deep space TLE biases have focused often on ML techniques, specifically large neural networks. Although effective, these methods often result in 'black box' models where their inner workings are not well understood. The limited amount of state information, and its spatial distribution in the near-Earth environment, means that extrapolation of TLE bias models is almost guaranteed. The explainability of models, especially how they link to orbital regimes and specific orbits, are a key requirement for evaluating the level of confidence for this extrapolation.

Without access to higher-accuracy ephemerides, such as USSF's SP catalogue, analysis of TLEs is restricted typically to the small subset of satellites, typically scientific, with alternative publicly available orbit products. This contributes to the aforementioned issues whereby analysis focuses on limited orbits and orbital regimes. Critically, the TLEs of these RSOs may not be representative of the gen-

eral TLE population. Methods for evaluating TLEs, and TLE enhancement methods, without needing other sources of ephemerides would allow analysis to be expanded to the rest the TLE catalogue.

Therefore, the objectives of the thesis are to:

1. Assess whether TLE-based P-OD continues to improve the accuracy of state estimates based on contemporary TLEs;

2. Conduct further analysis into the biases present in deep space TLEs, including developing more-explainable bias models; and

3. Investigate methods for analysing TLE accuracy and precision without requiring alternative higher-accuracy ephemerides for RSOs.

1.7 Thesis Outline

In Chapter 2, the methodology for conducting P-OD on TLE series with batch least squares methods will be presented, including discussions on required physical model fidelity and TLE sampling techniques.

In Chapter 3, examples of conducting TLE-based P-OD for multiple geodesy satellites will be presented, followed by an exploration of the error characteristics of deep space TLEs, for the same geodesy satellites and for several GNSS constellations. This will include the presentation of several individual and group bias models which can be used to debias TLEs in MEO.

In Chapter 4, the use of TLEs as a reference instead of alternative higher-accuracy ephemerides will be discussed, including a comparison with higher-accuracy error metrics, their use for evaluating P-OD, and the presentation of initial results of estimating TLE bias models without high-accuracy reference ephemerides.

Finally, in Chapter 5, a summary of the results of the thesis will be presented, including the key contributions made to the state-of-the-art, and a brief discussion on the possible avenues of future work in TLE evaluation and enhancement.

1.8 Publications

Journal Articles

M. I. Hallgarten La Casta and D. Amato, 'Debiasing of two-line element sets for batch least squares pseudo-orbit determination in MEO and GEO,' *Advances in Space Research*, vol. 75, no. 10, 15th May 2025. Accessed: 6th May 2025. [Online]. Available: https://www.sciencedirect.com/science/article/pii/S0273117725002856.

Conference Papers

M. I. Hallgarten La Casta and D. Amato, 'Bias Correction of Two-line Element Sets in the MEO Regime,' presented at the NATO DIANA International Workshop, London, United Kingdom, 4th Apr. 2025.

M. I. Hallgarten La Casta and D. Amato, 'Generalisable Bias Correction of Two-line Element Sets in the Medium Earth Orbit Regime,' presented at the 9th European Conference on Space Debris, Bonn, Germany, Apr. 2025. Accessed: 28th Sep. 2025. [Online]. Available: https://conference.sdo.esoc.esa.int/proceedings/sdc9/paper/282.

E. Kaygorodov, M. Hjelmstad Rattigan, M. I. Hallgarten La Casta and D. Amato, 'Development and Operation of CICLOPS, the Compact Imperial College London Optical Sensor,' presented at the 9th European Conference on Space Debris, Bonn, Germany, Apr. 2025. Accessed: 28th Sep. 2025. [Online]. Available: https://conference.sdo.esoc.esa.int/proceedings/sdc9/paper/283.

M. I. Hallgarten La Casta and D. Amato, 'Revisiting Filtering of Two-line Element Sets for Higher Precision Ephemerides,' presented at the 29th International Symposium on Space Flight Dynamics, ESA ESOC, Darmstadt, Germany, Apr. 2024. Accessed: 28th Sep. 2025. [Online]. Available: https://www.researchgate.net/publication/380784772_Revisiting_Filtering_of_Two-line_Element_Sets_for_Higher_Precision_Ephemerides.

M. I. Hallgarten La Casta, D. Amato and M. Vasile, 'Chebyhsev-based Polynomial Algebra Monte Carlo Propagation with Generalised Equinoctial Orbital Elements,' presented at the 2nd International Stardust Conference, ESA ESTEC, Noordwijk, the Netherlands, 8th Nov. 2022.

M. I. Hallgarten La Casta, D. Amato and M. Vasile, ‘Polynomial Algebra for Uncertainty Propagation in Generalised Equinoctial Orbital Elements,’ presented at the 73rd International Astronautical Congress, Paris, France, 19th Sep. 2022. Accessed: 28th Sep. 2025. [Online]. Available: https://www.researchgate.net/publication/365114606_Polynomial_Algebra_for_Uncertainty_Propagation_in_Generalised_Equinoctial_Orbital_Elements.

M. I. Hallgarten La Casta, L. Sánchez Fernandez-Mellado, D. Amato and M. Vasile, ‘Non-linear set propagation with generalised equinoctial orbital elements,’ presented at the 5th International Workshop on Key Topics in Orbit Propagation Applied to Space Situational Awareness, Logroño, Spain, 23rd Jun. 2022.

Chapter 2

Pseudo-Orbit Determination

In this chapter, TLE-based P-OD will be introduced, using non-linear weighted batch least squares for state estimation. An overview of the dynamical system for TLE propagation will be presented, followed by an introduction to multiple TLE sampling strategies, the mathematical basis for the non-linear weighted batch least squares, methods for evaluating the results of state estimation, and implementation details specific to this thesis.

2.1 Two-Line Element Set Propagation

TLEs are propagated with two slightly different models, known as SGP4 and SDP4 respectively, depending on the orbital regime of the satellite. It should be noted that it has become common to refer to both propagators jointly as SGP4 [109]. Unless otherwise stated, the combined terminology will be used to refer to both propagators.

TLEs represent the state of objects with a number of parameters, including a set of mean elements and a ballistic coefficient:

t_0 Time at Epoch;

n_0 Mean Motion;

e_0 Eccentricity;

i_0 Inclination;

ω_0 Argument of Perigee;

Ω_0 Right Ascension of the Ascending Node (RAAN);

M_0 Mean Anomaly; and

B^* Atmospheric Drag Coefficient.

The element set, and associated equations used for propagation in SGP4, combine contributions from, among others, Brouwer and Kozai for the zonal theory, Lane for atmospheric drag, and Cranford and Hujsak for deep space perturbations [55, 59, 110].

For lower-altitude satellites, Earth gravitational harmonics and atmospheric drag are modelled, as these are the dominant perturbations for this orbital regime. For higher-altitude satellites, the deep space model is used which considers the gravitational effects of the Moon and the Sun, as well as additional Earth gravitational harmonics 'which are of particular importance for half-day and one-day period orbits' [110]. The higher-altitude regime, where the deep space SDP4 model is used, is defined as applying to objects with orbital periods greater than 225 minutes [59]. A summary of the perturbations is presented in Table 2.1.

It should be noted that, although SGP4 accounts for multiple perturbations, the propagator uses low-fidelity models, incorporating a large number of assumptions and simplifications to reduce computational complexity and increase computational performance. The propagator is designed for fast OD and approximate pass predictions, not high-accuracy propagation. A general rule of thumb is that state predictions based on TLEs provide sufficient accuracy for general situational awareness and the pointing of antennas, but not for precision applications.

One of the key simplifications, applied to multiple perturbations within SGP4, is the calculation of several constants at the epoch of the TLE which are then held fixed and applied for all future and past predictions made with the TLE. In effect, many perturbations are linearised at TLE epoch and then extrapolated to other times during the update cycle of the propagator. Furthermore, perturbations are based on simplified models: for example, atmospheric drag uses a simple power-law for the density of the atmosphere. Power series appear on multiple occasions throughout SGP4 and these are typically truncated to improve computational performance at the loss of some accuracy.

Table 2.1: Summary of the perturbations considered by SGP4/SDP4.

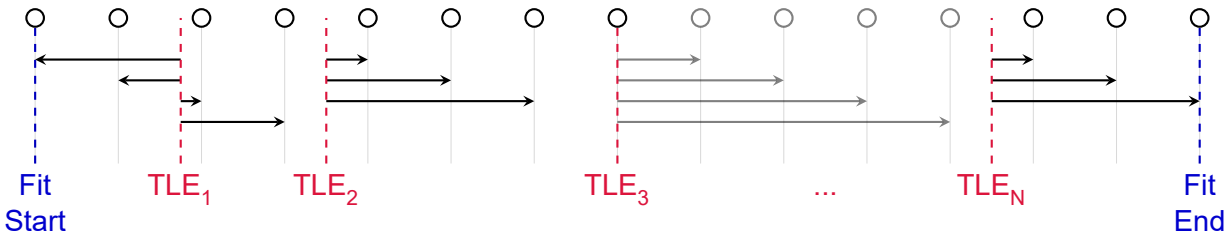
Perturbation	SGP4	SDP4
Earth Zonal Harmonics		
Secular	Up to J_4	
Long-Period	Up to J_4	
Short-Period	J_2	
Atmospheric Drag		
Secular	Y	N
Lunar and Solar Gravity		
Secular	N	Y
Long-Period	N	Y
Earth Resonance		
Secular	N	Y*

*For objects in half- or one-day resonance, including the (2,1), (3,1), and (3,3) tesserals.

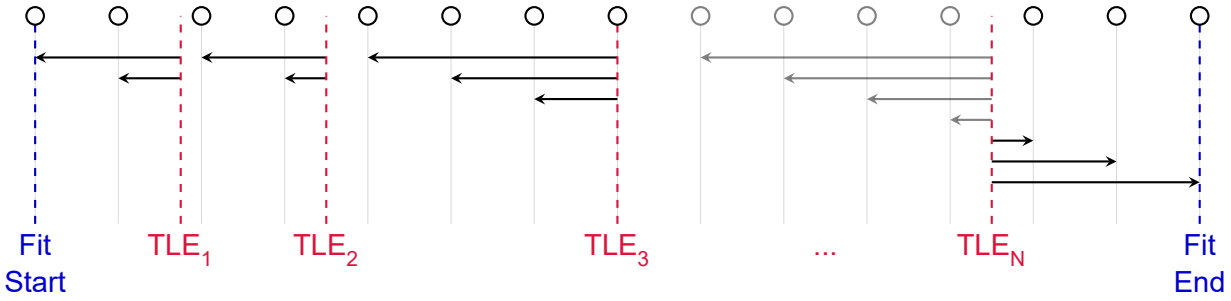
2.2 Two-Line Element Set Sampling

Levit and Marshall [86] proposed an equally-spaced sampling strategy for producing the pseudo-observations from a set of TLEs where sample times are distributed evenly with a fixed interval between the start and end epochs which define the fit window. Nevertheless, alternative strategies could be used when sampling the TLEs. The batch least squares estimation process, as with other estimation techniques, does not require samples to be equally-spaced in time, therefore there is significant flexibility. For example, Chen and Lin [99] demonstrated that P-OD on TLEs in the LEO regime was improved by restricting sampling to times within two orbital periods of each TLE epoch.

The pseudo-observed state at a given time is calculated by propagating a TLE with SGP4, either forward from the most recent TLE or backwards from the next TLE, as illustrated in Figure 2.1. For sample times which precede the first TLE or follow the last TLE, the pseudo-observed states can be calculated by propagating from the nearest TLE. This distinction can be important when considering TLE accuracy before and after epoch and the differences between ‘classic’ and ‘enhanced’ TLEs [92].



(a) Forward.



(b) Backward.

Figure 2.1: TLE sampling strategies.

The transition between two successive TLEs can introduce sharp discontinuities due to the updated orbital elements [111], particularly in the case of objects in LEO, where the inaccuracies of SGP4 can be particularly prominent, meaning that large updates may be required between TLE epochs. Nevertheless, for many objects in MEO and GEO, SGP4 is sufficiently accurate to ensure that any discontinuities remain relatively small.

Smoothing between TLEs can be conducted through a variety of methods, such as time-weighted averages or splining. For example, the Horizons system operated by the Jet Propulsion Laboratory (JPL) blends TLEs by using a weighted average of the forward and backward TLE propagations [112]:

$$\mathbf{r}(t) = W(t)\,\mathbf{r}_1(t) + [1 - W(t)]\,\mathbf{r}_2(t),$$

$$\mathbf{v}(t) = W(t)\,\mathbf{v}_1(t) + \left[1 - W(t)\right]\mathbf{v}_2(t) + W'(t)\left[\mathbf{r}_1(t) - \mathbf{r}_2(t)\right],$$

where:

$$W(t) = \frac{1}{2} + \frac{1}{2}\cos\left(\pi\frac{t - t_1}{t_2 - t_1}\right),$$

$$W'(t) = -\frac{1}{2}\frac{\pi}{t_2 - t_1}\sin\left(\pi\frac{t - t_1}{t_2 - t_1}\right),$$

t_1 and t_2 are the epochs of the two TLEs bracketing time t; and $\mathbf{r}_1, \mathbf{v}_1$ and $\mathbf{r}_2, \mathbf{v}_2$ are the respective positions and velocities when the TLEs are propagated to time t with SGP4.

One of the issues that P-OD seeks to mitigate is that 'TLEs possess potential wide variability' in quality [88]. For the scenario of conducting state estimation on a single poor-quality TLE, there is a possibility of a state estimate being significantly skewed with respect to the true state. By extending the fit window to include multiple TLEs, the influence of a single 'bad' TLE can be reduced [88].

2.3 Batch Least Squares State Estimation

2.3.1 Predictor

The predictor is an Initial Value Problem (IVP) where the state of an object at a given time can be predicted based on its initial state:

$$\mathbf{y}^*(t) = \mathbf{f}(\mathbf{X}, t),$$

where $\mathbf{y}^*(t)$ is the state $(m \times 1)$ at a future time t, and function $\mathbf{f}(\mathbf{X}, t)$ represents the numerical propagation based on an initial state, $\mathbf{X}$, which includes the initial state vector and other physical parameters $(n \times 1)$.

A single initial state can be mapped to l predicted states by concatenating the results of multiple propagations into a single vector $(ml \times 1)$:

$$\mathbf{Y}^* = \mathbf{F}(\mathbf{X}), \tag{2.1}$$

where:

$$\mathbf{Y}^* = \begin{bmatrix} [\mathbf{y}^*(t_0)] \\ [\mathbf{y}^*(t_1)] \\ [\mathbf{y}^*(t_2)] \\ \vdots \\ [\mathbf{y}^*(t_{l-1})] \end{bmatrix},$$

$$\mathbf{F}(\mathbf{X}) = \begin{bmatrix} [\mathbf{f}(\mathbf{X}, t_0)] \\ [\mathbf{f}(\mathbf{X}, t_1)] \\ [\mathbf{f}(\mathbf{X}, t_2)] \\ \vdots \\ [\mathbf{f}(\mathbf{X}, t_{l-1})] \end{bmatrix}.$$

2.3.2 Observer

Propagation with SGP4 can be expressed as:

$$\mathbf{y}(t) = \mathbf{R}_{\text{TEME}}(t)^T \, \mathbf{g}(\{\mathbf{z}_0, \mathbf{z}_1, \dots, \mathbf{z}_{k-1}\}, t),$$

where $\mathbf{y}(t)$ is the pseudo-observed state at time t; $\mathbf{R}_{\text{TEME}}(t)$ is the rotation matrix from the Geocentric Celestial Reference Frame (GCRF) to the True Equator, Mean Equinox (TEME) reference frame; $\mathbf{g}(\{\mathbf{z}_0, \mathbf{z}_1, \dots, \mathbf{z}_{k-1}\}, t)$ represents the SGP4 algorithm, as described in Sections 2.1 and 2.2; and $\{\mathbf{z}_0, \mathbf{z}_1, \dots, \mathbf{z}_{k-1}\}$ is the set of TLEs.

The pseudo-observed states, generated for the same l times as the predicted states, are concatenated into a single vector:

$$\mathbf{Y} = \begin{bmatrix} [\mathbf{y}(t_0)] \\ [\mathbf{y}(t_1)] \\ [\mathbf{y}(t_2)] \\ \vdots \\ [\mathbf{y}(t_{l-1})] \end{bmatrix}.$$

This column vector is an equivalent counterpart to the predicted column vector of states.

Internally, SGP4 conducts propagation in its set of mean elements. Following propagation, these are converted to Cartesian position and velocity in the TEME frame. The transformation from TEME to GCRF ensures that the state vectors of the predictor and observer are compared in a common reference frame. Unfortunately, this transformation introduces an ambiguity due to the transformation matrix, $\mathbf{R}_{\text{TEME}}(t)$, lacking a rigorous definition [109]. Two potential definitions exists: ‘of epoch’, where

the transformation is calculated once at the epoch of the TLE and applied for any corresponding pseudo-observations; or 'of date', where the transformation is calculated and applied at the time of each separate pseudo-observation [109]. In this case, the 'of date' interpretation is being used as this is generally accepted as the correct interpretation [109].

2.3.3 Solver

The error between a set of pseudo-observations and a set of predictions is expressed as a set of residuals:

$$\begin{aligned} \mathbf{b} &= \mathbf{Y} - \mathbf{Y}^*, \\ &= \mathbf{Y} - \mathbf{F}(\mathbf{X}), \end{aligned} \tag{2.2}$$

where $\mathbf{b}$ is the residual vector ($ml \times 1$).

The state estimation process is expressed as a minimisation problem with the objective of minimising the weighted sum of the square of the state residuals:

$$\min_{\mathbf{X}} J(\mathbf{X}) = \frac{1}{2}\mathbf{b}(\mathbf{X})^T \mathbf{W} \mathbf{b}(\mathbf{X}),$$

where $J(\mathbf{X})$ is the objective function; and $\mathbf{W}$ is the weighting matrix ($ml \times ml$), a diagonal matrix of coefficients which capture the expected noise in the observations:

$$\mathbf{W}_i = \begin{bmatrix} \frac{1}{\sigma_{i,1}} & & & \\ & \frac{1}{\sigma_{i,2}} & & \\ & & \ddots & \\ & & & \frac{1}{\sigma_{i,m}} \end{bmatrix},$$

$$\mathbf{W} = \begin{bmatrix} [\mathbf{W}_0] & & & \\ & [\mathbf{W}_1] & & \\ & & \ddots & \\ & & & [\mathbf{W}_{n-1}] \end{bmatrix}, \tag{2.3}$$

where $\sigma_{i,0}$ through $\sigma_{i,m}$ are the standard deviations of the measurement noises for each of the corresponding observed state variables of the i-th sample.

The objective function is minimised when its derivative is zero:

$$\left.\frac{\partial J(\mathbf{X})}{\partial \mathbf{X}}\right|_{\mathbf{X}=\hat{\mathbf{X}}} = \mathbf{0}, \tag{2.4}$$

where $\hat{\mathbf{X}}$ is the best estimate of the optimal decision vector. This condition is true also when the objective function is maximised, or at a saddle point, therefore the Hessian of the objective function must be positive-definite to guarantee that the solver has reached a local minimum.

The objective function can be linearised by considering a first-order Taylor expansion of the predicted states from Equation (2.1) about a reference decision vector, $\bar{\mathbf{X}}$:

$$\begin{aligned}
\mathbf{Y}^*(\mathbf{X}) &\approx \mathbf{F}(\bar{\mathbf{X}}) + \mathbf{A}(\mathbf{X} - \bar{\mathbf{X}}), \\
\mathbf{b}(\mathbf{X}) &\approx \mathbf{Y} - \mathbf{F}(\bar{\mathbf{X}}) - \mathbf{A}(\mathbf{X} - \bar{\mathbf{X}}), \\
J(\mathbf{X}) &\approx \frac{1}{2}\left[\mathbf{Y} - \mathbf{F}(\bar{\mathbf{X}}) - \mathbf{A}(\mathbf{X} - \bar{\mathbf{X}})\right]^T \mathbf{W}\left[\mathbf{Y} - \mathbf{F}(\bar{\mathbf{X}}) - \mathbf{A}(\mathbf{X} - \bar{\mathbf{X}})\right],
\end{aligned} \tag{2.5}$$

where $\mathbf{A} = \left.\frac{\partial \mathbf{F}(\mathbf{X})}{\partial \mathbf{X}}\right|_{\mathbf{X}=\bar{\mathbf{X}}}$.

The chain rule for two vectors, $\mathbf{u}^T$ and $\mathbf{v}$, is applied to find the derivative of Equation (2.5):

$$\frac{\partial \mathbf{u}^T\mathbf{v}}{\partial \mathbf{X}} = \frac{\partial \mathbf{u}}{\partial \mathbf{X}}\mathbf{v} + \frac{\partial \mathbf{v}}{\partial \mathbf{X}}\mathbf{u},$$

where $\mathbf{u} = \mathbf{Y} - \mathbf{F}(\bar{\mathbf{X}}) - \mathbf{A}\left(\hat{\mathbf{X}} - \bar{\mathbf{X}}\right)$ and $\mathbf{v} = \mathbf{W}\left[\mathbf{Y} - \mathbf{F}(\bar{\mathbf{X}}) - \mathbf{A}\left(\hat{\mathbf{X}} - \bar{\mathbf{X}}\right)\right]$.

This results in an expression for the objective function derivative:

$$\begin{aligned}
\left.\frac{\partial J(\mathbf{X})}{\partial \mathbf{X}}\right|_{\mathbf{X}=\hat{\mathbf{X}}} &\approx \frac{1}{2}\left\{-\mathbf{A}^T\mathbf{W}\left[\mathbf{Y} - \mathbf{F}(\bar{\mathbf{X}}) - \mathbf{A}\left(\hat{\mathbf{X}} - \bar{\mathbf{X}}\right)\right] - (\mathbf{WA})^T\left[\mathbf{Y} - \mathbf{F}(\bar{\mathbf{X}}) - \mathbf{A}\left(\hat{\mathbf{X}} - \bar{\mathbf{X}}\right)\right]\right\}, \\
&= \frac{1}{2}\left\{-\mathbf{A}^T\mathbf{W}\left[\mathbf{Y} - \mathbf{F}(\bar{\mathbf{X}}) - \mathbf{A}\left(\hat{\mathbf{X}} - \bar{\mathbf{X}}\right)\right] - \mathbf{A}^T\mathbf{W}\left[\mathbf{Y} - \mathbf{F}(\bar{\mathbf{X}}) - \mathbf{A}\left(\hat{\mathbf{X}} - \bar{\mathbf{X}}\right)\right]\right\}, \\
&= -\mathbf{A}^T\mathbf{W}\left[\mathbf{Y} - \mathbf{F}(\bar{\mathbf{X}}) - \mathbf{A}\left(\hat{\mathbf{X}} - \bar{\mathbf{X}}\right)\right],
\end{aligned}$$

considering that the weighting matrix is symmetric ($\mathbf{W} = \mathbf{W}^T$).

By substituting the first-order approximation of the objective function derivative into Equation (2.4), an expression is found for the optimal decision vector:

$$-\mathbf{A}^T\mathbf{W}\left[\mathbf{Y} - \mathbf{F}(\bar{\mathbf{X}}) - \mathbf{A}\left(\hat{\mathbf{X}} - \bar{\mathbf{X}}\right)\right] = \mathbf{0},$$

$$\mathbf{A}^T\mathbf{W}\mathbf{A}\left(\hat{\mathbf{X}} - \bar{\mathbf{X}}\right) = \mathbf{A}^T\mathbf{W}\left[\mathbf{Y} - \mathbf{F}(\bar{\mathbf{X}})\right].$$

The minimisation is treated iteratively, re-linearising the predicted states with each iteration, j, until convergence:

$$\mathbf{A}_j^T\mathbf{W}\mathbf{A}_j\left(\mathbf{X}_{j+1} - \mathbf{X}_j\right) = \mathbf{A}_j^T\mathbf{W}\left[\mathbf{Y} - \mathbf{F}(\mathbf{X}_j)\right],$$

where $\mathbf{X}_j = \bar{\mathbf{X}}$, $\mathbf{A}_j = \left.\frac{\partial \mathbf{F}(\mathbf{X})}{\partial \mathbf{X}}\right|_{\mathbf{X}=\mathbf{X}_j}$, and $\mathbf{X}_{j+1} = \hat{\mathbf{X}}$.

An extension to the Gauss-Newton method, the Levenberg-Marquardt method [113, 114], was used due to its improved performance. This method introduces an additional gradient descent term into the update equation to speed up the initial rate of convergence:

$$\left[\mathbf{A}_j^T\mathbf{W}\mathbf{A}_j + \lambda\ \mathrm{diag}\left(\mathbf{A}_j^T\mathbf{W}\mathbf{A}_j\right)\right]\left(\mathbf{X}_{j+1} - \mathbf{X}_j\right) = \mathbf{A}_j^T\mathbf{W}\left[\mathbf{Y} - \mathbf{F}(\mathbf{X}_j)\right],$$

where λ is the damping coefficient, a term which controls the influence of the gradient descent term. During iteration the damping coefficient is reduced, transitioning the solver towards a conventional Gauss-Newton solution as it approaches the local minimum. The value of the damping coefficient can be calculated iteratively to improve solver performance, as described by [115, 116, 117].

2.4 State Estimation Evaluation

State estimation can be evaluated in a variety of ways. The two main qualities considered for this investigation were the accuracy of the fit, following further propagation after the fit window; and the uncertainty of the fit, based on information known during the fit process.

Post-fit prediction accuracy can be evaluated with position Root-Mean-Square Error (RMSE):

$$\Delta r_{\mathrm{RMSE}} = \sqrt{\frac{1}{l^*}\sum_{i=0}^{l^*-1}||\mathbf{r}_i^* - \mathbf{r}_i||^2}, \tag{2.6}$$

where l^* is the number of post-fit samples; and $\mathbf{r}_i^*$ and $\mathbf{r}_i$ are the predicted and reference positions, respectively, at the i-th epoch. The reference positions can be derived from high-accuracy SLR or GNSS solutions. The use of other references sources, such as future TLEs, is discussed in Chapter 4.

Alternatively, the mean position error can be used:

$$\overline{\Delta r} = \frac{1}{l^*} \sum_{i=0}^{l^*-1} ||\mathbf{r}_i^* - \mathbf{r}_i||. \tag{2.7}$$

Equivalent expressions can be made to evaluate velocity error:

$$\Delta v_{\text{RMSE}} = \sqrt{\frac{1}{l^*} \sum_{i=0}^{l^*-1} ||\mathbf{v}_i^* - \mathbf{v}_i||^2}, \tag{2.8}$$

$$\overline{\Delta v} = \frac{1}{l^*} \sum_{i=0}^{l^*-1} ||\mathbf{v}_i^* - \mathbf{v}_i||, \tag{2.9}$$

where $\mathbf{v}_i^*$ and $\mathbf{v}_i$ are the predicted and reference velocities, respectively, at the i-th epoch.

One feature of RMSEs, in general, is the increased weight placed on outliers. This results from the individual errors being squared before the mean is calculated. This behaviour is useful as, during comparisons, it can highlight cases where the post-fit predictions contain instances of significantly larger errors.

The uncertainty of a fit from the batch least squares solver can be calculated directly during the estimation process and represented by a covariance matrix ($m \times m$):

$$\mathbf{P} = \left(\mathbf{A}^T \mathbf{W} \mathbf{A}\right)^{-1},$$

however, this requires a well-tuned weighting matrix [118]. Furthermore, due to the fits being conducted in GCRF, the covariance matrices from different fits are difficult to compare due to the differing orientations at various initial states.

To avoid these issues, the sample covariance matrix in the Radial, Transverse, Normal (RTN) frame can be used instead, where each of the residuals are rotated into their local RTN frame:

$$\hat{\mathbf{P}} = \frac{1}{l-1} \left(\mathbf{B} - \bar{\mathbf{b}}\right)\left(\mathbf{B} - \bar{\mathbf{b}}\right)^{\mathsf{T}},$$

where:

$$\hat{\mathbf{R}} = \frac{\mathbf{r}}{||\mathbf{r}||},$$

$$\hat{\mathbf{N}} = \frac{\mathbf{r} \times \mathbf{v}}{||\mathbf{r} \times \mathbf{v}||},$$

$$\hat{\mathbf{T}} = \hat{\mathbf{N}} \times \hat{\mathbf{R}},$$

$$\mathbf{R}_{\text{RTN}} = \begin{bmatrix} [\hat{\mathbf{R}}] & [\hat{\mathbf{T}}] & [\hat{\mathbf{N}}] & & & \\ & & & [\hat{\mathbf{R}}] & [\hat{\mathbf{T}}] & [\hat{\mathbf{N}}] \end{bmatrix},$$

$$\tilde{\mathbf{b}}_i = \mathbf{R}_{\text{RTN}}(\mathbf{y}_i)\left(\mathbf{y}_i - \mathbf{y}_i^*\right),$$

$$\mathbf{B} = \left[\left[\tilde{\mathbf{b}}_0\right] \quad \left[\tilde{\mathbf{b}}_1\right] \quad \ldots \quad \left[\tilde{\mathbf{b}}_{n-1}\right]\right],$$

$$\bar{\mathbf{b}} = \frac{1}{l}\sum_{i=0}^{l-1} \mathbf{b}_i.$$

Direct comparison of covariance matrices presents a challenge due to their multi-dimensional nature. The volume of the 3σ ellipsoid can be used to aid comparison:

$$V_{3\sigma} = \frac{4}{3}\pi\left(3\sigma_{r,1}\right)\left(3\sigma_{r,2}\right)\left(3\sigma_{r,3}\right),$$

$$= 36\pi\left(\sigma_{r,1}\right)\left(\sigma_{r,2}\right)\left(\sigma_{r,3}\right),$$

where $\sigma_{r,1}$, $\sigma_{r,2}$, and $\sigma_{r,3}$ are the position standard deviations in the principal axes (i.e. the eigenvalues of the position covariance matrix, the upper 3 × 3 block of $\hat{\mathbf{P}}$).

Additionally, the equivalent radius of the uncertainty ellipsoid, that is the radius of a sphere of equivalent volume, can be used for comparison:

$$R_{3\sigma} = \sqrt[3]{\left(3\sigma_{r,1}\right)\left(3\sigma_{r,2}\right)\left(3\sigma_{r,3}\right)},$$

$$= 3\sqrt[3]{\left(\sigma_{r,1}\right)\left(\sigma_{r,2}\right)\left(\sigma_{r,3}\right)}. \tag{2.10}$$

2.5 Implementation Considerations

Four calibration satellites were considered for initial testing: both pairs each of the LAGEOS and Etalon satellites, as listed in Table 2.2. These calibration satellites were designed for geodesy and are covered in retroreflectors which are designed to reflect beams of light back to their point of origin [119]. These allow ground-based laser systems to make highly precise ranging measurements (typically at centimetre-level) based on the two-way time-of-flight of laser pulses, as discussed in Section 1.4.2. TLEs for the calibration satellites were provided by USSF via Space-Track [56] and high-accuracy SLR-derived ephemerides were retrieved from the CDDIS [62].

Table 2.2: Approximate orbital elements of the calibration satellites (1st January 2022).

Satellite	NORAD ID	Semi-major axis [km]	Eccentricity [-]	Inclination [deg]
LAGEOS-1	8820	12,270	0.005	110
LAGEOS-2	22195	12,160	0.014	52.6
Etalon 1	19751	25,500	0.002	64.3
Etalon 2	20026	25,500	0.002	65.6

The calibration satellites were selected due to a number of advantages. First, their altitudes in MEO reduce the influence of certain perturbations, such as atmospheric drag which is effectively not present. Second, their low area-to-mass ratios limit the effect of SRP. Third, most importantly, their role as geodesy satellites means that accurate ephemerides are readily available for validating fit accuracy. The lack of atmospheric drag and SRP meant that these perturbations could be ignored. This simplified the numerical model and removed the need to estimate drag and reflection coefficients.

2.5.1 Two-Line Element Set Sampling

The three sampling methods presented in Section 2.2 were compared for the calibration satellites in Figure 2.2. It was seen that there was no discernible difference between the three methods. This was likely due to the high update rate of the TLEs, approximately every one to two days, resulting in a limited amount of error due to propagation with SGP4. The impact of propagation time was further limited by these objects being in MEO, where the lack of atmospheric drag prevents the along-track divergence seen for LEO TLEs.

The difference between the three methods was seen more easily in Figure 2.3, where gaps in TLE availability were added artificially so that TLE error could grow during propagation. Both the forward and backward sampling techniques were seen to diverge significantly from the true state following the approximately 30 days of propagation between TLEs. On the other hand, the blended solution did not grow so large in error, as expected, due to its averaging between the two solutions. At certain times, the blended solution was less accurate than the forward or backward solutions, however it ensured that errors did not grow as significantly.

The weighting matrix, Equation (2.3), was calculated by using TLE noise estimates from literature, as presented in Table 2.3. These noise estimates from literature were defined in the RTN frame, however the state estimation was conducted in GCRF. Therefore, at each pseudo-observation epoch, the noises were rotated into inertial space by considering the respective RTN transformations. This transformation introduces cross terms which were ignored when constructing the weighting matrix. It should be noted that the estimates in Table 2.3 correspond to TLEs in LEO and, therefore, underestimate the noise at high altitudes which is typically higher [93].

Table 2.3: Mean TLE uncertainty in the RTN frame at epoch, for 'enhanced' TLEs released after 2013. Adapted from [92].

Type	σ_R	σ_T	σ_N
Position [m]	1.2×10^{2}	2.0×10^{3}	8.0×10^{1}
Velocity [m/s]	2.4×10^{0}	1.3×10^{-1}	6.8×10^{-2}

2.5.2 Physical Model

Numerical propagation was conducted using THALASSA [120]. This numerical propagation code was designed for rapid propagation of orbits in near-Earth and cislunar space by leveraging regularised equations of motion. The EDromo(C) regularised formulation was used for propagation as it is a non-singular method which works well for weakly perturbed orbits, such as those examined in this work [120, 121]. Internally, THALASSA uses the Livermore Solver for Ordinary Differential Equations with Automatic Method Switching for Stiff and Non-Stiff Problems and with Root-Finding (LSODAR) numerical integrator which provides automatic switching between non-stiff and stiff methods, Adams and Backward Differentiation Formulae (BDF) respectively, and root finding capabilities [122].

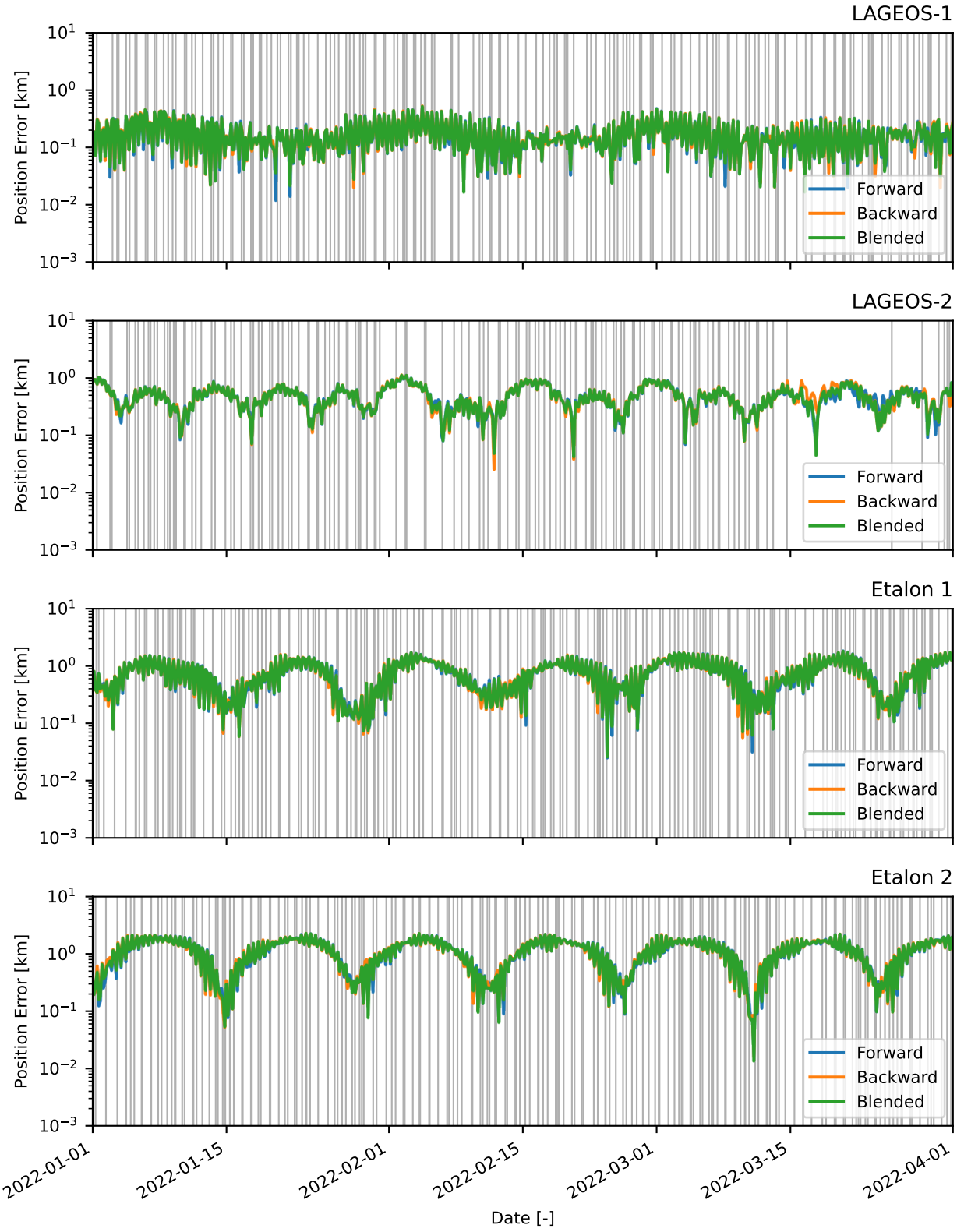


Figure 2.2: Position errors for calibration satellite TLEs for the first quarter of the year 2022, when using the forward, backward, and blended propagation methods. The epoch of each TLE is indicated by the grey vertical lines.

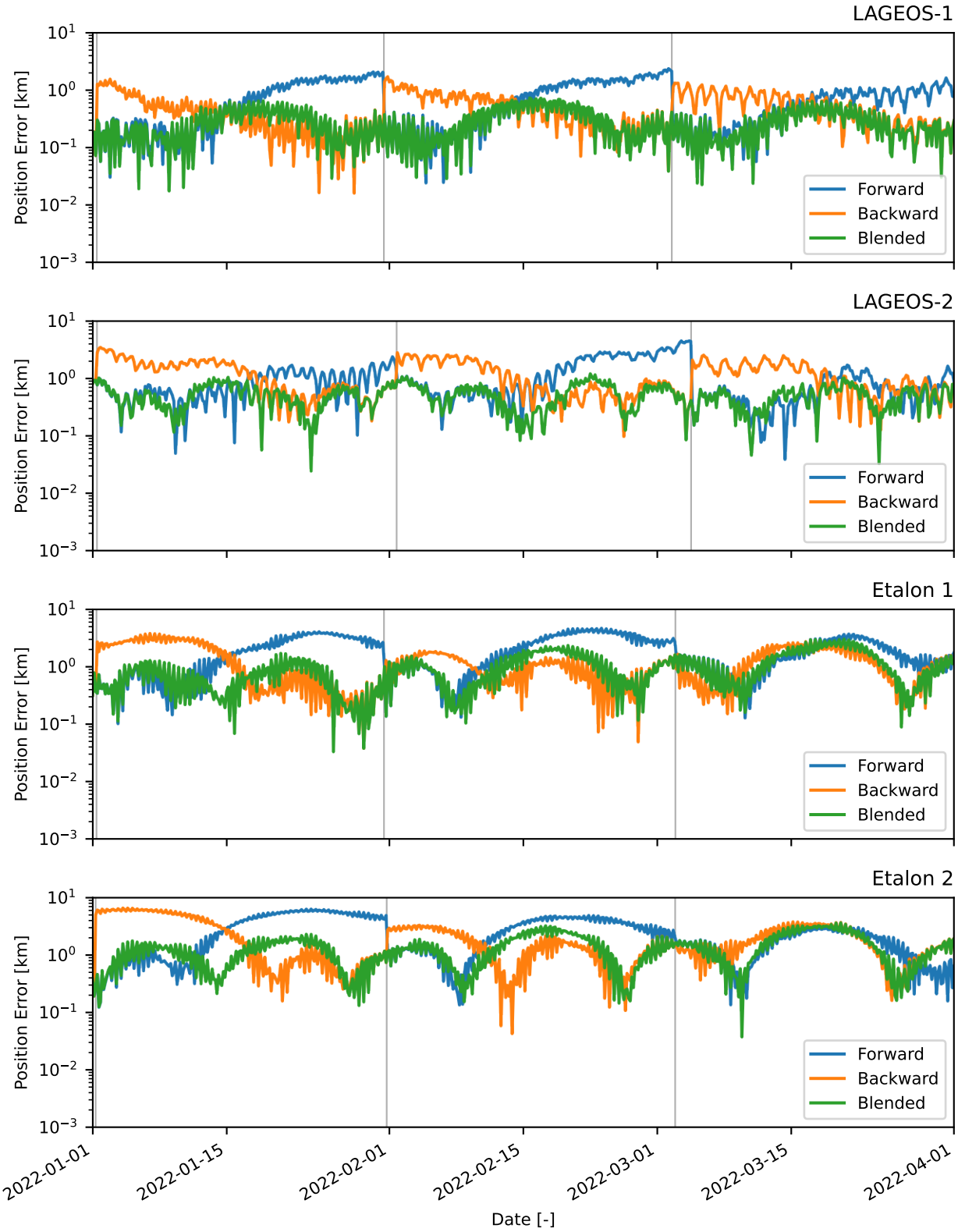


Figure 2.3: Position errors for calibration satellite TLEs for the first quarter of the year 2022, when using the forward, backward, and blended propagation methods. The TLEs for each satellite have been downsampled to artificially introduce 30-day gaps in availability. The epoch of each TLE is indicated by the grey vertical lines.

It was decided to use a 'minimal model' where model parameters are such that computational cost is minimised while maintaining an acceptable tolerance for propagation accuracy. The target tolerance was a position RMSE an order of magnitude below the expected TLE error for a given fit. For the calibration satellites, this corresponded to a target error of the order of hundreds of metres or smaller, against the error of the TLEs which were of the order of kilometres.

Initial testing of the P-OD methodology indicated that gravitational perturbations were the most critical part of the physical model, in particular geopotential and third-body perturbations. The physical model is summarised in Table 2.4, including a truncated GRIM5-S1 gravity field model [123]; lunisolar perturbations using the DE431 planetary and lunar ephemerides [124]; and, where included, a 'cannonball' SRP approximation using a conical Earth shadow model. THALASSA provides an alternative to DE431 in the form of simplified analytical expressions [125]; however, the increased computational cost of using DE431 was not significant and, moreover, the use of DE431 maximised the accuracy of the ephemerides, removing a potential source of error.

Table 2.4: Summary of the physical model.

Perturbation	Model	Data Source
Geopotential	10-by-10	GRIM5-S1
Third-body	Moon, Sun	DE431
SRP	'Cannonball' with conical Earth shadow	-

The 'minimal model' was tuned by conducting batch least squares fits on the SLR-derived states of each calibration satellite. By testing model perturbations separately, their effect on the accuracy and performance of the state estimation process could be evaluated to determine both which perturbations had to be included and, additionally, their required level of fidelity. A 120-day fit window was used to represent the longest propagation duration presented in the following analysis in Chapter 3.

For near-Earth orbits above LEO, lunisolar perturbations represent a significant perturbation as illustrated by Table 2.5: for all of the calibration satellites, the absence of either the Moon or the Sun in the physical model resulted in significant position RMSEs during the evaluation period. Conversely, as altitude increases, the fidelity of the geopotential model becomes less critical. It was found that truncating the geopotential model to a 10-by-10 subset of the coefficients was found to provide sufficient accuracy for all four calibration satellites, as demonstrated in Figure 2.4.

Table 2.5: Position RMSEs, with respect to SLR, for 120-day fits with different lunisolar perturbations.

Satellite	Position RMSE [m]			
	Moon & Sun	Moon Only	Sun Only	Neither
LAGEOS-1	1.337×10^2	2.656×10^3	8.580×10^2	2.987×10^3
LAGEOS-2	1.084×10^2	3.296×10^3	1.474×10^3	3.766×10^3
Etalon 1	2.071×10^2	1.261×10^4	6.987×10^3	1.347×10^4
Etalon 2	2.344×10^2	2.573×10^4	2.127×10^4	3.839×10^4

Following selection of the physical model, the integrator tolerance was tuned to determine the largest tolerance, and therefore minimal computational cost, which achieved the targeted maximum error for the 120-day fits. The results are presented in Figure 2.5. The chosen integrator tolerance of 10^{-10} ensured that computational cost was minimised without compromising fit accuracy, lying right at the edge of the plateau before fit errors started to oscillate and increase above the target position RMSE with looser integration tolerances.

2.5.3 Non-Dimensionalisation

A challenge with numerical optimisation, both generally and specifically with gradient-based methods, is the relative magnitudes of values in the decision vector and their impact on the derivatives of the objective function. For the calibration satellites, position and velocity components are of the order of approximately 10^6 m and 10^3 m/s, respectively. This could cause issues with the Levenberg-Marquardt solver, potentially placing additional weighting on certain components when seeking to minimise the objective function which could result in a worse converged state estimate if the solver were to become trapped in a local minimum.

The solution was to scale the decision vector components to have similar magnitudes, in this case using the semi-major axis and corresponding circular orbital velocity of the initial orbit:

$$DU = \frac{1}{\frac{2}{||\mathbf{r}_0||} - \frac{||\mathbf{v}_0||^2}{\mu}},$$

$$VU = \sqrt{\frac{\mu}{DU}},$$

where $\mathbf{r}_0$ and $\mathbf{v}_0$ are the initial position and velocity vectors, respectively; and μ is the gravitational parameter.

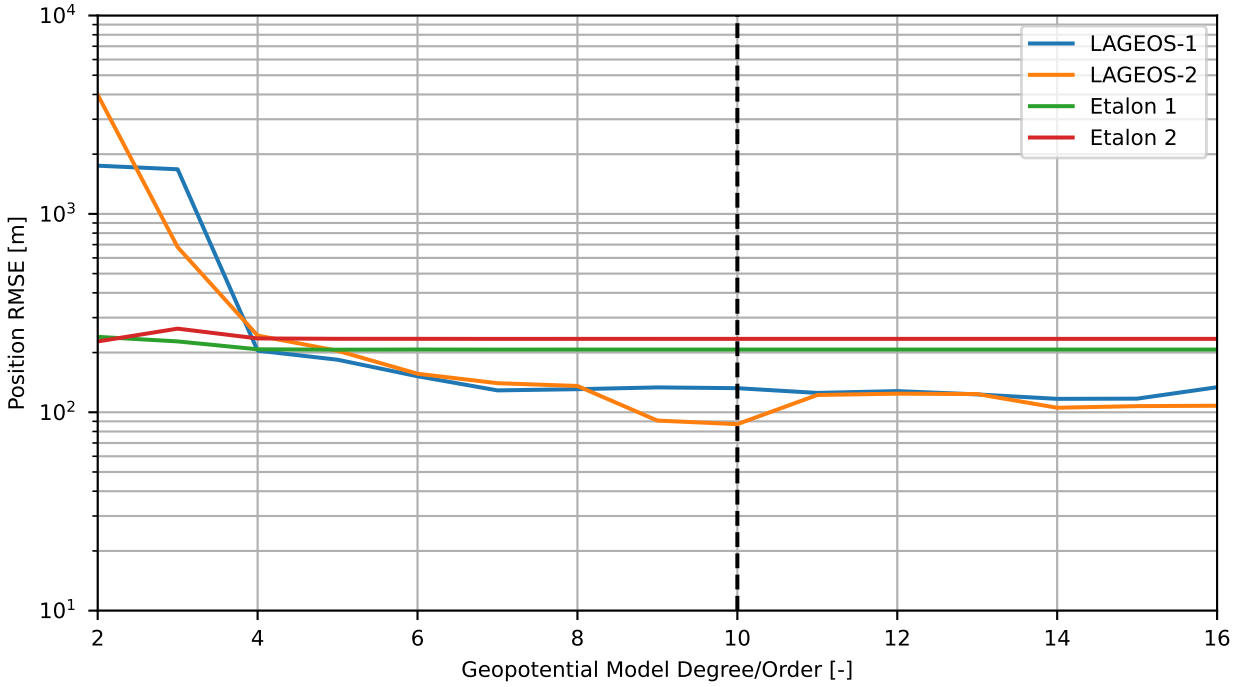


Figure 2.4: Position RMSEs, with respect to SLR, for 120-day fits with varying geopotential model degrees and orders. A 10-by-10 geopotential model provides sufficient accuracy for position RMSE to remain an order of magnitude below the expected TLE error.

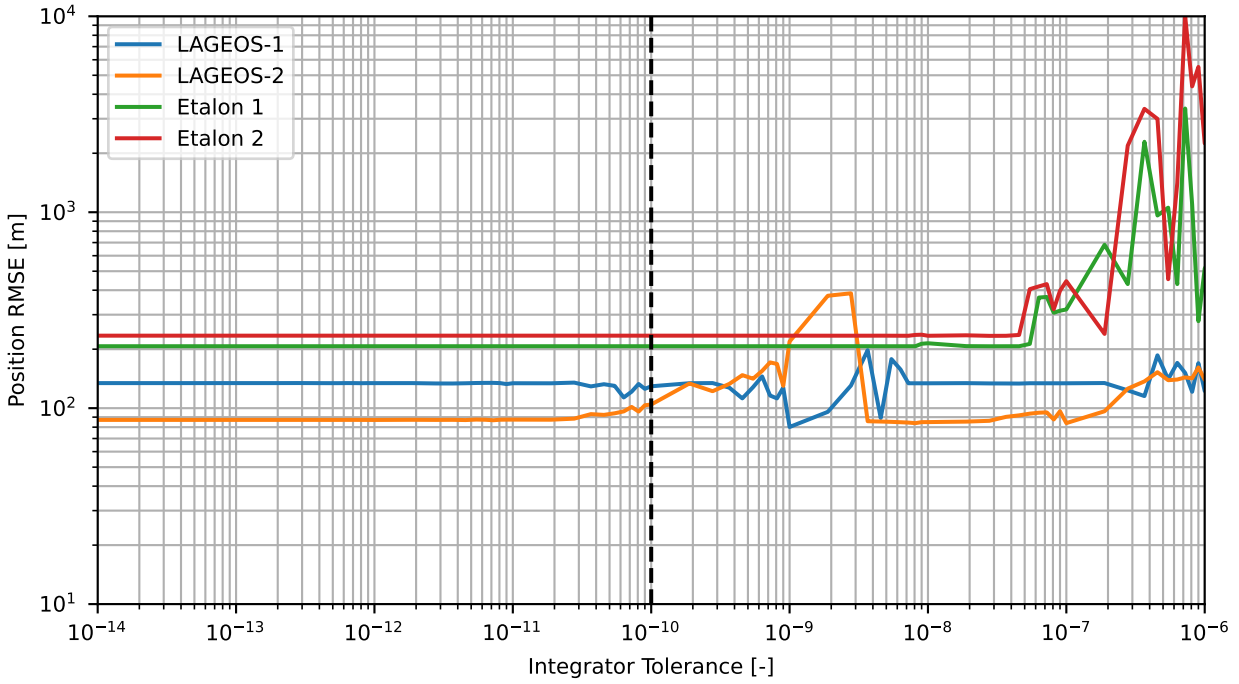


Figure 2.5: Position RMSEs, with respect to SLR, for 120-day fits with varying integrator tolerances. An integrator tolerance of 10^{-10} provides sufficient accuracy for position RMSE to remain an order of magnitude below the expected TLE error.

The applicability of the chosen scaling parameters is demonstrated in Table 2.6, where initial state vectors for the calibration satellites are presented in both dimensional and non-dimensional forms. The wide range of magnitudes was highly apparent for the dimensional representation, where decision vectors would contain values ranging from 10^7 m to 10^1 m/s, a range of six orders of magnitude. On the other hand, the non-dimensional representation closed this gap to only two orders of magnitude, greatly improving the numerical conditioning.

Table 2.6: Comparison of calibration satellite state vectors on the 1st January 2022, before and after non-dimensionalisation.

(a) Dimensional.

Satellite	Position [m]			Velocity [m/s]		
	X	Y	Z	X	Y	Z
LAGEOS-1	1.127×10^7	-4.484×10^6	1.759×10^6	-1.416×10^3	-1.539×10^3	5.308×10^3
LAGEOS-2	-4.657×10^6	-9.372×10^6	6.479×10^6	4.562×10^3	9.334×10^1	3.344×10^3
Etalon 1	-4.510×10^5	-1.535×10^7	2.036×10^7	2.775×10^3	-2.273×10^3	-1.663×10^3
Etalon 2	2.541×10^7	2.529×10^6	-1.446×10^5	-1.381×10^2	1.629×10^3	3.594×10^3

(b) Non-Dimensional.

Satellite	Position [-]			Velocity [-]		
	X	Y	Z	X	Y	Z
LAGEOS-1	9.185×10^{-1}	-3.653×10^{-1}	1.433×10^{-1}	-2.485×10^{-1}	-2.700×10^{-1}	9.315×10^{-1}
LAGEOS-2	-3.829×10^{-1}	-7.705×10^{-1}	5.327×10^{-1}	7.969×10^{-1}	1.630×10^{-2}	5.841×10^{-1}
Etalon 1	-1.768×10^{-2}	-6.018×10^{-1}	7.984×10^{-1}	7.018×10^{-1}	-5.749×10^{-1}	-4.206×10^{-1}
Etalon 2	9.964×10^{-1}	9.916×10^{-2}	-5.670×10^{-3}	-3.492×10^{-2}	4.120×10^{-1}	9.090×10^{-1}

2.5.4 Finite Differencing

It is impossible to calculate the partial derivatives matrix analytically in the general case, therefore the partial derivatives were calculated numerically through finite differences [126]. Although not available through THALASSA, it should be noted that there are examples of propagation software, such as Orekit [127] and Heyoka [128], which support automatic differentiation. Methods such as these can calculate derivatives without the drawbacks of finite differences, however they require intrusive changes to the propagation code.

Finite differences approximate derivatives by considering perturbations in each of the variables of the function. The Jacobian of the propagation function is comprised of first-order partial derivatives

in each variable:

$$\mathbf{A} = \left[\left[\frac{\partial \mathbf{F}(\mathbf{X})}{\partial x_1} \right] \quad \left[\frac{\partial \mathbf{F}(\mathbf{X})}{\partial x_2} \right] \quad \cdots \quad \left[\frac{\partial \mathbf{F}(\mathbf{X})}{\partial x_n} \right] \right].$$

Two methods for calculating finite differences were considered for estimating the Jacobian matrix. Firstly, first-order forward differencing:

$$\frac{\partial \mathbf{F}(\mathbf{X})}{\partial x_i} \approx \frac{\mathbf{F}(\mathbf{X} + \boldsymbol{\delta}_i) - \mathbf{F}(\mathbf{X})}{||\boldsymbol{\delta}_i||},$$

and, secondly, second-order central differencing:

$$\frac{\partial \mathbf{F}(\mathbf{X})}{\partial x_i} \approx \frac{\mathbf{F}(\mathbf{X} + \boldsymbol{\delta}_i) - \mathbf{F}(\mathbf{X} - \boldsymbol{\delta}_i)}{2||\boldsymbol{\delta}_i||},$$

where $\boldsymbol{\delta}_i$ is a small perturbation in the i-th variable of $\mathbf{X}$.

Finite differences introduce several considerations, primarily the introduction of additional computational cost, and potential issues, such as truncation and round-off, which must be addressed with care to avoid inaccuracy of the estimate. Finite differences linearise about a point by perturbing the initial conditions, therefore multiple propagations are required for the calculation: $n + 1$ propagations, in the case of first-order forward differencing; or $2n$ propagations, in the case of second-order central differencing. Higher-order finite differencing methods exist to address numerical concerns; however, for a decision vector containing six elements, as is the case here, the use of a second-order method would represent an approximate 70 % increase in computational cost.

The forward and central finite differencing schemes were compared to evaluate their suitability for this application. The two schemes were evaluated by comparing estimated Jacobian matrices for a range of different step sizes against a reference Jacobian. The results of comparing the two schemes are presented in Figures 2.6 and 2.7. For all four cases, there was a region of convergence between the forward and central differencing schemes where the Jacobians generated were approximately the same and invariant with respect to the step size, for step sizes between approximately 10^{-10} and 10^{-6}. In both cases, further increasing the step size eventually resulted in the RMSE increasing. Notably, as expected, the forward differencing scheme started to diverge sooner than the central differencing scheme. Critically, for step sizes equivalent to distances of centimetres to metres, the forward differencing scheme remained valid and within 5 % of the central differencing scheme without the penalty of a 70 % increase in computational cost.

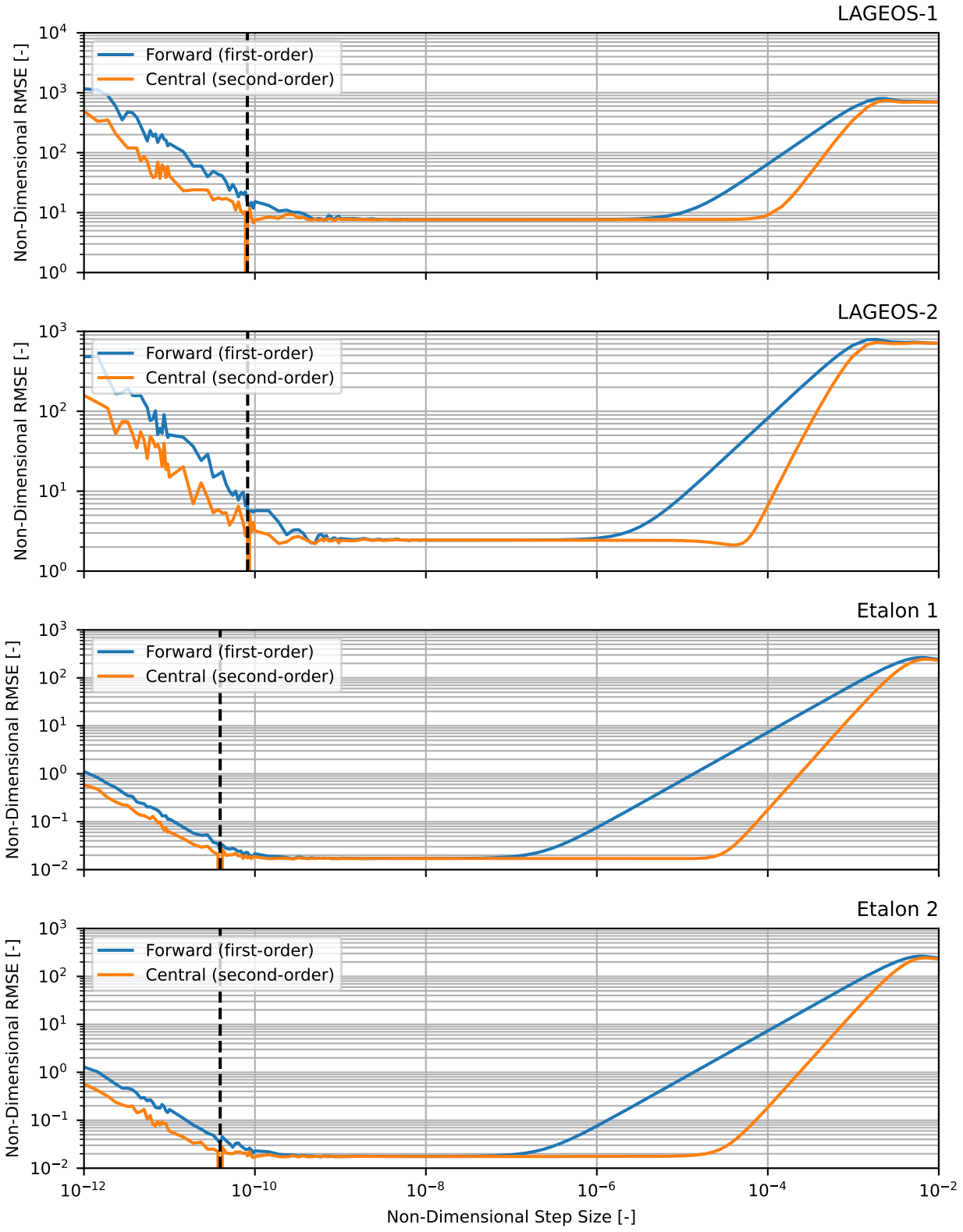


Figure 2.6: Comparison of finite differencing schemes for estimating the Jacobian matrix of the calibration satellites over a 30-day propagation. The Jacobian calculated with the central differencing scheme with a step size equivalent to a 1 mm perturbation was used as a reference solution, indicated by the dashed line.

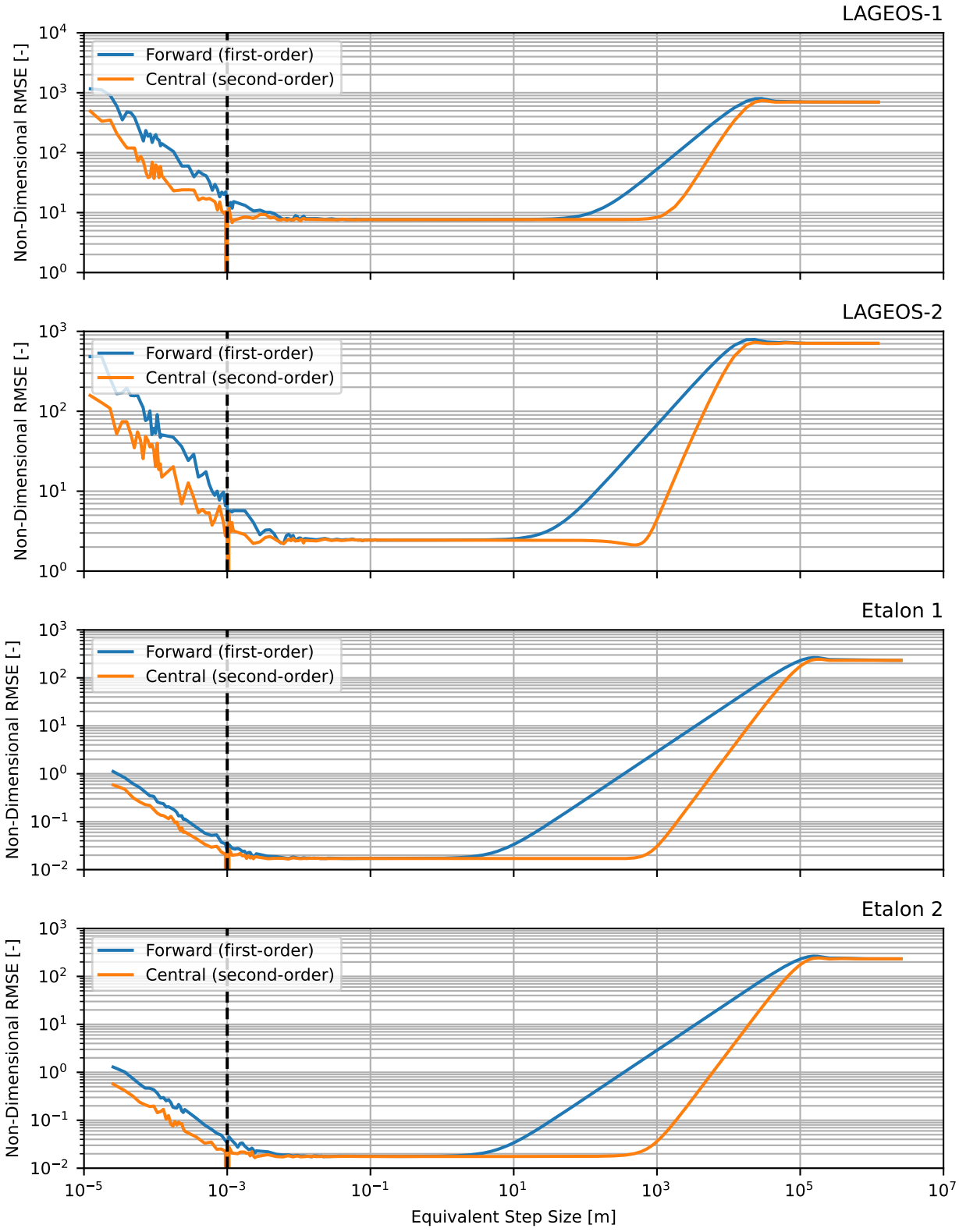


Figure 2.7: Comparison of finite differencing schemes for estimating the Jacobian matrix of the calibration satellites over a 30-day propagation. The Jacobian calculated with the central differencing scheme with a step size equivalent to a 1 mm perturbation was used as a reference solution, indicated by the dashed line.

These results confirmed that the choice of using the first-order forward finite differencing method was justified, under the condition of careful selection of the perturbation step size to avoid either numerical issues or reduced accuracy. A nominal non-dimensional perturbation size of 10^{-8} was used for the following examples of TLE-based P-OD.

Chapter 3

Two-Line Element Set Biases

In this chapter, the initial results of conducting P-OD on TLEs, as described in Chapter 2, will be presented to demonstrate how the method can be used to improve state estimates for RSOs in near-Earth orbits. It will be demonstrated that, although the method can improve state estimates, in many cases these are not consistently better, and sometimes worse, that those provided naively by the TLEs. It will be shown that P-OD quality varies due to the presence of periodic biases in the TLEs. An analysis of the biases in TLEs that affect P-OD will be presented. This includes identification of the dominant position and velocity error components, frequency analysis to reveal potential drivers of error, and data-driven bias models which can be used to debias pseudo-observations prior to state estimation. These models, initially tested on the same calibration satellites considered in Chapter 2, will be extended to consider various GNSS constellations in MEO to produce more general, large-scale bias models. Results in this chapter were presented in [102, 104, 105].

3.1 Pseudo-Orbit Determination on Two-Line Element Sets

The P-OD method described in Chapter 2 was tested initially on the calibration satellites, LAGEOS-1 and -2, and Etalon 1 and 2, with the objective of confirming that TLE-based P-OD remains applicable and effective at improving state estimates for deep-space satellites, despite the changes known to have been made by USAF and USSF in the TLE generation pipeline.

Firstly, the quality of the calibration satellites' TLEs was evaluated to provide a benchmark for fit performance. The position RMSEs for the TLEs of the calibration satellites are presented in Figure 3.1, calculated by propagating each of the TLEs for 30 days after their epoch and evaluating their RMSEs with respect to the SLR-derived states. All four calibration satellites showed periodic variations in RMSE throughout the year, albeit with differing behaviours. LAGEOS-1 had largely periodic behaviour which remained below 1 km for the majority of the year. Etalon 1 and 2 had higher RMSEs with larger oscillations which remained bounded between approximately 1 to 4.5 km and 1.5 to 4.5 km respectively. Notably, the frequency of the error behaviour for Etalon 1 and 2 was approximately double that of LAGEOS-1. LAGEOS-2 had the most irregular behaviour with no obvious pattern, remaining bounded between approximately 0.75 to 2.5 km. The lower bounds of these errors provided a useful point of reference: consistently meeting the bound throughout the year alone would be a significant improvement as this would represent the removal of the oscillations and more consistent state estimates.

Fits on the calibration satellites were conducted using TLE and SLR data from the year 2022, considering combinations of fit midpoints and window sizes, as presented in Table 3.1. The motivation of these tests was to investigate the influence of the fit epoch and fit window size on the quality of fits, and whether a specific combination of these parameters was particular effective in mitigating the impact of biases in pseudo-observations. The results of conducting these fits are presented in Figures 3.2 and 3.3.

Table 3.1: Fit sweep parameters.

Term	Fit Midpoint Interval [days]	No. Samples [-]	Fit Window Size [days]
Short	2	100	2, 3, 4, 5, 6, 7, 8, 9, 10
Long	3	100	10, 20, 30, 40, 50, 60, 70, 80, 90

Fits on all four of the calibration satellites showed similar behaviour for the short-term cases: fit error was primarily driven by the fit window midpoint, noticeable as vertical banding throughout the year, particularly for Etalon 1 and 2. Fit window size appeared to have minimal impact on the fit error for the short-term cases with increased sizes not being associated with any change in error. LAGEOS-2 saw a significant improvement in fit quality towards the end of 2022, both in terms of typical error and the magnitude of the oscillations.

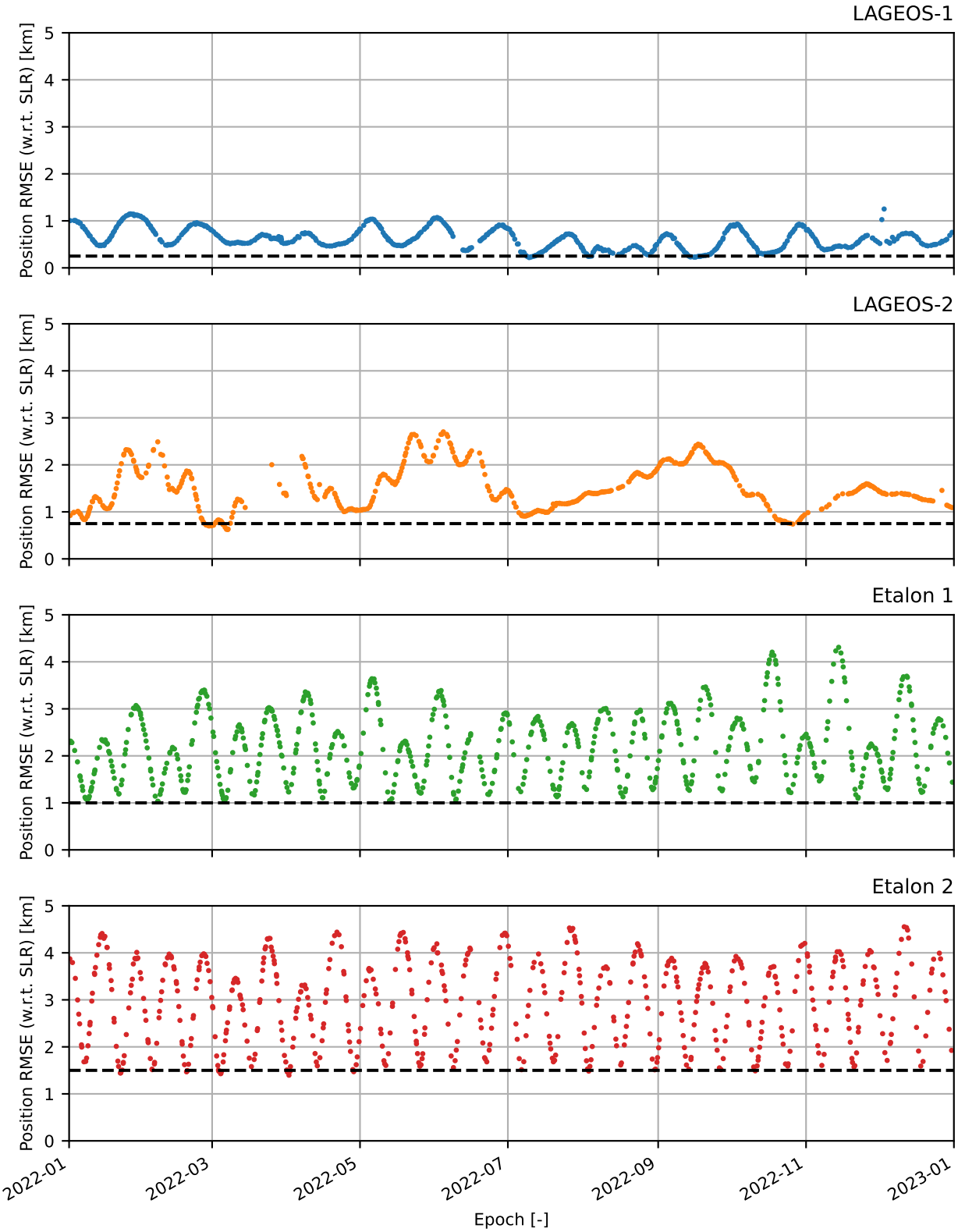


Figure 3.1: Position RMSE, with respect to SLR, during 30 days post-epoch for calibration satellite TLEs. New TLEs were published approximately daily, except for some multi-days gaps in availability seen with LAGEOS-1 and -2. Periodic variations in position RMSE are highly visible due to varying bias in the TLEs. The dashed lines represent the established baselines for each satellite.

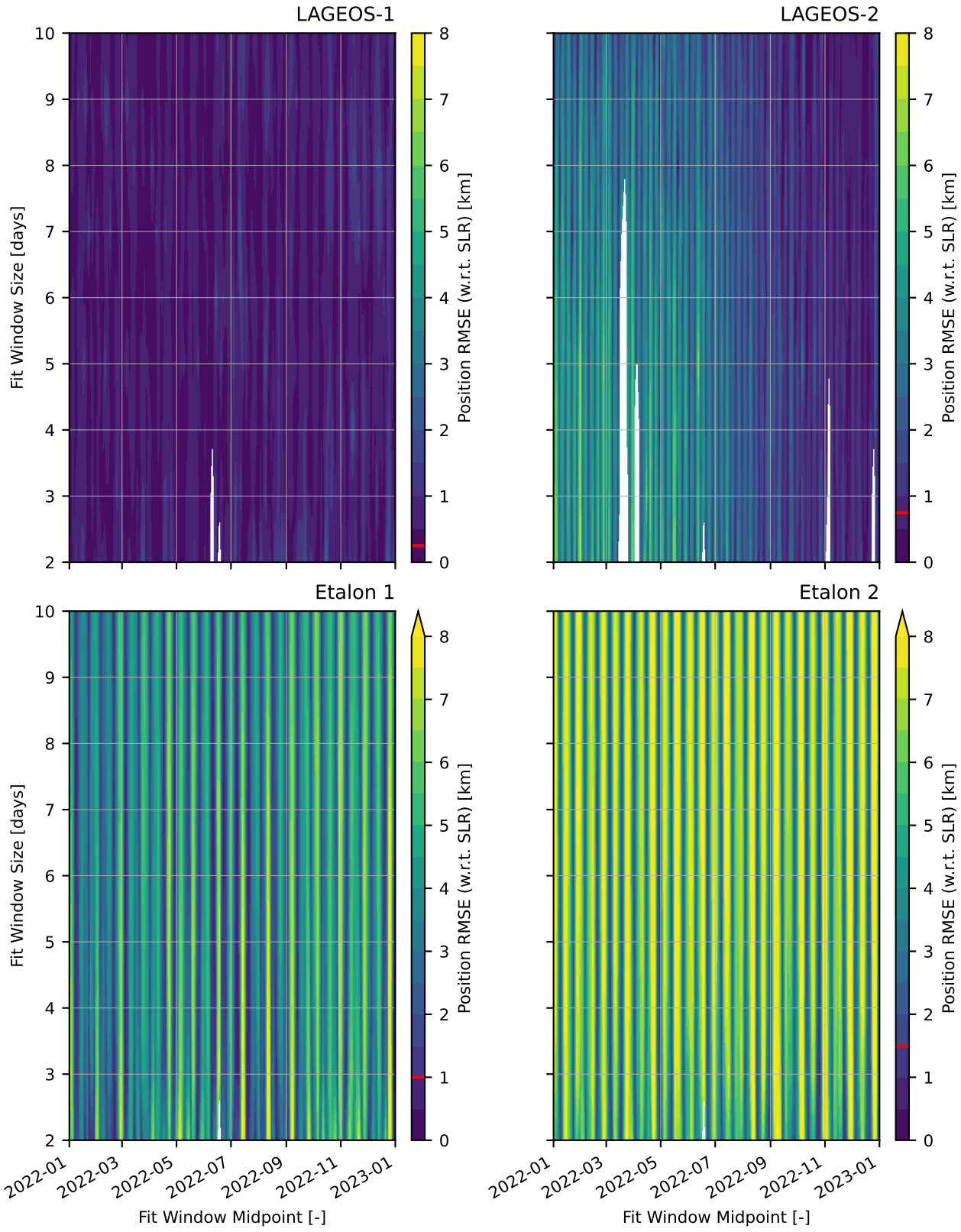


Figure 3.2: Position RMSE during the 30 days post-fit for short-term biased fits of the calibration satellites. The red marker in the colour bar indicates the RMSE baseline derived from TLEs. Note that white regions indicate failed cases due to a lack of TLEs within the window.

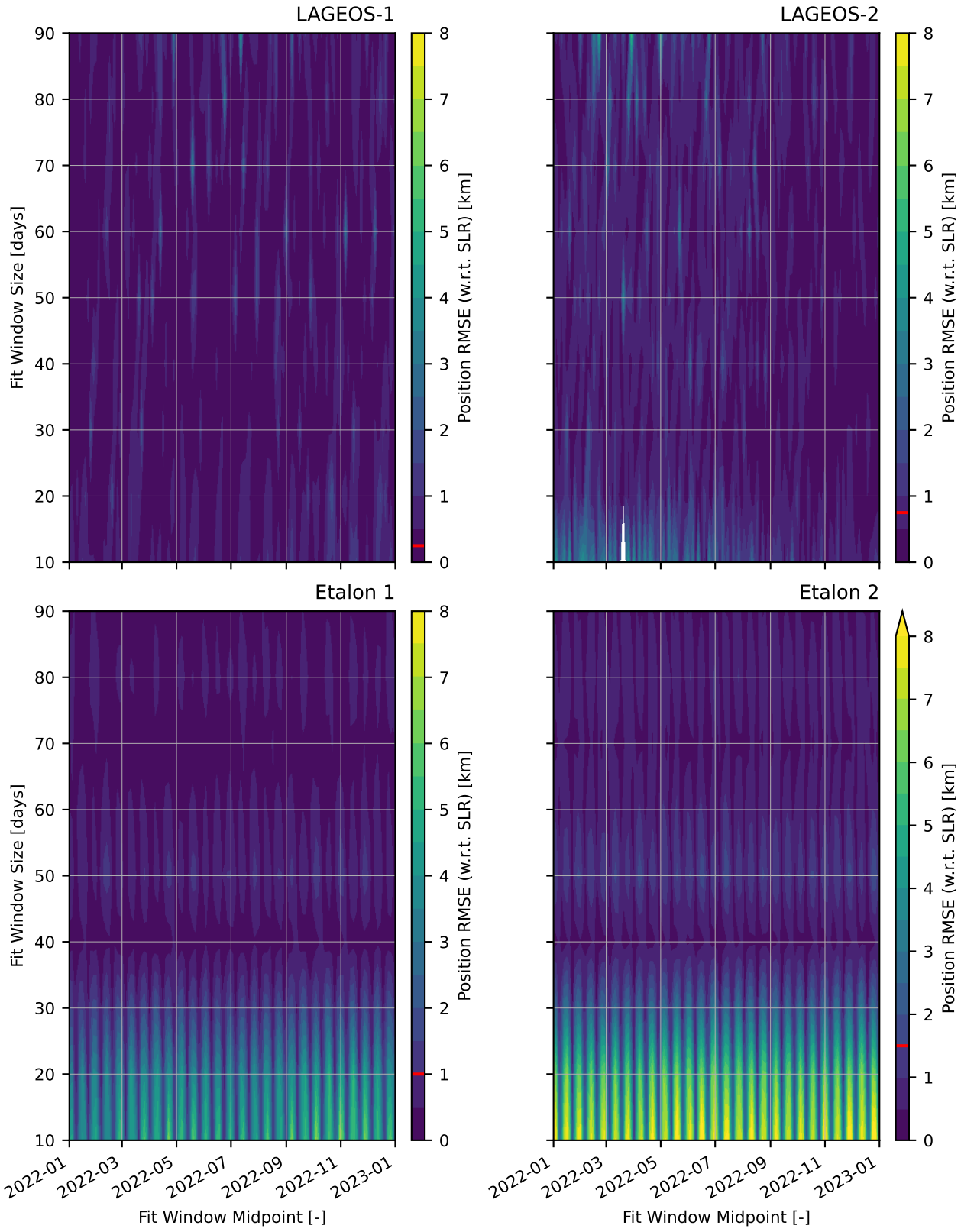


Figure 3.3: Position RMSE during the 30 days post-fit for long-term biased fits of the calibration satellites. The red marker in the colour bar indicates the RMSE baseline derived from TLEs. Note that white regions indicate failed cases due to a lack of TLEs within the window.

For the long-term fits, the dependence on fit window midpoint remained for smaller windows. Nevertheless, the variation throughout the year reduced as the size of the windows increased. Above 40 days, the oscillations in fit error became significantly smaller for all four satellites, eventually converging to errors significantly lower than those seen for the short-term fits. Notably, for Etalon 1 and 2, some slight banding reappeared for fit windows around 50 days and 80 days, which demonstrated that the periodic influence of the bias was not completely eliminated in all cases by extending the fit windows. In any case, for the extended windows, the post-fit errors were typically at or below the baselines established in Figure 3.1, suggesting that, for long-term fits, prediction accuracy was improved over the best case TLE-based predictions.

The impact of increasing the size of the fit window was further illustrated by considering the aggregate behaviour on fit error for each object. The mean position RMSE for each object as a function of the fit window size is presented in Figure 3.4. For the short-term fits, the mean error remained largely constant for all four objects, other than a slight reduction for LAGEOS-2 and slight increase for Etalon 2. Significant reductions did not occur until the fit window size was increased past 10 days with all four objects reaching their respective baselines after 40 days. The slight banding for Etalon 1 and 2 at 50 days and 80 days was seen as slight increases in the mean error.

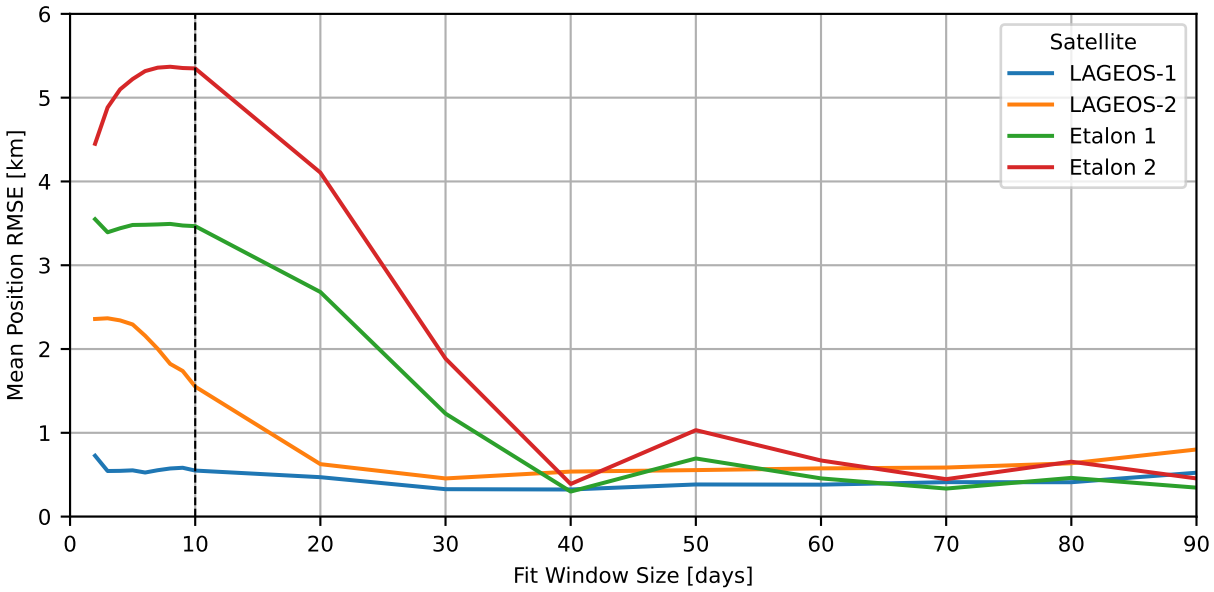


Figure 3.4: Mean position RMSE during the 30 days post-fit for short-term and long-term biased fits of the calibration satellites.

Importantly, many of the short-term fits had significantly higher errors than simply propagating TLEs directly with SGP4. For example, fits on Etalon 1 and 2 often had errors double that of the worst cases presented in Figure 3.1. The implication of these results is that, without properly understanding the biases in the TLE series, it is unknown whether a given P-OD fit was conducted on accurate TLEs, where the bias is close to zero, or on inaccurate TLEs, where the TLEs are highly biased. TLE-based P-OD cannot be applied without careful selection of parameters nor without considering the impact of bias. In the absence of bias modelling, long fit windows are required to apply P-OD techniques successfully to TLE series.

The number of iterations required for the state estimator to converge for the biased calibration satellite fits are presented in Figure 3.5. In all of the cases, the state estimator reached the convergence criterion of no further updates to the decision vector. For all four satellites, only a few iterations were required for the state estimator to converge, typically in the single-digit range. Generally, the number of iterations required increased as the fit window duration was increased. On average, LAGEOS-1 and -2 required five to six iterations, respectively, to converge; meanwhile, Etalon 1 and 2 required approximately only three iterations. These corresponded to the state estimator requiring an average of 36, 43, and 22 evaluations of the propagator, respectively.

3.2 Error Characteristics of Deep Space Two-Line Element Sets

The periodic variations in P-OD post-fit accuracy seen in Figures 3.2 and 3.3 suggested that there was a systematic driver in TLE accuracy affecting the state estimation process. It was decided, therefore, to analyse the errors present in the TLEs of the calibration satellites in an attempt to reveal potential sources of error.

The errors in TLEs can be evaluated by considering the relative position and velocity between the TLE-derived positions and those sourced from a higher-accuracy ephemeris:

$$\Delta\mathbf{r} = \mathbf{r}_{\text{TLE}} - \mathbf{r}_{\text{SP3}},$$

$$\Delta\mathbf{v} = \mathbf{v}_{\text{TLE}} - \mathbf{v}_{\text{SP3}}.$$

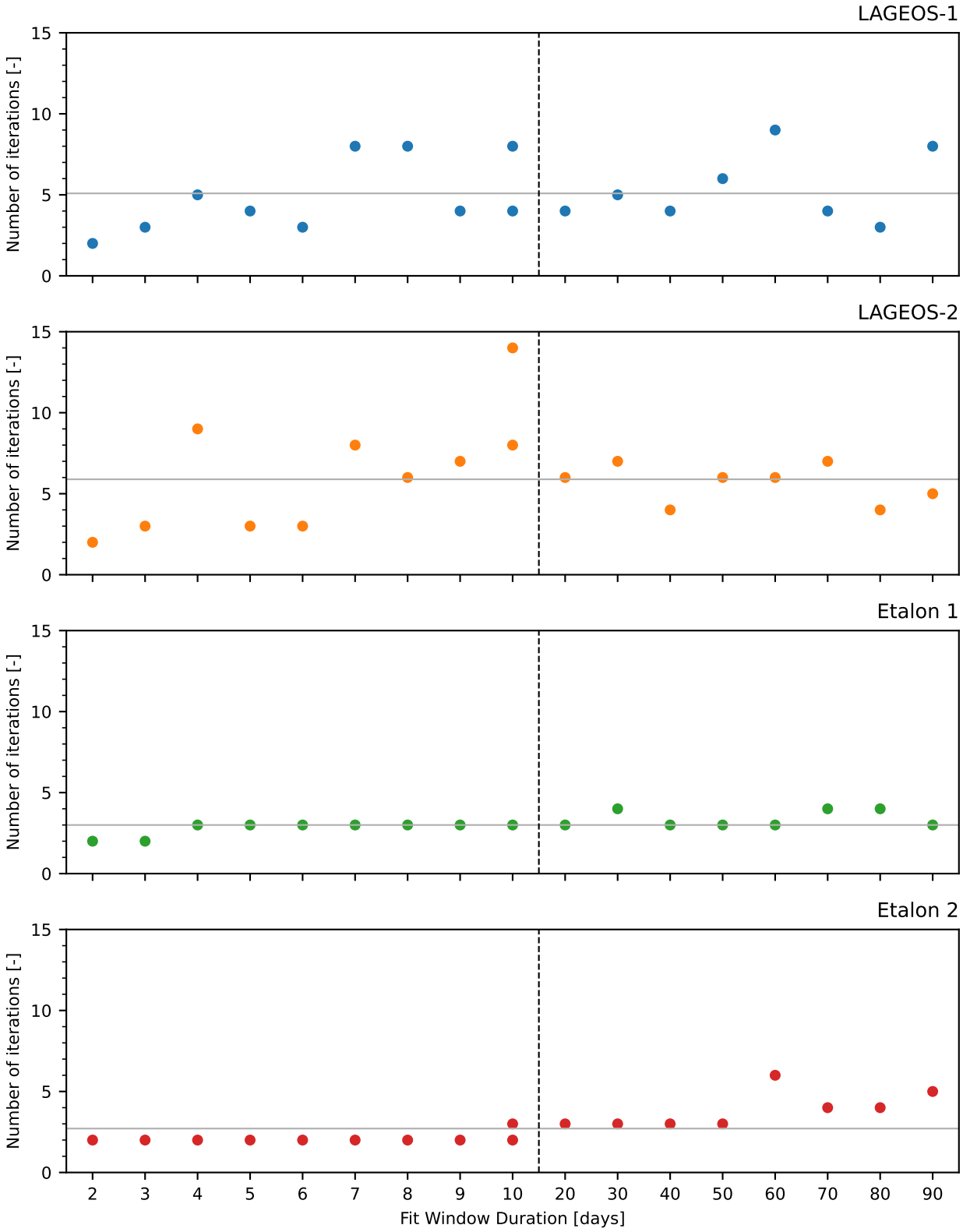


Figure 3.5: Number of iterations required for the state estimator to converge for the short- and long-term biased calibration satellite fits. The average number of iterations is illustrated by the grey line. Note the change in fit window size interval between the short- and long-term fits.

The position errors between TLEs and SLR for the calibration satellites are presented in Figure 3.6. For LAGEOS-1 and -2, the position error remained mainly below 0.5 km and 1 km respectively; while, for Etalon 1 and 2, the position error remained below 2.5 km throughout the year. Notably, all four satellites showed periodic behaviour, most prominently in the cases of Etalon 1 and 2.

The errors can be further investigated in the RTN frame:

$$\Delta\mathbf{r}_{\text{RTN}} = \mathbf{R}_{\text{RTN}}(\mathbf{r}_{\text{TLE}}, \mathbf{v}_{\text{TLE}})\,\Delta\mathbf{r},$$

$$\Delta\mathbf{v}_{\text{RTN}} = \mathbf{R}_{\text{RTN}}(\mathbf{r}_{\text{TLE}}, \mathbf{v}_{\text{TLE}})\,\Delta\mathbf{v}.$$

In this case, the errors and the RTN frame are defined relative to the TLE-derived position to ensure that the biases are defined by the 'known' ephemerides. Nevertheless, it should be noted that the two RTN frames are approximately the same in cases of small relative position and velocity errors.

The RTN position and velocity errors can be normalised by the position magnitude of the TLE-based solution to produce angular errors:

$$\Delta\boldsymbol{\theta}_{\text{RTN}} \approx \frac{\Delta\mathbf{r}_{\text{RTN}}}{||\mathbf{r}_{\text{TLE}}||},$$

$$\Delta\boldsymbol{\omega}_{\text{RTN}} \approx \frac{\Delta\mathbf{v}_{\text{RTN}}}{||\mathbf{r}_{\text{TLE}}||}.$$

The angular position error components for the calibration satellites are presented in Figure 3.7. For LAGEOS-1, and Etalon 1 and 2 the along-track position error components dominated, with significantly larger minimum and maximum values when compared to the other error components. This was the case for LAGEOS-2 at the start of the year; however, by the end of the year the along-track position error was similar in magnitude to the normal error, suggesting a different error behaviour.

The angular velocity error components for the calibration satellites are presented in Figure 3.8. The radial velocity error dominated for all four satellites. Notably, the radial velocity error had the same structure as the along-track position error. This was particularly noticeable for LAGEOS-2. At the same time, the two errors components appeared to be mirrored in the y-axis: positive along-track position errors were accompanied by negative radial velocity errors and vice versa. Interestingly, the angular radial velocity errors were significantly smaller for Etalon 1 and 2 than LAGEOS-1 and -2, in contrast to the converse relationship for angular along-track position errors.

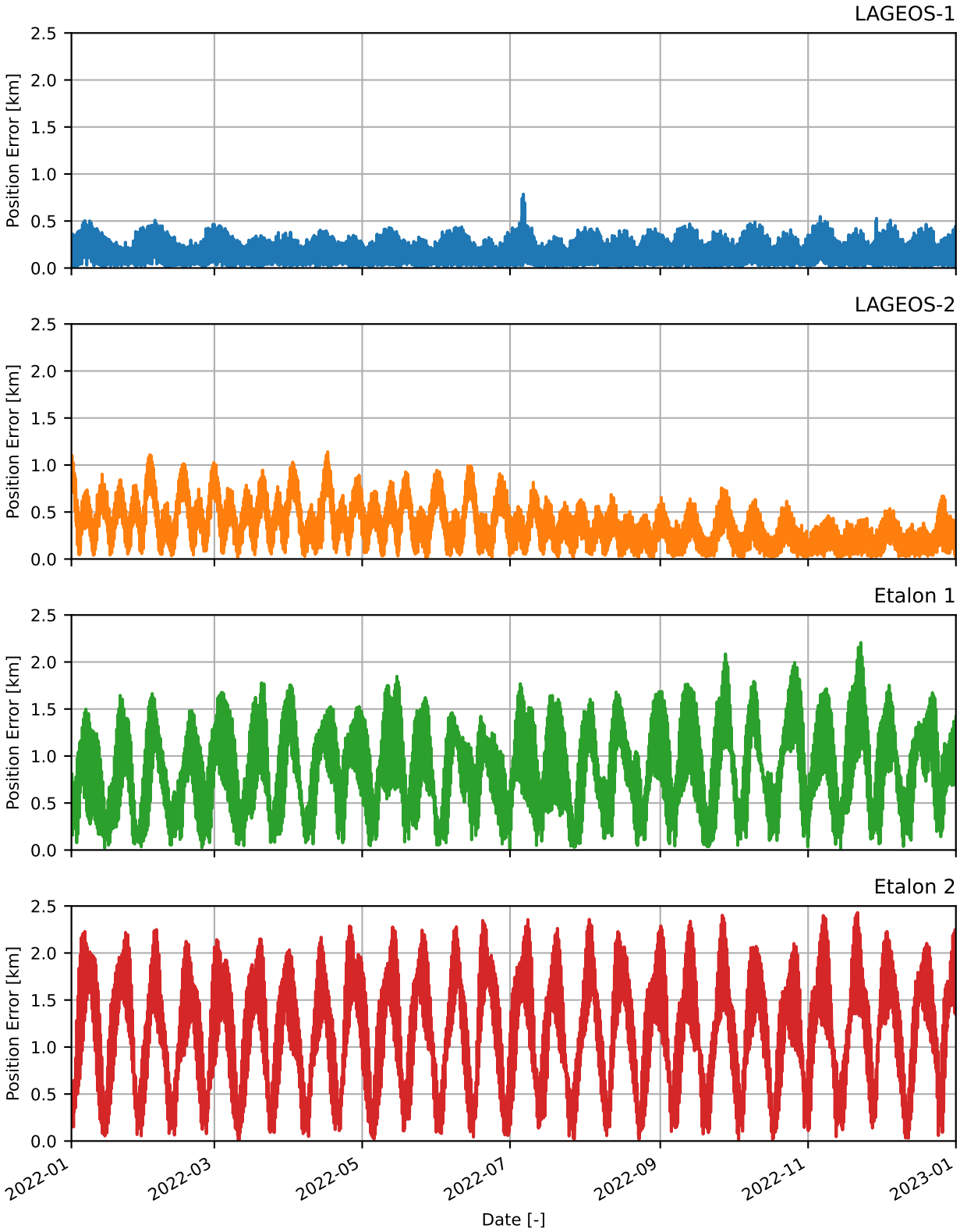


Figure 3.6: Position errors of calibration satellite TLEs for the year 2022.

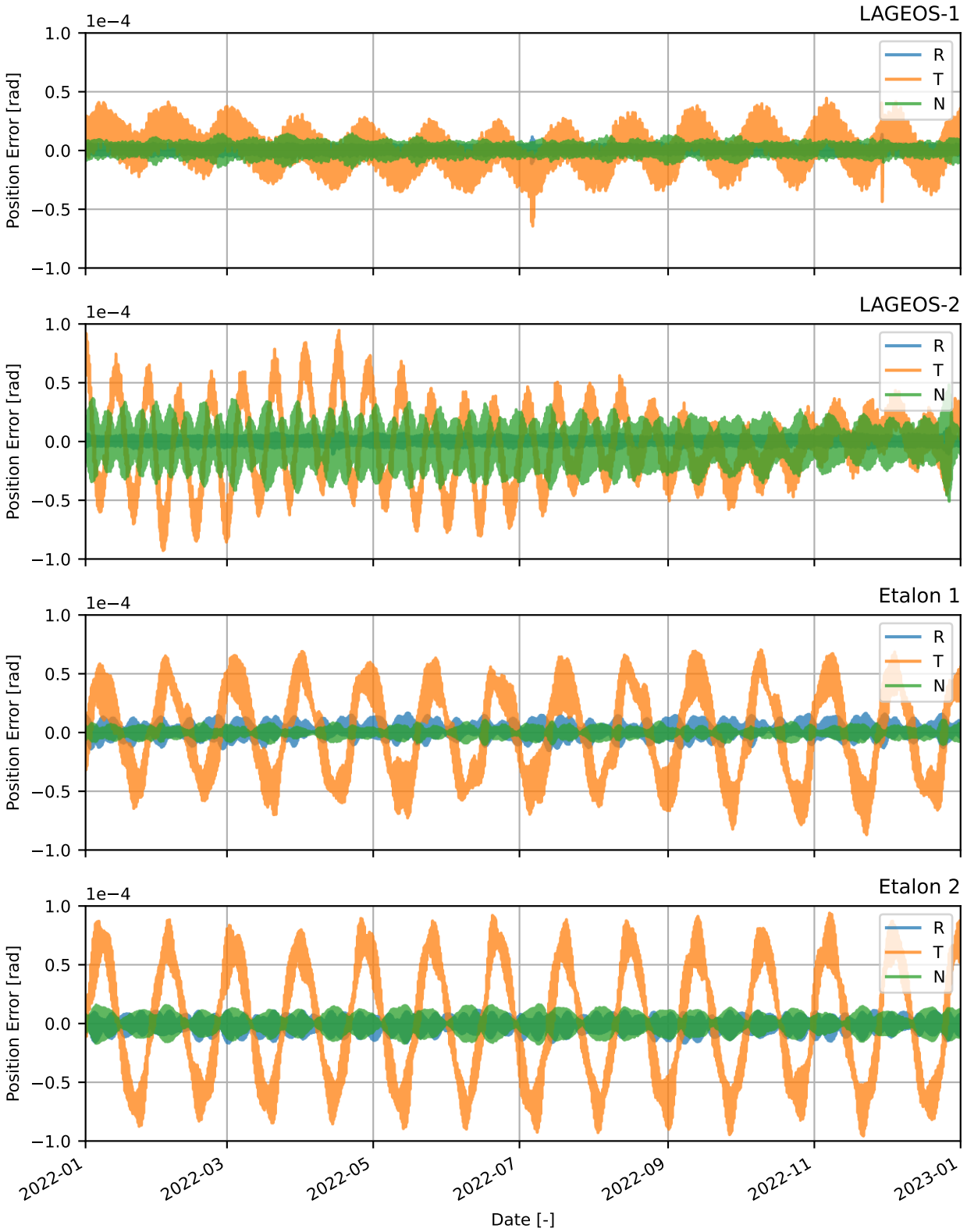


Figure 3.7: Angular RTN position errors of calibration satellite TLEs for the year 2022.

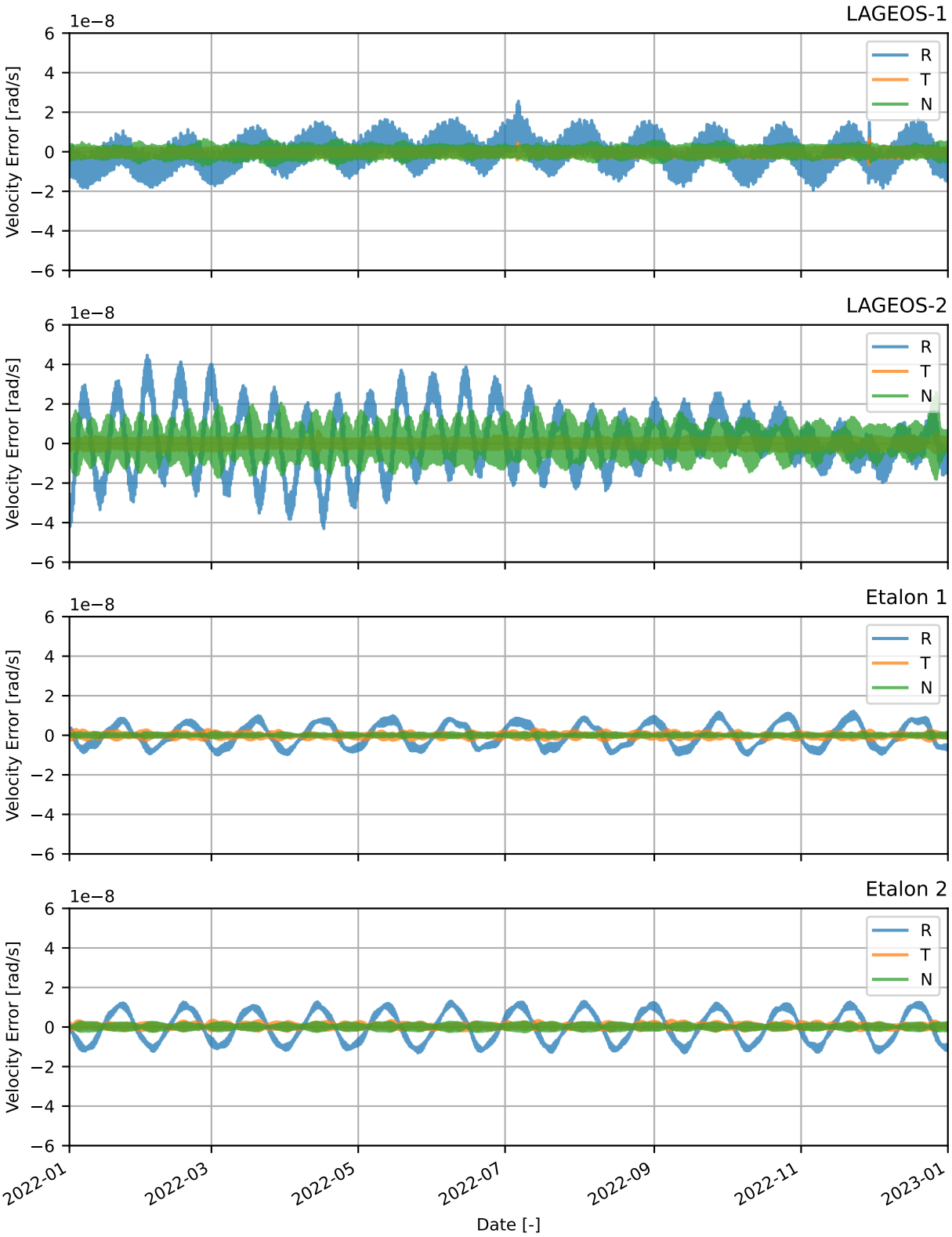


Figure 3.8: Angular RTN velocity errors of calibration satellite TLEs for the year 2022.

Relative dynamics could explain the link between the along-track position error and the radial velocity error seen in Figures 3.7 and 3.8. The calibration satellites are in approximately circular orbits, therefore the radial velocity error can be interpreted as a semi-major axis error rate. A positive radial velocity error would imply that the semi-major axis is increasing, resulting in a decreasing orbital velocity and the satellite starting to drift in the negative along-track direction. The opposite is true for a negative radial velocity error.

The longer-term evolution of the calibration satellites' along-track position and radial velocity errors is presented in Figures 3.9 and 3.10. Etalon 1 and 2 had the most consistent variation in both along-track position and radial velocity error with the amplitude of the oscillations remaining virtually unchanged over the seven years of data. LAGEOS-1 and -2, on the other hand, showed repetitions of the behaviours seen in Figures 3.7 and 3.8. LAGEOS-1 had an approximately yearly variation superimposed over the aforementioned monthly variation. The variation seen over the timespan of a year for LAGEOS-2 appeared to cycle approximately every 18 months.

3.2.1 Bias Frequency Analysis

The along-track position and radial velocity errors contained multiple periodic components at the scale of both months and years, as highlighted in Figures 3.9 and 3.10. Frequency analysis can provide further insight into the structure of these components which can be used to tie them to suspected and known sources of error, such as, for example, mismodelling of lunisolar effects. These would manifest in a frequency analysis as components with periods of approximately one year and one month, for the Sun and Moon respectively, and any integer multiple harmonics.

Several methods exist for transforming a time series into the frequency domain. The time series, specifically the various TLE error components in this case, are represented by a series of discrete samples taken at a constant sampling rate. This makes the Fast Fourier Transform (FFT) [129] an ideal choice for frequency analysis to find the key periodic components in TLE bias. An FFT analysis of the along-track angular position errors and the radial angular velocity errors is presented in Figures 3.11 and 3.12. A sampling period of 30 minutes was used for the FFTs. The LAGEOS satellites had the lowest of the calibration satellites' orbital periods at approximately 225 minutes. The Nyquist frequency, therefore, was approximately eight times larger than the expected signal bandwidth, meaning that aliasing was not expected.

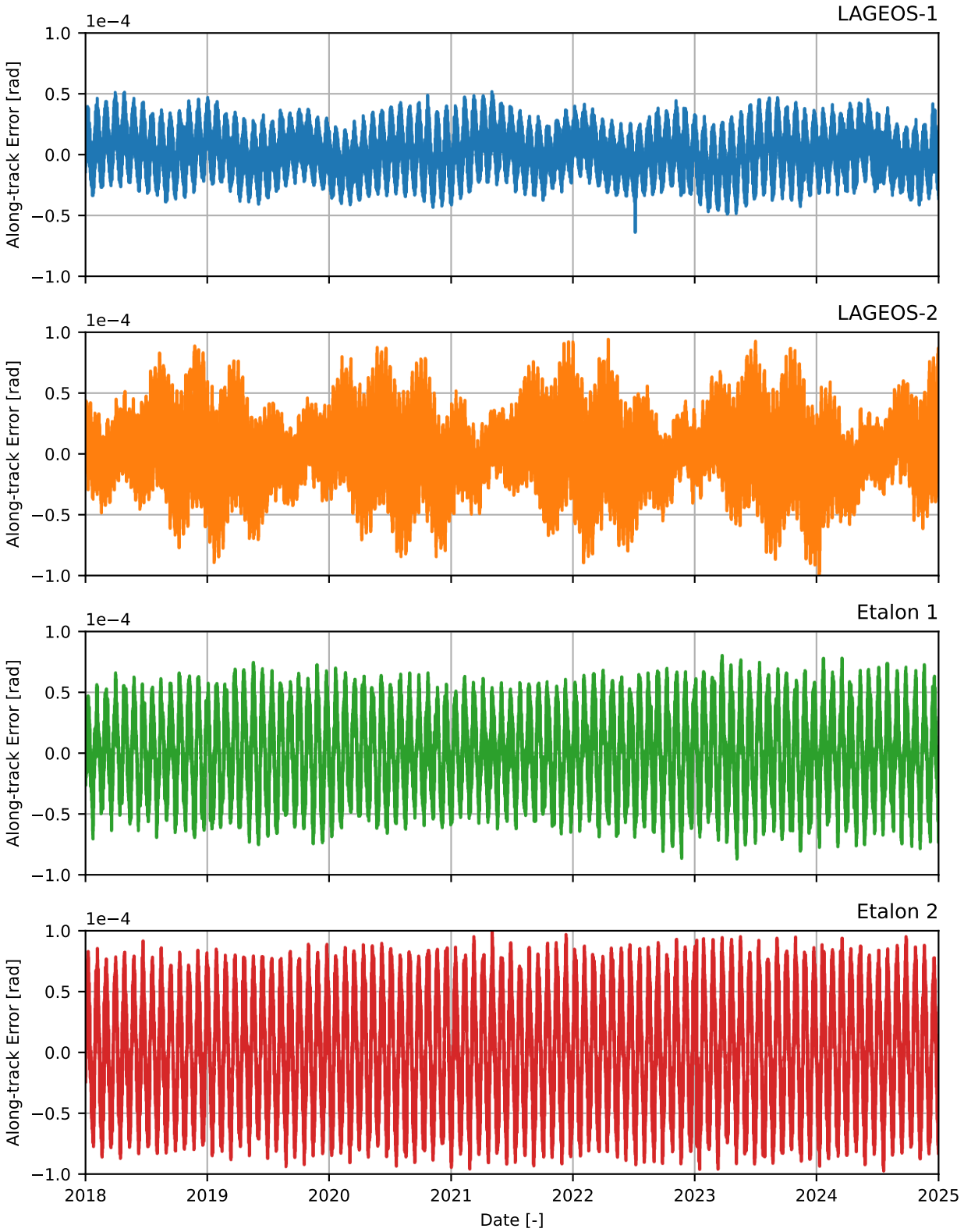


Figure 3.9: Angular along-track position error of calibration satellite TLEs for the years 2018 to 2025.

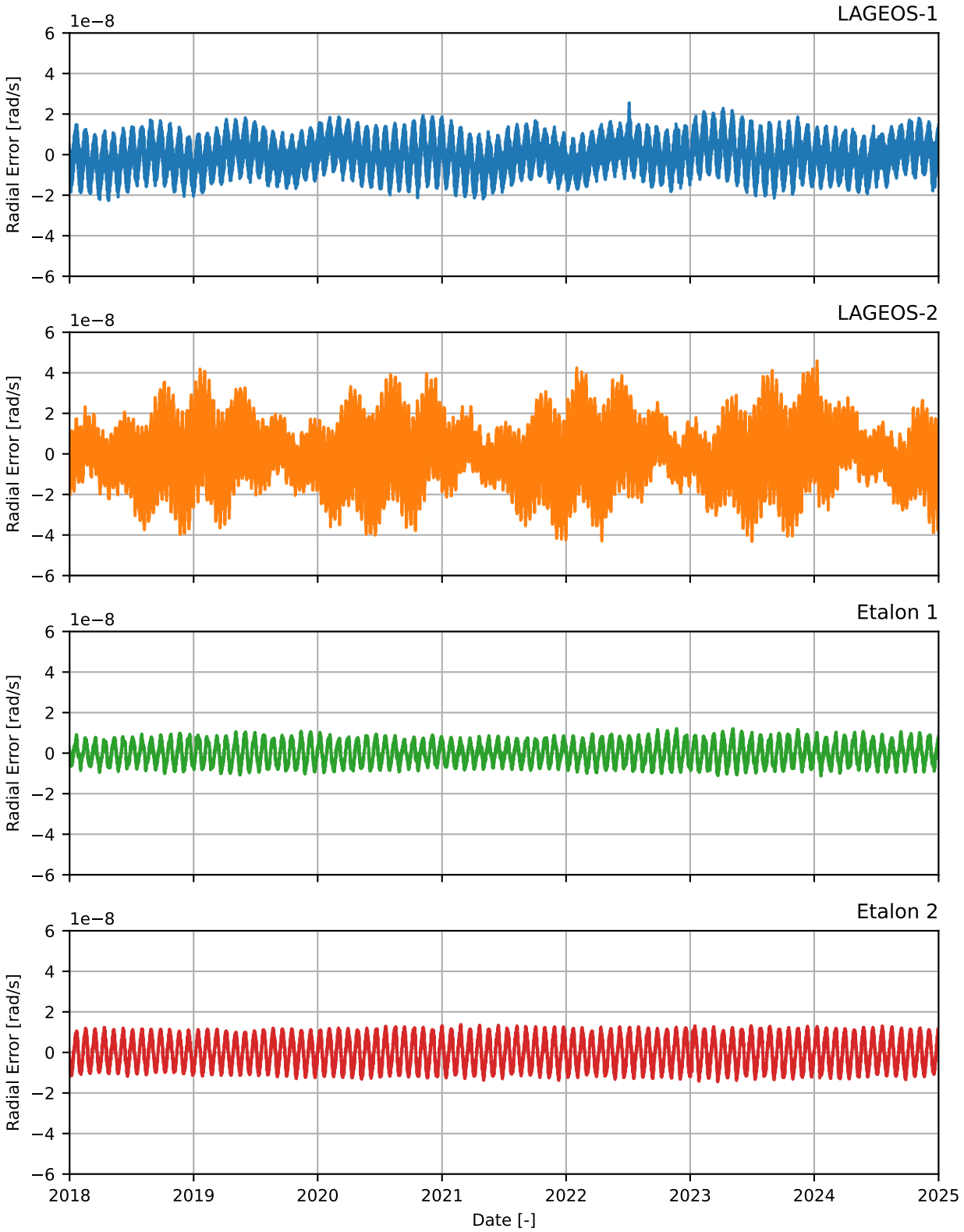


Figure 3.10: Angular radial velocity error of calibration satellite TLEs for the years 2018 to 2025.

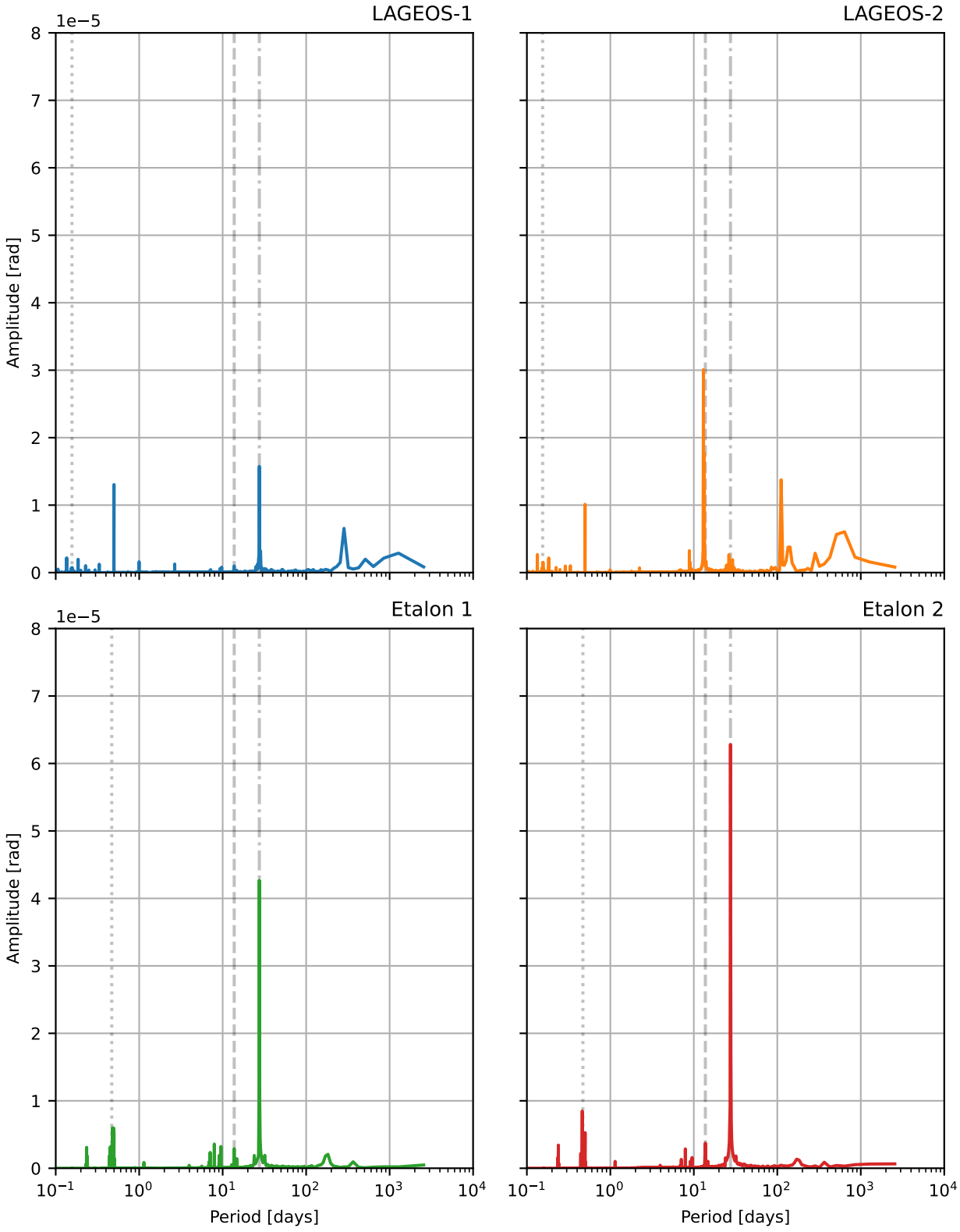


Figure 3.11: FFT analysis of the along-track angular position errors of the calibration satellites for the years 2018 to 2025. The orbital period of each satellite, the half period of the Moon, and the Moon's orbital period are represented by the dotted, dashed, and dash-dotted lines respectively.

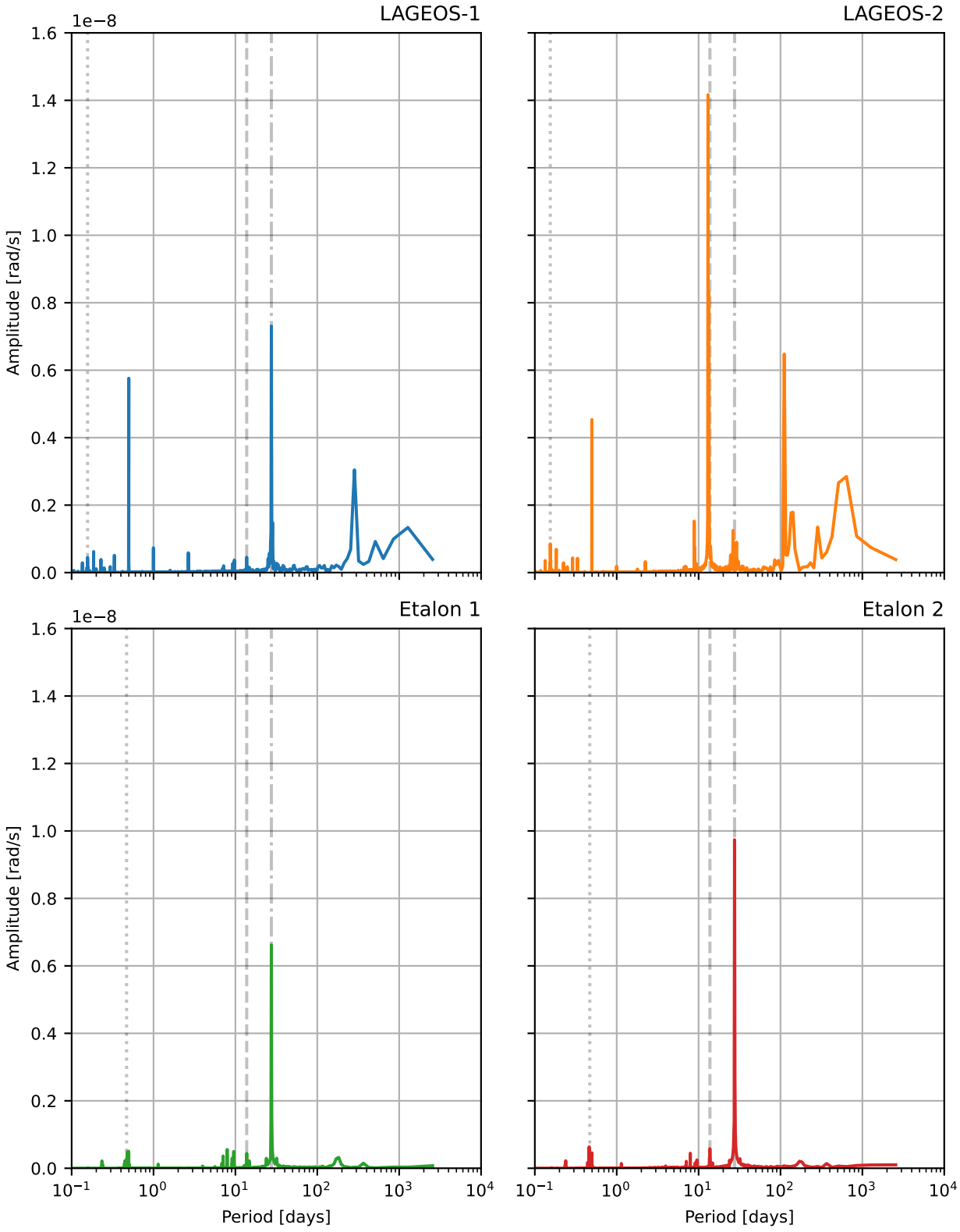


Figure 3.12: FFT analysis of the radial angular velocity errors of the calibration satellites for the years 2018 to 2025. The orbital period of each satellite, the half period of the Moon, and the Moon's orbital period are represented by the dotted, dashed, and dash-dotted lines respectively.

LAGEOS-1, and Etalon 1 and 2 showed strong peaks in amplitude at the period of the Moon's orbit about the Earth. LAGEOS-2, conversely, showed this peak at the half-period of the Moon's orbit. All four cases showed a peak at approximately 12 hours. In the case of Etalon 1 and 2, this corresponded to their orbital periods. However, this was approximately three times the orbital periods of LAGEOS-1 and -2. LAGEOS-1 and -2 had additional longer-period oscillations with peaks at approximately 300 and 100 days respectively, corresponding to the longer-term evolution seen in Figures 3.9 and 3.10. There was a significant difference in the largest amplitudes for Etalon 1 and 2: Etalon 2's amplitude was 47.1 % larger, despite the two satellites having very similar orbits, with matching semi-major axis, eccentricity, and inclination, as highlighted in Table 2.2. The fast variable of true, mean, or eccentric anomaly could be ignored due to the period of the bias being significantly larger than the orbital periods, as could angle of perigee due to the near-circular orbits of the satellites. This left RAAN as the distinguishing factor between the satellites. This could suggest that the orientation of their orbital planes, perhaps with respect to the orbital plane of the Moon, dictated the magnitude of the oscillation in along-track position error.

3.2.2 Impact of Increasing Window Size on Error Characteristics

The presence of several key periodic components for each satellite's errors suggests that, for example, the superposition of a set of periodic components could be used to model the along-track position error:

$$\Delta\theta_T(t) \approx \sum_i a_i \cos\left[\frac{2\pi}{b_i}\left(t + c_i\right)\right] + d, \tag{3.1}$$

or the radial velocity error:

$$\Delta\omega_R(t) \approx \sum_i e_i \cos\left[\frac{2\pi}{f_i}\left(t + g_i\right)\right] + h,$$

where a_i, b_i, c_i, and e_i, f_i, g_i are the bias amplitude, period, and phase respectively of each component; and d and h are the mean offsets; and t is the time from a set epoch. Additional bias models will be discussed in greater detail in Section 3.3.

It was seen in Figures 3.2 and 3.3 that increasing the size of the P-OD fit window reduced post-fit error significantly while, at the same time, suppressing the periodic variations. This suggests that

the state estimate was improved by including pseudo-observations from across a wide range of bias conditions, at multiple points along the TLE biases illustrated in Figures 3.7 and 3.8.

The impact of increasing the size of the window can be analysed by considering the mean error for a given window. Using the superposition of periodic components proposed to model the along-track position error in Equation (3.1), as an example, the mean error can be determined analytically:

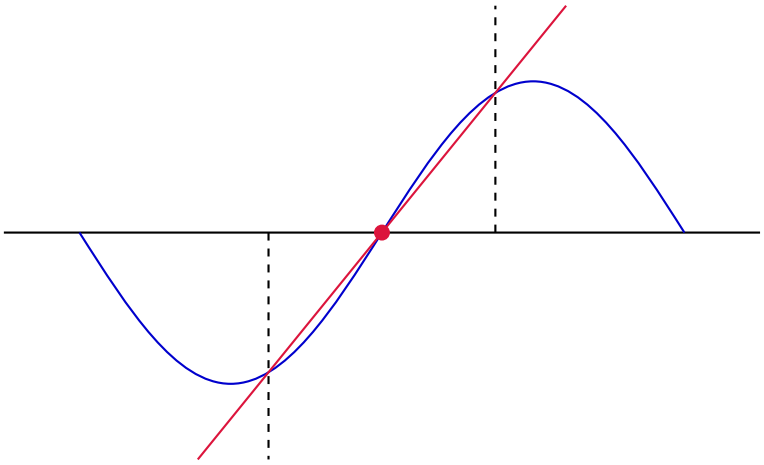
$$\begin{aligned}
\overline{\Delta\theta_T}(t^*, \Delta t) &= \frac{1}{\Delta t} \int_{t^* - \frac{\Delta t}{2}}^{t^* + \frac{\Delta t}{2}} \Delta\theta_T(t)\, dt, \\
&\approx \frac{1}{\Delta t} \int_{t^* - \frac{\Delta t}{2}}^{t^* + \frac{\Delta t}{2}} \sum_i a_i \cos\left[\frac{2\pi}{b_i}\left(t + c_i\right)\right] + d\ dt, \\
&= \frac{1}{\Delta t}\left[\sum_i \frac{a_i b_i}{2\pi} \sin\left[\frac{2\pi}{b_i}\left(t + c_i\right)\right] + td\right]_{t^* - \frac{\Delta t}{2}}^{t^* + \frac{\Delta t}{2}}, \\
&= \sum_i \frac{a_i b_i}{\pi \Delta t} \cos\left[\frac{2\pi}{b_i}\left(t^* + c_i\right)\right] \sin\left(\frac{\pi \Delta t}{b_i}\right) + d,
\end{aligned} \tag{3.2}$$

where t^* is the midpoint of the window and Δt its size.

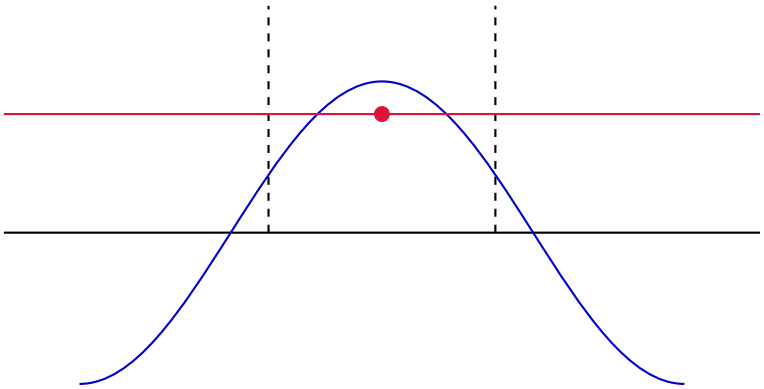
Similarly, the mean error rate with respect to the window midpoint can be evaluated:

$$\begin{aligned}
\dot{\overline{\Delta\theta_T}}(t^*, \Delta t) &= \frac{\partial}{\partial t^*}\left[\overline{\Delta\theta_T}(t^*, \Delta t)\right], \\
&\approx \frac{\partial}{\partial t^*}\left[\sum_i \frac{a_i b_i}{\pi \Delta t} \cos\left[\frac{2\pi}{b_i}\left(t^* + c_i\right)\right] \sin\left(\frac{\pi \Delta t}{b_i}\right) + d\right], \\
&= -\sum_i \frac{2a_i}{\Delta t} \sin\left[\frac{2\pi}{b_i}\left(t^* + c_i\right)\right] \sin\left(\frac{\pi \Delta t}{b_i}\right).
\end{aligned} \tag{3.3}$$

Notably, the period and phase of the error are unaffected by the averaging process, and remain independent of the size of the fit window. This result matches the behaviour seen in Figures 3.2 and 3.3 where the variations in RMSE remained in phase as the size of the window increased. Another feature is the phase offset of the mean error rate, with respect to the mean error, by 90° which would suggest that the amplitude of the mean error rate is highest when the mean error is minimised and vice-versa, as depicted in Figure 3.13.



(a) Centred about a zero crossing, demonstrating zero mean error but a non-zero mean error rate.



(b) Centred about a peak, demonstrating a non-zero mean error but zero mean error rate.

Figure 3.13: Example of averaging a bias model (blue), illustrated by considering a line of best fit (red) for a restricted domain (black, dashed).

Equations (3.2) and (3.3) reveal two methods for reducing the mean error and rate. Firstly, due to the inclusion of the reciprocal of the window size in both equations, increasing the size of the window results in a smaller mean error and error rate. In the limit, this results in the periodic behaviour being removed entirely, leaving only the constant bias term in the mean error:

$$\lim_{\Delta t \to \infty} \overline{\Delta\theta_T}(t^*, \Delta t) \approx d,$$

$$\lim_{\Delta t \to \infty} \dot{\overline{\Delta\theta_T}}(t^*, \Delta t) \approx 0,$$

and, by extension:

$$\lim_{\Delta t \to \infty} \overline{\Delta\omega_R}(t^*, \Delta t) \approx h,$$

$$\lim_{\Delta t \to \infty} \dot{\overline{\Delta\omega_R}}(t^*, \Delta t) \approx 0.$$

Secondly, the mean error and error rate of a given bias component can be reduced by considering the sinusoidal component present in both equations:

$$\sin\left(\frac{\pi\Delta t}{b_i}\right) = 0,$$

$$\frac{\pi\Delta t}{b_i} = \pi n,$$

$$\frac{\Delta t}{b_i} = n,$$

and, by extension:

$$\frac{\Delta t}{f_i} = n,$$

where n is an integer. In other words, a fit window with a duration that is an integer multiple of the bias component period removes its periodic behaviour.

The effect of averaging the along-track position errors of the calibration satellites for windows of various sizes is presented in Figure 3.14. In the cases of Etalon 1 and 2, the behaviour suggested by Equation (3.2) was highly apparent: roots existed at integer multiples of the Moon's orbital period, the dominant mode for these satellites; and the magnitude of the mean along-track error faded as the size of the window was increased. Furthermore, the pattern of the cosine-sine product in Equa-

tion (3.2), which accounts for the midpoint of the window and window size respectively, was highly visible. LAGEOS-1 and -2 showed significantly different behaviour, although with hints of similarity to Etalon 1 and 2: for example, crossovers could be seen at the Moon's orbital period and half-period respectively for each satellite. LAGEOS-2's shorter primary frequency was highly visible in the oscillations with respect to the window midpoint. Some of these features could be seen in Figures 3.2 and 3.3, however the limited resolution in fit window size of the P-OD sweeps prevented the zero crossings from being apparent.

Histograms of along-track position errors are presented in Figure 3.15 for a variety of window sizes. The mean along-track error for all four satellites reduced in magnitude as the size of the fit window was increased. Etalon 1 and 2 had the most improved along-track errors, almost reaching 0 rad. For Etalon 1 and 2, the longer windows resulted in a bimodal distribution with two peaks which were approximately symmetric about zero. This is explained by considering the dominant periodic component of the error and that a greater proportion of time is spent near the peak and trough of the wave rather than at the zero crossing point. The bimodal distribution was visible for LAGEOS-2 at 5 days, potentially due to the smaller bias amplitude for this satellite's TLEs around July 2022 when compared to Etalon 1 and 2.

3.3 Data-Driven Bias Models

Extended fit windows have a major limitation in that they cannot account for changes in an RSO's orbit which are a result of perturbations not present in the physical model of the predictor, in this case the higher-fidelity numerical propagator. For example, manoeuvres conducted by active payloads or changes in velocity from collisions between passive debris would affect the results of P-OD, unless additional manoeuvre detection and estimation were included in the state estimation process.

The alternative to extended fit windows is to account for the biases with a model. By estimating the bias for a given TLE at a given time, it can be removed to provide a more accurate pseudo-observed state. This should improve P-OD results by reducing the amount of bias in a given fit window and, potentially, improving the distribution of residuals to better match the statistical properties assumed by the particular OD method. It is proposed to use data-driven models, using the errors between TLEs and higher-accuracy ephemerides, as presented in Section 3.2.

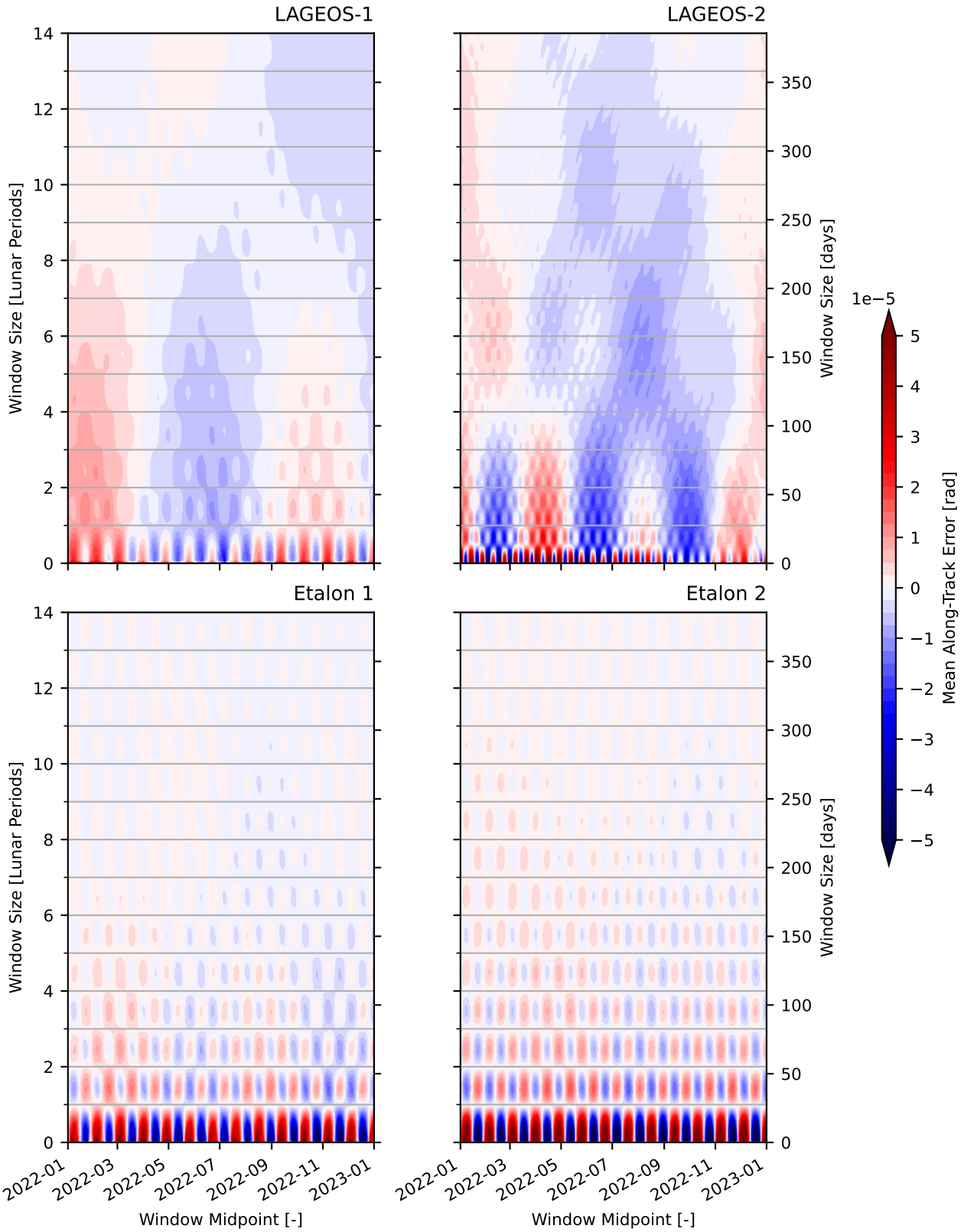
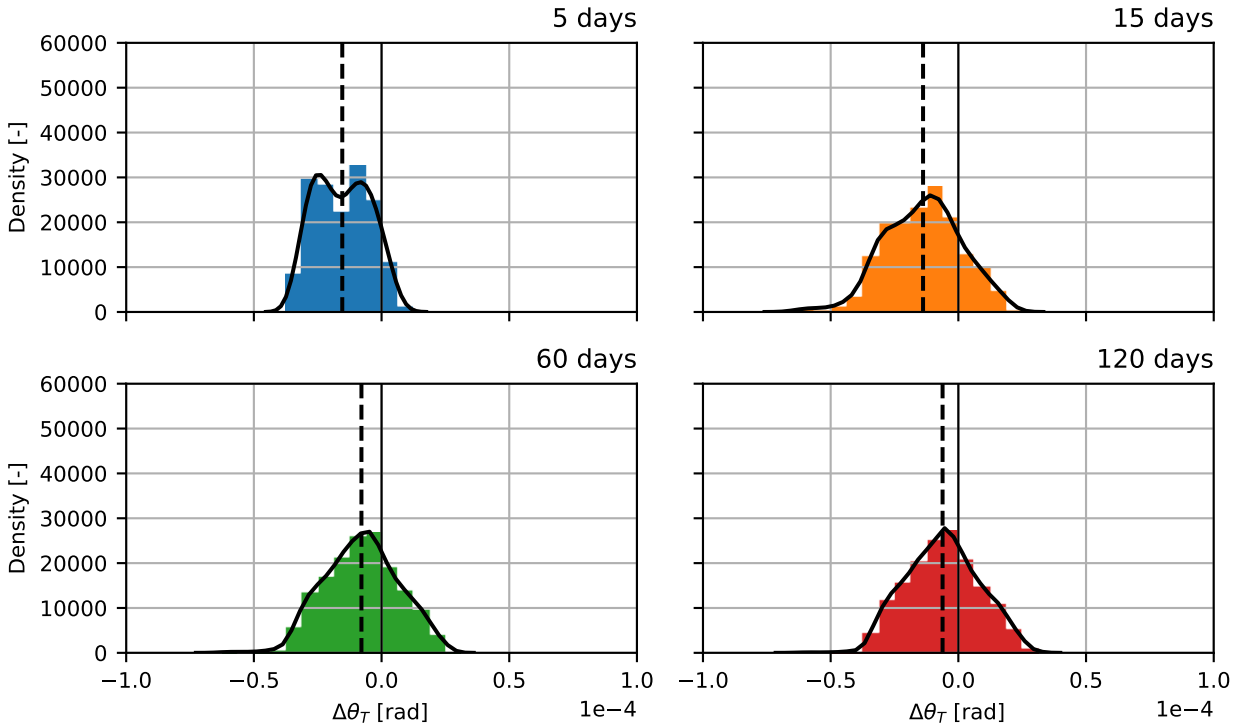
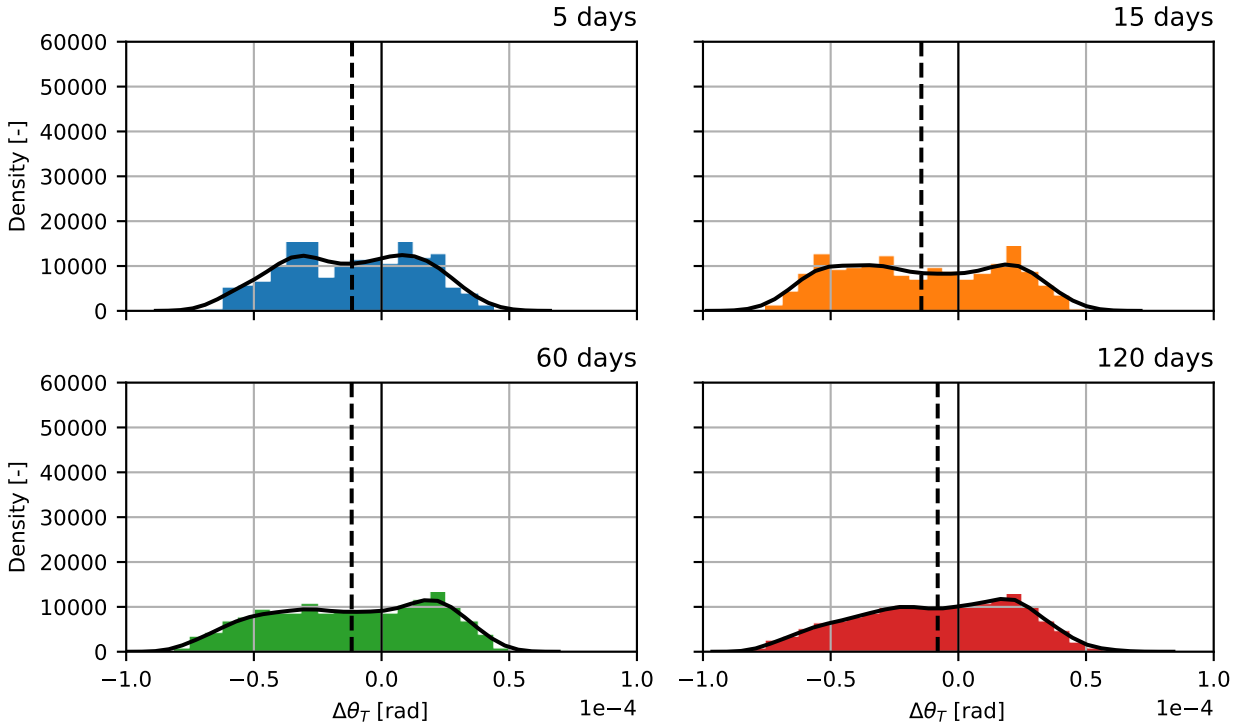


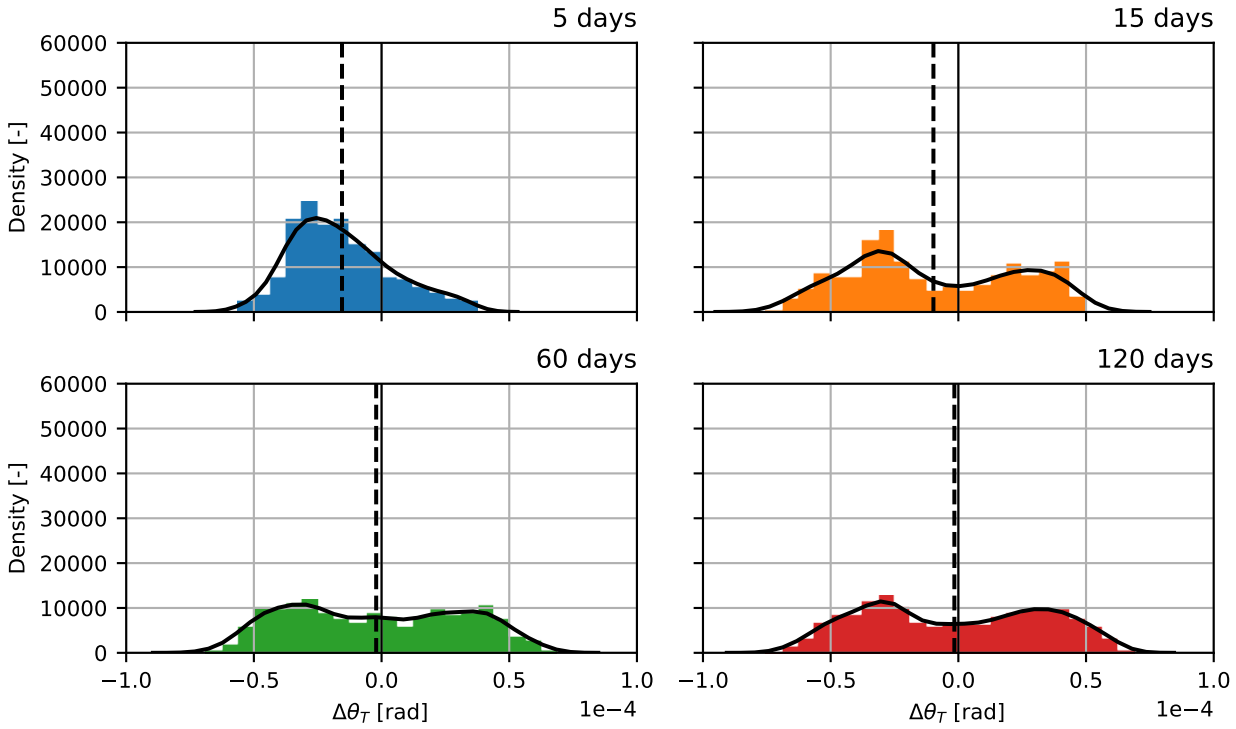
Figure 3.14: Numerically-calculated mean along-track position error for calibration satellite TLEs as a function of window midpoint and size.



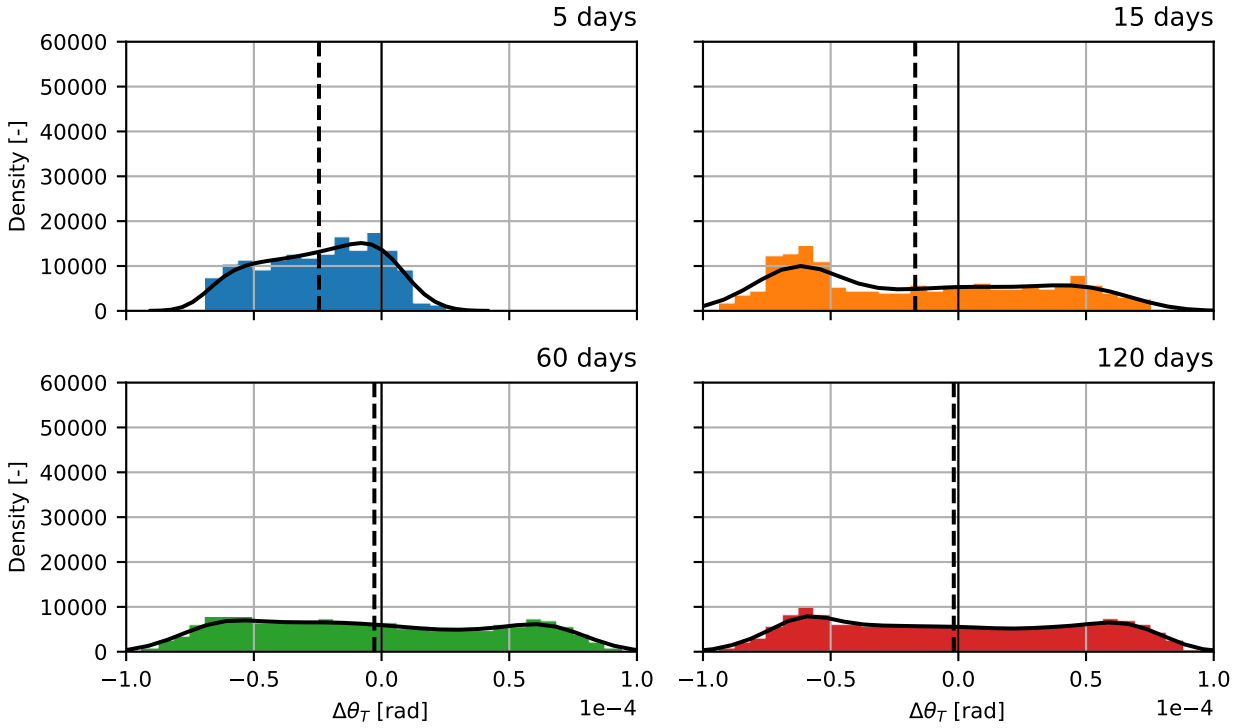
(a) LAGEOS-1.



(b) LAGEOS-2.



(c) Etalon 1.



(d) Etalon 2.

Figure 3.15: Example along-track position error distributions for windows centred on 1st July 2022. The dashed lines indicate the mean error for each window. Densities are presented due to the different number of samples in each window.

Bias models will not account for manoeuvres. However, in theory they should be immediately applicable for TLEs in the days following a manoeuvre, once USSF have updated the post-manoeuvre state of the satellite. Importantly, bias models should reduce the size of the fit window required for an accurate P-OD fit, allowing P-OD to be used more widely on active satellites as extended fit windows are more likely to include manoeuvres. Additionally, bias models may enable the use of sequential filters which typically struggle in biased conditions.

The P-OD process can compensate for biases by removing them from the pseudo-observations:

$$\mathbf{y}_{\text{debiased}} = \mathbf{y} - \mathbf{y}_{\text{bias}},$$

resulting in an updated version of Equation (2.2) which considers the effect of the bias:

$$\begin{aligned}\mathbf{b}_{\text{debiased}} &= \mathbf{Y}_{\text{debiased}} - \mathbf{Y}^*, \\ &= \mathbf{Y} - \mathbf{Y}_{\text{bias}} - \mathbf{Y}^*,\end{aligned}$$

where $\mathbf{b}_{\text{debiased}}$ is the debiased residual vector.

The bias vector can be calculated from angular models defined in the RTN frame:

$$\mathbf{y}_{\text{bias}} = \mathbf{R}_{\text{RTN}}\left(\mathbf{r}_{\text{TLE}}, \mathbf{v}_{\text{TLE}}\right)^T ||\mathbf{r}_{\text{TLE}}|| \begin{bmatrix} \Delta\theta_R \\ \Delta\theta_T \\ \Delta\theta_N \\ \Delta\omega_R \\ \Delta\omega_T \\ \Delta\omega_N \end{bmatrix}.$$

3.3.1 Batch Least Squares for Bias Model Fitting

A given bias model is not useful without the parameters required for it to effectively predict TLE errors. The parameters can be estimated through a variety of different methods. In this case, data-driven numerical methods can be used to fit bias models to the TLE errors seen in Section 3.2. This section outlines the procedure used to fit a given bias model with batch least squares methods, following a similar derivation to that of batch least squares P-OD in Section 2.3.

The overall TLE bias is modelled using a vector function:

$$\mathbf{y}^*_{\text{bias}}(\mathbf{u}) = \mathbf{f}_{\text{bias}}(\boldsymbol{\mu}, \mathbf{u}),$$

where $\boldsymbol{\mu}$ are the model parameters; and $\mathbf{u}$ are a set of inputs, such as time or parameters of a perturbing acceleration.

A single set of model parameters is mapped to multiple predicted biases in a concatenated vector:

$$\mathbf{Y}^*_{\text{bias}} = \mathbf{F}_{\text{bias}}(\boldsymbol{\mu}),$$

where:

$$\mathbf{Y}^*_{\text{bias}} = \begin{bmatrix} \left[\mathbf{y}^*_{\text{bias}}(\mathbf{u}_0)\right] \\ \left[\mathbf{y}^*_{\text{bias}}(\mathbf{u}_1)\right] \\ \left[\mathbf{y}^*_{\text{bias}}(\mathbf{u}_2)\right] \\ \vdots \\ \left[\mathbf{y}^*_{\text{bias}}(\mathbf{u}_{l-1})\right] \end{bmatrix},$$

$$\mathbf{F}_{\text{bias}}(\boldsymbol{\mu}) = \begin{bmatrix} \left[\mathbf{f}_{\text{bias}}(\boldsymbol{\mu}, \mathbf{u}_0)\right] \\ \left[\mathbf{f}_{\text{bias}}(\boldsymbol{\mu}, \mathbf{u}_1)\right] \\ \left[\mathbf{f}_{\text{bias}}(\boldsymbol{\mu}, \mathbf{u}_2)\right] \\ \vdots \\ \left[\mathbf{f}_{\text{bias}}(\boldsymbol{\mu}, \mathbf{u}_{l-1})\right] \end{bmatrix}.$$

The error between the TLE biases and the predicted biases is expressed as a set of residuals:

$$\mathbf{b}_{\text{bias}} = \mathbf{Y}_{\text{bias}} - \mathbf{Y}^*_{\text{bias}},$$

which is linearised using the same method as in Section 2.3:

$$\begin{aligned} \mathbf{b}_{\text{bias}}(\boldsymbol{\mu}) &= \mathbf{Y}_{\text{bias}} - \mathbf{F}_{\text{bias}}(\boldsymbol{\mu}), \\ &\approx \mathbf{Y}_{\text{bias}} - \mathbf{F}_{\text{bias}}(\bar{\boldsymbol{\mu}}) - \mathbf{A}_{\text{bias}}(\boldsymbol{\mu} - \bar{\boldsymbol{\mu}}), \end{aligned}$$

where the derivatives matrix, $\mathbf{A}_{\text{bias}}$, is estimated through finite differencing.

The parameter fitting process is expressed as a least-squares minimisation problem, in this case without any weighting (i.e. $\mathbf{W} = \mathbf{I}$):

$$\min_{\boldsymbol{\mu}} J(\boldsymbol{\mu}) = \frac{1}{2}\mathbf{b}_{\text{bias}}(\boldsymbol{\mu})^T\mathbf{b}_{\text{bias}}(\boldsymbol{\mu}),$$

resulting in the unweighted Levenberg-Marquardt solution:

$$\left[\mathbf{A}_{\text{bias},j}^T\mathbf{A}_{\text{bias},j} + \lambda\ \text{diag}\left(\mathbf{A}_{\text{bias},j}^T\mathbf{A}_{\text{bias},j}\right)\right]\left(\boldsymbol{\mu}_{j+1} - \boldsymbol{\mu}_j\right) = \mathbf{A}_{\text{bias},j}^T\left[\mathbf{Y}_{\text{bias}} - \mathbf{F}_{\text{bias}}(\boldsymbol{\mu}_j)\right],$$

where j is the iteration index. The solution is iterated until convergence, as in Section 2.3.

The GNSS satellites are active, meaning that their TLEs are affected by occasional station-keeping manoeuvres. This results in significant errors between the TLE and SP3 datasets which are not a direct result of TLE mismodelling but due to the elements not being updated to correspond to the new orbit. Outlier rejection was required, therefore, to not skew the model fitting process. Outliers were removed according to two criteria: position errors greater than 50 km, or position errors greater than the mean plus three standard deviations for the considered time period. States from two days either side of detected outliers were removed to ensure that TLEs which might have been affected by any manoeuvres would not skew the fit results.

This method was sufficient for this study; however, it should be emphasised that this is not a robust method for identifying manoeuvres as it required manual tuning and resulted in a small number of false positives and negatives. Future studies should consider more robust methods for identifying anomalous TLEs, ideally considering methods that do not require reference ephemerides to enable analysis for any RSO [130, 131, 132, 133].

3.3.2 Bias Model Evaluation

Bias models can be evaluated in the same manner as P-OD fits, using modified versions of Equations (2.6) to (2.9) which consider the impact of the debiasing process on the pseudo-observations. In this instance, the debiased pseudo-observations are compared against the reference ephemerides to evaluate whether the estimated position and velocity vectors have been improved:

$$\Delta r_{\text{RMSE}} = \sqrt{\frac{1}{l}\sum_{i=0}^{l-1}||\mathbf{r}_i^* - \mathbf{r}_{\text{bias},i} - \mathbf{r}_i||^2},$$

$$\overline{\Delta r} = \frac{1}{l}\sum_{i=0}^{l-1} ||\mathbf{r}_i^* - \mathbf{r}_{\text{bias},i} - \mathbf{r}_i||,$$

$$\Delta v_{\text{RMSE}} = \sqrt{\frac{1}{l}\sum_{i=0}^{l-1} ||\mathbf{v}_i^* - \mathbf{v}_{\text{bias},i} - \mathbf{v}_i||^2},$$

$$\overline{\Delta v} = \frac{1}{l}\sum_{i=0}^{l-1} ||\mathbf{v}_i^* - \mathbf{v}_{\text{bias},i} - \mathbf{v}_i||,$$

where $\mathbf{r}_i^*$ and $\mathbf{v}_i^*$ are the pseudo-observed positions and velocities, $\mathbf{r}_{\text{bias},i}$ and $\mathbf{v}_{\text{bias},i}$ are the estimated position and velocity biases, and $\mathbf{r}_i$ and $\mathbf{v}_i$ are the reference positions and velocities, respectively.

3.3.3 Time-Based Bias Model

A simple model for estimating the along-track biases considers a single component of Equation (3.1):

$$\Delta\theta_T(t) \approx a_t \cos\left[\frac{2\pi}{b_t}\left(t + c_t\right)\right] + d_t, \tag{3.4}$$

where t is time, expressed in days since the J2000 epoch[1]; and a_t, b_t, c_t, and d_t are model parameters, corresponding to the amplitude, period, phase, and offset of the periodic component, respectively.

Each model was fitted using the batch least squares procedure outlined in Section 3.3.1 with an initial guess of an amplitude of 10^{-4} rad, a period of 27.5 days, a phase of 0 days, and a mean offset of 0 rad. It was found, particularly in the case of LAGEOS-2, that the solver could be very sensitive to the initial guess of the model's period as the solver was easily trapped in local minima.

The fitted time-based models for the calibration satellites are presented in Table 3.2 and Figure 3.16. The model showed good agreement with the along-track errors of Etalon 1 and 2, and limited agreement for LAGEOS-1, where the additional longer-term variation was present. LAGEOS-2's model had a complete lack of agreement due to the significantly different along-track error behaviour resulting from the additional longer-period components.

The fitted amplitudes of LAGEOS-1, and Etalon 1 and 2 remained very close to the corresponding peaks in the FFTs presented in Figure 3.11: the amplitudes were within 5.77 %, 5.72 %, and 6.72 %, respectively, and the periods were within 0.20 %, 0.20 %, and 0.22 %, respectively. All four models

[1] 1st January 2000 at 12:00 Terrestrial Time (TT)

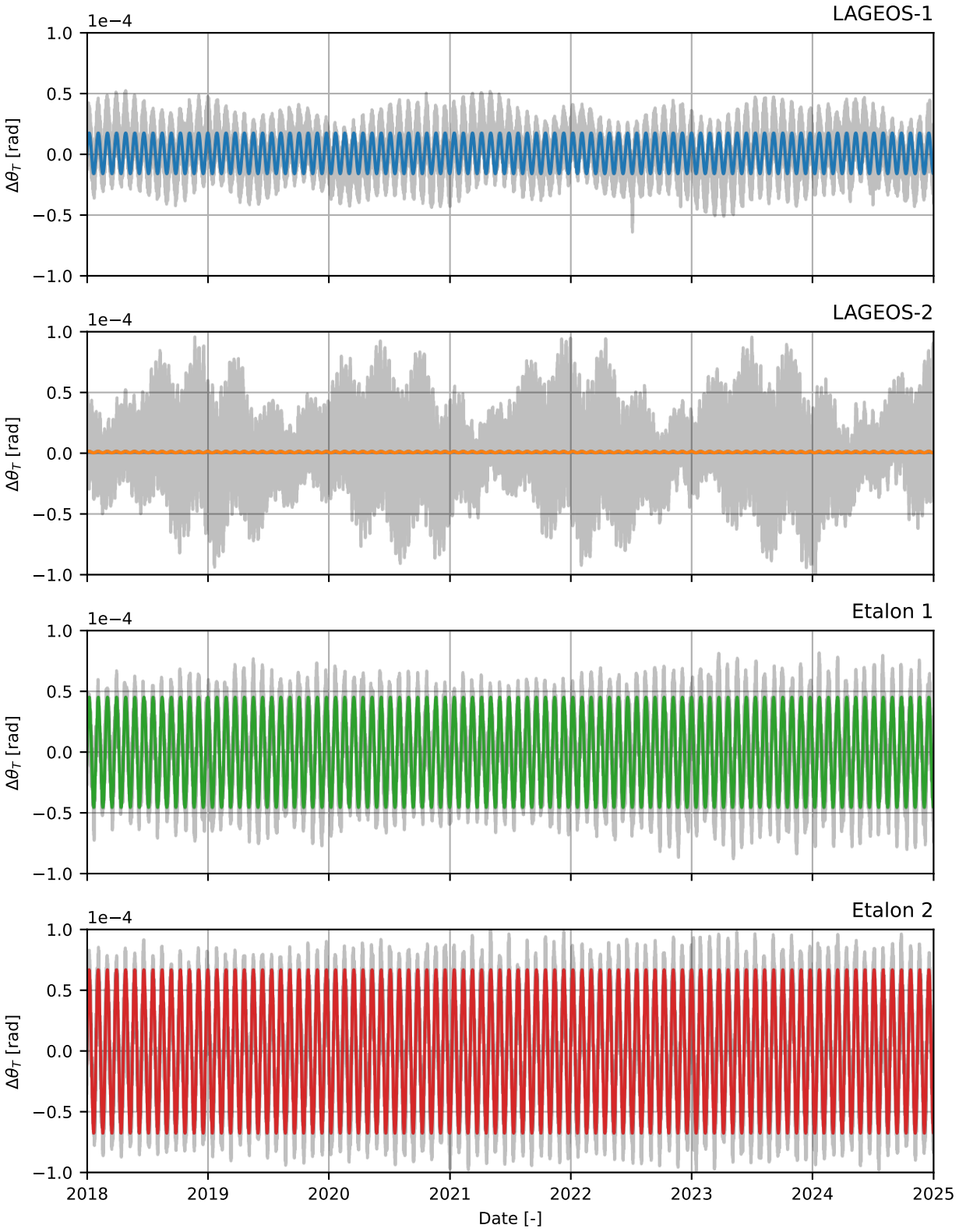


Figure 3.16: Time-based along-track position error models for the calibration satellites for the years 2018 to 2025. The along-track position error of the TLEs and the models are presented in grey and colour, respectively.

Table 3.2: Individual calibration satellite time-based models for the years 2018 to 2025.

Satellite	a_t [rad]	b_t [days]	c_t [days]	d_t [rad]
LAGEOS-1	1.665×10^{-5}	27.55	2.057	6.969×10^{-7}
LAEGOS-2	6.781×10^{-7}	27.55	3.519	8.481×10^{-7}
Etalon 1	4.514×10^{-5}	27.55	1.891	-3.541×10^{-7}
Etalon 2	6.703×10^{-5}	27.55	3.376	-1.587×10^{-7}

converged to a period of 27.55 days which corresponds to the anomalistic month or, in other words, the period between each perigee crossing for the Moon, highlighting the link between the Moon and TLE bias. The model phases for LAGEOS-1, and Etalon 1 and 2 matched each other very closely: the maximum difference in phase of 1.49 days, between Etalon 1 and 2, represented a band of only 5.42 % of the model period. The phases of the satellites placed the initial zero-crossing points of the models within a date range from the 4$^{\text{th}}$ to 6$^{\text{th}}$ January 2000. Notably, this lined up with the Moon being at apogee on the 4$^{\text{th}}$ January 2000. It will be shown in Section 3.3.4 that the TLE bias is near-zero when the Moon is at perigee or apogee.

The results of fitting the single-component time-based models highlighted that, although effective in the cases of Etalon 1 and 2, improvements would be needed for the other calibration satellites, particularly LAGEOS-2. The introduction of additional harmonics, guided by the results from the frequency analysis in Section 3.2.1, would create more representative models. These higher-order time-based models will be discussed in Section 3.7.

3.3.4 Moon-Based Bias Model

The results from the FFT analysis in Section 3.2.1 and the time-based models in Section 3.3.3 support the idea that the dominant component of the TLE bias variation is a product of mismodelling of the lunar third-body perturbation. One of the fast variables of the orbit of the Moon can be used to parametrise the periodic position of the Moon, resulting in an alternative formulation which more directly considers the position-based nature of the perturbation mismodelling:

$$\Delta\theta_T(M) \approx a_m \sin\left(M + c_m\right) + d_m, \tag{3.5}$$

where M is the mean anomaly of the Moon; and a_m, c_m, and d_m are model parameters, corresponding to the amplitude, phase, and offset of the periodic component, respectively.

The fitted Moon-based models for the calibration satellites are presented in Table 3.3 and Figures 3.17 and 3.18. The model showed good agreement with the along-track errors for LAGEOS-1, and Etalon 1 and 2. LAGEOS-2, on the other hand, showed poor agreement with limited relationship apparent between the Moon's mean anomaly and the amount of along-track bias present in the TLEs.

Table 3.3: Individual calibration satellite Moon-based models for the years 2018 to 2025.

Satellite	a_m [rad]	c_m [rad]	d_m [rad]
LAGEOS-1	1.612×10^{-5}	2.735×10^{-2}	7.634×10^{-7}
LAGEOS-2	7.406×10^{-7}	2.153×10^{-2}	8.508×10^{-7}
Etalon 1	4.368×10^{-5}	4.862×10^{-3}	-2.103×10^{-7}
Etalon 2	6.562×10^{-5}	7.724×10^{-3}	7.032×10^{-8}

The Moon-based model effectively acted as a time-based model with the anomalistic month as the period, as highlighted by Figure 3.18. This was relatively effective for LAGEOS-1, and Etalon 1 and 2 where their largest time-based periodic components match the anomalistic month. This was apparent in the amplitudes of the Moon-based models which were only 3.13 %, 3.23 %, and 2.10 % smaller, respectively, than in the time-based models. The additional longer-term variations for the satellites, which are especially important for the along-track position error of LAGEOS-1 and -2, were not visible when plotting the error as a function of the Moon's mean anomaly. These longer-term variations most likely manifested as a larger scatter about the Moon-based model, as slight differences in period and phase accumulated with time.

Figure 3.17 highlights some anomalous along-track position errors near $M = 180°$ for Etalon 2. These were not readily visible in the time series due to the level of zoom. These were the result of poor quality TLEs, resulting in incorrect pseudo-observed states which departed significantly from the generally observed bias variation. These erroneous states highlight two important points: firstly, how the use of an alternative state space can aid in the identification of anomalous TLE behaviour; and, secondly, how a bias model will not capture unexpected behaviour, such as that resulting from anomalies in the TLE generation pipeline. The latter will be highlighted using Etalon 2 in Figures 3.19 and 3.20. Methods which can identify anomalous TLEs, for further analysis or removal, will remain applicable as part of the suite of tools for improving both P-OD and bias model generation.

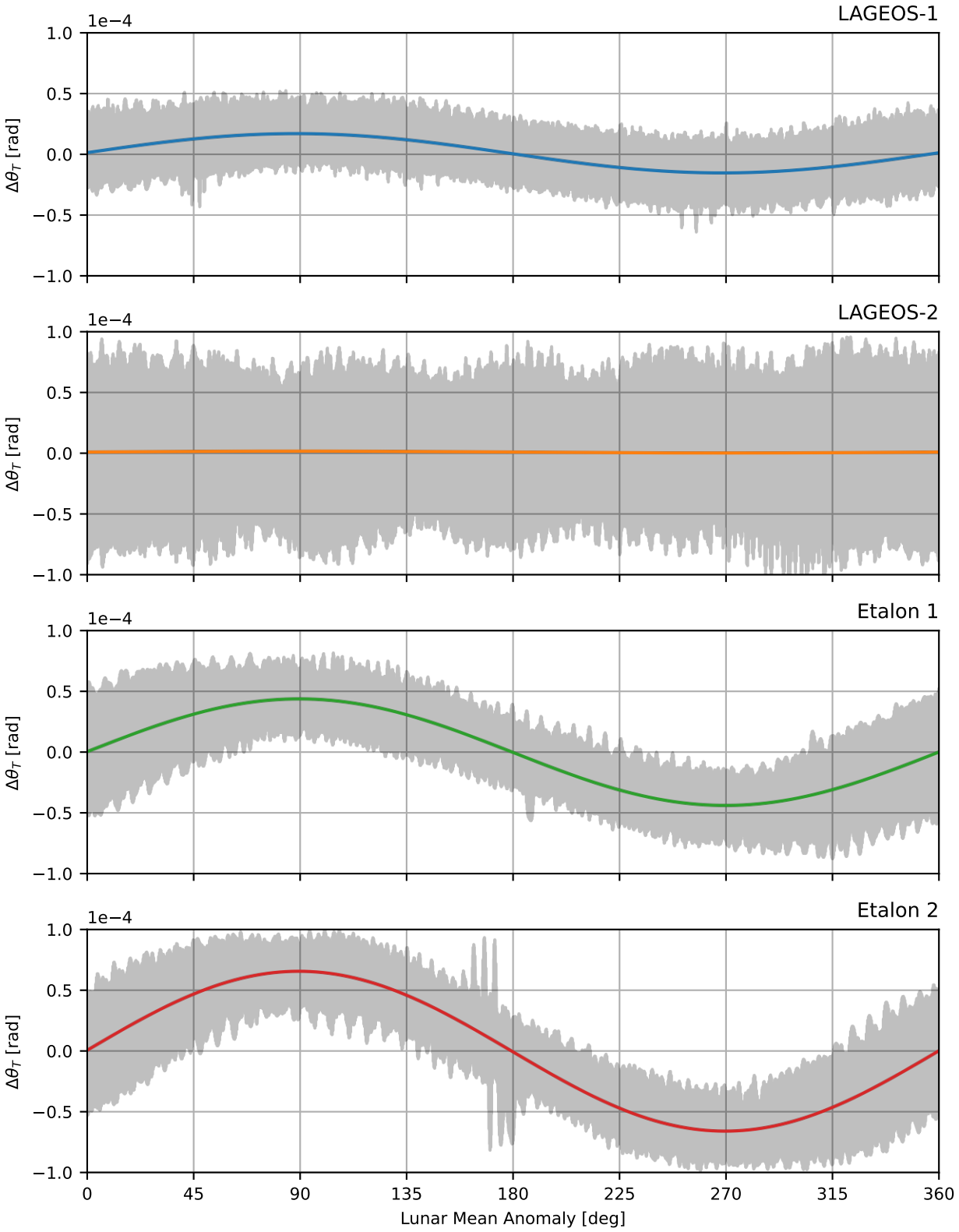


Figure 3.17: Moon-based along-track position error models for the calibration satellites for the years 2018 to 2025. The along-track position error of the TLEs and the models are presented in grey and colour, respectively.

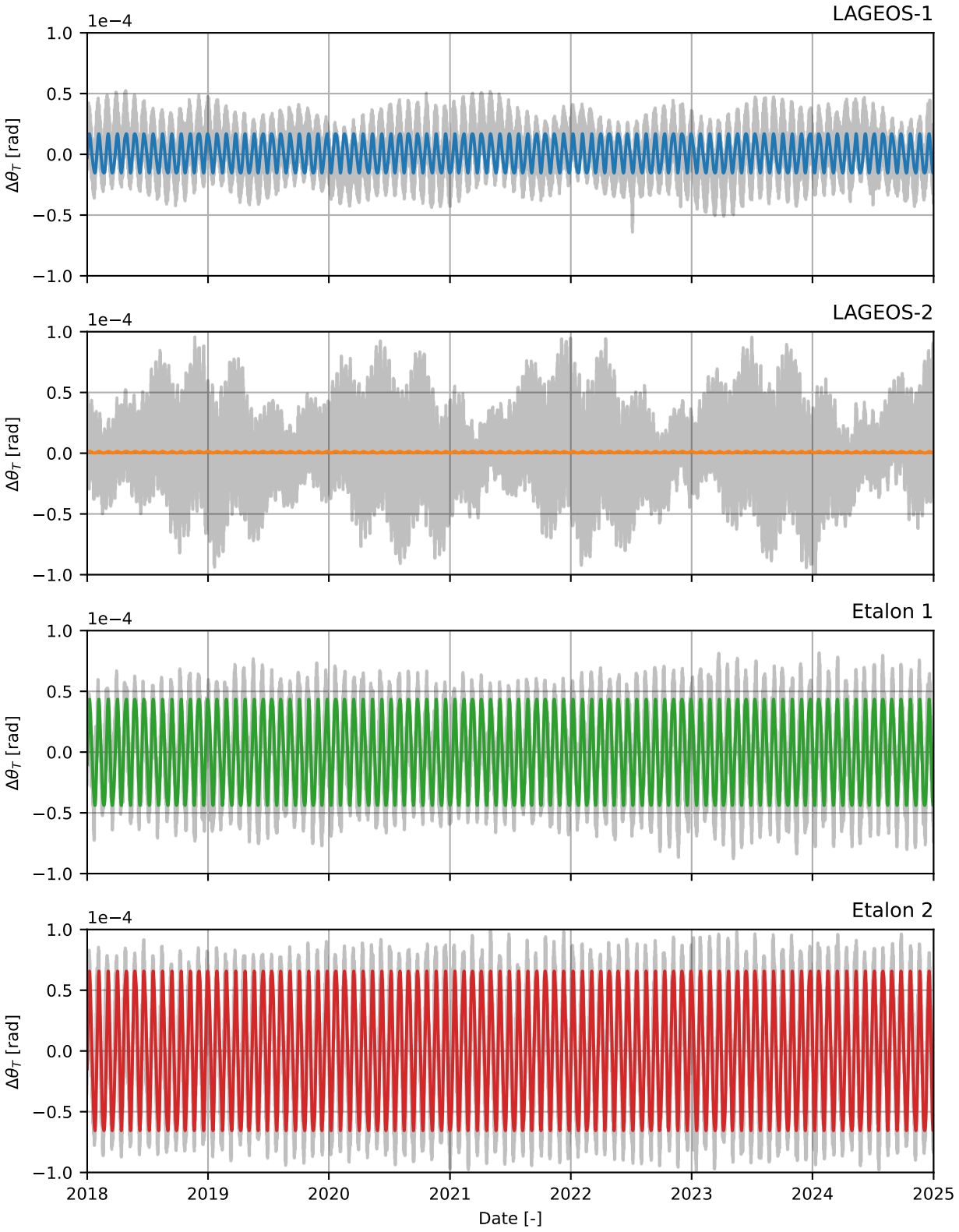


Figure 3.18: Moon-based along-track position error models, as a function of time, for the calibration satellites for the years 2018 to 2025. The along-track position error of the TLEs and the models are presented in grey and colour, respectively.

3.4 Impacts of Debiasing on Residual Bias Characteristics

The residual along-track position errors following debiasing with the individual time- and Moon-based models are presented in Figures 3.19 and 3.20. The effectiveness of the bias models can be examined by comparing these residuals to the original along-track position errors presented in Figure 3.9. The most extreme values of along-track position error for LAGEOS-1 were slightly reduced by both models with the errors no longer reaching $\pm 0.5 \times 10^{-4}$ rad. Nevertheless, the longer-period oscillation remained highly visible throughout the seven years. LAGEOS-2's residuals were unaffected by either model, as expected due to the poor fit of both models. The residuals for Etalon 1 and 2 had the most improvement with the monthly variation being suppressed effectively and residuals remaining within a $\pm 0.5 \times 10^{-4}$ rad band. The effect of debiasing was particularly pronounced for Etalon 2 which, prior to debiasing, had errors approaching $\pm 10^{-4}$ rad. The time-based models were slightly more effective at debiasing, visible as slightly smaller residual peak amplitudes.

The effectiveness of the individual models at suppressing the bias can be evaluated by considering the RMSE and dispersion of the along-track position residuals. When using the time-based models, the along-track position RMSEs were reduced by 27.3 %, 0.049 %, 62.1 %, and 74.5 %, respectively; and the along-track position error standard deviations by 27.3 %, 0.012 % 62.1 %, and 74.5 %, respectively. When using the Moon-based models, the along-track position RMSEs were reduced by 25.4 %, 0.051 %, 55.5 %, and 67.8 %, respectively; and the along-track position error standard deviations by 25.3 %, 0.014 %, 55.5 %, and 67.8 %, respectively. These results confirmed that the time-based models were slightly more effective at reducing the amount of variation in along-track position error. The residual along-track position errors for LAGEOS-2 models were largely unaffected by debiasing with either individual model, as anticipated due to the very small amplitudes of the models.

Examples of along-track position error distributions, following debiasing with the individual time-based models, are presented in Figure 3.21. The mean offset in along-track position error was almost eliminated for even the shortest of the presented Etalon 1 and 2 windows, demonstrating the ability of a well-fitted bias model to eliminate the short-term impact of bias. Furthermore, the long-term behaviour was improved too which was highly visible as a reduction in variance. The bimodal distributions seen in Figure 3.15 were replaced with unimodal distributions. Importantly, these distributions better match the statistical assumptions made for the batch least squares state estimator.

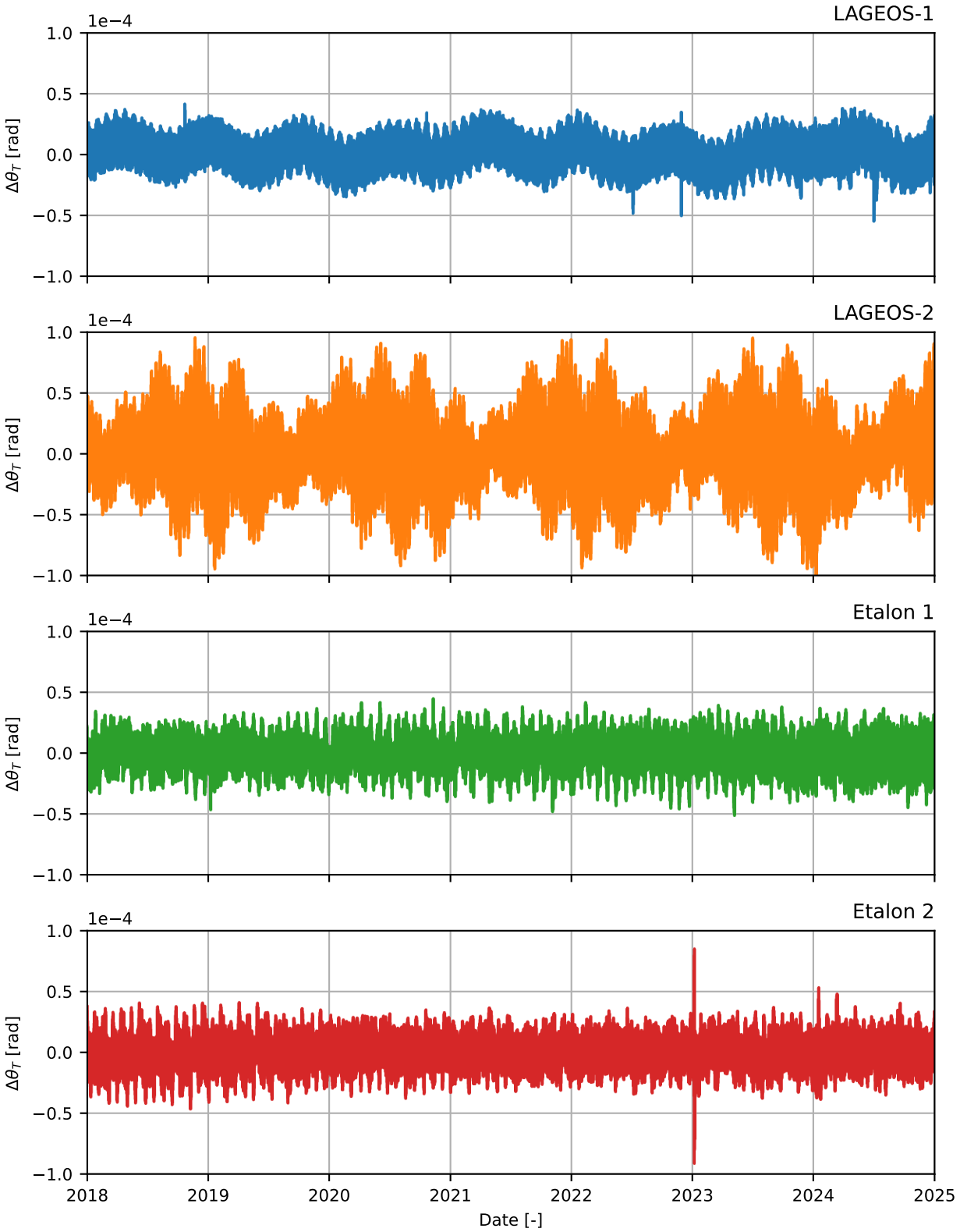


Figure 3.19: Residual along-track position error for the calibration satellites following debiasing with the individual time-based models for the years 2018 to 2025.

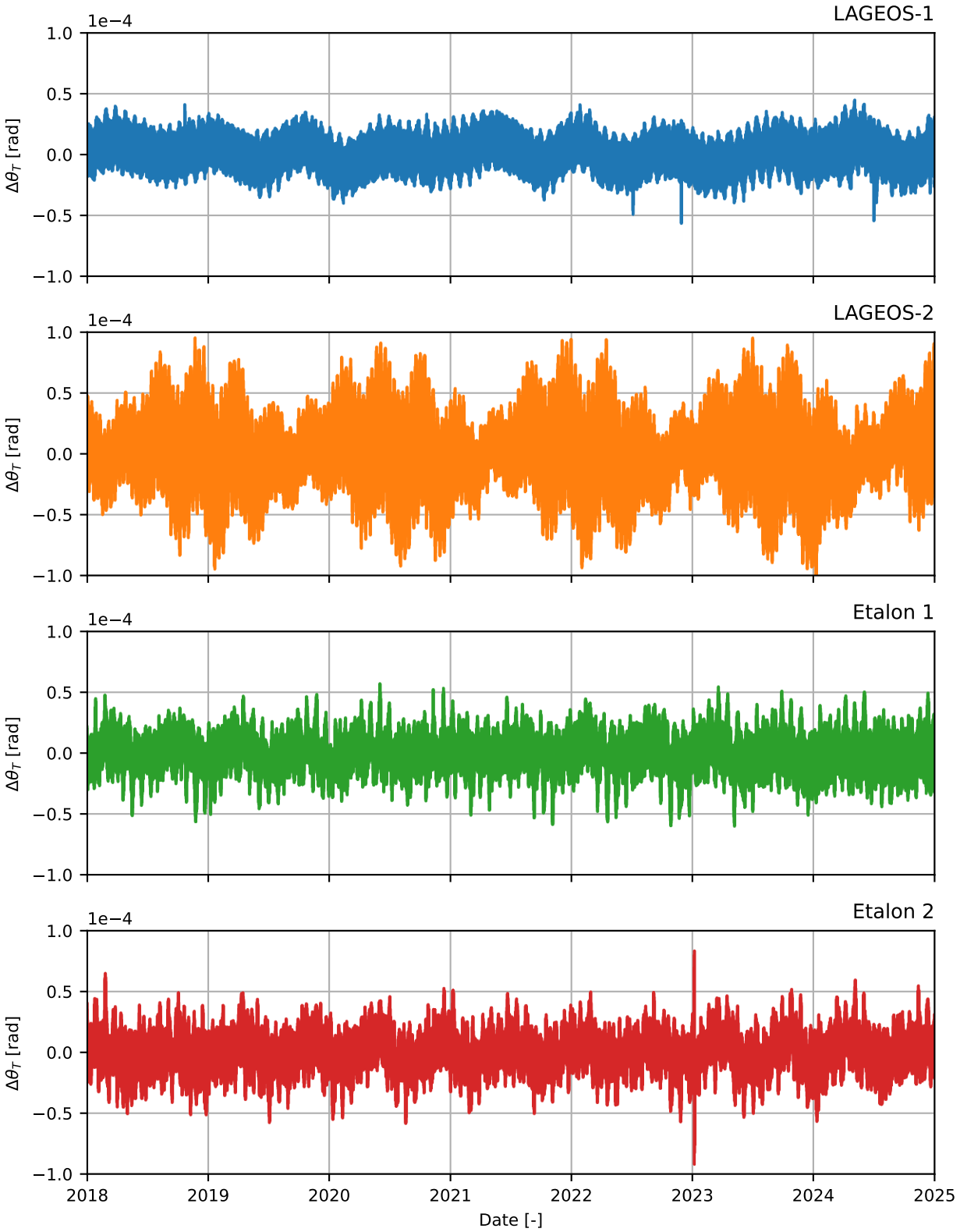
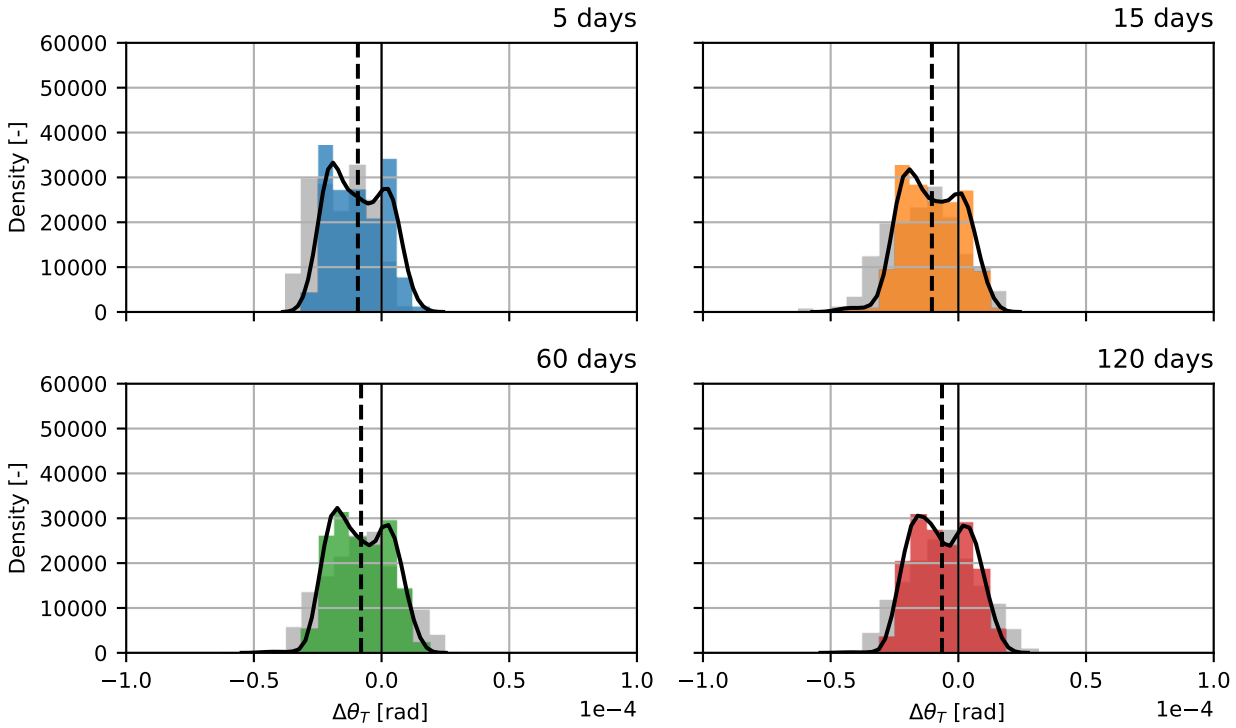
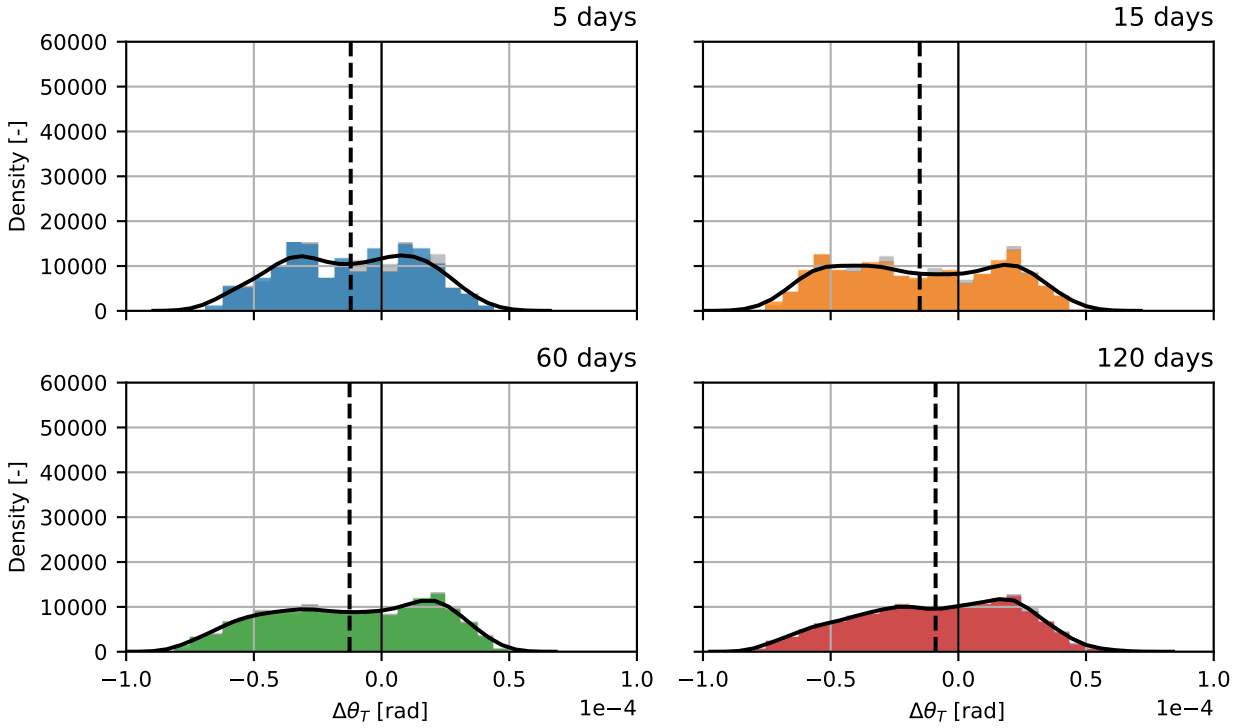


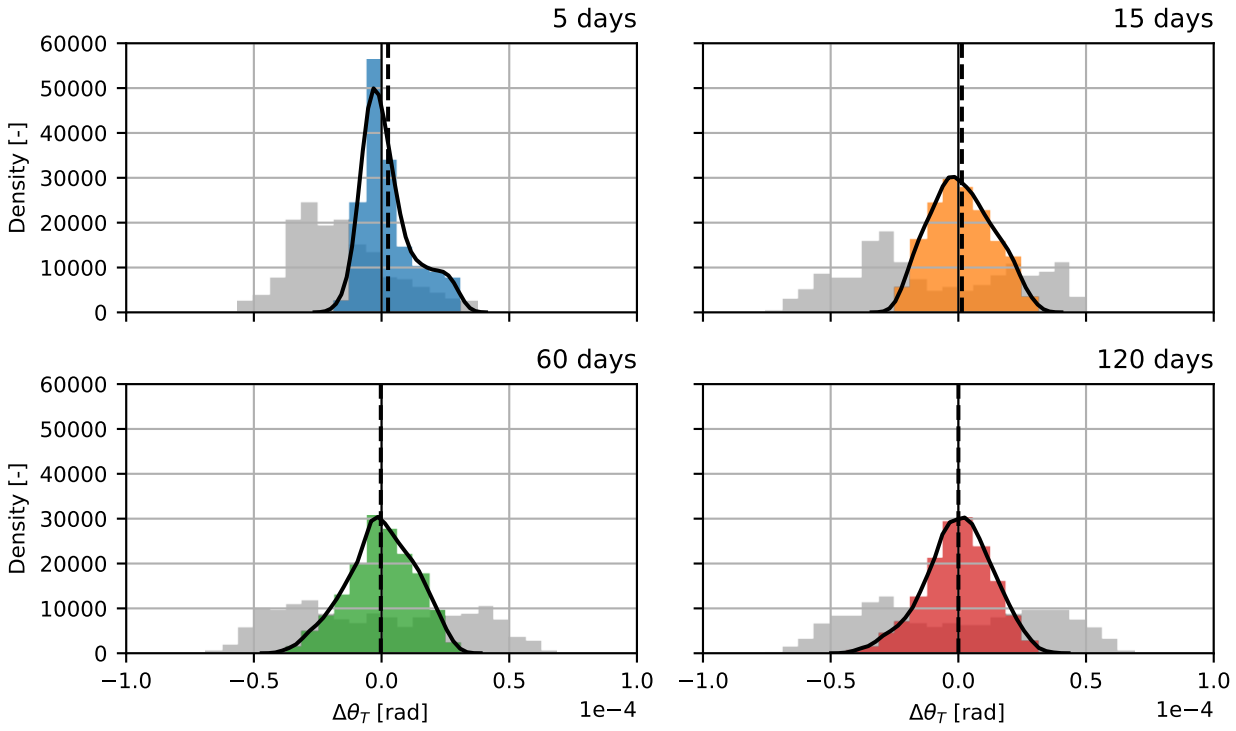
Figure 3.20: Residual along-track position error for the calibration satellites following debiasing with the individual Moon-based models for the years 2018 to 2025.



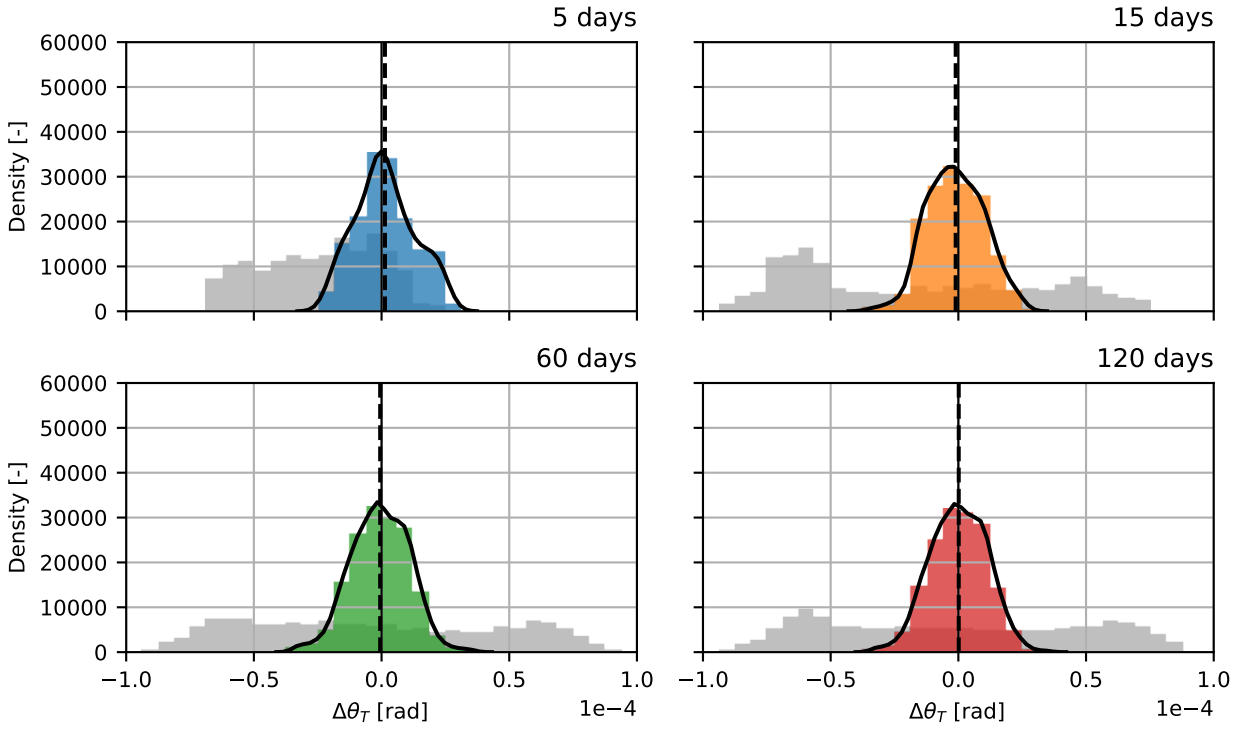
(a) LAGEOS-1.



(b) LAGEOS-2.



(c) Etalon 1.



(d) Etalon 2.

Figure 3.21: Example along-track position error distributions for windows centred on 1st July 2022, following debiasing with individual time-based bias models. The dashed lines indicate the mean error for each window. The original biased distributions from Figure 3.15 are included in grey. Densities are presented due to the different number of samples in each window.

3.5 Impacts of Debiasing on Pseudo-Orbit Determination

The results of fits on the calibration satellites, following debiasing with the individual time-based model using the procedure detailed in Section 3.3, are presented in Figures 3.22 and 3.23. The fits on LAGEOS-1 saw minor reductions in error with respect to the biased fits presented in Figures 3.2 and 3.3, with some suppression of the periodic behaviour for short fit windows. The results for LAGEOS-2 remained mainly unaffected, demonstrating the same error periodic behaviour which decayed to smaller post-fit errors towards the end of the year. This was expected due to the corresponding debiasing model having very little impact on the along-track position. The fits on Etalon 1 and 2 saw the most significant changes in error due to the debiasing process: although the periodic variations were still visible, the peak errors were reduced from approximately 10 to 2 km.

The suppression of oscillations in post-fit position error by using debiased pseudo-observations was seen in the reduction of the mean position RMSE in Figure 3.24. For short-term fits of Etalon 1, the mean position error changed from an approximately constant 3.5 km to a decreasing trend from approximately 2.5 to 0.5 km, representing an approximate reduction in error of 30 % for two-day fits to 85 % for ten-day fits. For Etalon 2, the mean error was reduced from approximately 5 to 1 km, an 80 % reduction. For the long-term fits, in addition to the mean position errors converging sooner for a small fit window size, the peaks at 50 and 80 days were removed with mean errors remaining below 1 km after fit windows larger than 20 days. Although increasing the size of the fit window decreased post-fit position RMSE, this trend started to reverse as the fit window size approached 90 days. This was most pronounced for LAGEOS-1 and -2, however Etalon 1 and 2 were affected too. One potential explanation for this was that the extended timespan of propagation (120 days total, comprised of a fit of 90 days followed by 30 days of evaluation) started to test the fidelity of the physical model.

The distributions of post-fit position RMSE for both biased and debiased fits of the calibration satellites are presented in Figure 3.25. The general trend of position RMSEs dropping as fit window size increases can be seen with the reduction both in median position RMSE and by the variance reducing as well. The debiasing had limited effect on the LAGEOS-1 and -2 fits, as expected due to the limited impact of the presented time-based models. The significant reduction in position RMSE for debiased short-term fits was highly apparent for Etalon 1 and 2, as well as the significant reduction in variation in RMSE about the mean: from approximately ±5 to ±1 km. Critically, the use of debias-

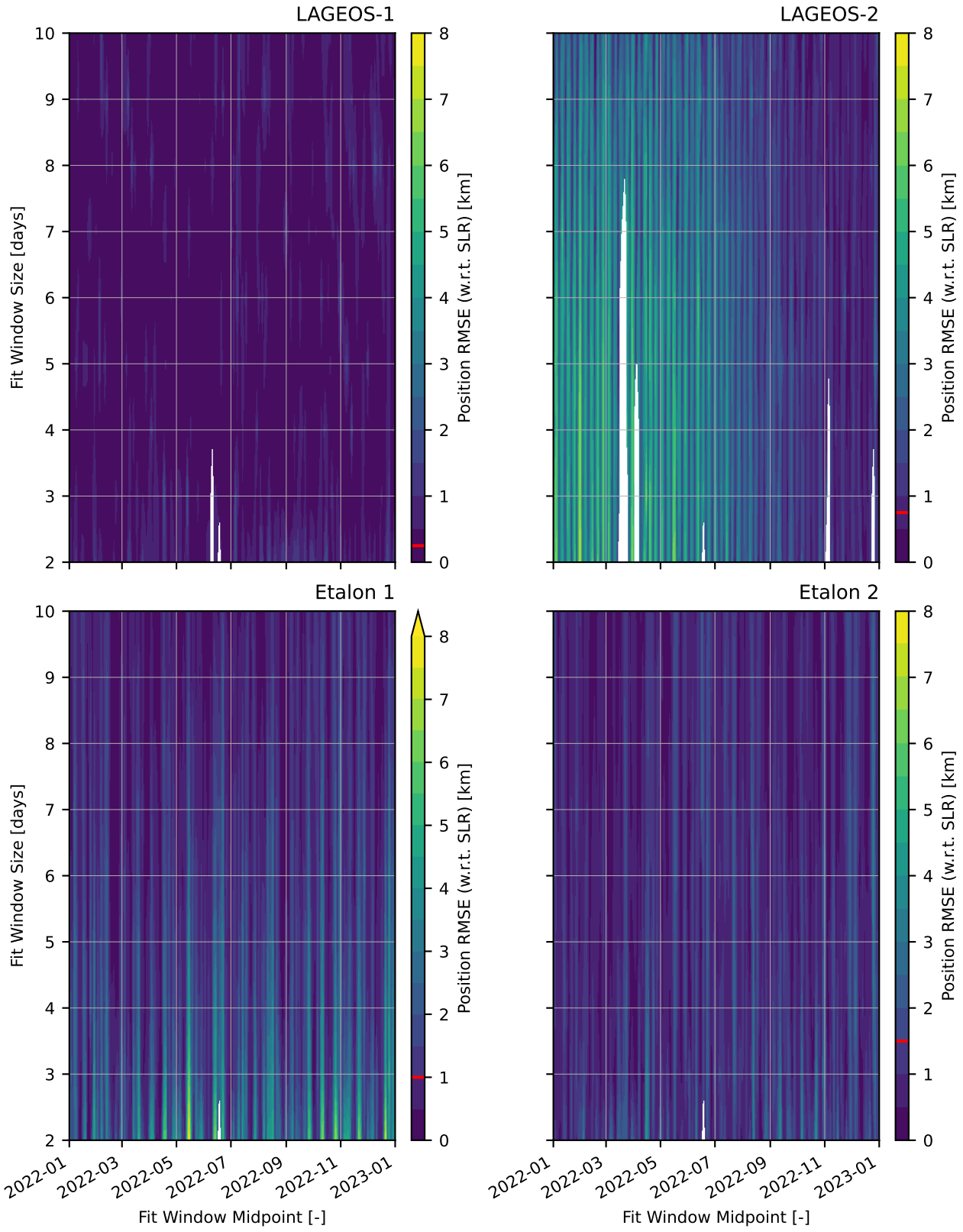


Figure 3.22: Position RMSE during the 30 days post-fit for short-term debiased fits of the calibration satellites. The red marker in the colour bar indicates the RMSE baseline derived from TLEs. Note that the white regions indicate failed cases due to a lack of TLEs within the window.

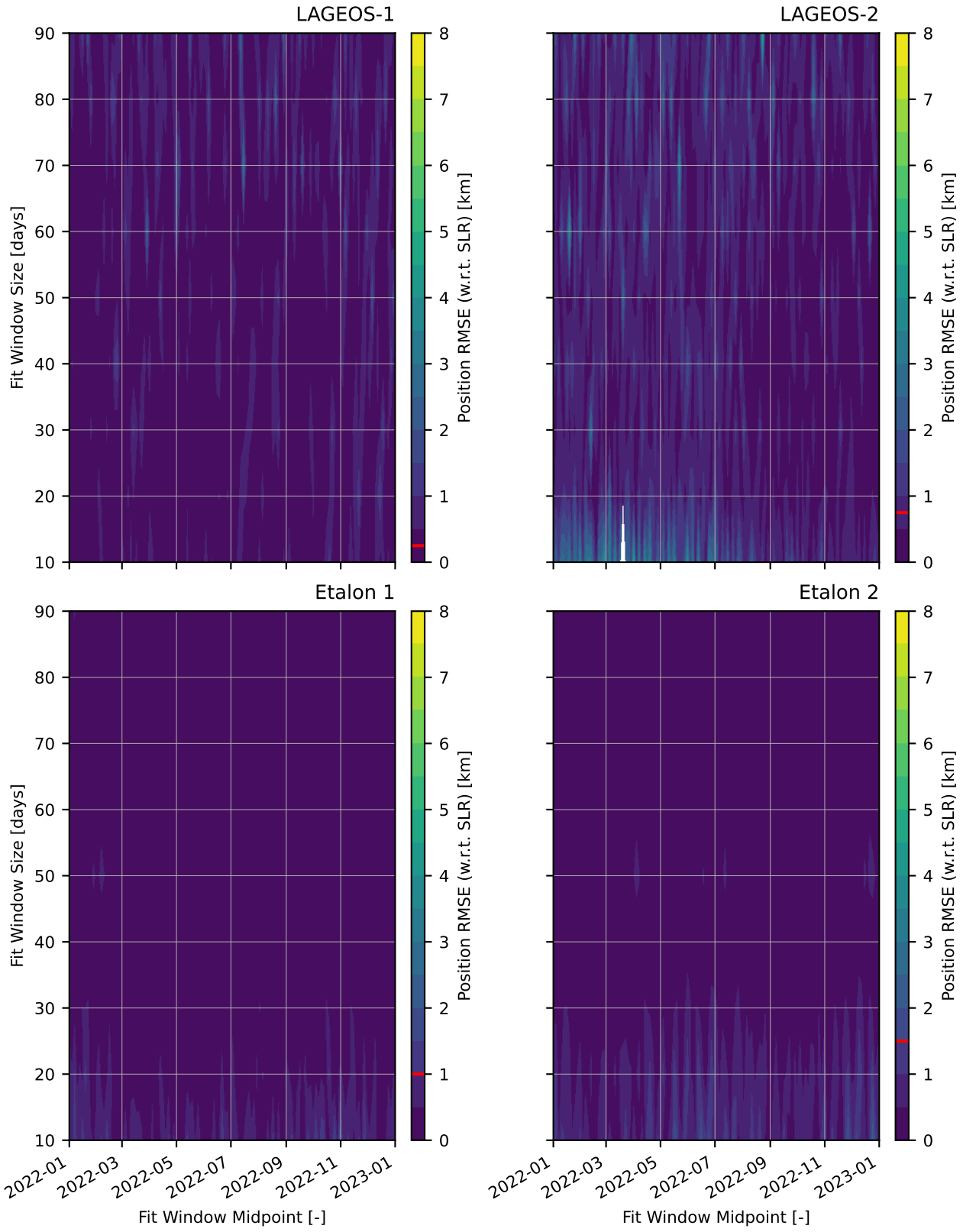


Figure 3.23: Position RMSE during the 30 days post-fit for long-term debiased fits of the calibration satellites. The red marker in the colour bar indicates the RMSE baseline derived from TLEs. Note that the white regions indicate failed cases due to a lack of TLEs within the window.

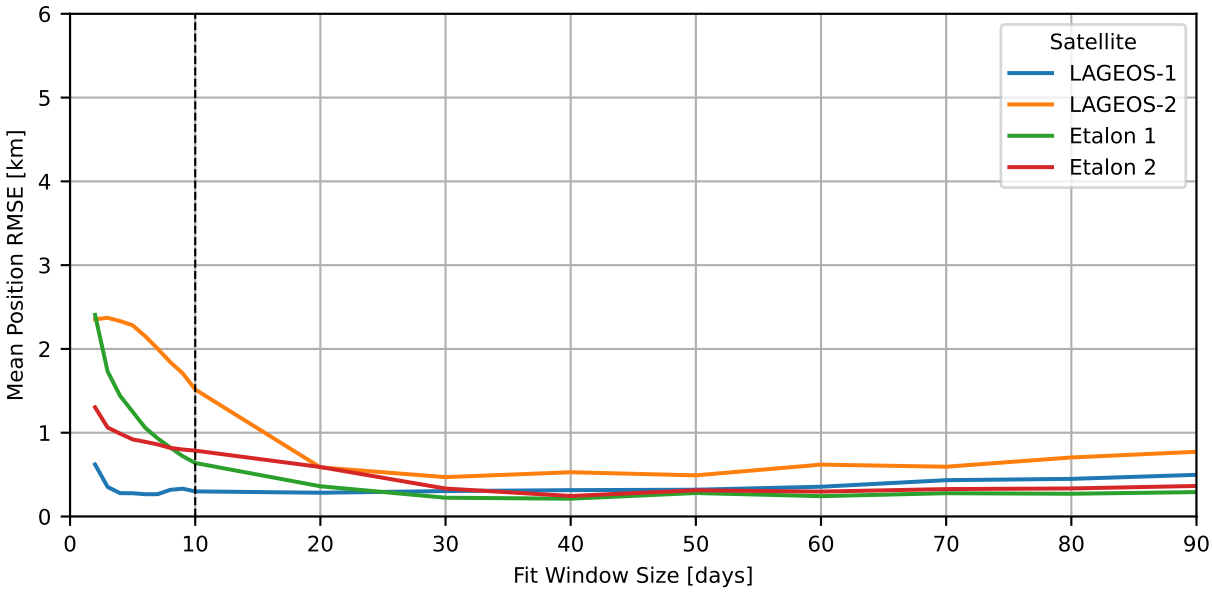


Figure 3.24: Mean position RMSE during the 30 days post-fit for short-term and long-term debiased fits of the calibration satellites.

ing significantly reduced the required fit window size to meet a desired post-fit position RMSE as fit windows of 30 days produced equivalent solutions to fit windows of 90 days.

The distributions of equivalent radius for both biased and debiased fits of the calibration satellites are presented in Figure 3.26. The equivalent radii were calculated for each fit window separately with the fit residuals and Equation (2.10). Generally, equivalent radius increased as the size of the fit window was increased. This follows when considering that the along-track position variance is the primary driver of the equivalent radius and that, as the size of the window increases, the spread in along-track position error increases, as illustrated in Figure 3.15. Interestingly, the growth in equivalent radius was opposite to the decrease in post-fit position RMSE. Notably, for the Etalon 1 and 2 fits, both the biased and debiased equivalent radii appeared to be converge on an upper bound, in a behaviour not seen with LAGEOS-1 and -2. This matched the expected behaviour as, once the window was sufficiently large, it captured the maximum and minimum along-track position errors due to the systematic TLE bias.

For LAGEOS-1 and -2, the biased and debiased equivalent radius distributions remained very similar for each fit window size, showing the limited influence of their respective bias models. For Etalon 1 and 2, there was a significant difference in the equivalent radii for biased and debiased fits

for extended fit windows, in this case greater than 10 days. Above this threshold, the equivalent radii were reduced on average by approximately 30 %. The spread of equivalent radii increased for LAGEOS-1 and -2 as fit window size was increased; however, for Etalon 1 and 2, the spread remained relatively constant and independent of fit window size.

Examples of fit residual scatters are presented in Figure 3.27, for both short- and long-term, and biased and debiased Etalon 1 fits. The scatters are presented both relative to the TLEs, or in other words the residuals of the converged fit as 'seen' by the state estimator, and relative to the true SLR-derived states. This highlights the potential differences in the distributions of the pseudo-observed states and the true states for a P-OD fit.

For the short-term fit, it can be seen that the covariance ellipses with respect to the TLEs were very similar, both in dimensions and orientation. However, when considering the residual scatter with respect to SLR, the biased fit has a significantly larger scatter in along-track position and a mean position which trails the true position by approximately 500 m. The issue with short-term fit windows is that the set of pseudo-observations will be skewed, either leading or lagging the true states, unless the window is centred about a zero-crossing point in along-track position bias. This effect is particularly pronounced for windows shorter than half of a bias cycle which can result in sets of pseudo-observations which are offset in only one along-track direction. This highlights how the residual scatter cannot be used to determine fit accuracy under biased conditions for short-term fits.

The behaviour was reversed for the long-term fit. For the residuals with respect to the TLEs, the biased fit had a significantly larger scatter in the along-track axis when compared to the debiased fit. On the other hand, the biased and debiased scatters with respect to SLR were very similar, both in radial and along-track variance. The longer fit window meant that several cycles of the bias variation were present in the set of pseudo-observations. The variance in along-track error, therefore, was artificially inflated by the TLE bias variation but not offset on average. At the same time, the state estimators, both biased and debiased, produced accurate and similar fits, hence the very similar scatters with respect to SLR. This demonstrated the longer-term windows converting what would be short-term bias into long-term noise.

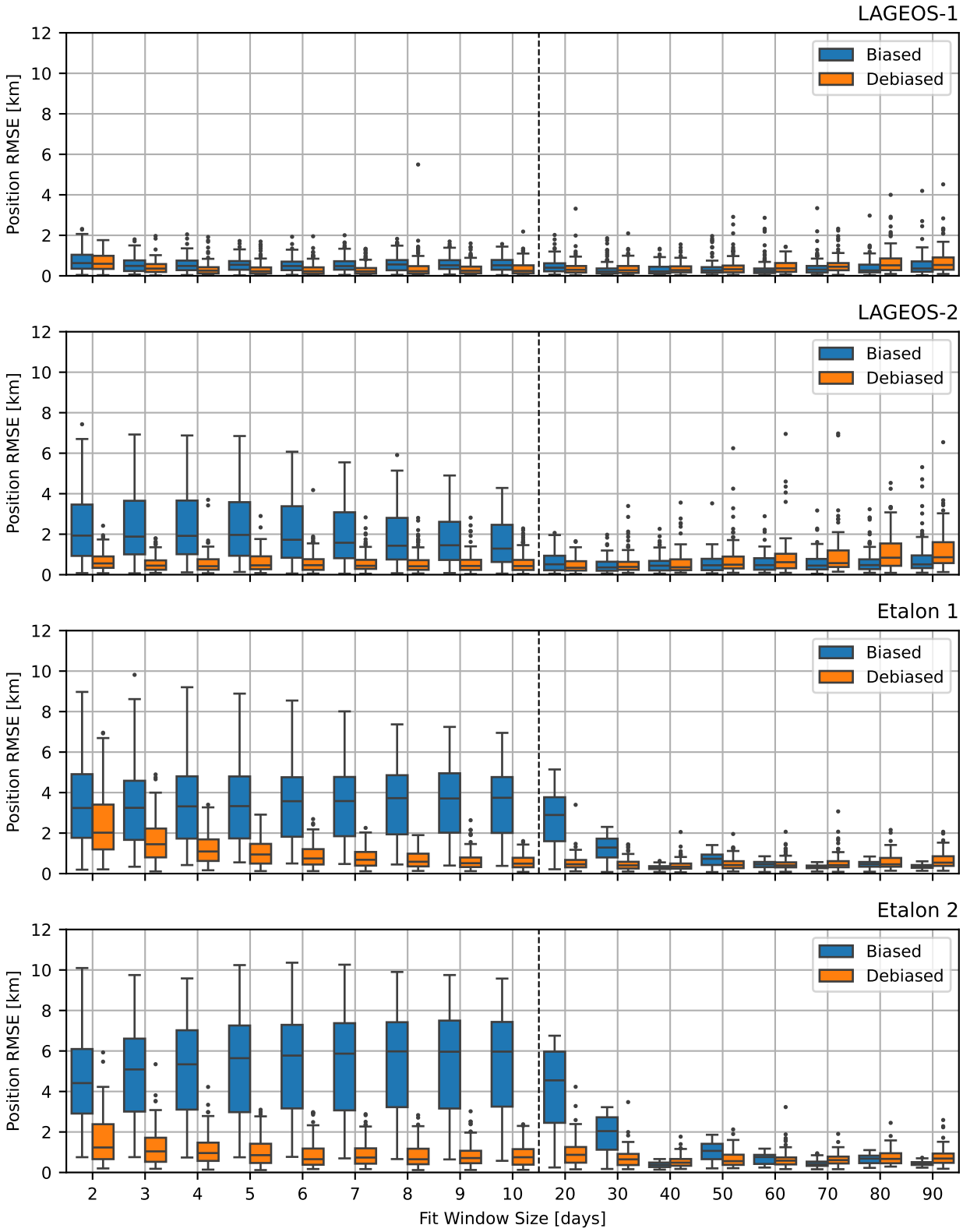


Figure 3.25: Position RMSE distributions during the 30 days post-fit for calibration satellite fits during the year 2022 as a function of fit window size (with and without time-based model debiasing). Note the change in fit window size interval between the short- and long-term fits.

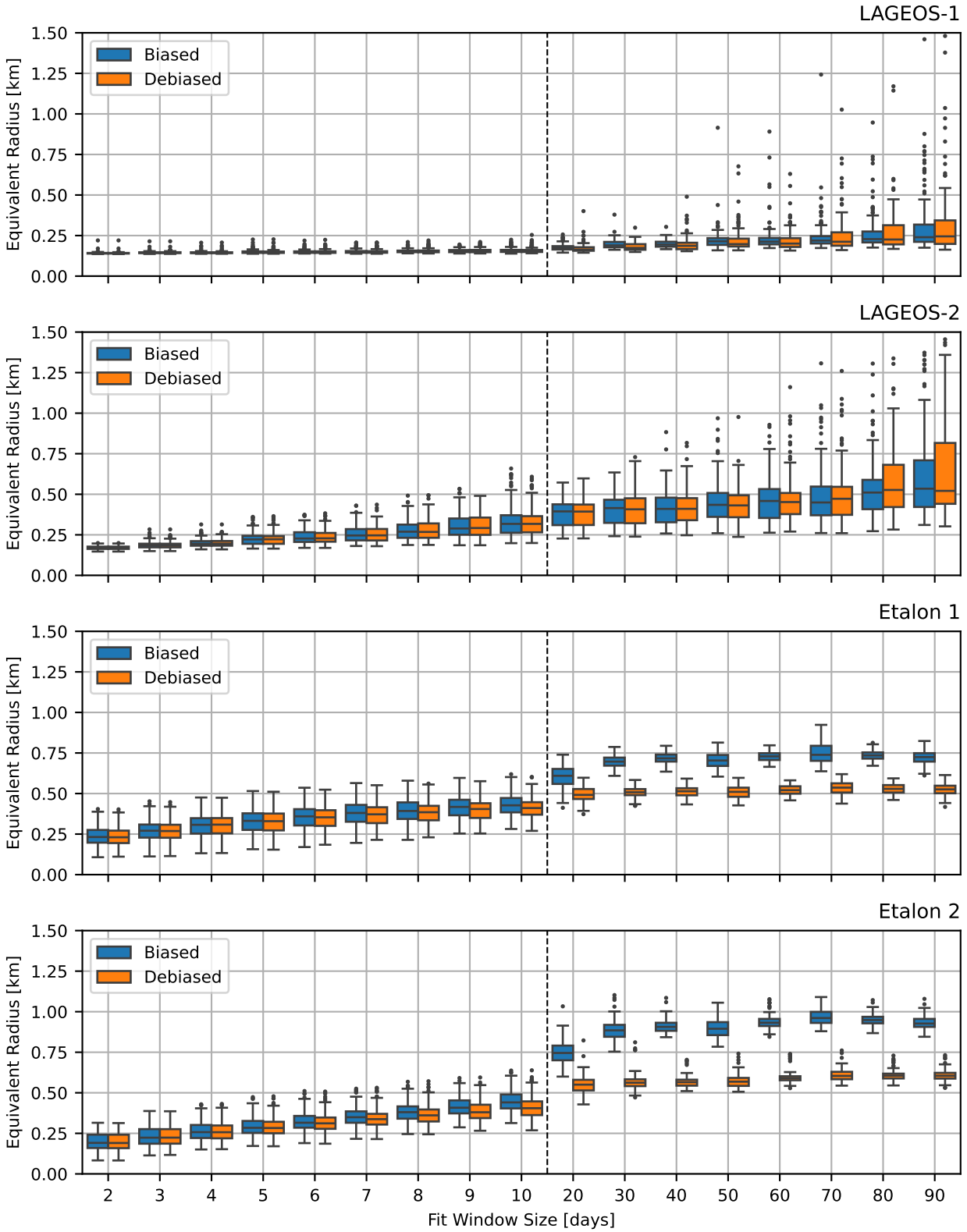
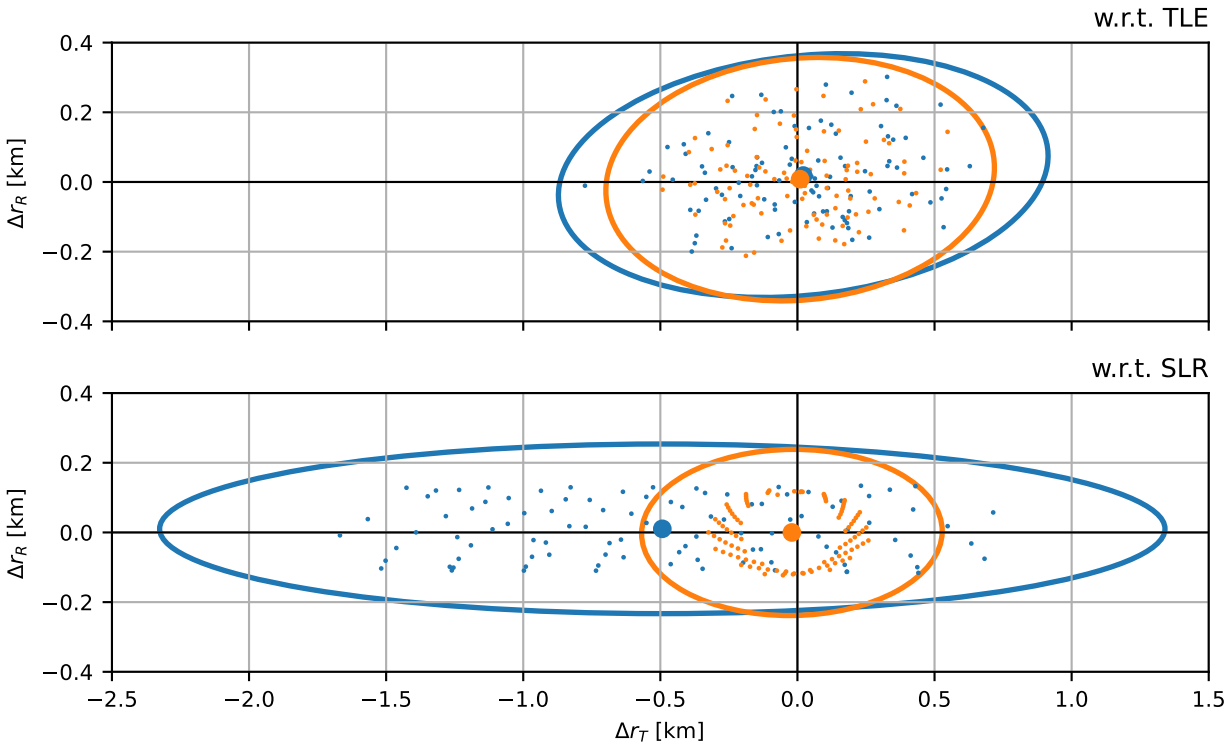
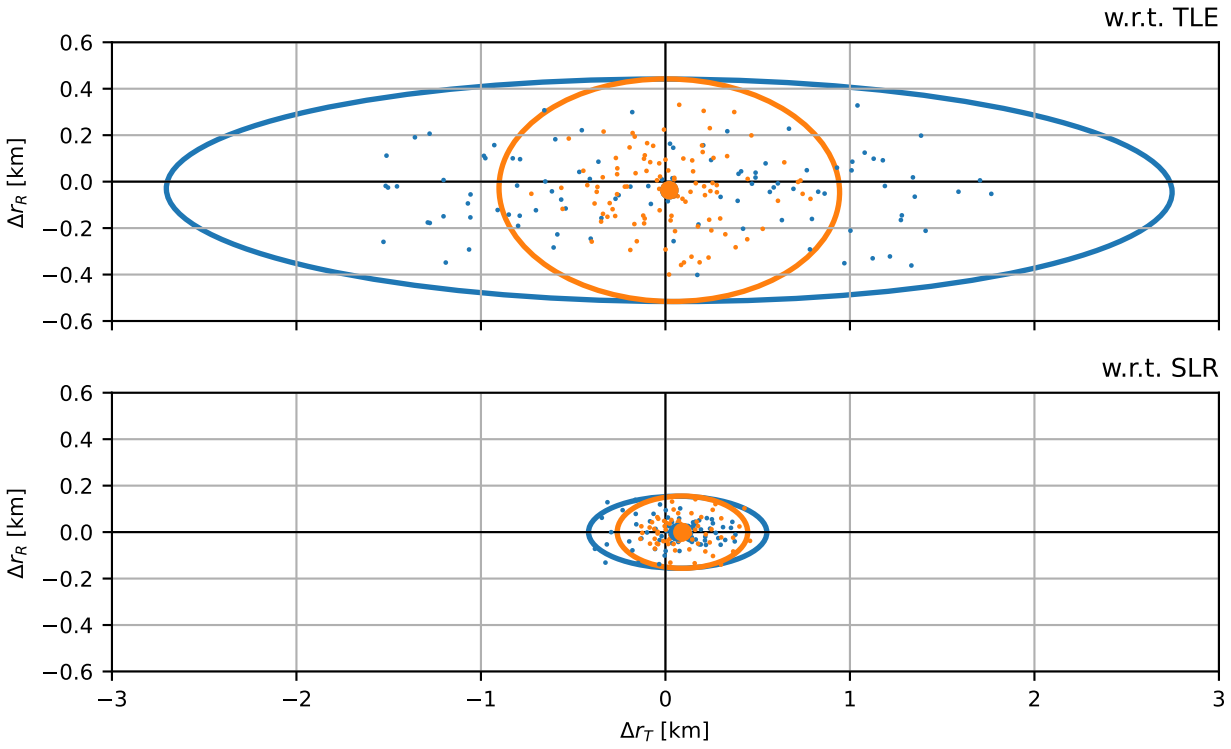


Figure 3.26: Equivalent radius distributions for calibration satellite fits during the year 2022 as a function of fit window size (with and without time-based model debiasing). Note the change in fit window size interval between the short- and long-term fits, and that the y-axes has been cropped due to the presence of extreme outliers.



(a) Short-term fit (10 day window, centred on 2nd July 2022).



(b) Long-term fit (90 day window, centred on 23rd March 2022).

Figure 3.27: Example residual scatters in the radial-along-track plane for Etalon 1 fits, with the biased fit residuals and 3σ boundary (blue), and the debiased fit residuals and 3σ boundary (orange).

3.6 Large-Scale Bias Modelling

GNSS constellations are an excellent test case for bias models due to the high-accuracy, publicly available ephemerides produced via the IGS [70], as discussed in Section 1.4.4. The GPS, GLONASS, Galileo, and BeiDou constellation are comprised of over 100 satellites in MEO, providing a wealth of information to investigate bias modelling at a large scale. Nonetheless, using the GNSS datasets still has its limitations when considering the orbital elements of the constellations, illustrated in Table 3.4. The various constellations use the same semi-major axis band, approximately 25,500 to 30,000 km; the same inclination band, approximately 55 to 65°; and a limited number of orbital planes, distributed in orientation by RAAN.

Table 3.4: Approximate orbital elements of the GNSS constellations (1st January 2024).

Constellation	Semi-major axis [km]	Eccentricity [-]	Inclination [deg]	No. Orbital Planes [-]
GPS	26,800	0.009	55.6	6
GLONASS	25,500	0.002	64.9	3
Galileo	29,500	0.006	55.6	3
BeiDou	27,900	0.001	55.1	3

Along-track position error behaviours for examples of each GNSS constellation are presented in Figure 3.28. All four examples showed periodic behaviour, including the same monthly variation seen for the calibration satellites. At the same time, there were additional behaviours not seen with the calibration satellites which complicate the process of creating bias models, both for individual GNSS satellites and for the constellations as a whole, including large shifts in error magnitude, as seen with the GLONASS and BeiDou examples; changing mean offsets, as seen with the GPS example; and the presence of manoeuvres, seen in all four examples as abrupt spikes in error magnitude.

3.6.1 Individual Time-Based Models

Individual time-based models were fitted to GNSS satellites from various constellations, including GPS, GLONASS, Galileo, and BeiDou. In the case of the BeiDou constellation, only its satellites in MEO were included to match the orbital regime of the other constellations. The model parameters of these individual fits were compared against a subset of Keplerian orbital elements, with the exception of angle of perigee which was not considered due to all of the orbits being near-circular. Generally, there was limited correlation between the Keplerian orbital elements and the model parameters.

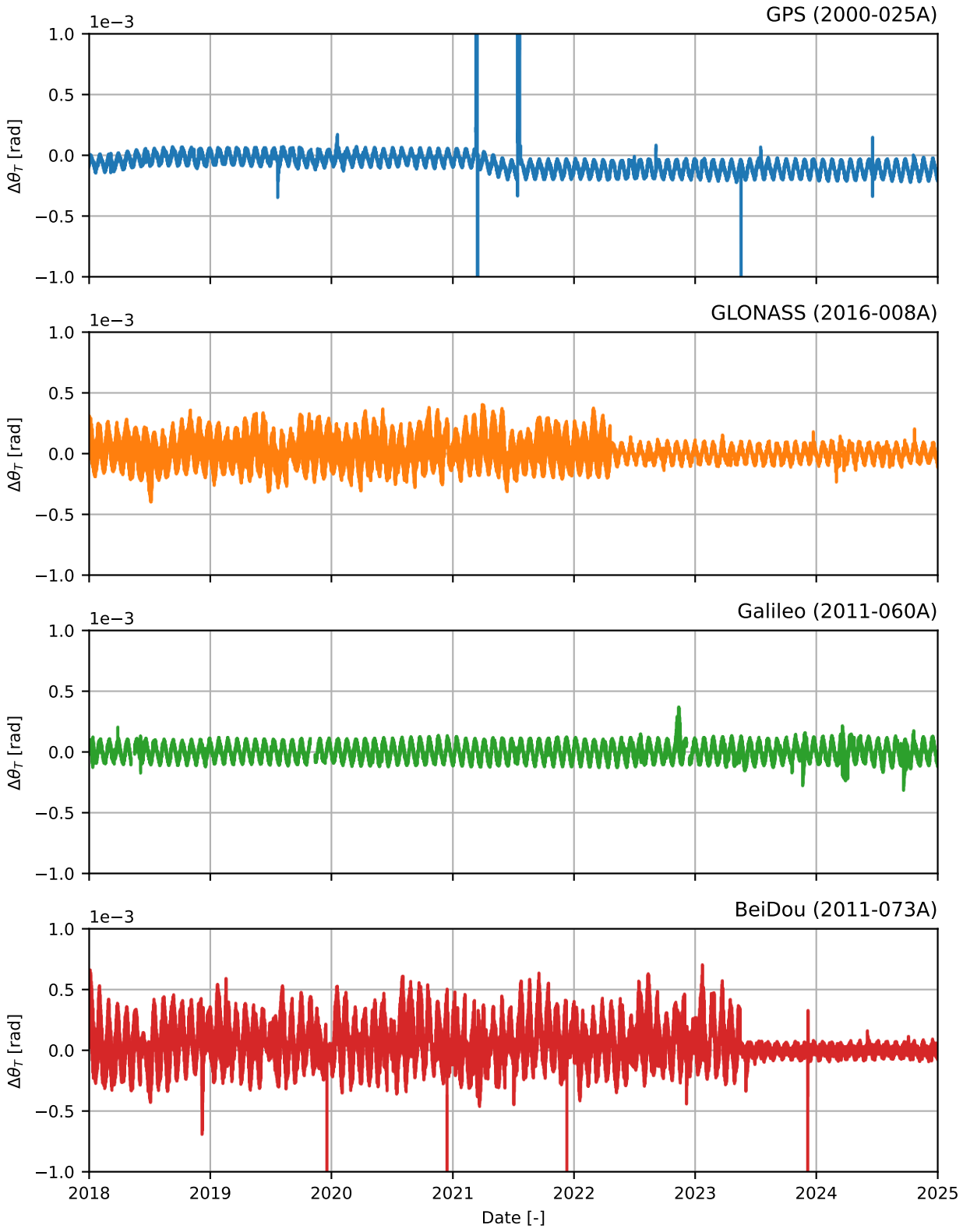


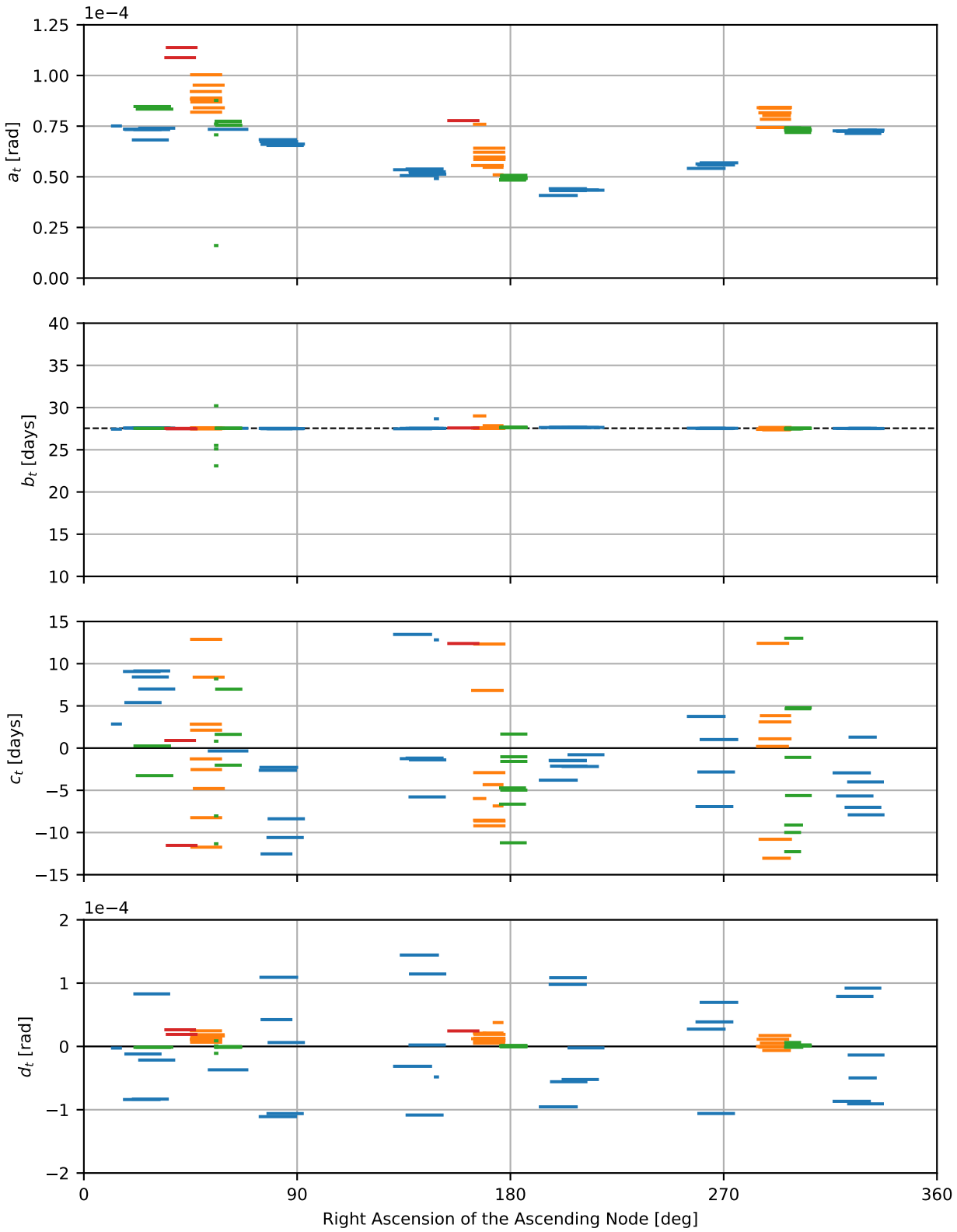
Figure 3.28: Examples from each GNSS constellation of along-track position error for the years 2018 to 2025. Note the larger y-axis magnitude compared to the equivalent figures for the calibration satellites.

The exception to the limited correlation between model parameters and Keplerian elements was an apparent relationship between the amplitudes of the models and RAAN, as illustrated in Figure 3.29. The models for orbits with RAANs near 0°/360° typically had the highest amplitudes. Conversely, model amplitudes reduced as the RAANs of orbits approached 180°. This suggests that the orientation of the orbital plane was a driving factor behind the amplitude of the bias oscillation.

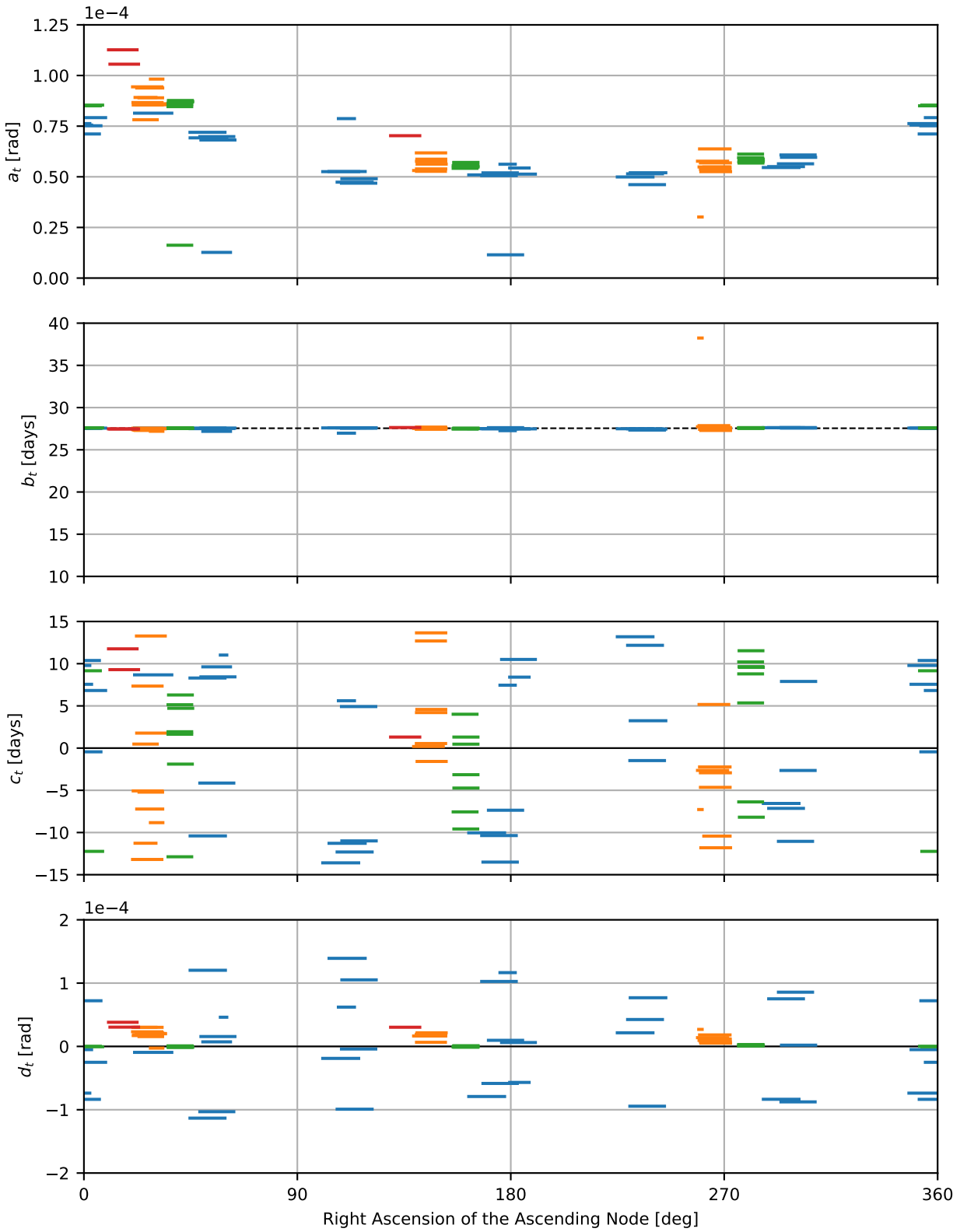
The periods of the fitted models remained close to the initial guess of 27.5 days with some minor variations across the presented years. Some outliers existed, in particular two GLONASS cases in 2020 and 2022, however these were likely the result of poor fits due to the aforementioned shifting error behaviour for some satellites. The model phases, on the other hand, were distributed significantly for all of the constellations and years. It should be noted, however, that this does not indicate necessarily that the models were significantly out-of-phase which each other: each individual model had a slightly different period which meant that the phase at a given epoch could vary significantly.

One issue with the analysis on GNSS satellites was the presence of gaps in the dataset from individual satellites having both planned and unplanned outages, due to a variety of events, such as PRN code reassignments and manoeuvres. These prevented frequency analysis of the bias, as presented in Section 3.2.1, as FFTs require complete time series with a constant time step. One option would be to apply FFT analysis to the periods of contiguous data, however with the caveat that a minimum time period would be needed to provide results representative of the true frequency content of the TLE errors. Alternative methods, such as the Non-Uniform Fast Fourier Transform (NUFFT) [134] or Lomb-Scargle periodograms [135, 136] could be used directly for frequency analysis on non-contiguous datasets to guide the initial guesses for the GNSS time-based models.

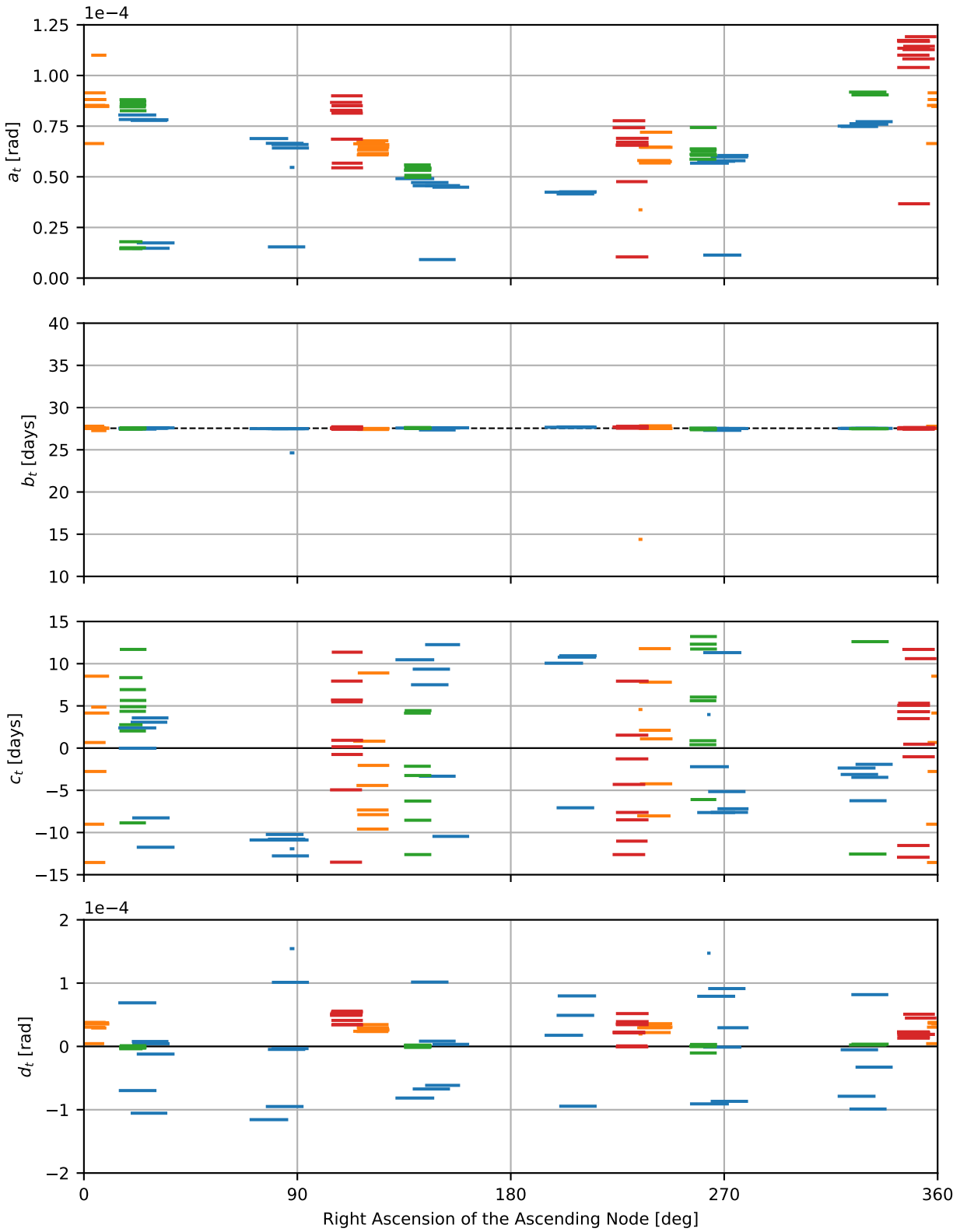
The mean offsets of the model varied significantly between constellations. The fits on GPS satellites showed significant variation in mean offsets throughout the years, distributed primarily within a $\pm 10^{-4}$ rad band. Some examples for this constellation approached almost $\pm 2 \times 10^{-4}$ rad. This major variation across the constellation, seemingly without any correlation to the Keplerian elements, matched the behaviour seen by Ly, Lucken, and Giolito [97]. Both GLONASS and BeiDou fits showed some mean offset, skewed positive by up to 0.5×10^{-4} rad in the earlier years; however, by 2024 these had been reduced to near-zero in all cases. The mean offsets for Galileo fits remained near-zero across all four presented years. The apparent lack of correlation between the offsets for the GPS constellation may present a challenge for generalising bias models if it emerges that the variation is


1e−4
1.25
1.00
0.75
0.50
0.25
0.00
a_t [rad]
40
35
30
25
20
15
10
b_t [days]
15
10
5
0
−5
−10
−15
c_t [days]
1e−4
2
1
0
−1
−2
d_t [rad]
0
90
180
270
360
Right Ascension of the Ascending Node [deg]

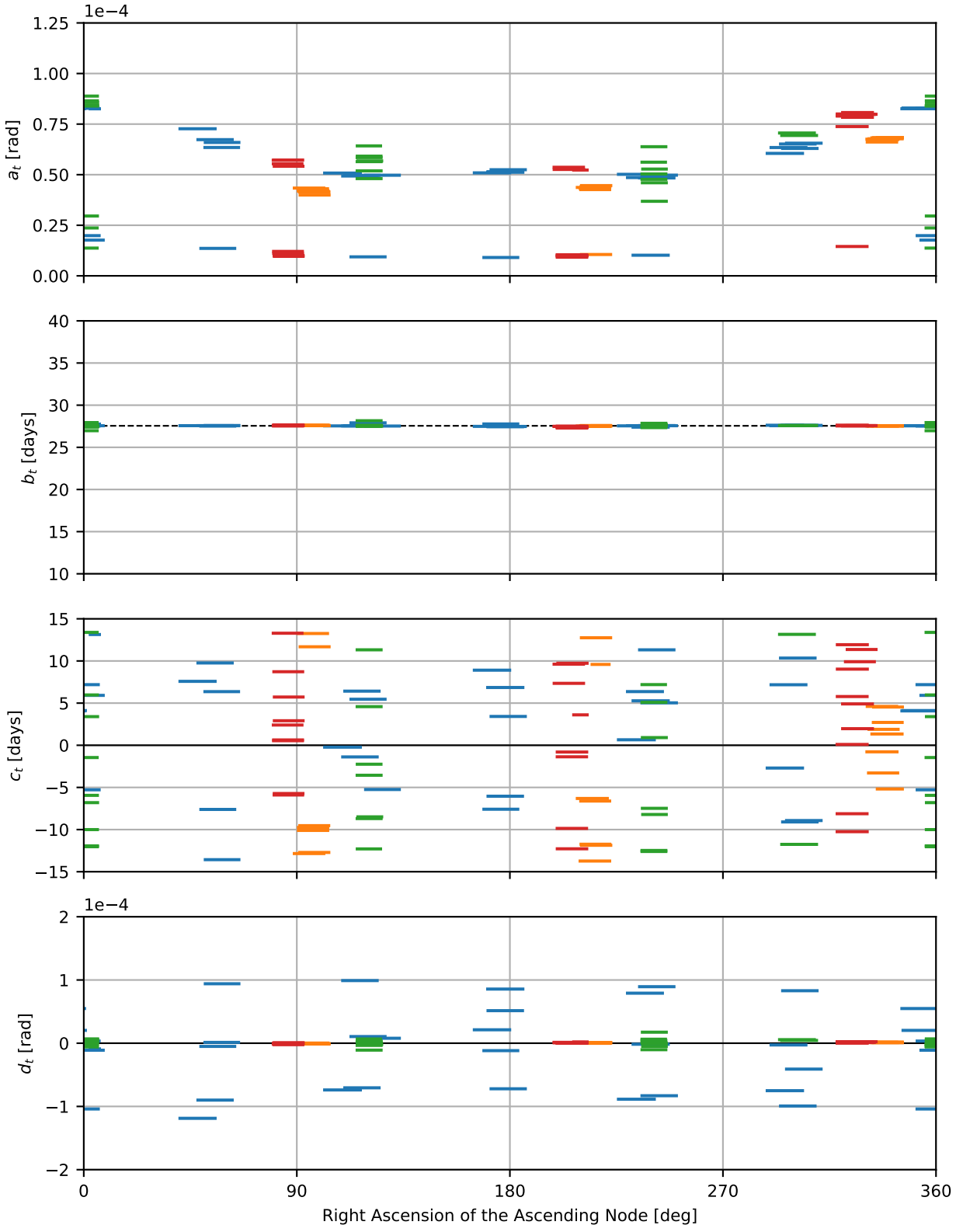
(a) 2018.


1e−4
1.25
1.00
0.75
0.50
0.25
0.00
a_t [rad]
40
35
30
25
20
15
10
b_t [days]
15
10
5
0
−5
−10
−15
c_t [days]
1e−4
2
1
0
−1
−2
d_t [rad]
0
90
180
270
360
Right Ascension of the Ascending Node [deg]

(b) 2020.


1e−4
1.25
1.00
0.75
0.50
0.25
0.00
a_t [rad]
40
35
30
25
20
15
10
b_t [days]
15
10
5
0
−5
−10
−15
c_t [days]
1e−4
2
1
0
−1
−2
d_t [rad]
0
90
180
270
360
Right Ascension of the Ascending Node [deg]

(c) 2022.



(d) 2024.

Figure 3.29: Time-based model parameters for individual GNSS fits as a function of each satellite's RAAN, including GPS (blue), GLONASS (orange), Galileo (green), and BeiDou (red).

not a direct result of SGP4 mismodelling. It is possible that there are factors in USSF's TLE generation pipeline affecting TLE accuracy which may account for these offsets and the sudden shifts in TLE quality, such as those seen for GLONASS and BeiDou.

3.6.2 Amplitude Model

The relationship between the RAAN of the satellites and the amplitude of their respective individual time-based models was approximated with an additional cosine function:

$$a(\Omega) \approx \alpha \cos(\Omega + \beta) + \gamma, \tag{3.6}$$

where Ω is the RAAN of the satellite, and α, β, γ are model parameters.

Due to the error behaviours differing slightly between GNSS constellations, Equation (3.6) was fitted to each constellation separately, and then to all four of the constellations together, to investigate any differences in RAAN-amplitude behaviour. Moreover, amplitude outliers were found to skew the results of the fitting process, therefore a $\pm 0.25 \times 10^{-4}$ rad band was applied to the model to reject outliers. It is important to note that the amplitudes of the fitted individual time- and Moon-based models are constant, despite the satellites precessing in RAAN, which may affect the fits of the amplitude models. The fits are presented in Table 3.5 and Figure 3.30.

The models for GLONASS, Galileo, and Beidou were particularly susceptible to overfitting due to the limited number of orbital planes in each of these constellations: only three compared to GPS' six. This resulted in significant changes in model amplitude and phase not seen as severely with the GPS models. This is effect was particularly noticeable for BeiDou in 2018 and 2020 where data points existed for only two orbital planes.

For GPS the minimum and maximum model values (i.e. $\gamma \pm \alpha$) only differed by up to 10.5 % and 10.5 % each over the four years, while GLONASS saw a 71.6 % and 38.7 % spread, respectively; Galileo, 8.9 % and 12.4 %; and BeiDou 51.3 % and 41.2 %. This highlights the consistency of the RAAN-amplitude behaviour for GPS over the years. Nevertheless, it should be noted that both GLONASS and BeiDou TLEs saw a significant reduction in position error in 2022 which manifested as a reduction in individual model amplitudes.

Table 3.5: RAAN-based amplitude models.

(a) 2018.

Constellation	α [rad]	β [rad]	γ [rad]
GPS	1.552×10^{-5}	-2.626×10^{-1}	6.024×10^{-5}
GLONASS	1.729×10^{-5}	-1.233×10^{-1}	7.663×10^{-5}
Galileo	1.747×10^{-5}	-1.448×10^{-1}	6.669×10^{-5}
BeiDou	2.081×10^{-5}	-5.444×10^{-1}	9.085×10^{-5}
All	1.733×10^{-5}	-2.589×10^{-1}	6.784×10^{-5}

(b) 2020.

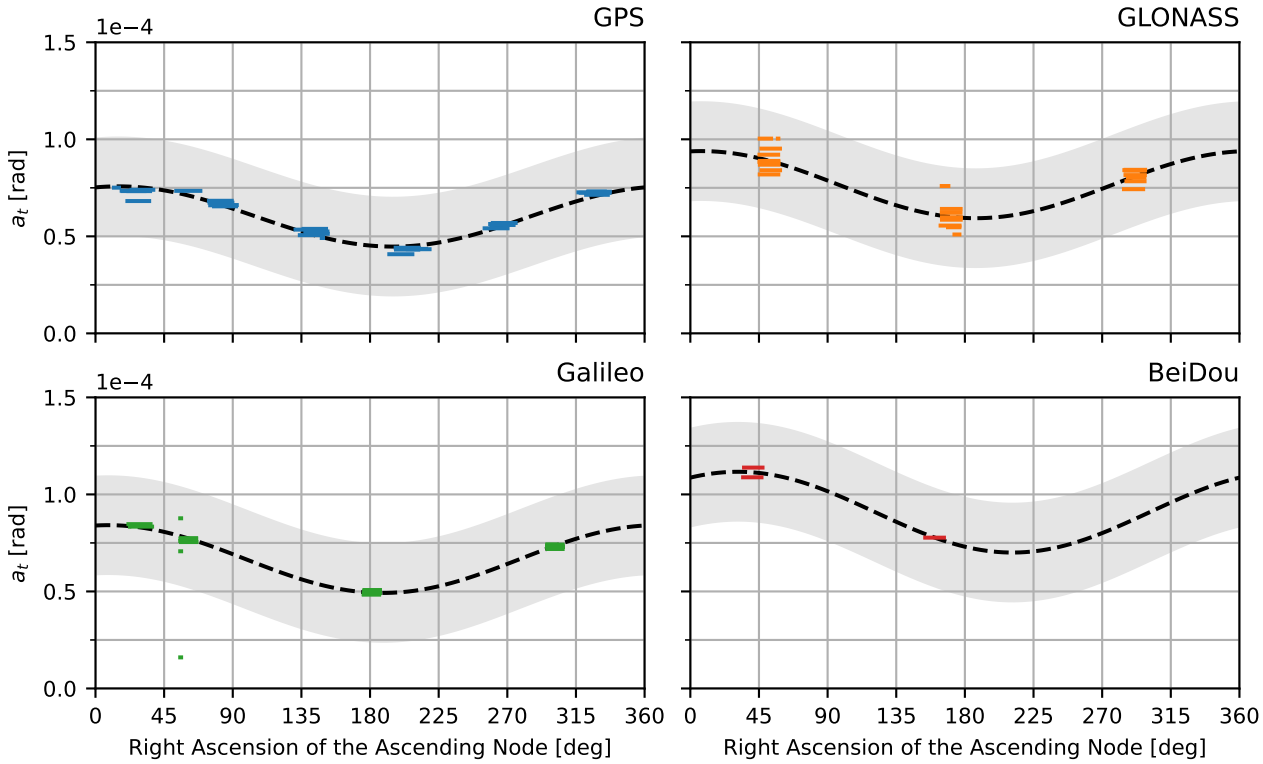
Constellation	α [rad]	β [rad]	γ [rad]
GPS	1.315×10^{-5}	-2.614×10^{-1}	5.935×10^{-5}
GLONASS	2.157×10^{-5}	-4.637×10^{-1}	6.703×10^{-5}
Galileo	1.997×10^{-5}	-6.182×10^{-1}	6.704×10^{-5}
BeiDou	2.271×10^{-5}	1.655×10^{-1}	8.884×10^{-5}
All	1.859×10^{-5}	-4.553×10^{-1}	6.457×10^{-5}

(c) 2022.

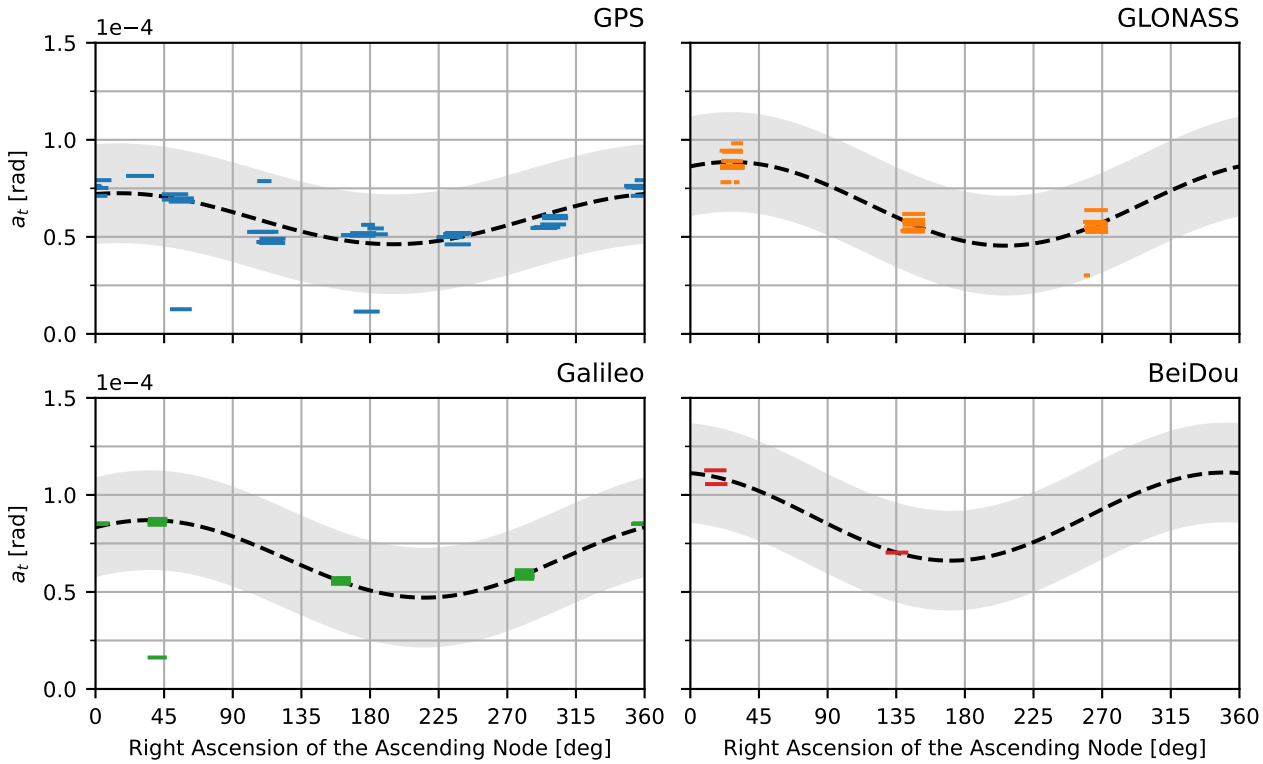
Constellation	α [rad]	β [rad]	γ [rad]
GPS	1.913×10^{-5}	-1.459×10^{-1}	6.096×10^{-5}
GLONASS	1.471×10^{-5}	-1.009×10^{-1}	7.078×10^{-5}
Galileo	2.036×10^{-5}	-3.751×10^{-2}	6.777×10^{-5}
BeiDou	2.345×10^{-5}	-9.253×10^{-2}	8.305×10^{-5}
All	2.030×10^{-5}	-1.224×10^{-1}	7.053×10^{-5}

(d) 2024.

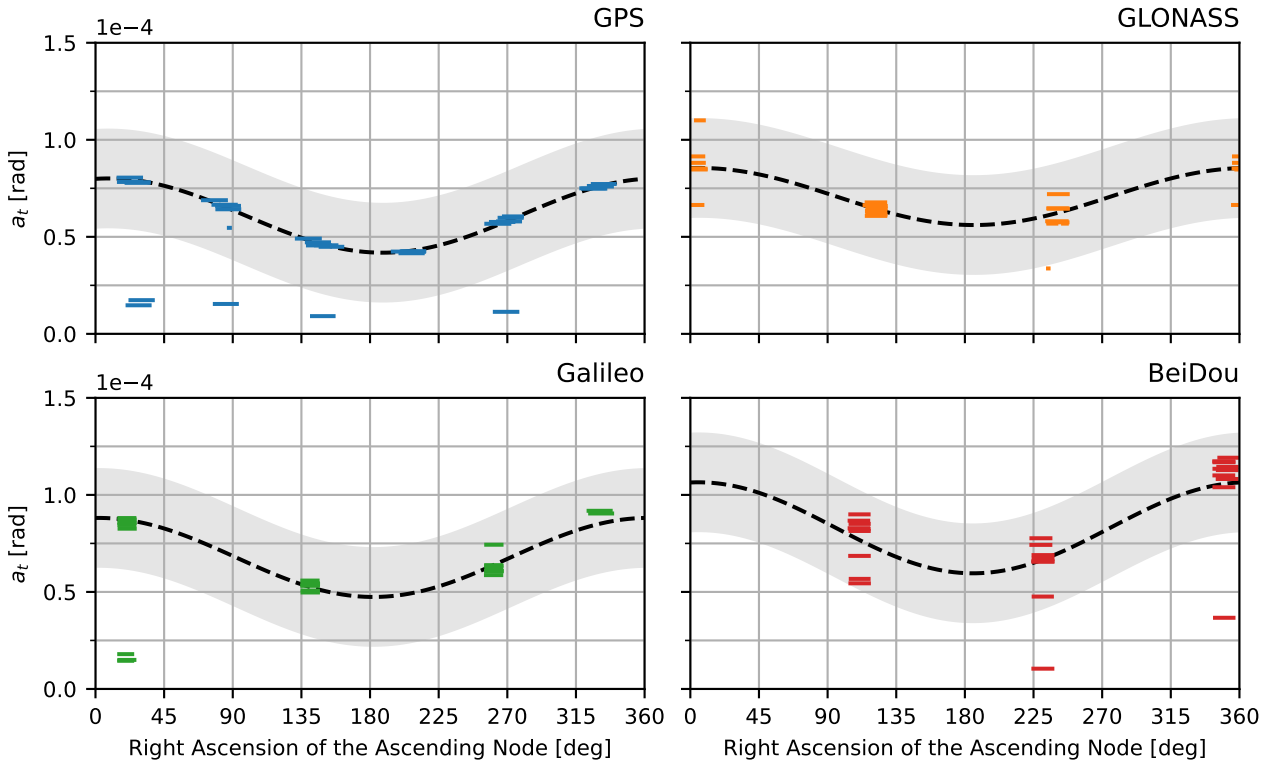
Constellation	α [rad]	β [rad]	γ [rad]
GPS	1.497×10^{-5}	-5.998×10^{-2}	6.009×10^{-5}
GLONASS	1.657×10^{-5}	4.693×10^{-1}	5.114×10^{-5}
Galileo	1.659×10^{-5}	-1.933×10^{-1}	6.180×10^{-5}
BeiDou	1.638×10^{-5}	4.871×10^{-1}	6.268×10^{-5}
All	1.591×10^{-5}	1.513×10^{-1}	5.865×10^{-5}


GPS
GLONASS
Galileo
BeiDou
1e−4
1.5
1.0
0.5
0.0
a_t [rad]
0
45
90
135
180
225
270
315
360
Right Ascension of the Ascending Node [deg]

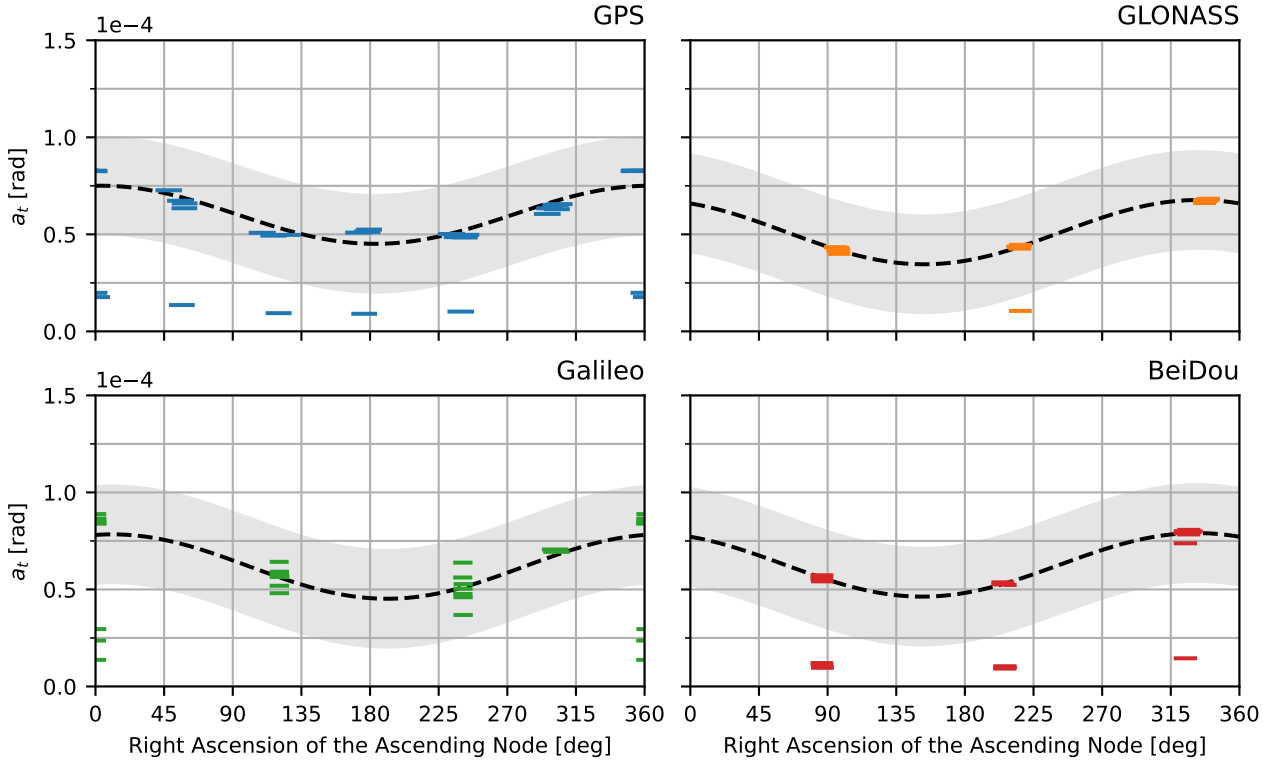
(a) 2018.


GPS
GLONASS
Galileo
BeiDou
1e−4
1.5
1.0
0.5
0.0
a_t [rad]
0
45
90
135
180
225
270
315
360
Right Ascension of the Ascending Node [deg]

(b) 2020.



(c) 2022.



(d) 2024.

Figure 3.30: Time-based model amplitudes for individual GNSS fits as a function of the osculating RAAN. The dashed lines represents the fitted amplitude models for each constellation, excluding the outliers outside of the shaded regions.

3.6.3 Ensemble Time- and Moon-Based Bias Models

'Ensemble' versions of the time- and Moon-based bias models, as presented in Equations (3.4) and (3.5), are proposed which replace the constant amplitude parameter with the RAAN-based relationship of Equation (3.6):

$$\Delta\theta_T(t,\Omega) \approx a(\Omega)\cos\left[\frac{2\pi}{b_t}\left(t + c_t\right)\right] + d_t,$$

$$\Delta\theta_T(M,\Omega) \approx a(\Omega)\sin\left(M + c_m\right) + d_m.$$

Due to the inclusion of RAAN in these models, the fit process requires multiple satellites with a good distribution in RAAN. Fitting these models, therefore, must be done at least by constellation or, ideally, with all of the constellations.

The fitted parameters for the ensemble models are presented in Table 3.6. The parameters of the ensemble models specific to the time- and Moon-based components generally behaved as expected. In the case of the time-based models, the period, b_t, remained consistent at 27.56 and 27.57 days, matching the calibration satellite results at 27.55 days, while the phases lay within a five-day band, only a few days delayed when compared to the individual calibration satellite models. Notably, the mean offsets for all of the models remained near-zero, suggesting that the variation seen in this parameter, particularly with the GPS constellation, averaged out to zero. The RAAN-amplitude model parameters remained similar between the time- and Moon-based ensemble models, following similar trends year-to-year, however with slightly differing amplitudes, phases, and offsets when considering individual years. The RAAN-amplitude component of both long-term models (those including the years 2018 to 2025) were nearly identical with very similar amplitudes, α, and phases, β, within 1.55 % and 3.00 % respectively, and almost no difference in offset, γ.

When comparing the amplitude model parameters of the ensemble models to the all-constellation fits of the RAAN-amplitude model presented in Table 3.5, the ensemble models for the years 2020 and 2022 had significantly smaller amplitudes, α, while the ensemble models for the years 2022 and 2024 had significantly smaller offsets, γ. This suggested that it was important to fit all the parameters of the ensemble model concurrently: the fits of the RAAN-amplitude model to individual models were useful for providing initial parameter guesses but not to provide effective estimates for direct integration of the model into the individual time- and Moon-based models.

Table 3.6: Ensemble bias models, each fit to all of the GNSS satellites.

(a) Time-based.

Year(s)	α [rad]	β [rad]	γ [rad]	b_t [days]	c_t [days]	d_t [rad]
2018	1.758×10^{-5}	-2.396×10^{-1}	6.944×10^{-5}	27.56	6.439	5.159×10^{-6}
2020	1.398×10^{-5}	-5.165×10^{-1}	6.452×10^{-5}	27.56	5.287	7.594×10^{-6}
2022	1.527×10^{-5}	3.695×10^{-2}	6.504×10^{-5}	27.57	9.001	1.222×10^{-5}
2024	1.783×10^{-5}	4.038×10^{-1}	4.919×10^{-5}	27.56	4.243	-1.885×10^{-6}
2018 to 2025	1.504×10^{-5}	-0.261×10^{-1}	6.114×10^{-5}	27.57	7.762	5.661×10^{-6}

(b) Moon-based.

Year(s)	α [rad]	β [rad]	γ [rad]	c_m [rad]	d_m [rad]
2018	1.832×10^{-5}	-2.424×10^{-1}	6.695×10^{-5}	3.473×10^{-1}	5.858×10^{-6}
2020	1.350×10^{-5}	-4.999×10^{-1}	6.258×10^{-5}	2.899×10^{-1}	8.078×10^{-6}
2022	1.593×10^{-5}	9.664×10^{-2}	6.284×10^{-5}	4.253×10^{-1}	1.257×10^{-5}
2024	1.777×10^{-5}	3.795×10^{-1}	4.814×10^{-5}	7.146×10^{-2}	-1.330×10^{-6}
2018 to 2025	1.527×10^{-5}	-0.202×10^{-1}	5.932×10^{-5}	3.025×10^{-1}	6.485×10^{-6}

3.6.4 Large-Scale Bias Model Evaluation

The position RMSE and position error standard deviation distributions, per-constellation and following debiasing with both the individual and ensemble models, are presented in Figures 3.31 and 3.32. Generally, the models did result in some improvement, both in terms of overall accuracy and dispersion. As expected, the individual models tended to have better performance than their ensemble equivalents. Nevertheless, there were a few examples where use of the models did result in degraded position estimates.

For GPS, the individual models were highly effective, reducing the typical median position RMSE by 80 %. The ensemble models, on the other hand, had less of an impact on the position RMSE, at most reducing its median value by 20 %. Furthermore, the reduction in dispersion seen with the individual models was not seen with the ensemble models. The typical position error standard deviation was reduced by approximately 75 % by the individual models and 50 % by the ensemble models. This suggested that even though the ensemble models were not affecting the position RMSE significantly, they removed still the dominant monthly oscillations in along-track position error. The mean offset in along-track position error, which varied significantly by GPS satellite, could not be addressed by the ensemble models' near-zero offset.

For GLONASS, both the individual and ensemble models had limited effect on the position RMSE distribution until the year 2024, at which point the position RMSE was reduced significantly, by up to 65 % in some cases. It should be noted, however, that TLE quality significantly improved too, following the change in quality mentioned previously. Both the individual and ensemble models improved the consistency of the pseudo-observations with reductions of the position error standard deviation by approximately 20 % which rose to 50 % by the year 2024.

For Galileo, the trend seen with GLONASS and BeiDou of model performance improving when approaching the year 2024 was reversed. Until the year 2024, both the individual and ensemble models were highly effective at reducing the position RMSE and standard deviation with typical reductions of up to 50 %; however, for the year 2024, this was halved to only 25 % for position RMSE and almost eliminated for position error standard deviation.

For BeiDou, the models followed similar trends to GLONASS. TLE quality for this constellation was markedly worse than for the other constellations, resulting in large errors position RMSE for most of the test cases. Nevertheless, TLE quality improved significantly by the year 2024. The large dispersion in position RMSE in the year 2022 might be attributed to shifts in TLE quality occurring at different times for the various satellites in the constellation. The individual models were more effective at reducing errors than the ensemble models with typical reductions by approximately 20 % and 10 %, respectively. In the year 2024, however, this increased to an approximately 60 % reduction in the median position RMSE. The typical position error standard deviation was reduced by approximately 30 % by the individual models and 15 % by the ensemble models, increasing to approximately 80 % in the year 2024, suggesting that pseudo-observation consistency was still improved through application of the bias models.

The results of debiasing with the long-term bias models (i.e. those fitted to the full dataset for the years 2018 to 2025) are presented in Figures 3.33 and 3.34. The individual time- and Moon-based models remained most effective for the GPS satellites while the performance of the ensemble models remained similar for all of the constellations. Importantly for GLONASS and BeiDou, these results included errors from both before and after their respective shifts in TLE quality, therefore the position RMSE and position error standard deviation for each individual satellite remained high, despite the improvements after the year 2023.

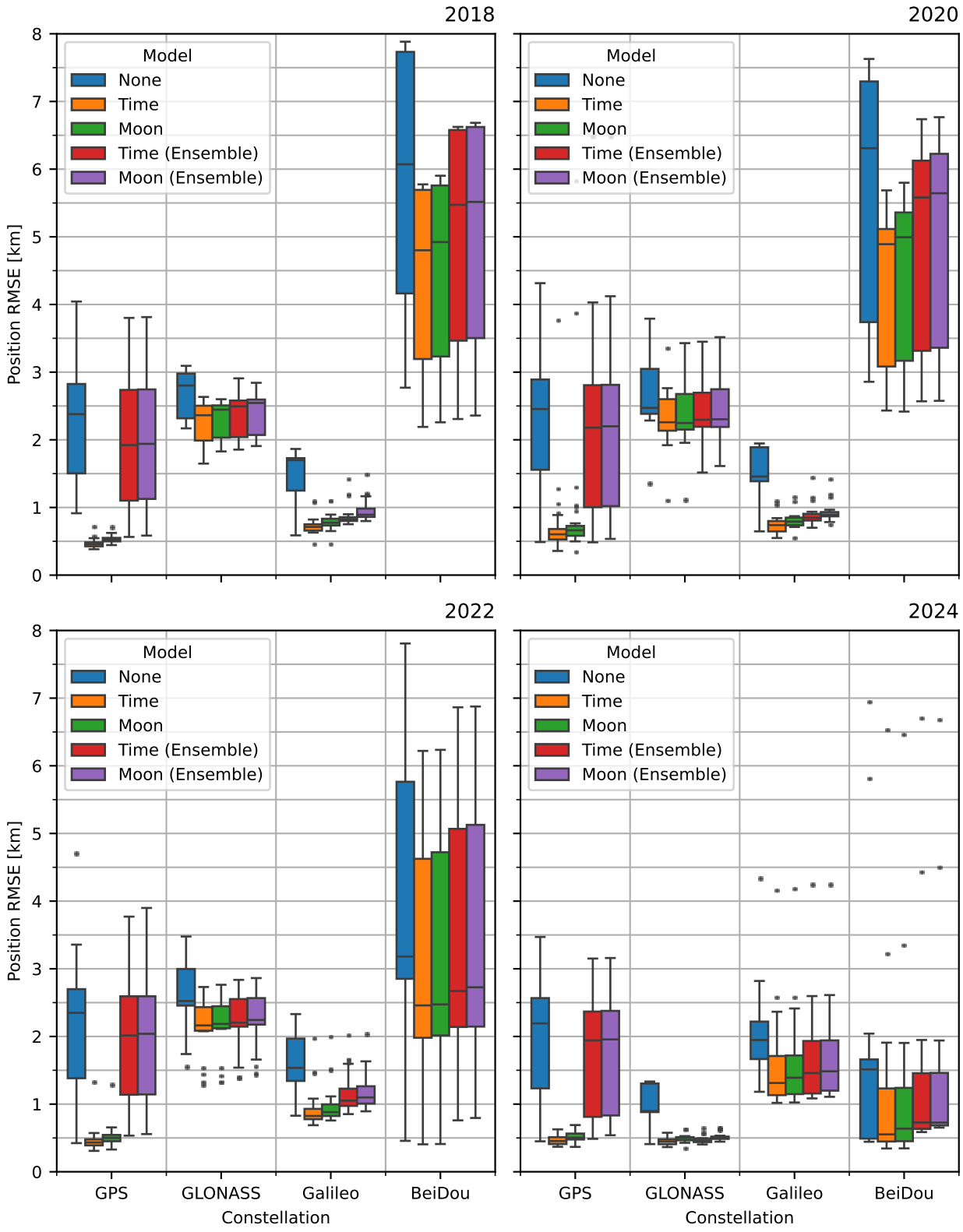


Figure 3.31: Position RMSE distributions for GNSS satellite TLEs following debiasing with individual and ensemble time- and Moon-based models. The box plots indicate the median, upper and lower quartiles, and the IQR [137, 138]. Outliers are indicated by points.

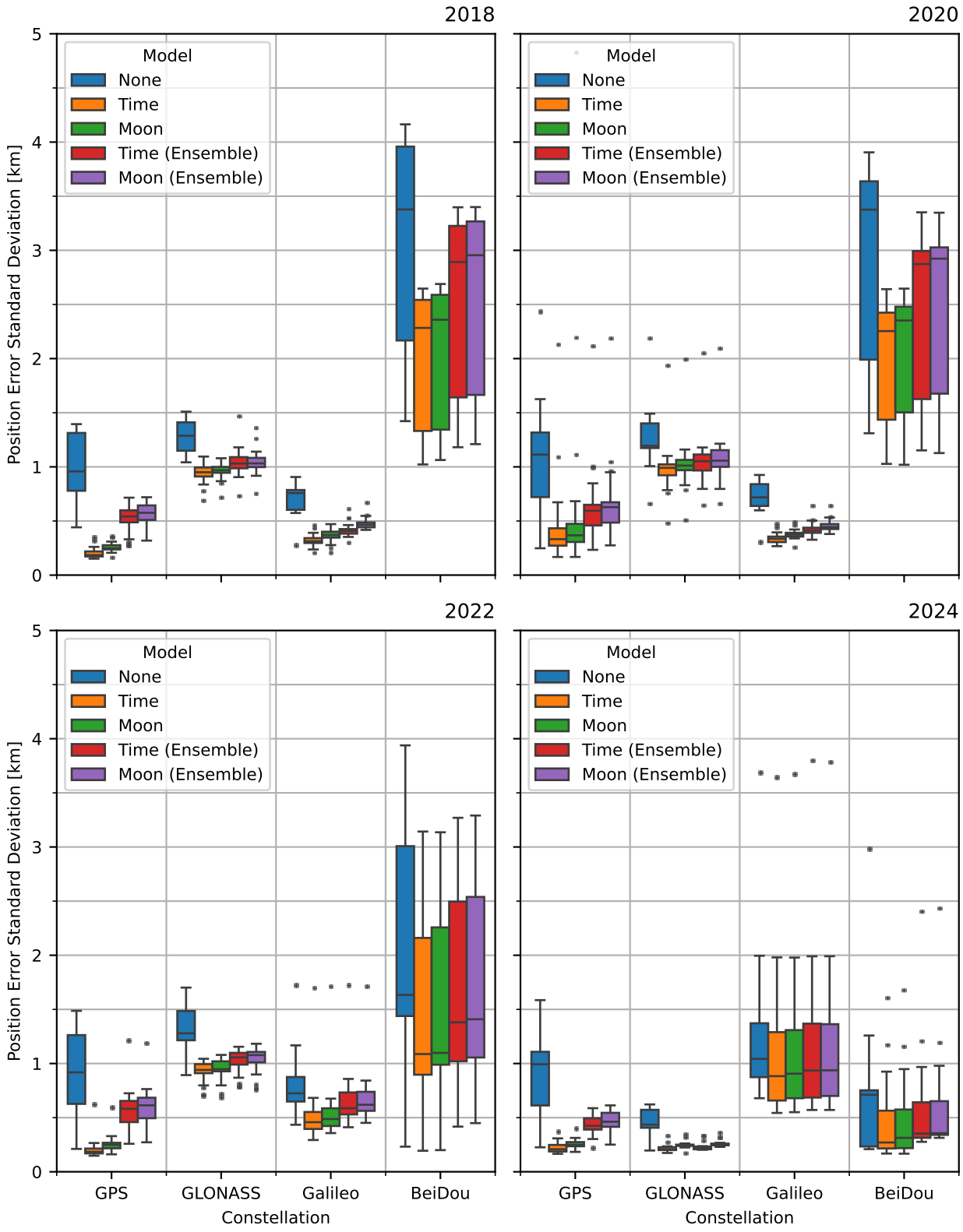


Figure 3.32: Position error standard deviation distribution for GNSS satellite TLEs following debiasing with individual and ensemble time- and Moon-based models. Note that the y-axis has been cropped due to extreme outliers.

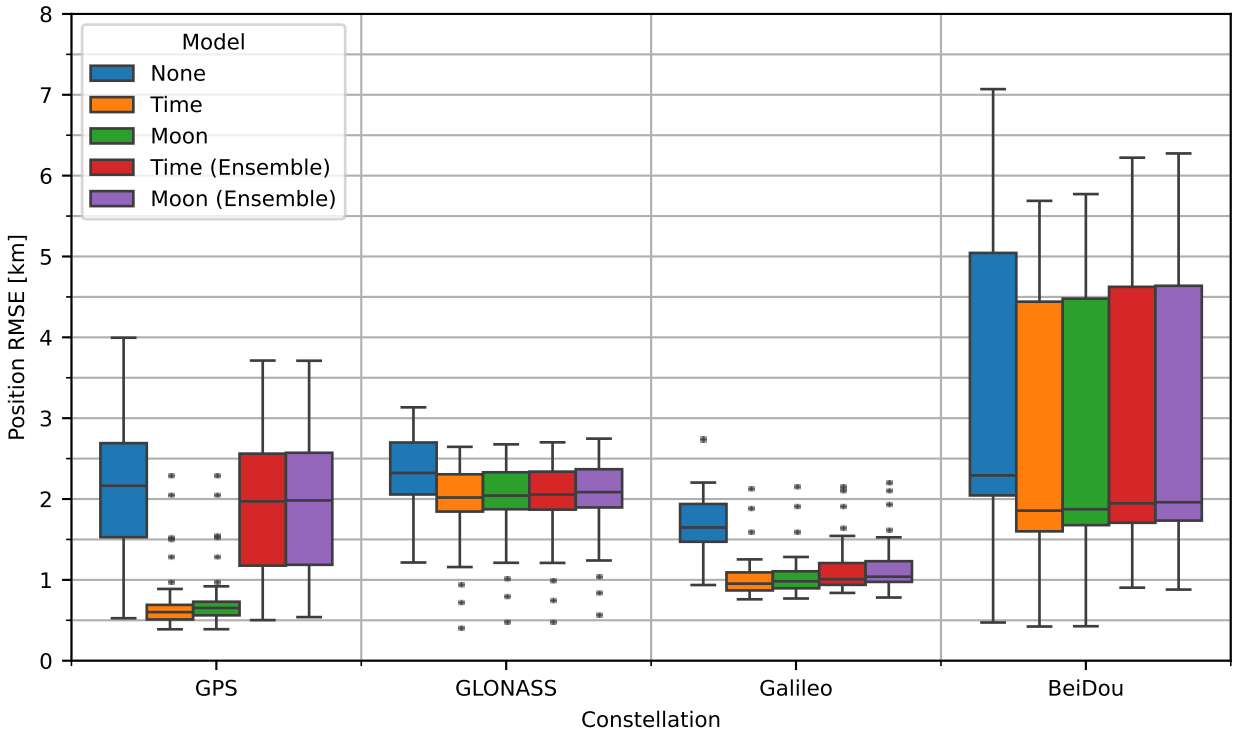


Figure 3.33: Position RMSE distributions for GNSS satellite TLEs, following debiasing with individual and ensemble time- and Moon-based models, for the years 2018 to 2025.

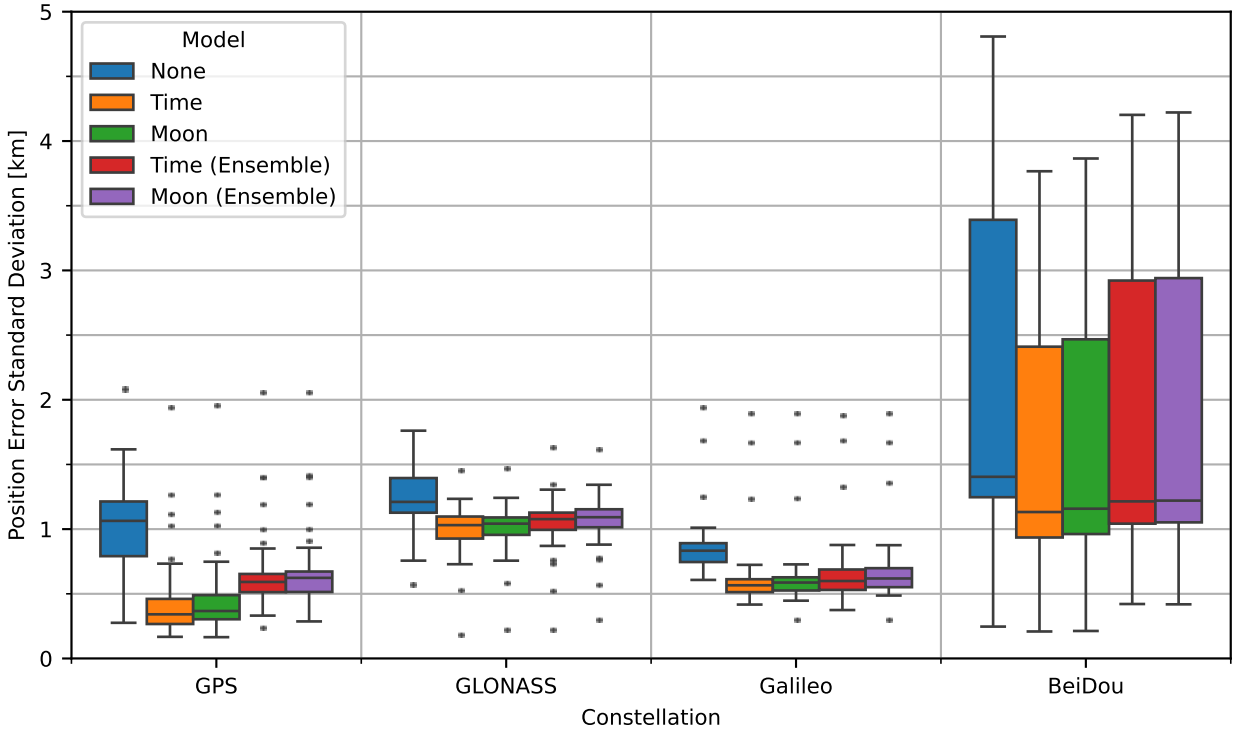


Figure 3.34: Position error standard deviation distribution for GNSS satellite TLEs, following debiasing with individual and ensemble time- and Moon-based models, for the years 2018 to 2025.

An important question when creating data-driven models is whether they can be extrapolated, in this case to satellites in various orbital regimes. It was decided, for this reason, to test the ensemble time-based model on the calibration satellites. The model was expected to perform well for Etalon 1 and 2, due to their orbits closely matching those of GNSS satellites. Conversely, the model was expected to perform poorly for LAGEOS-1 and -2, both due to the significantly different structure in error behaviour, as shown previously, and their significantly lower altitudes and LAGEOS-1's significantly different inclination.

The predicted along-track position errors and residuals for the calibration satellites, using the GNSS-derived ensemble time-based model, are presented in Figures 3.35 and 3.36. For Etalon 1 and 2, the along-track position error was reduced to within a $\pm 0.5 \times 10^{-4}$ rad band, similar to the individual time- and Moon-based models. The standard deviation of along-track position error was reduced by 49.1 % and 59.2 %, respectively, for Etalon 1 and 2. Although less effective than the individual time-based models, by approximately 15 percentage points, this represents still a significant improvement in bias behaviour and demonstrates that bias models generated using data from other satellites can be applied to satellites in a similar orbital regime. The model performed very poorly for LAGEOS-1 and -2, significantly increasing the amount of error instead of reducing it due to the amplitude being grossly overestimated.

Interestingly, Figure 3.35 highlighted the large, periodic changes in RAAN for both LAGEOS-1 and -2, made visible as the changing amplitude of the models with respect to time. Notably, in the case of LAGEOS-2, the changes in RAAN appeared to correlate with the longer-period behaviour of its along-track position error, albeit in opposite phase. This suggests that RAAN continued to be an important factor affecting bias amplitude for these satellites, however with a different relationship than that of the GNSS and Etalon satellites. This would make sense, given the large difference in semi-major axes and inclinations between the two sets of satellites.

3.6.5 Coplanarity Amplitude Model

In Section 3.2, it was proposed that the along-track position and radial velocity errors could be related to slight changes in semi-major axis due to the perturbation mismodelling. By considering the Gauss planetary equations [126], specifically the equation for the rate of change of semi-major axis, and by assuming that the eccentricity is near-zero (i.e. $e \approx 0$ and $a \approx r$), we can see that the change in

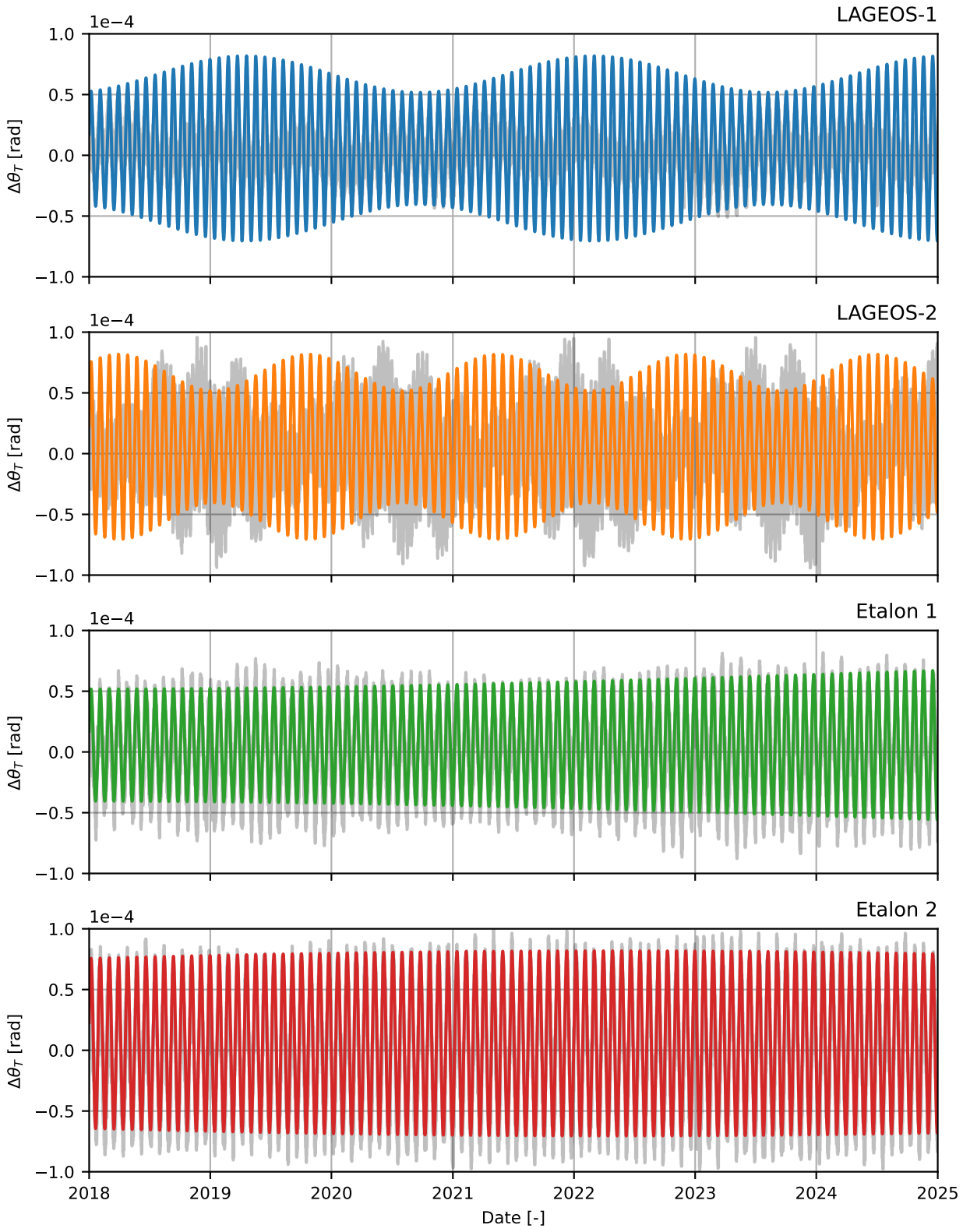


Figure 3.35: GNSS-derived ensemble time-based model along-track position error for the calibration satellites for the years 2018 to 2025. The along-track position error of the TLEs and the model are presented in grey and colour, respectively.

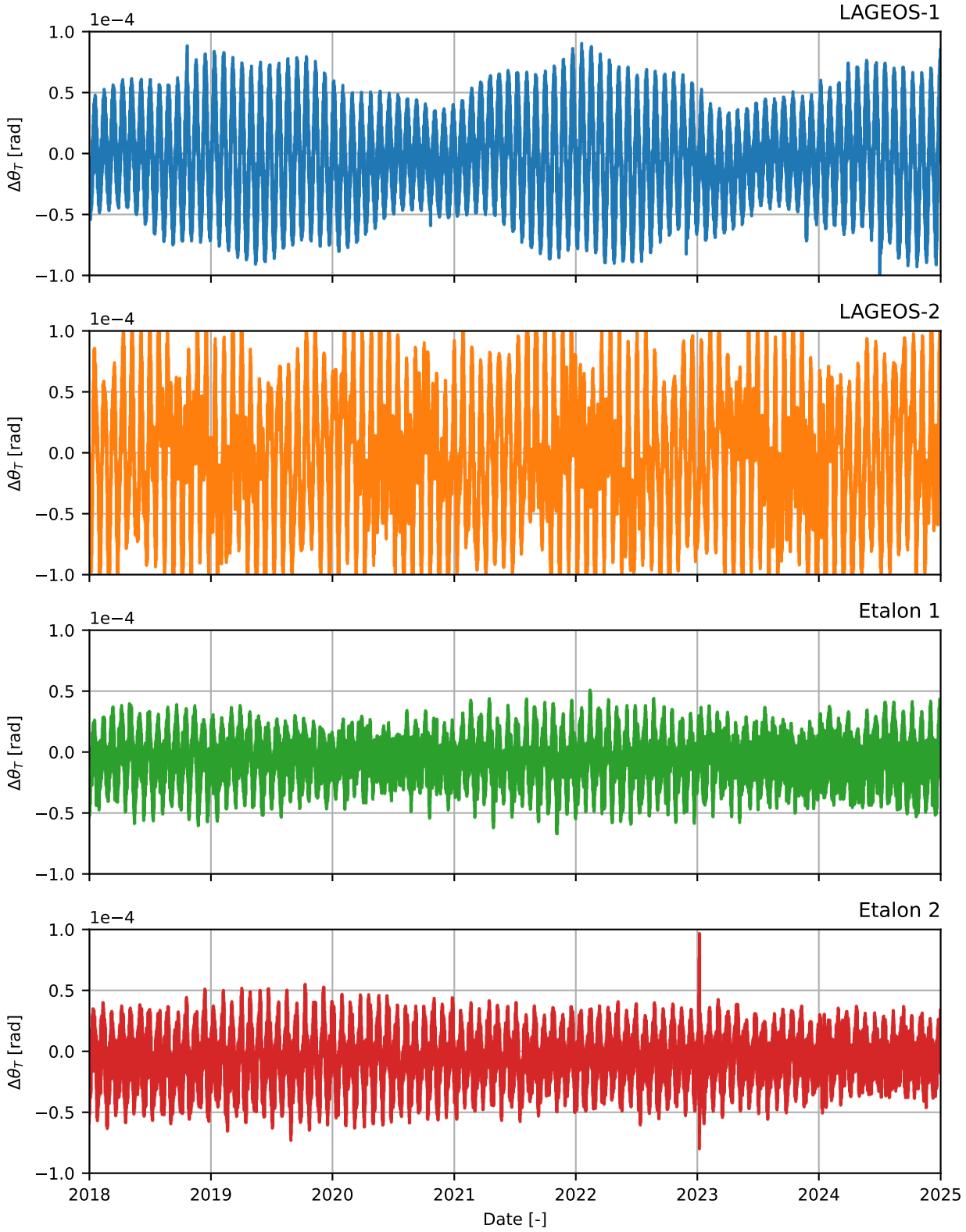


Figure 3.36: Residual along-track position error for the calibration satellites following debiasing with the GNSS-derived ensemble time-based model for the years 2018 to 2025.

semi-major axis is proportional to the perturbing force in the along-track direction, F_T:

$$\frac{da}{dt} = \frac{2}{n\sqrt{1-e^2}}\left[e\sin(v)F_R + \frac{a\left(1-e^2\right)}{r}F_T\right],$$

$$\approx \frac{2}{n}F_T.$$

The largest changes in semi-major axis, and therefore the largest oscillations in along-track position and radial velocity error, will occur when the perturbation error is fully in-plane.

It is proposed that the amplitude of the along-track position error is a function of the coplanarity of the satellite's orbit with the orbit of the Moon. In Equation (3.6), RAAN acts as a proxy to capture the coplanarity, albeit one which applies only for a given orbital inclination. A more intuitive, and potentially more generalisable, amplitude model could consider directly the angle between the angular momentum vectors of each orbit:

$$\mathbf{h}_{\text{TLE}} = \mathbf{r}_{\text{TLE}} \times \mathbf{v}_{\text{TLE}},$$

$$\mathbf{h}_{\text{moon}} = \mathbf{r}_{\text{moon}} \times \mathbf{v}_{\text{moon}},$$

$$\mathbf{h}_{\text{TLE}} \cdot \mathbf{h}_{\text{moon}} = ||\mathbf{h}_{\text{TLE}}|| \cdot ||\mathbf{h}_{\text{moon}}|| \cos\theta,$$

$$\theta = \arccos\left(\frac{\mathbf{h}_{\text{TLE}} \cdot \mathbf{h}_{\text{moon}}}{||\mathbf{h}_{\text{TLE}}|| \cdot ||\mathbf{h}_{\text{moon}}||}\right),$$

where 0° indicates that the orbits are coplanar, 90° indicates that the orbits are orthogonal, and 180° indicates that the orbits are coplanar but rotating in opposite directions.

The amplitudes of the individual GNSS-derived time-based models are presented in Figure 3.37 as a function of coplanarity with the orbit of the Moon. There was a very strong correlation between model amplitude and coplanarity. The highest amplitudes occurred for the most coplanar orbits, decreasing as the coplanarity reduced. There appeared to be an almost linear relationship between model amplitude and coplanarity, most noticeably for GPS throughout the years and for all of the constellations in the year 2024. Notably, none of the fits appeared to exceed 90°, although several GLONASS satellites were close in the year 2024. It was suspected that the amplitude would increase again past 90° as this would represent increasing coplanarity, however confirmation of this behaviour will require testing with satellites with retrograde motion with respect to the Moon.

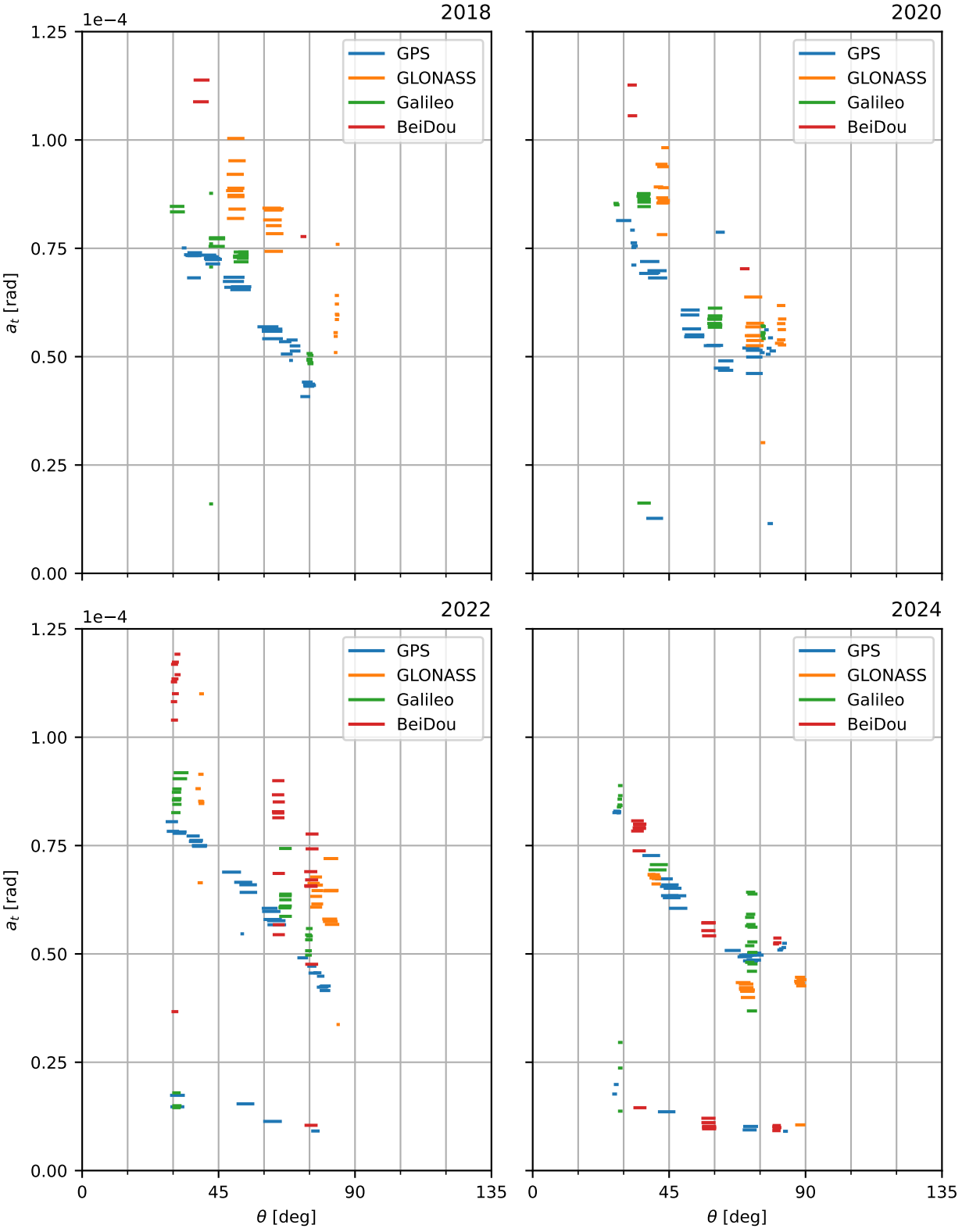


Figure 3.37: Time-based model amplitudes for individual GNSS fits as a function of coplanarity with the orbit of the Moon.

3.7 Higher-Order Bias Models

The single-component time-based models from Section 3.3.3, despite effectively suppressing TLE bias for three of the four calibration satellites, presented a number of disadvantages which may prevent the method for being applied more generally. Critically, it failed to accurately capture outlying bias behaviour, particularly in cases where multiple periodic components were contributing to the variation of the bias. This was highlighted in the case of LAGEOS-2: firstly, due to the presence of multiple significant periodic components; and, secondly, due to the numerical solver failing to capture the dominant periodic component with a period of 13.05 days. The latter issue highlighted one of the issues when using local solvers: poor initial guesses can result in the solver being trapped in local minima and unable to reach the most appropriate solution. In this case, the assumption of a single periodic component with a approximately 27.5-day period resulted in a poor model fit.

An alternative to the model fitting procedure presented in Section 3.3.1 is to use the results of the FFTs presented in Section 3.2.1 to create a multiple-component time-based model:

$$\Delta\theta_T(t) \approx \sum_i a_{t,i} \cos\left[\frac{2\pi}{b_{t,i}}\left(t + c_{t,i}\right)\right] + d_t.$$

In addition to not being subject to the limitations of the numerical solver, this method makes it significantly easier to combine multiple periodic components to produce a more representative bias model. Most importantly, this method does not require prior assumptions about the dominant periodic components as this information is recovered directly from the FFT.

FFT-derived time-based models were created for each of the calibration satellites, as presented in Table 3.7 and Figure 3.38. The 20 largest periodic components were selected and the constant offset, although these were very small, as seen originally with the single-component models. Components with a period smaller than one day were ignored to prevent the model from capturing short period oscillations in TLE quality instead of the longer period bias variation.

The same period of approximately 27.49 days was shared by the dominant periodic components of the models for LAGEOS-1, and Etalon 1 and 2. This differed slightly from their single-component models which shared a period of 27.55 days. Moreover, the amplitudes of the dominant periodic components were slightly lower than their single-component counterparts. Nevertheless, it can be seen

Table 3.7: Individual calibration satellite FFT-derived time-based models for the years 2018 to 2025. The 20 largest periodic components with a period greater than one day were included, in addition to the constant offset. The largest amplitude component is highlighted in bold.

(a) LAGEOS-1.

a_t [rad]	b_t [days]	c_t [days]	d_t [rad]
1.574×10^{-5}	**2.749×10^{1}**	**-1.347×10^{1}**	**-**
6.556×10^{-6}	2.841×10^{2}	-1.106×10^{2}	-
3.517×10^{-6}	2.779×10^{1}	-1.214×10^{1}	-
3.195×10^{-6}	2.841×10^{1}	-1.303×10^{1}	-
2.879×10^{-6}	1.279×10^{3}	-1.835×10^{2}	-
2.562×10^{-6}	2.720×10^{1}	-5.110×10^{-1}	-
2.143×10^{-6}	8.523×10^{2}	-1.616×10^{2}	-
1.986×10^{-6}	5.114×10^{2}	-7.380×10^{1}	-
1.975×10^{-6}	2.692×10^{1}	-1.269×10^{1}	-
1.818×10^{-6}	2.810×10^{1}	4.312×10^{0}	-
1.485×10^{-6}	2.557×10^{2}	-1.067×10^{2}	-
1.267×10^{-6}	2.664×10^{0}	7.903×10^{-1}	-
1.234×10^{-6}	2.609×10^{1}	-1.038×10^{1}	-
1.058×10^{-6}	2.873×10^{1}	1.339×10^{1}	-
9.825×10^{-7}	1.375×10^{1}	3.719×10^{0}	-
8.997×10^{-7}	2.507×10^{1}	9.231×10^{0}	-
8.965×10^{-7}	2.325×10^{2}	3.330×10^{1}	-
8.928×10^{-7}	6.393×10^{2}	2.111×10^{2}	-
8.427×10^{-7}	2.557×10^{3}	7.690×10^{2}	-
8.273×10^{-7}	2.664×10^{1}	-9.821×10^{0}	-
-	-	-	7.187×10^{-7}

(b) LAGEOS-2.

a_t [rad]	b_t [days]	c_t [days]	d_t [rad]
3.008×10^{-5}	**1.305×10^{1}**	**5.428×10^{-1}**	**-**
1.769×10^{-5}	1.332×10^{1}	-3.978×10^{0}	-
1.376×10^{-5}	1.112×10^{2}	-1.851×10^{1}	-
9.022×10^{-6}	1.339×10^{1}	-2.381×10^{0}	-
6.387×10^{-6}	1.298×10^{1}	-4.274×10^{-1}	-
6.046×10^{-6}	6.393×10^{2}	-2.570×10^{2}	-
5.652×10^{-6}	5.114×10^{2}	2.337×10^{2}	-
3.931×10^{-6}	1.346×10^{1}	5.426×10^{0}	-
3.796×10^{-6}	1.421×10^{2}	-5.366×10^{1}	-
3.762×10^{-6}	1.346×10^{2}	-6.459×10^{1}	-
3.462×10^{-6}	1.291×10^{1}	4.900×10^{0}	-
3.240×10^{-6}	8.848×10^{0}	-1.801×10^{0}	-
2.981×10^{-6}	1.311×10^{1}	-4.434×10^{0}	-
2.980×10^{-6}	1.325×10^{1}	1.653×10^{0}	-
2.962×10^{-6}	1.353×10^{1}	-3.302×10^{-1}	-
2.869×10^{-6}	2.841×10^{2}	7.771×10^{1}	-
2.645×10^{-6}	2.636×10^{1}	8.784×10^{0}	-
2.323×10^{-6}	1.285×10^{1}	-2.475×10^{0}	-
2.280×10^{-6}	8.523×10^{2}	1.658×10^{2}	-
2.267×10^{-6}	4.262×10^{2}	-5.326×10^{1}	-
-	-	-	8.489×10^{-7}

(c) Etalon 1.

a_t [rad]	b_t [days]	c_t [days]	d_t [rad]
4.270×10^{-5}	**2.749×10^{1}**	**-1.361×10^{1}**	**-**
1.006×10^{-5}	2.779×10^{1}	-1.137×10^{1}	-
9.100×10^{-6}	2.720×10^{1}	-1.382×10^{0}	-
4.508×10^{-6}	2.810×10^{1}	4.460×10^{0}	-
3.587×10^{-6}	7.941×10^{0}	-2.432×10^{0}	-
3.219×10^{-6}	9.541×10^{0}	1.061×10^{0}	-
2.924×10^{-6}	2.841×10^{1}	-7.733×10^{0}	-
2.901×10^{-6}	1.375×10^{1}	3.748×10^{0}	-
2.347×10^{-6}	7.083×10^{0}	-9.548×10^{-1}	-
2.215×10^{-6}	2.692×10^{1}	-9.354×10^{-1}	-
2.156×10^{-6}	2.873×10^{1}	8.730×10^{0}	-
2.065×10^{-6}	1.826×10^{2}	-6.033×10^{1}	-
1.924×10^{-6}	9.132×10^{0}	4.479×10^{0}	-
1.922×10^{-6}	3.196×10^{1}	-1.206×10^{1}	-
1.891×10^{-6}	2.390×10^{1}	-6.185×10^{0}	-
1.835×10^{-6}	1.705×10^{2}	-7.353×10^{1}	-
1.783×10^{-6}	2.906×10^{1}	-3.628×10^{0}	-
1.655×10^{-6}	2.664×10^{1}	-5.345×10^{0}	-
1.646×10^{-6}	1.382×10^{1}	4.478×10^{0}	-
1.630×10^{-6}	3.157×10^{1}	-8.724×10^{0}	-
-	-	-	-2.939×10^{-7}

(d) Etalon 2.

a_t [rad]	b_t [days]	c_t [days]	d_t [rad]
6.281×10^{-5}	**2.749×10^{1}**	**-1.362×10^{1}**	**-**
1.684×10^{-5}	2.779×10^{1}	-1.135×10^{1}	-
9.056×10^{-6}	2.720×10^{1}	-1.262×10^{0}	-
6.893×10^{-6}	2.810×10^{1}	4.516×10^{0}	-
6.028×10^{-6}	2.692×10^{1}	1.256×10^{1}	-
4.326×10^{-6}	2.841×10^{1}	-7.669×10^{0}	-
3.889×10^{-6}	2.664×10^{1}	-5.003×10^{0}	-
3.725×10^{-6}	1.375×10^{1}	3.450×10^{0}	-
3.164×10^{-6}	2.873×10^{1}	8.700×10^{0}	-
2.928×10^{-6}	2.636×10^{1}	6.319×10^{0}	-
2.868×10^{-6}	7.916×10^{0}	-3.758×10^{0}	-
2.552×10^{-6}	2.906×10^{1}	-3.596×10^{0}	-
2.340×10^{-6}	1.382×10^{1}	4.739×10^{0}	-
2.338×10^{-6}	2.609×10^{1}	-8.580×10^{0}	-
2.114×10^{-6}	2.939×10^{1}	1.310×10^{1}	-
2.040×10^{-6}	1.360×10^{1}	4.613×10^{0}	-
1.886×10^{-6}	2.583×10^{1}	2.450×10^{0}	-
1.827×10^{-6}	3.196×10^{1}	1.015×10^{1}	-
1.780×10^{-6}	2.973×10^{1}	5.720×10^{-1}	-
1.697×10^{-6}	3.008×10^{1}	-1.227×10^{1}	-
-	-	-	-6.247×10^{-8}

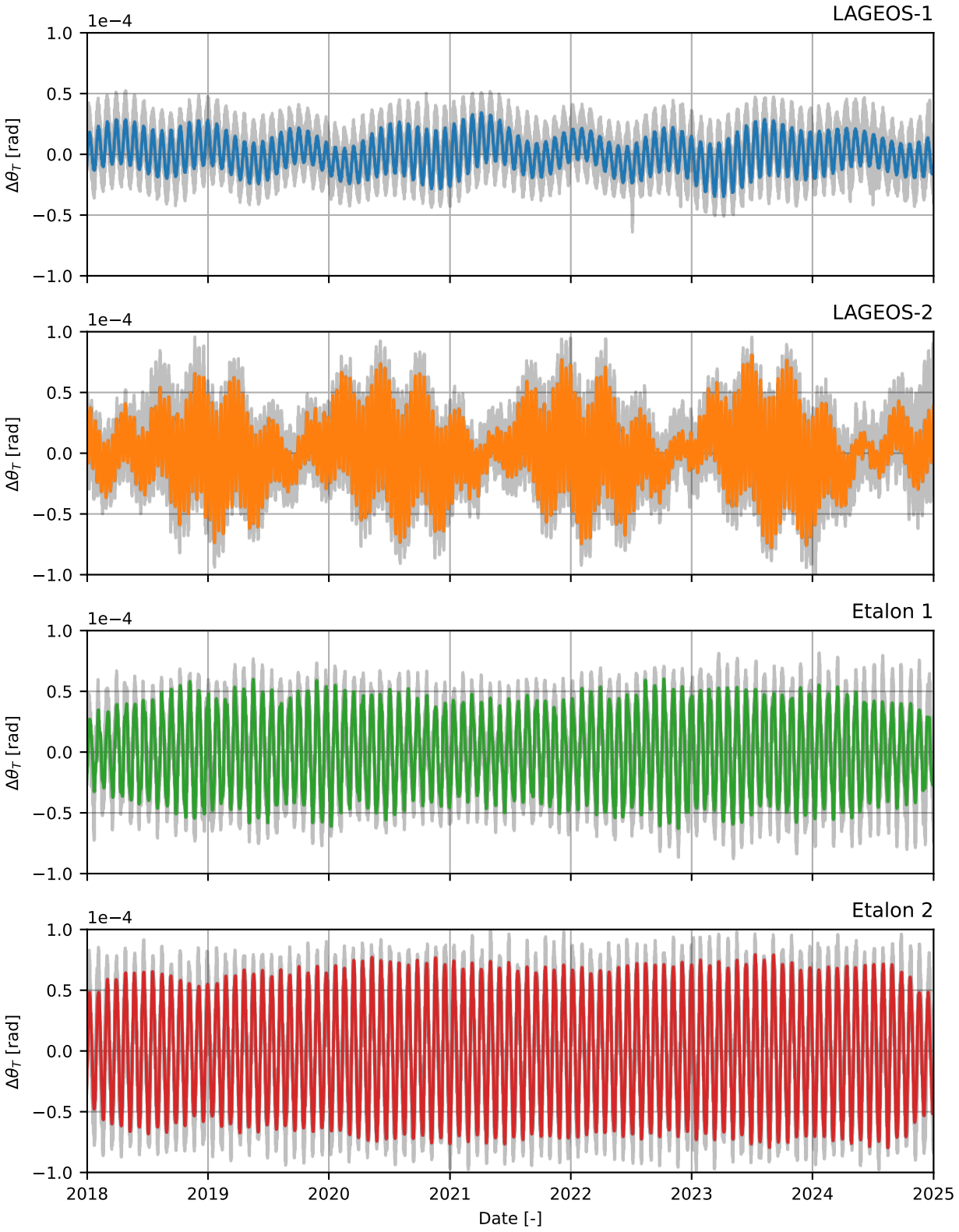


Figure 3.38: FFT-derived time-based along-track position error models for the calibration satellites for the years 2018 to 2025. The along-track position error of the TLEs and the models are presented in grey and colour, respectively.

that there were multiple periodic components in the vicinity of dominant periodic component which, in aggregate, combined to produce overall amplitudes similar to those from the single-component models.

The residual along-track position errors for the calibration satellites following debiasing with the individual FFT-derived time-based models are presented in Figure 3.39. The residuals for all four satellites remained within a $\pm 0.25 \times 10^{-4}$ rad band for almost the entire timespan. Interestingly, towards the start and end times of the window, all four models appeared to deviate from the relatively consistent band with the minimum and maximum residuals reaching over $\pm 0.5 \times 10^{-4}$ rad, in the case of Etalon 2. One potential explanation for this behaviour is the spectral leakage that was introduced in the FFT due to the windowing of the bias signal.

These results highlighted the improved ability of the FFT-derived models to more generally capture bias oscillations, particularly in the case of LAGEOS-2, where the bias model is significantly improved over the single-component counterpart, but also for LAGEOS-1, where the more subtle longer-term oscillations were also suppressed. This was made apparent in Figure 3.40 where, in contrast to the results presented in Figure 3.21, even LAGEOS-2 showed a significant improvement in post-debiasing along-track error.

An extension to these models would include additional error components, such as the radial velocity error, to improve other less-significant components of TLEs. An advantage of using FFTs-derived models is that their fidelity can be tuned through the selection of the number of periodic components, and within that the selection of specific periodic components, and the inclusion of terms for different components of the error, such as specific position and velocity components. Further insight may be available through multi-dimensional FFTs, however it is expected that the primary driver in error dynamics would remain the lunisolar perturbations, as seen through time.

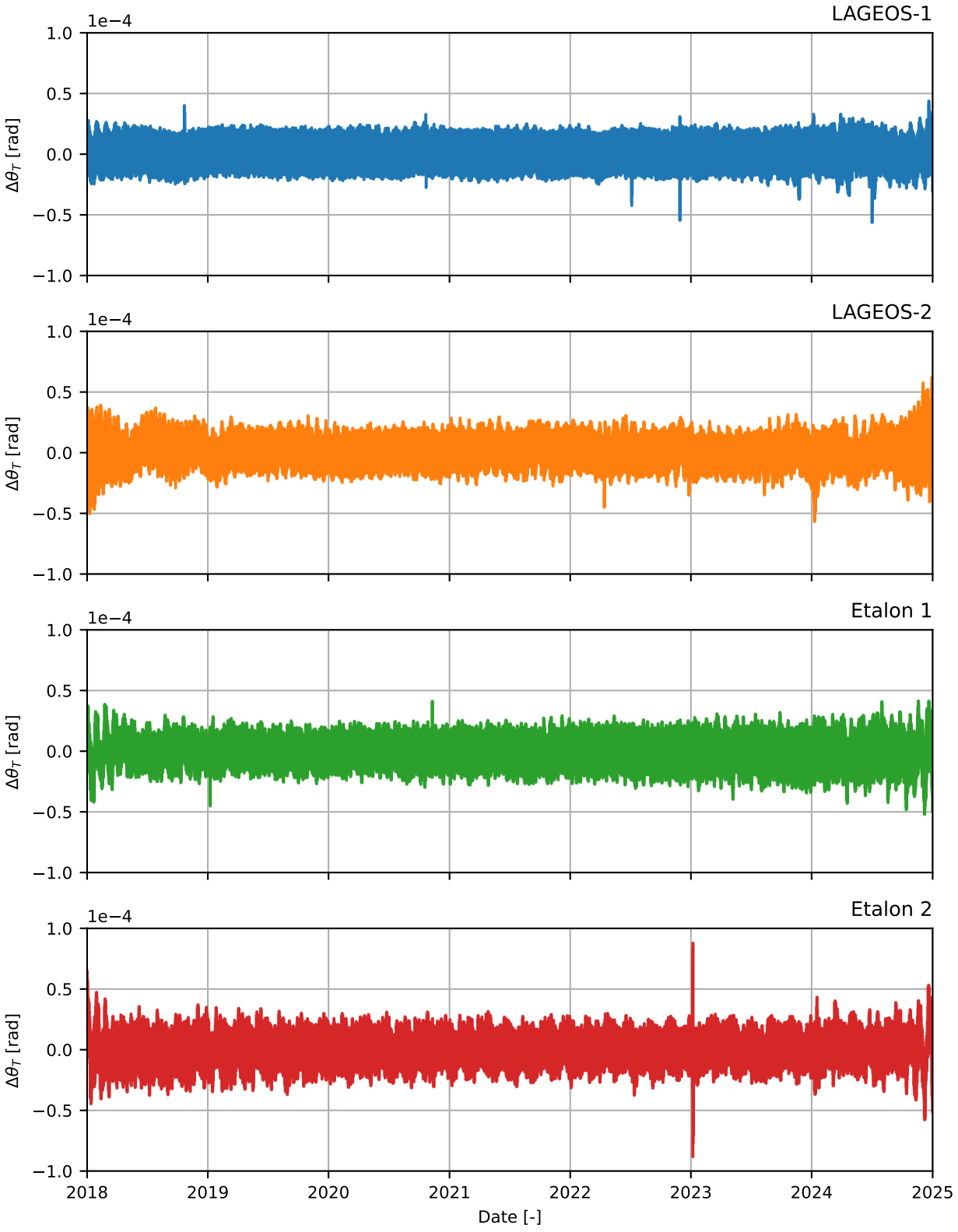
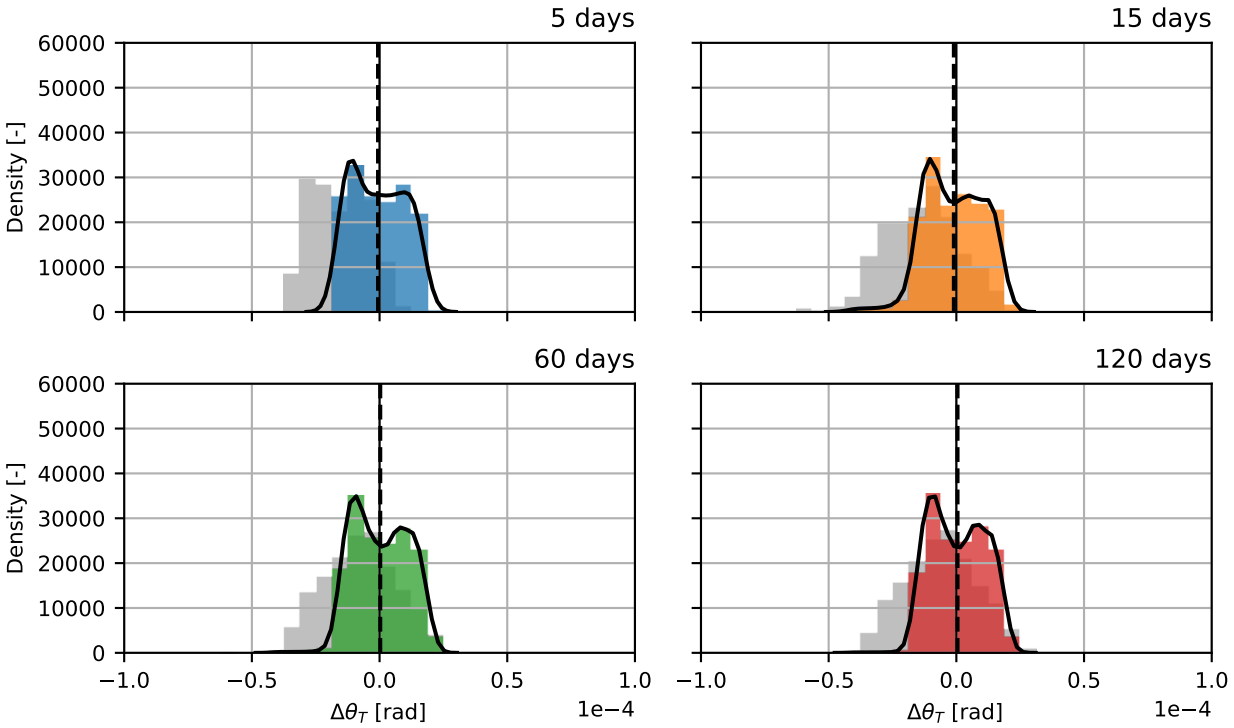
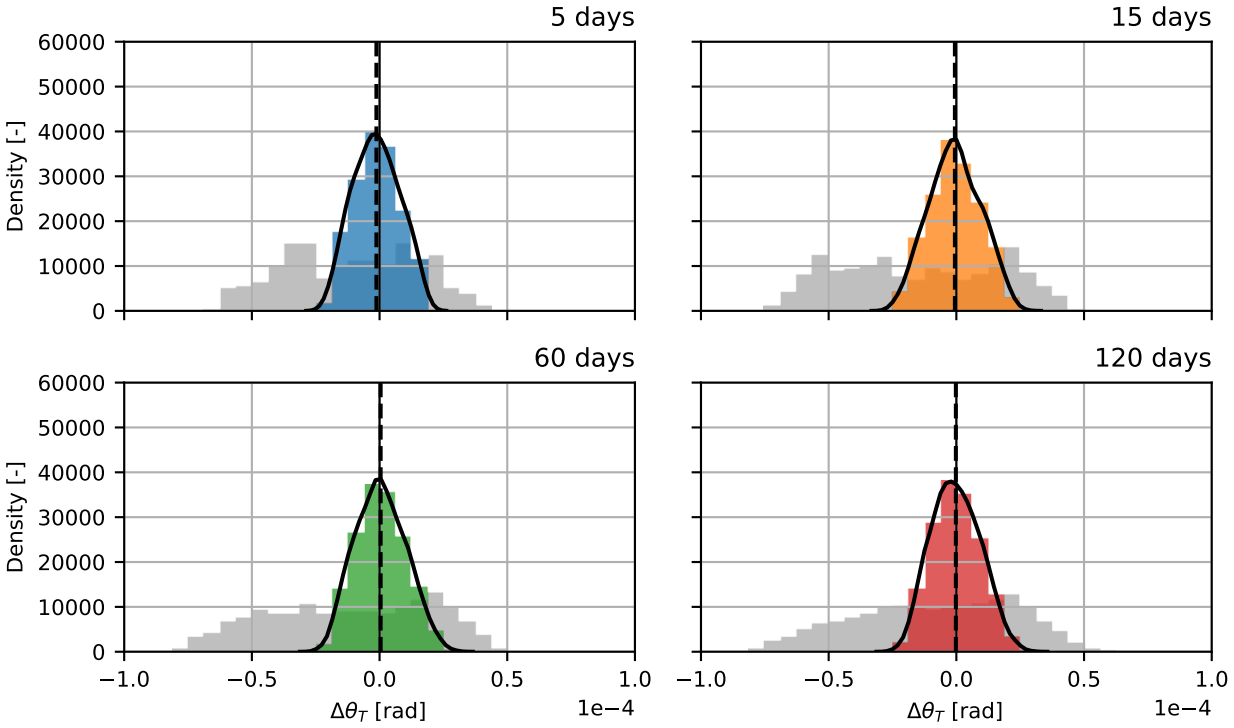


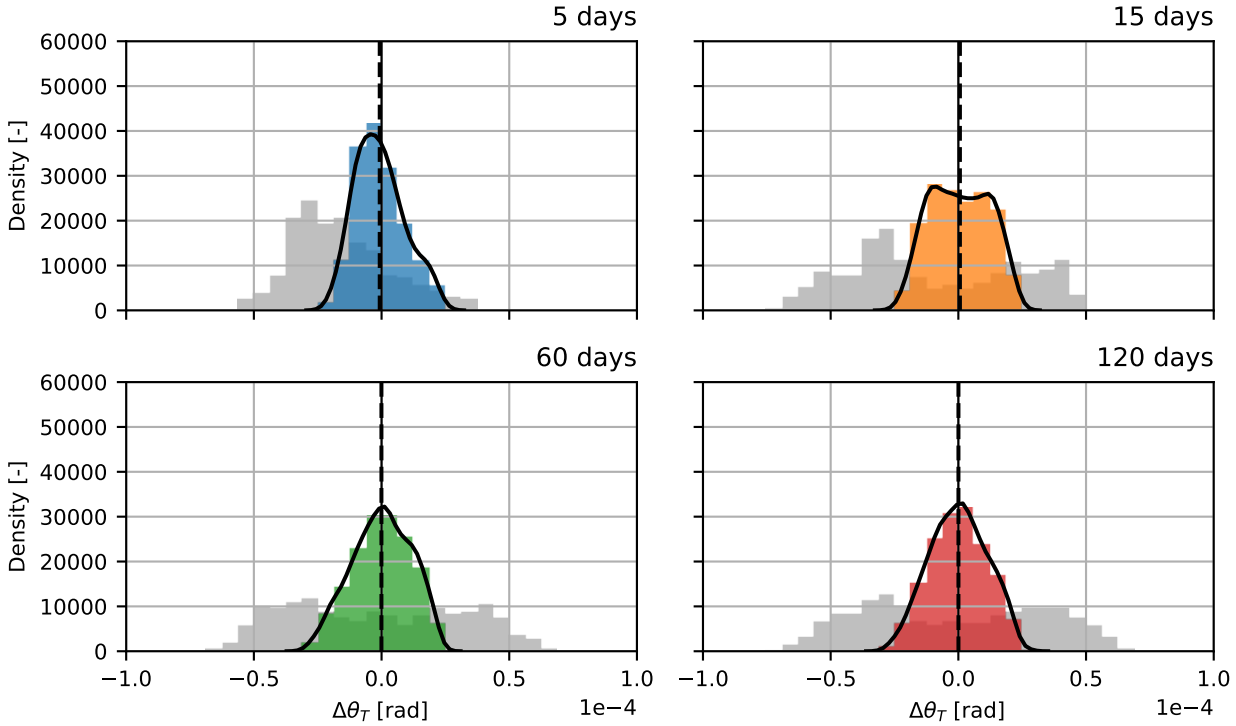
Figure 3.39: Residual along-track position error for the calibration satellites following debiasing with the individual FFT-derived time-based models for the years 2018 to 2025.



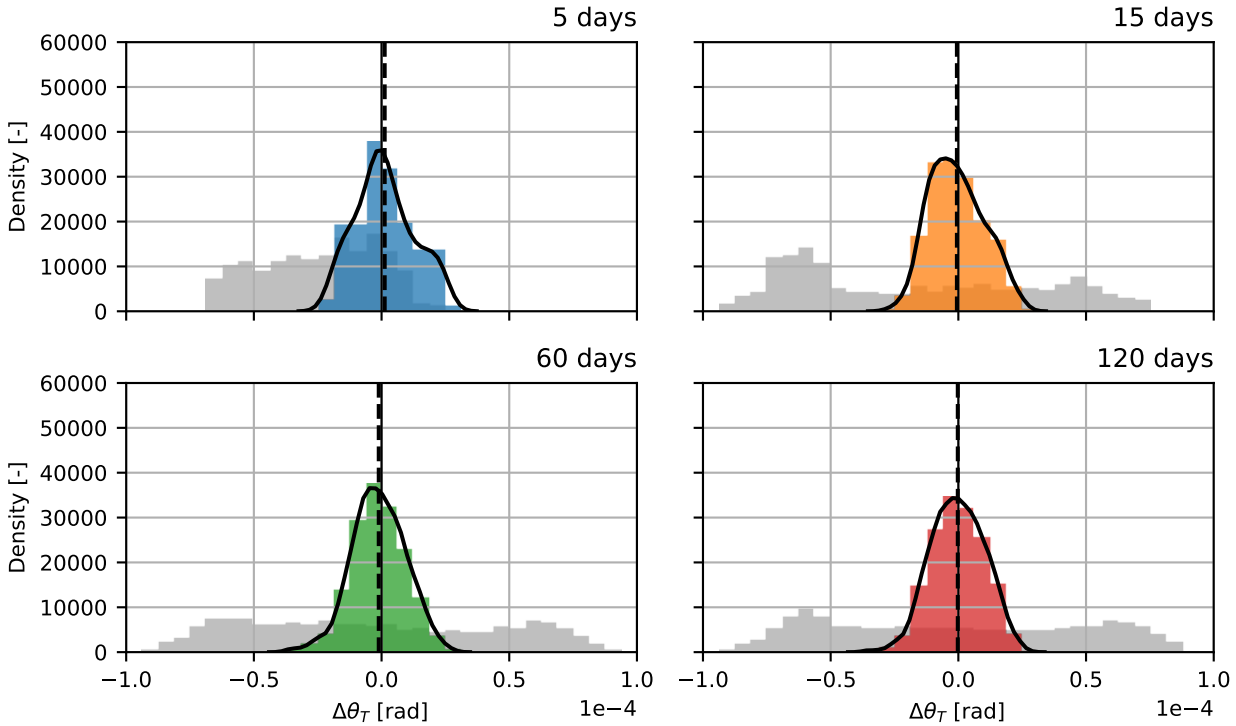
(a) LAGEOS-1.



(b) LAGEOS-2.



(c) Etalon 1.



(d) Etalon 2.

Figure 3.40: Example along-track position error distributions for windows centred on 1st July 2022, following debiasing with individual FFT-derived time-based bias models. The dashed lines indicate the mean error for each window. The original biased distributions from Figure 3.15 are included in grey. Densities are presented due to the different number of samples in each window.

Chapter 4

Pseudo-Orbit Determination in the Absence of Higher-Accuracy Ephemerides

In the previous chapters, it was demonstrated that both P-OD and bias models can be used, either separately or together, to improve the accuracy of TLE-derived pseudo-observed states. Nevertheless, these analyses were predicated on the availability of high-accuracy reference ephemerides. These ephemerides were important for evaluating post-fit P-OD performance but crucial for creating the bias models. Since high-accuracy reference ephemerides are not available publicly for the vast majority of RSOs, alternative methods are required to enable P-OD evaluation and bias model creation for the rest of the TLE catalogue.

In this chapter, the use of TLEs as a proxy for higher-accuracy reference ephemerides, such as the SLR and GNSS pseudo-ranging products used in Chapters 2 and 3, will be investigated by considering how using them as a reference solution can introduce additional error into metrics. This will include evaluation of calibration satellite P-OD fits against TLEs and a demonstration of P-OD for additional RSOs in MEO and GEO. By extension, it will be shown that P-OD-derived states can be used to estimate TLE bias and to create bias models, thereby highlighting how P-OD can be used to enhance the rest of the TLE catalogue. Results in this chapter were presented in [102].

4.1 Two-Line Element Sets as Reference Ephemerides

Due to the intrinsic errors present in TLEs, as discussed in Section 3.2, there are limitations when using TLEs as reference ephemerides for evaluating accuracy. It was decided to investigate how error metrics evaluated with respect to TLEs compare to those evaluated with respect to SP3 ephemerides, to better understand the applicability of using TLEs as an alternative 'ground truth' reference in the absence of higher-quality ephemerides.

The position error geometry for TLEs is presented in Figure 4.1, considering the position errors for a test point, $\mathbf{r}$, with respect to both a given TLE-derived position and an SP3-derived position; and the position error between the TLE-derived and SP3-derived positions:

$$\Delta\mathbf{r}_{\text{TLE}} = \mathbf{r} - \mathbf{r}_{\text{TLE}},$$

$$\Delta\mathbf{r}_{\text{SP3}} = \mathbf{r} - \mathbf{r}_{\text{SP3}},$$

$$\Delta\mathbf{r}_{\text{TLE-SP3}} = \mathbf{r}_{\text{TLE}} - \mathbf{r}_{\text{SP3}}.$$

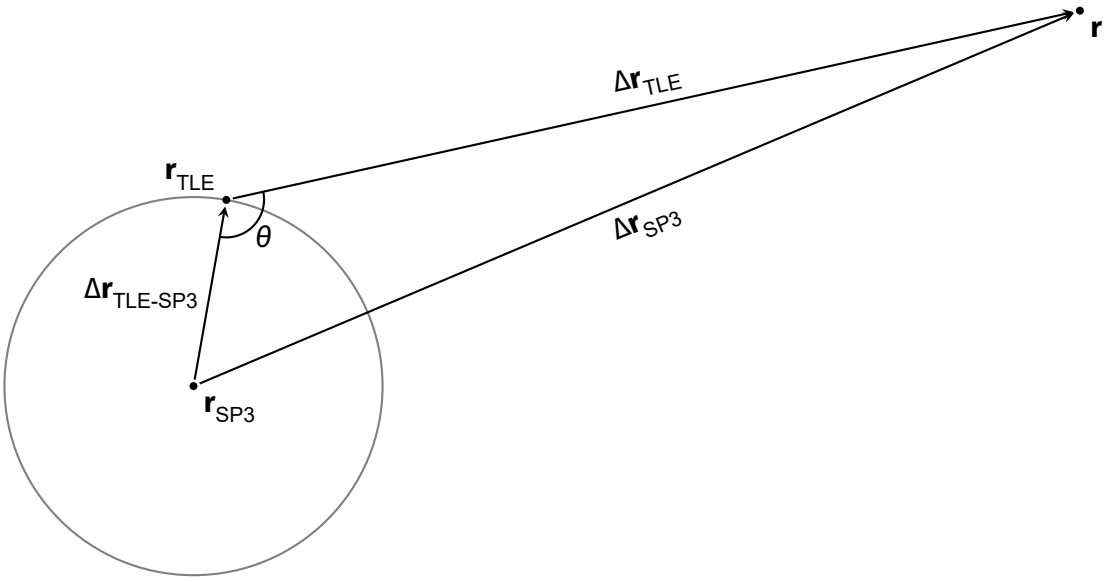


Figure 4.1: TLE-based position error geometry. The three-dimensional geometry can be analysed in two dimensions as the three position vectors are coplanar.

The relationship between the SP3- and TLE-based metrics can be expressed by the cosine rule:

$$||\Delta\mathbf{r}_{\text{SP3}}||^2 = ||\Delta\mathbf{r}_{\text{TLE}}||^2 + ||\Delta\mathbf{r}_{\text{TLE-SP3}}||^2 - 2||\Delta\mathbf{r}_{\text{TLE}}|| \cdot ||\Delta\mathbf{r}_{\text{TLE-SP3}}|| \cos\theta,$$

$$\frac{||\Delta \mathbf{r}_{SP3}||^2}{||\Delta \mathbf{r}_{TLE}||^2} = 1 + \frac{||\Delta \mathbf{r}_{TLE\text{-}SP3}||^2}{||\Delta \mathbf{r}_{TLE}||^2} - \frac{2||\Delta \mathbf{r}_{TLE\text{-}SP3}|| \cos\theta}{||\Delta \mathbf{r}_{TLE}||},$$

$$\frac{||\Delta \mathbf{r}_{SP3}||}{||\Delta \mathbf{r}_{TLE}||} = \sqrt{1 + \frac{||\Delta \mathbf{r}_{TLE\text{-}SP3}||^2}{||\Delta \mathbf{r}_{TLE}||^2} - \frac{2||\Delta \mathbf{r}_{TLE\text{-}SP3}|| \cos\theta}{||\Delta \mathbf{r}_{TLE}||}}.$$

The error between the two metrics can be expressed as a percentage difference:

$$\varepsilon = \frac{||\Delta \mathbf{r}_{SP3}||}{||\Delta \mathbf{r}_{TLE}||} - 1,$$

$$= \sqrt{1 + \frac{||\Delta \mathbf{r}_{TLE\text{-}SP3}||^2}{||\Delta \mathbf{r}_{TLE}||^2} - \frac{2||\Delta \mathbf{r}_{TLE\text{-}SP3}|| \cos\theta}{||\Delta \mathbf{r}_{TLE}||}} - 1.$$

The angles corresponding to the smallest and largest errors between the two metrics can be found by differentiating with respect to angle θ:

$$\frac{\partial \varepsilon}{\partial \theta} = \frac{||\Delta \mathbf{r}_{TLE\text{-}SP3}|| \sin\theta}{||\Delta \mathbf{r}_{TLE}|| \sqrt{1 + \frac{||\Delta \mathbf{r}_{TLE\text{-}SP3}||^2}{||\Delta \mathbf{r}_{TLE}||^2} - \frac{2||\Delta \mathbf{r}_{TLE\text{-}SP3}|| \cos\theta}{||\Delta \mathbf{r}_{TLE}||}}},$$

$$\left.\frac{\partial \varepsilon}{\partial \theta}\right|_{\theta=\hat{\theta}} = 0,$$

$$\sin\hat{\theta} = 0,$$

$$\cos\hat{\theta} = \pm 1.$$

Intuitively, this corresponds to $\hat{\theta} = 0°$ or $180°$, the two cases where all three vectors $\Delta \mathbf{r}_{TLE}$, $\Delta \mathbf{r}_{SP3}$, and $\Delta \mathbf{r}_{TLE\text{-}SP3}$ are collinear, resulting in the following expression for the error bounds:

$$\sqrt{\left(\frac{||\Delta \mathbf{r}_{TLE\text{-}SP3}||}{||\Delta \mathbf{r}_{TLE}||} - 1\right)^2} - 1 \le \varepsilon \le \sqrt{\left(\frac{||\Delta \mathbf{r}_{TLE\text{-}SP3}||}{||\Delta \mathbf{r}_{TLE}||} + 1\right)^2} - 1. \tag{4.1}$$

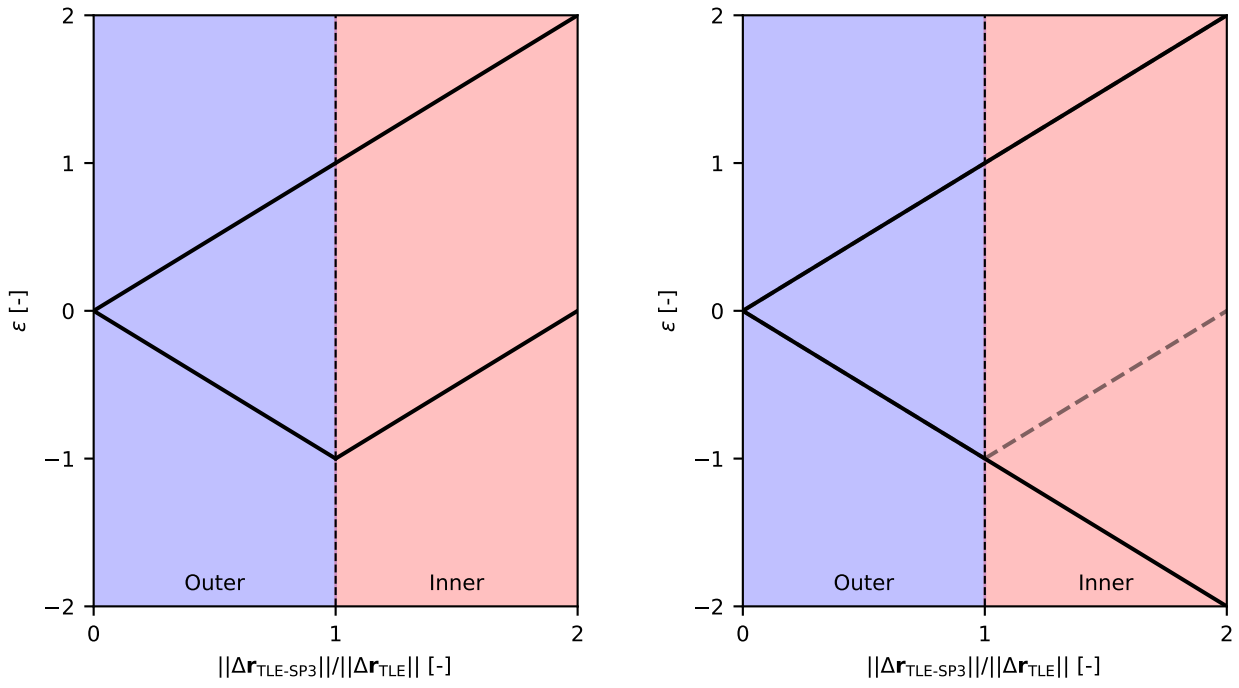
The error bound expression contains two regimes with different behaviours:

$$\frac{||\Delta \mathbf{r}_{TLE\text{-}SP3}||}{||\Delta \mathbf{r}_{TLE}||} - 2 \le \varepsilon \le \frac{||\Delta \mathbf{r}_{TLE\text{-}SP3}||}{||\Delta \mathbf{r}_{TLE}||},$$

$$-\frac{||\Delta \mathbf{r}_{TLE\text{-}SP3}||}{||\Delta \mathbf{r}_{TLE}||} \le \varepsilon \le \frac{||\Delta \mathbf{r}_{TLE\text{-}SP3}||}{||\Delta \mathbf{r}_{TLE}||}, \tag{4.2}$$

corresponding to the test point, $\mathbf{r}$, lying either inside or outside of the grey circle illustrated in Figure 4.1, respectively. The 'inner' regime corresponds to the scenario where the TLE- and SP3-based metrics are smaller than error between the TLE- and SP3-derived positions (i.e. $||\Delta\mathbf{r}_{\text{TLE}}|| < ||\Delta\mathbf{r}_{\text{TLE-SP3}}||$ and $||\Delta\mathbf{r}_{\text{SP3}}|| < ||\Delta\mathbf{r}_{\text{TLE-SP3}}||$), and vice versa.

The error bound expression can be simplified to Equation (4.2) by considering only the 'outer' regime. For the 'inner' regime, this results in a physically-inconsistent lower percentage error bound due to the implication of either metric being negative. However, considering the 'outer' regime provides a conservative estimate of the TLE-based metric's accuracy and aids further analysis. The full and simplified models are illustrated in Figure 4.2.



(a) Full.

(b) Simplified.

Figure 4.2: Error bound models, illustrating how the simplified model does not fully capture the error behaviour and produces a physically-inconsistent lower bound for the 'inner' regime.

Equation (4.2) can be used to find a threshold for the TLE-based error, above which a certain percentage error is guaranteed:

$$||\varepsilon|| \leq \frac{||\Delta\mathbf{r}_{\text{TLE-SP3}}||}{||\Delta\mathbf{r}_{\text{TLE}}||},$$

$$||\Delta\mathbf{r}_{\text{TLE}}||_{\text{tol}} > \frac{||\Delta\mathbf{r}_{\text{TLE-SP3}}||}{\varepsilon_{\text{tol}}},$$

where ε_{tol} is a prescribed allowable percentage error between the SP3- and TLE-based metrics. For example, for a tolerance of 10 %, the TLE-based position error would need to be at least ten times larger than the position error between the SP3 and TLE states, $||\Delta\mathbf{r}_{\text{TLE-SP3}}||$, to guarantee a 10 % level of agreement between the two metrics.

One challenge with guaranteeing a certain level of agreement between the two metrics is the dependence on knowing an upper bound of the position error of the TLE itself (i.e. $||\Delta\mathbf{r}_{\text{TLE-SP3}}||$). If we consider a typical TLE to have an upper position error bound in the order of kilometres, this would mean that the TLE-based position error would need to exceed tens of kilometres to satisfy, for example, a 10 % level of agreement.

The relationship between the two metrics, and estimation of the TLE position error bound, can be investigated using Monte Carlo (MC) methods. State vectors can be generated randomly in the vicinity of the TLE- and SP3-derived states and then evaluated against both. The 3σ bound for $||\Delta\mathbf{r}_{\text{TLE-SP3}}||$, denoted as $||\Delta\mathbf{r}_{\text{TLE-SP3}}||_{3\sigma}$, can then be calculated numerically from the sampled metrics by finding the bounds that encapsulate approximately 99.7 % of the samples.

The error metric bounds for the calibration satellites, calculated through MC analysis, are presented in Table 4.1. The bounds were as expected: the smallest for LAGEOS-1, at just under 0.5 km, and increasing to the largest for Etalon 2, at just over 2 km. The errors bounds matched the peak position errors seen for each of the calibration satellites in Section 3.2. Furthermore, the angular error bounds, calculated by normalising the position error bound by the average semi-major axis of each satellite, matched the peak angular along-track position errors presented in Figure 3.7.

Table 4.1: Estimated error bounds for the calibration satellites for the years 2018 to 2025.

Satellite	Error Bound (3σ) [km]	Error Bound (3σ) [rad]
LAGEOS-1	4.320×10^{-1}	3.520×10^{-5}
LAGEOS-2	7.154×10^{-1}	5.882×10^{-5}
Etalon 1	1.581×10^{0}	6.199×10^{-5}
Etalon 2	2.193×10^{0}	8.602×10^{-5}

The relationship between the two metrics is presented in Figure 4.3, highlighting the symmetry of the estimated bounds and the lower floor of error in both metrics, caused by the intrinsic error

in the TLEs themselves, which cannot be ignored. Figure 4.4 illustrates the large TLE-based errors required to guarantee a certain level of agreement between the metrics. For example, 10 km for 25 %, increasing to 100 km for 2.5 %, in the case of Etalon 2.

The full error bound model, Equation (4.1), is presented in Figure 4.5 alongside samples from the MC analyses of the calibration satellites. It can be seen that the results remained within the theorised error bounds, in both the 'inner' and 'outer' regimes. However, when using the fixed estimated error bounds from Table 4.1, a significant number of 'inner' regime samples lied outside of the lower bound as shown by Figure 4.6. In effect, some of the samples which should have been in the 'outer' regime were calculated as if they were in 'inner' regime, due to the fixed estimated error bound being larger than the actual intrinsic TLE error for the given sample. This highlights how estimation of the percentage error within the 'inner' regime can be problematic when using a fixed error bound estimate.

The analysis based on the geometry presented in Figure 4.1 includes a major simplification: that the position error of a given TLE with respect to the true state of the RSO is isotropic. However, as discussed in Section 3.2, TLEs have a highly anisotropic error behaviour, where along-track position error typically dominates with its significantly larger magnitude than the other components of the position error. The analysis presented above, therefore, is a conservative estimate which bounds the 'true' ellipsoidal error bounds (assuming a multi-dimensional Gaussian distribution). The effect that this can have on the TLE-based metric and its relationship with the SP3-based metric is illustrated in Figure 4.7. This figure highlights how the applicability of the isotropic model can vary with geometry: the model is more applicable when the error between the TLE and SP3 positions is primarily aligned with the major-axis of the ellipse rather than the minor-axis of the ellipse.

The elliptical error bound model, or ellipsoidal in the three dimensional case, would be more representative of the true behaviour of the TLE-based metric, with respect to the SP3-based metric, however the additional complexity of the geometry introduces additional challenges. The bound, $||\Delta\mathbf{r}_{\text{TLE-SP3}}||$, would not constant with respect to orientation with this model, introducing additional angular dependencies when estimating the amount of error between the metrics. Future work should investigate the applicability of an ellipsoidal model for assessing the error between SP3- and TLE-based metrics and, furthermore, the behaviour for each individual RTN component.

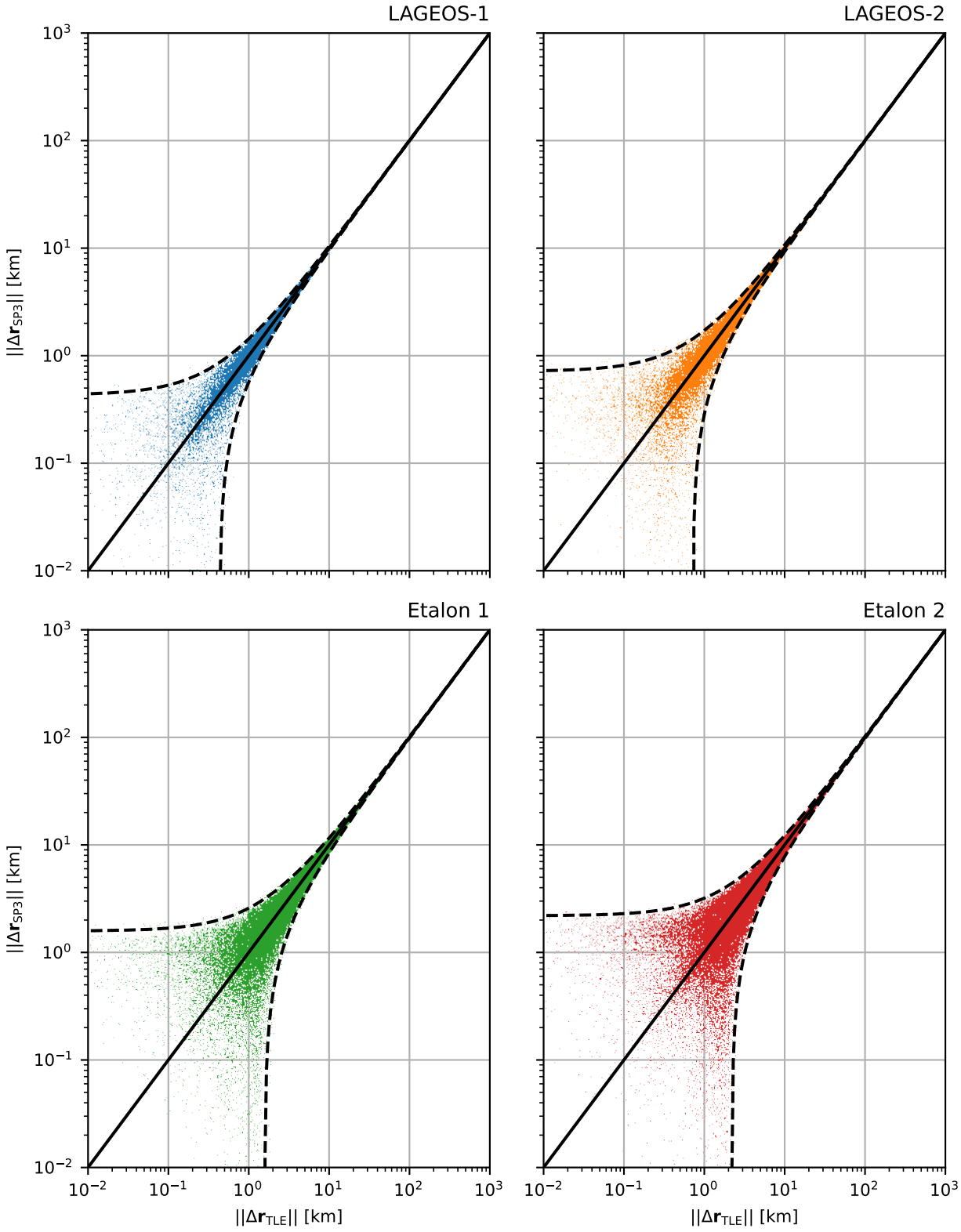


Figure 4.3: Relationship between the SLR- and TLE-based metrics for the calibration satellites. The solid line represents equal values of error, while the dashed lines represent the bounds from Table 4.1.

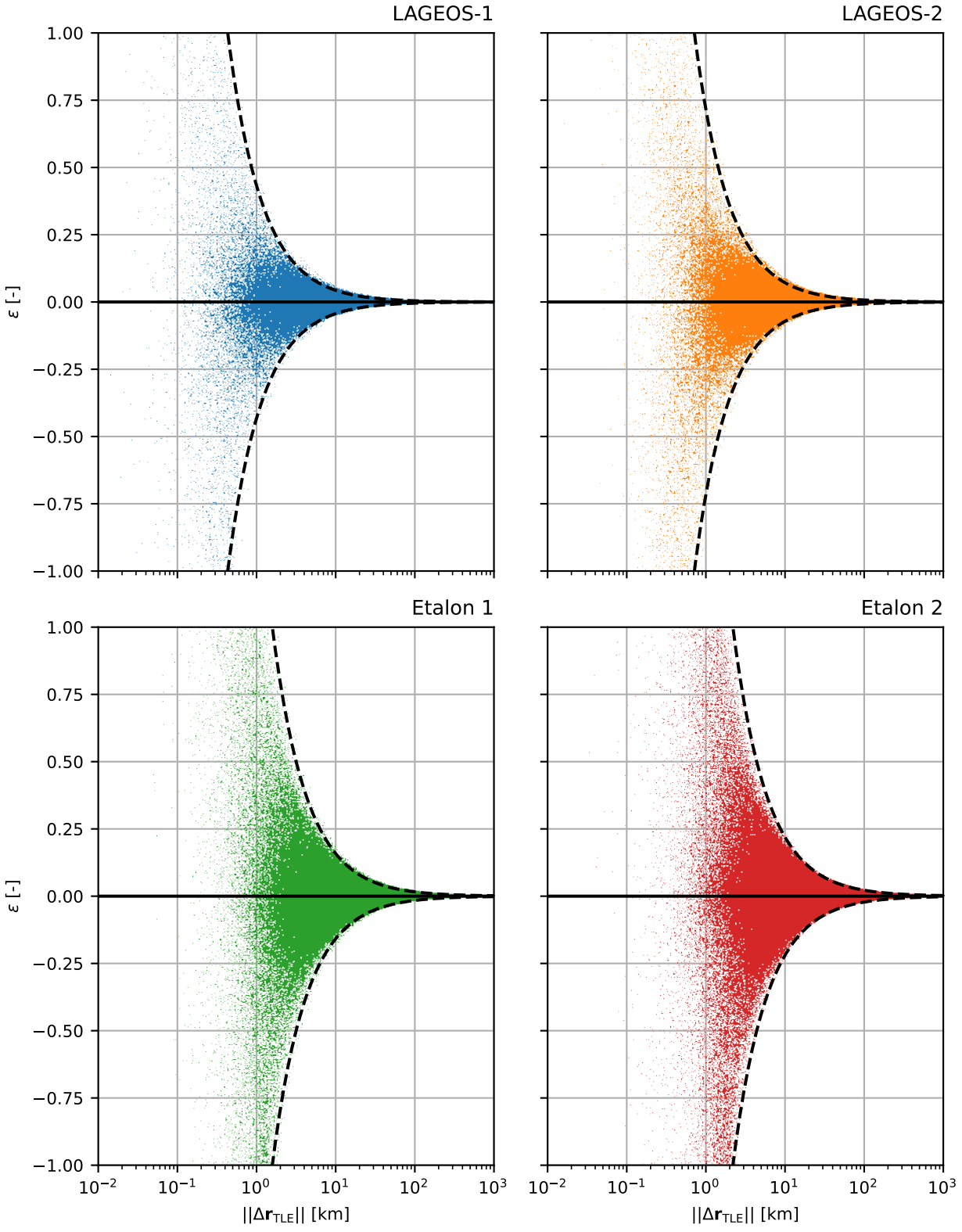


Figure 4.4: Percentage error between the SLR- and TLE-based metrics for the calibration satellites as a function of the TLE-based metric. The solid line represents equal values of error, while the dashed lines represent the bounds from Table 4.1.

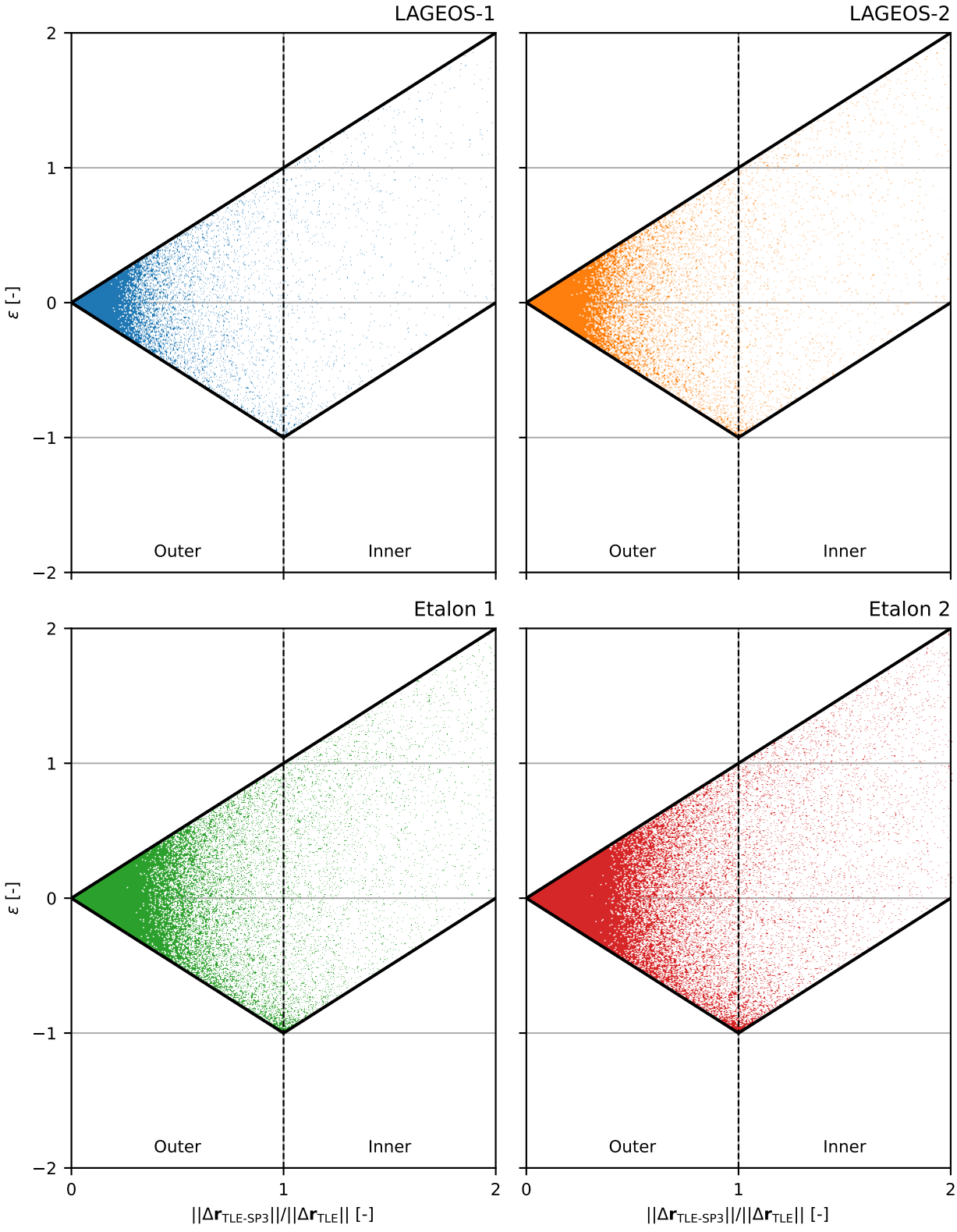


Figure 4.5: Percentage error between the SLR- and TLE-based metrics for the calibration satellites as a function of the ratio between the intrinsic TLE error and the TLE-based metric. The solid lines represent the full error bounds from Equation (4.1).

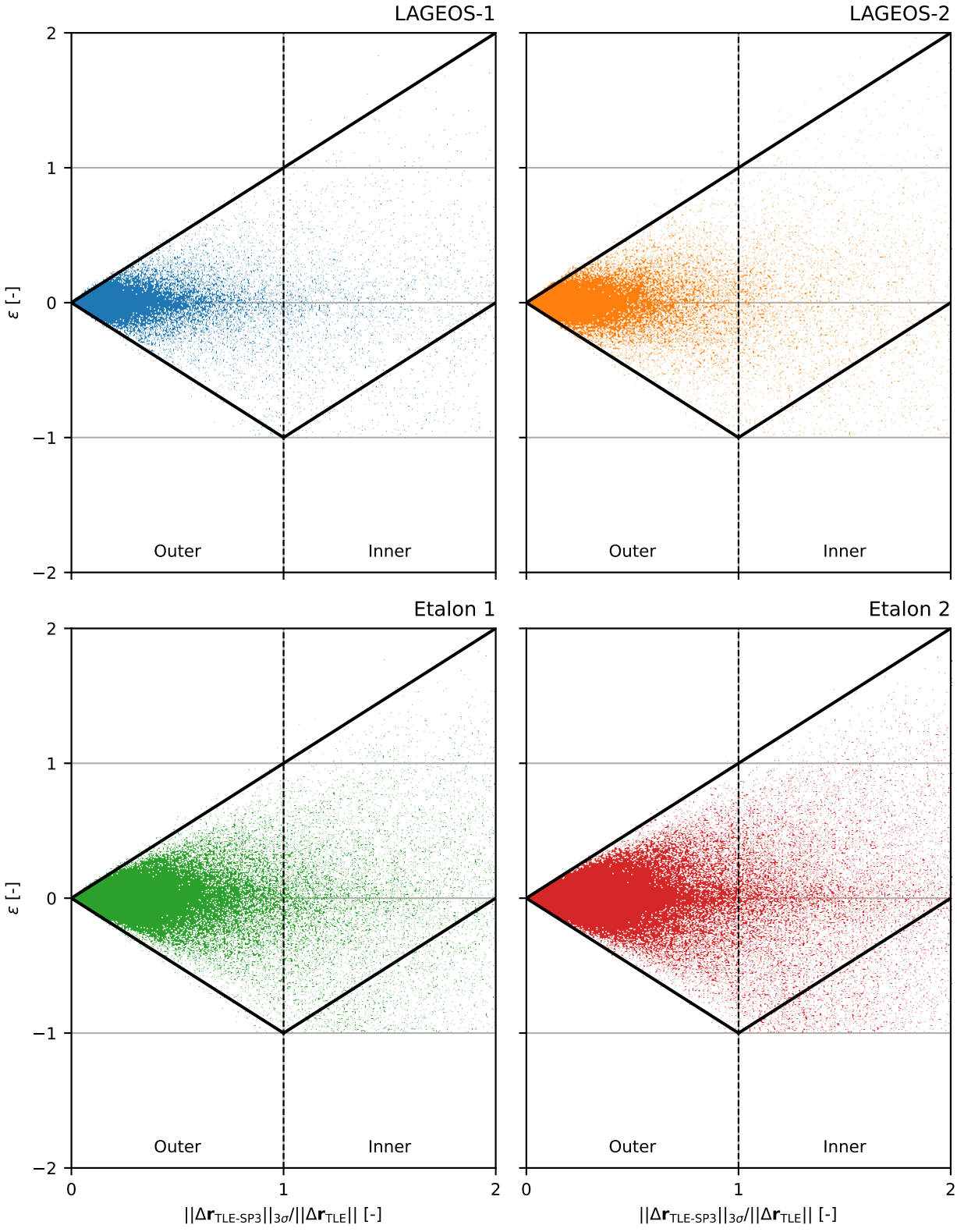
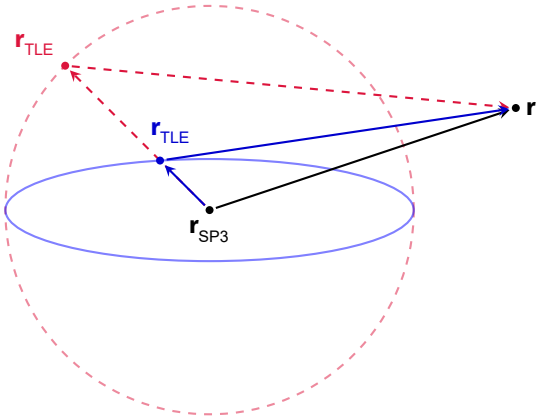
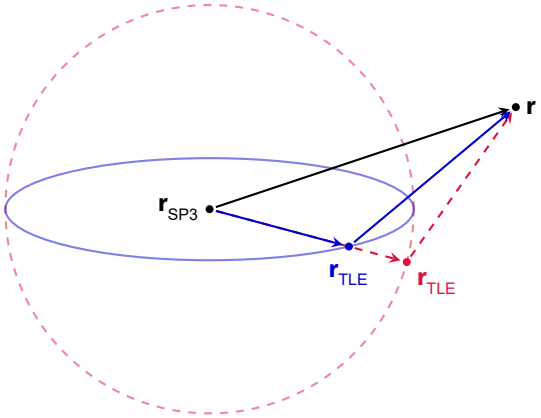


Figure 4.6: Percentage error between the SLR- and TLE-based metrics for the calibration satellites as a function of the ratio between the bounds from Table 4.1 and the TLE-based metric. The solid lines represent the full error bounds from Equation (4.1).

This analysis demonstrates the major issue when using TLEs as reference ephemerides: the position errors with respect to the TLEs need to be excessively large to guarantee a reasonable level of agreement with the true position error. For TLE-based P-OD, this would mean that only very large post-fit errors can be compared quantitatively with any level of confidence. It could be argued that comparing such inaccurate P-OD fits is not worthwhile in the first instance. Nevertheless, the metric can be used still for qualitative comparisons as low TLE-based position errors can be associated with proximity to the true state.



(a) Minor-axis case.



(b) Major-axis case.

Figure 4.7: A comparison of the elliptical (blue) and circular (red) error bound models. It can be seen that the difference in the TLE-based error metrics will be much larger for the minor-axis case than the major-axis case.

4.2 Evaluation of Pseudo-Orbit Determination Accuracy with Two-Line Element Sets

The biased and debiased P-OD fits presented in Sections 3.1 and 3.5 were re-evaluated, using the TLE-based position error metric instead of the original SLR-based metric, to investigate whether using TLEs as reference ephemerides could be used to evaluate the results of TLE-based P-OD. The results of using TLEs as the post-fit reference are presented in Figures 4.8 to 4.11.

The general features of the sweeps were preserved with the TLE-based error metric: for short-term fits, particularly the biased fits on Etalon 1 and 2, the importance of fit window midpoint and pseudo-observation quality remained highly visible as vertical banding; meanwhile, for the long-term fits, the same behaviour was seen where increasing fit window size beyond 30 days resulted in a significant reduction in post-fit error. Additionally, other features noted from the SLR-based analysis were preserved, such as the decrease in fit error towards the end of the year seen for LAGEOS-2 due to the decreasing amplitude of the along-track TLE bias.

The difference between the SLR- and TLE-based metrics are presented in Figures 4.12 to 4.15. In almost all cases, the TLE-based metric was approximately the same or larger than the SLR-based metric. Interestingly vertical banding is present in the error metric difference, particularly in the case of both biased and debiased short-term fits, and biased long-term fits on Etalon 1 and 2. The debiased long-term fits for all of the test satellites show limited banding. An explanation for this behaviour could be that these represent the most accurate fits, relative to the SLR ephemerides, and, therefore, the TLE-based error metric is primarily capturing only the TLE error, resulting in a consistent difference throughout the year.

Several additional objects, referred to as the test satellites and listed in Table 4.2, were considered for investigating whether or not P-OD could be conducted effectively on satellites for which high-quality reference ephemerides are not available. These included Navstar 1 and Navstar 2, the first two GPS satellites, in MEO; and Astra 1E and Astra 1H, two telecommunications satellites in near-GEO. Examination of the TLE series for each of these objects suggested no evidence of manoeuvres, allowing analysis to focus on perturbation mismodelling in the TLEs themselves.

Table 4.2: Approximate orbital elements of the test satellites (1st January 2022).

Name	NORAD ID	Semi-major axis [km]	Eccentricity [-]	Inclination [deg]
Navstar 1	19751	26,800	0.008	63.3
Navstar 2	20026	26,500	0.050	63.8
Astra 1E	23686	42,600	0.001	8.40
Astra 1H	25785	42,500	0.001	7.12

Modelling SRP was necessary for the test satellites due to their significantly higher area-to-mass ratios when compared to the calibration satellites from Table 2.2. The masses, areas, and reflection coefficient, C_R, of each satellite were not known accurately; therefore, the P-OD solver estimated the overall combined SRP coefficient, $C_R A/m$. The small perturbing force from SRP, combined with the large uncertainties present in the TLEs, raised questions regarding the observability of this parameter, particularly for smaller duration fit windows.

The post-fit evaluation window was extended from 30 days to 90 days for the test satellite fits, due to the change from the SLR-derived reference ephemerides to TLEs and concerns surrounding the impact of TLE bias on fit evaluation. By extending the post-fit window, more cycles of TLE bias would be included, ideally reducing its impact on the position RMSE and improving the consistency of the results. This assumed that the monthly bias variation still applied to the TLEs of these satellites.

The quality of the test satellites' TLEs was evaluated to establish a benchmark for each satellite, as in Section 3.1. For the test satellites, TLE quality was evaluated relative to future TLEs. The results are presented in Figure 4.16. Navstar 1 and 2, and Astra 1H showed periodic behaviour in error throughout the year, albeit each with different structures and periods. In the case of Navstar 1, the errors remained below 50 km throughout the year. In the case of Navstar 2 and Astra 1H, the errors oscillated in a band from 20 to 80 km. Astra 1E had errors which remained around 20 km, apart from a period between July and September where the error grew significantly to 90 km.

The results of fits on the test satellites are presented in Figure 4.17. In general, fits on the four satellites showed large domains where the fit performance met or exceeded their respective benchmarks, suggesting that the fits were successfully reducing the prediction errors with respect to propagating the TLEs directly. Increasing the fit window size was generally beneficial, although the error behaviour was more complex than for the calibration satellites.

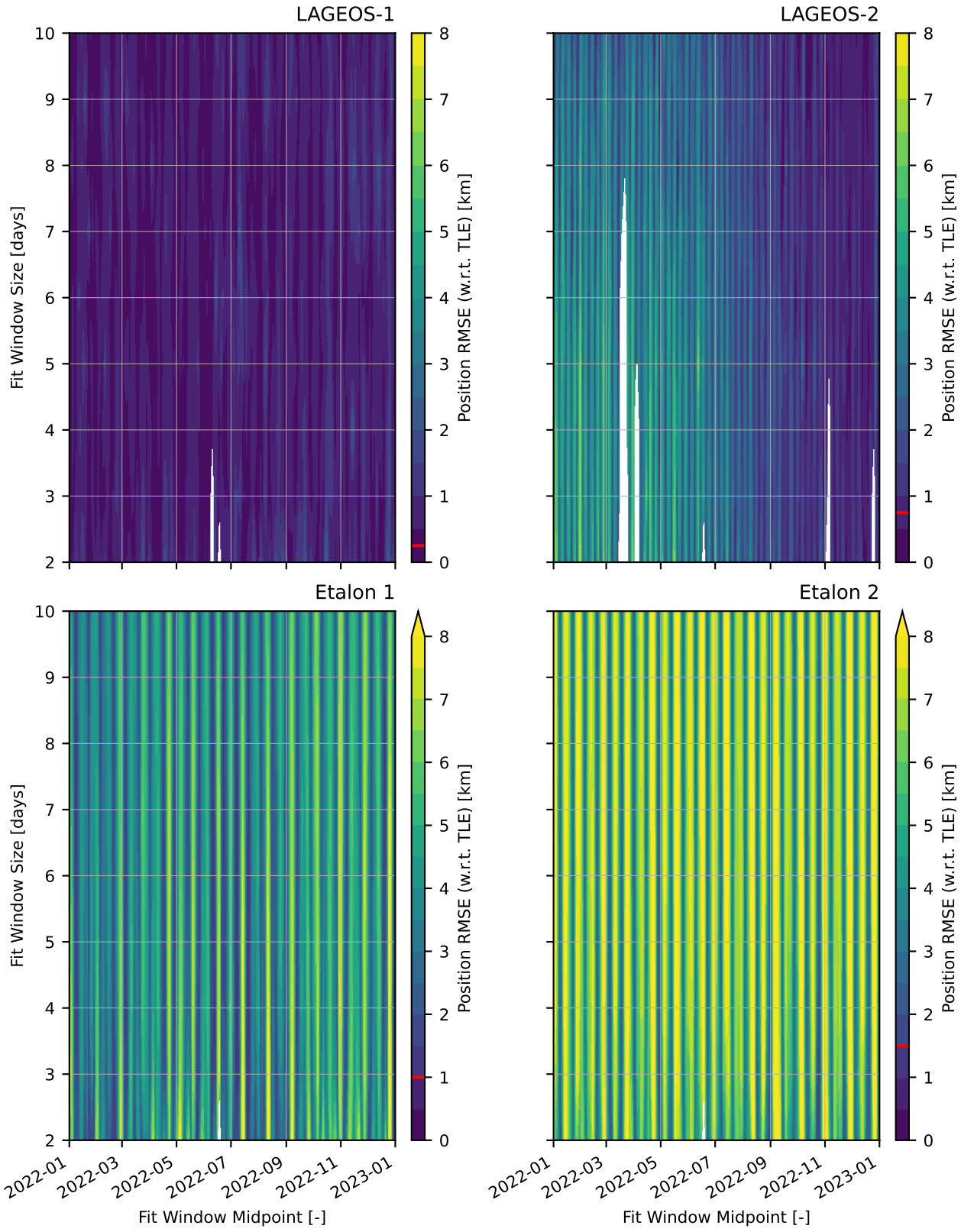


Figure 4.8: Position RMSE, relative to TLEs, during the 30 days post-fit for short-term biased fits of the calibration satellites. The red marker in the colour bar indicates the RMSE baseline derived from TLEs. Note that white regions indicate failed cases due to a lack of TLEs within the window.

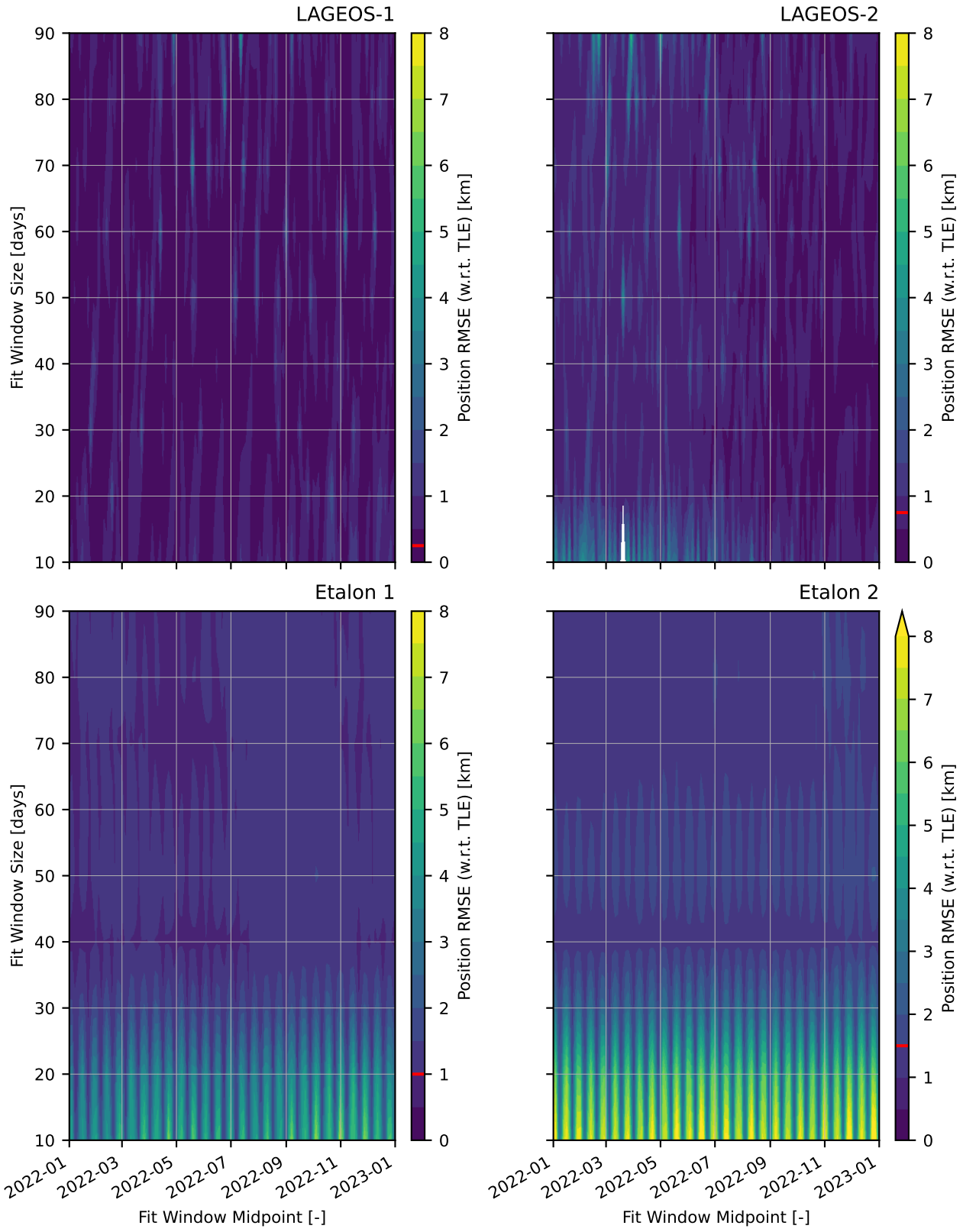


Figure 4.9: Position RMSE, relative to TLEs, during the 30 days post-fit for long-term biased fits of the calibration satellites. The red marker in the colour bar indicates the RMSE baseline derived from TLEs. Note that white regions indicate failed cases due to a lack of TLEs within the window.

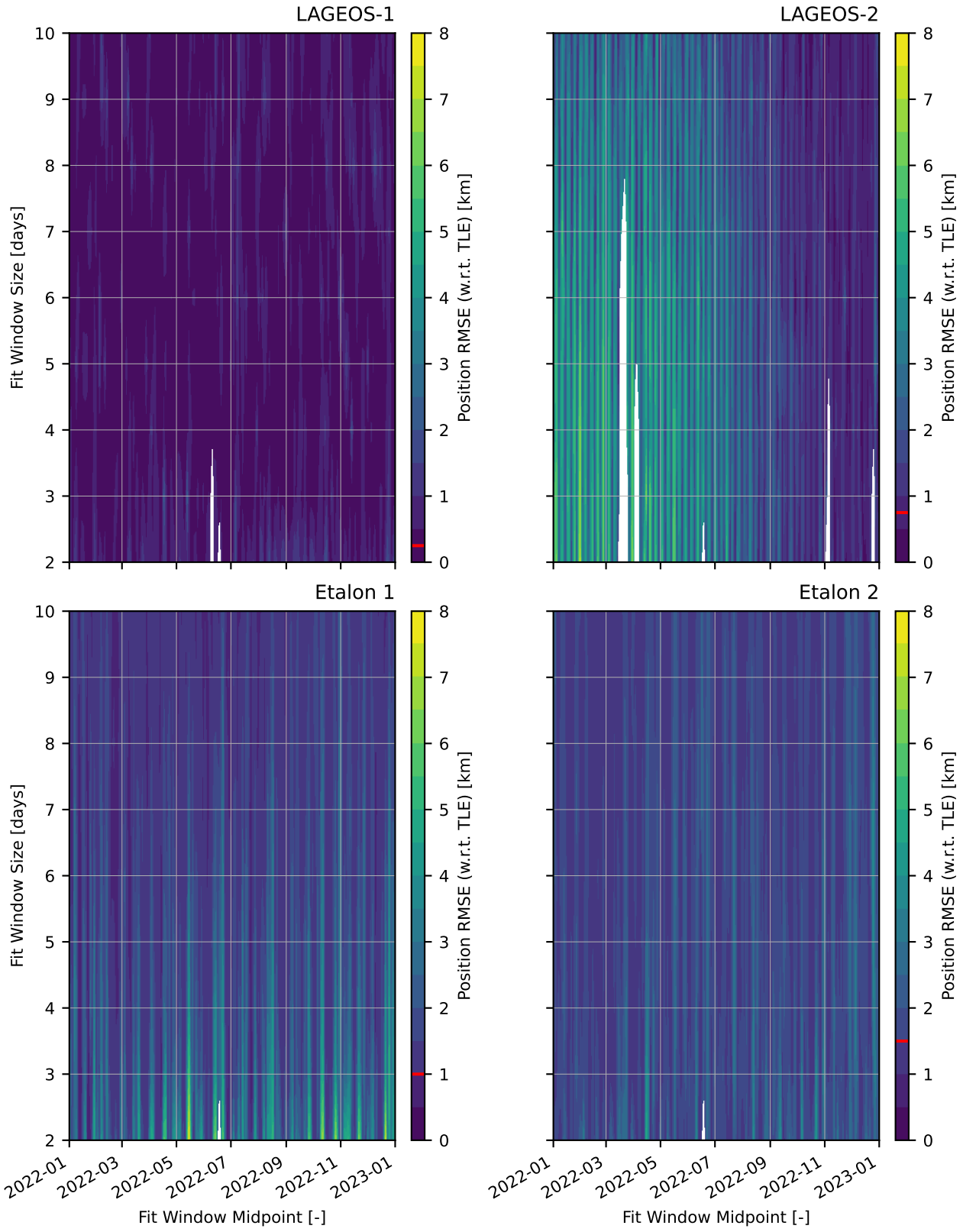


Figure 4.10: Position RMSE, relative to TLEs, during the 30 days post-fit for short-term debiased fits of the calibration satellites. The red marker in the colour bar indicates the RMSE baseline derived from TLEs. Note that white regions indicate failed cases due to a lack of TLEs within the window.

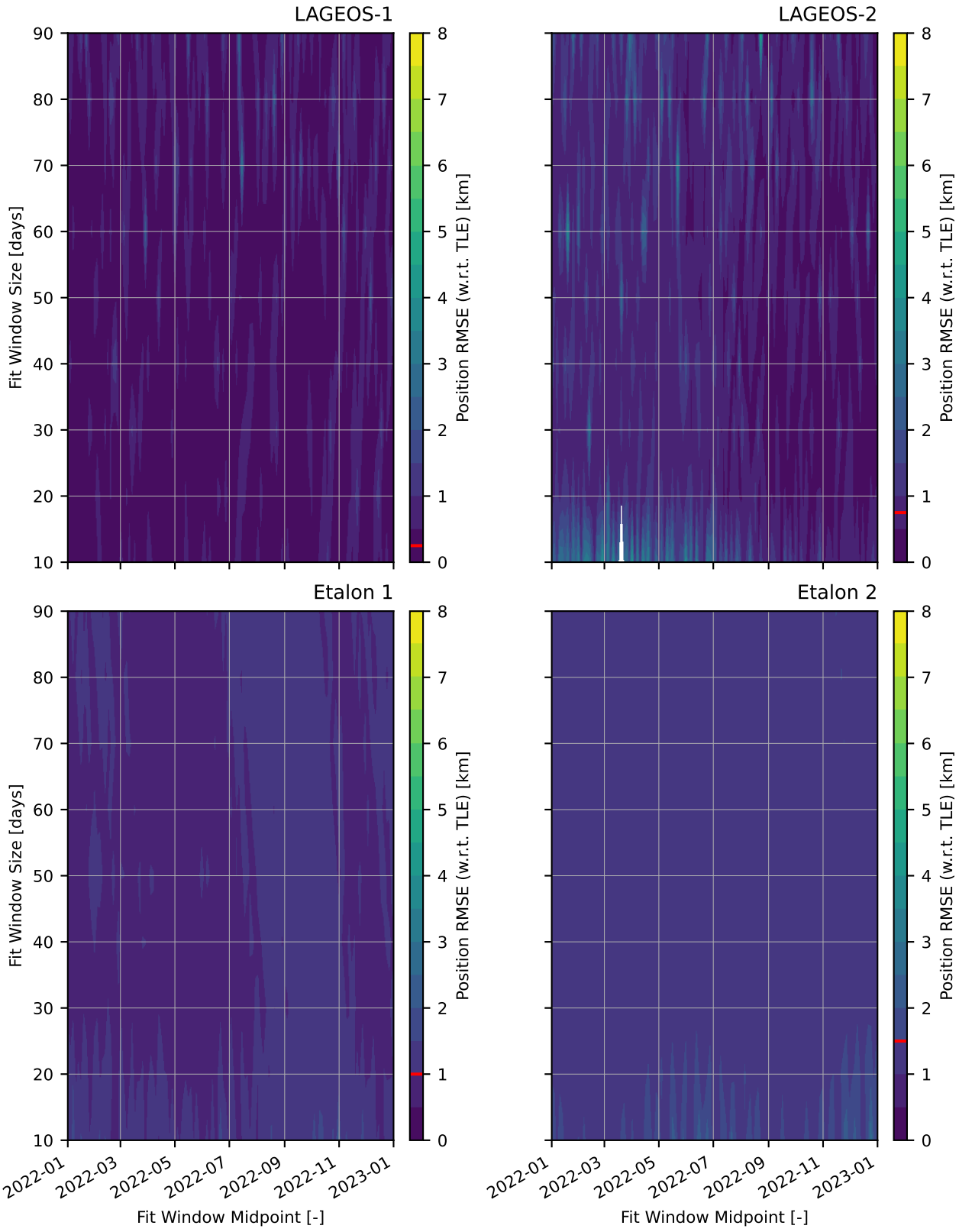


Figure 4.11: Position RMSE, relative to TLEs, during the 30 days post-fit for long-term debiased fits of the calibration satellites. The red marker in the colour bar indicates the RMSE baseline derived from TLEs. Note that white regions indicate failed cases due to a lack of TLEs within the window.

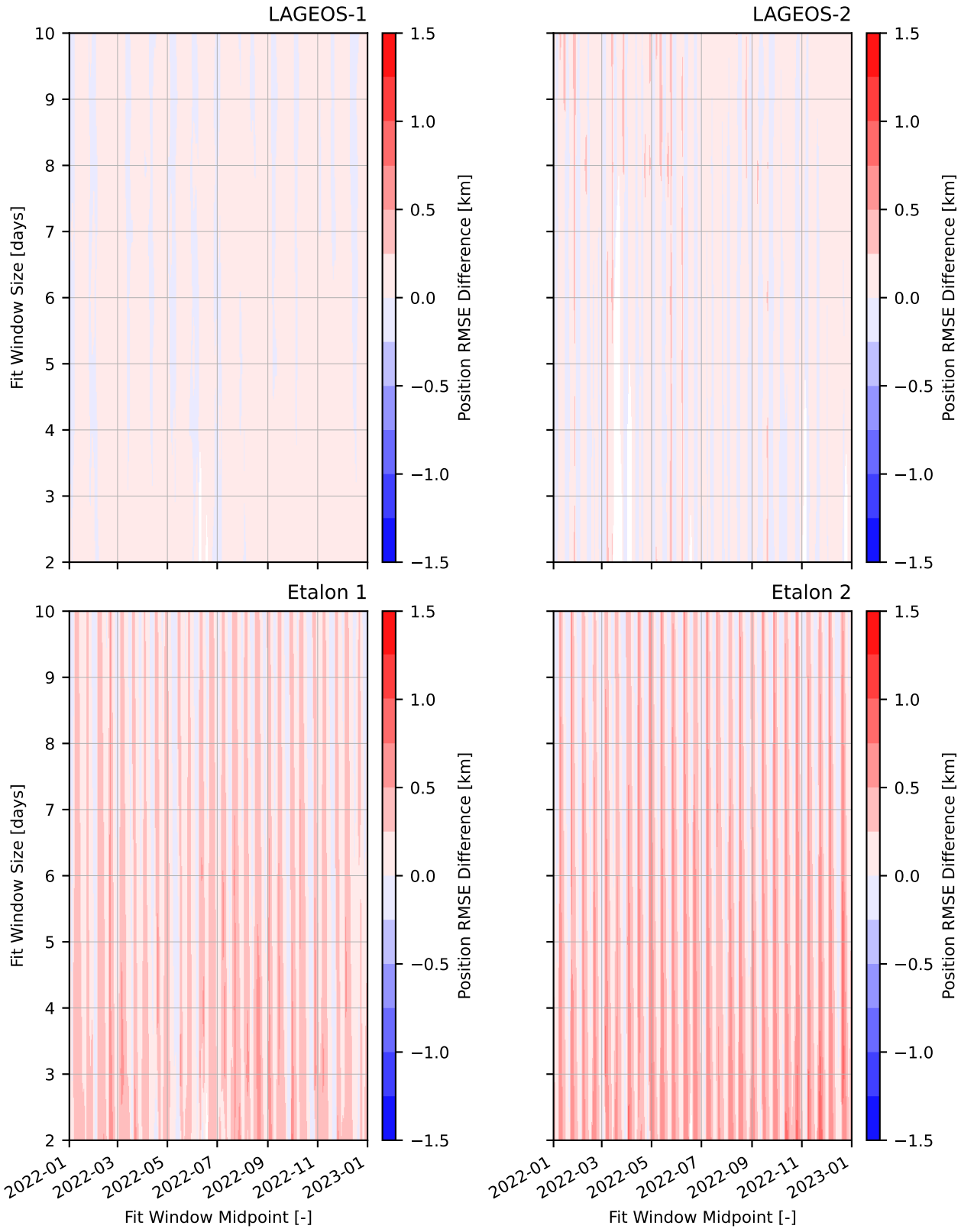


Figure 4.12: Difference between the TLE- and SLR-based position RMSE, during the 30 days post-fit for short-term biased fits of the calibration satellites. Positive values correspond to a larger TLE-based position RMSE.

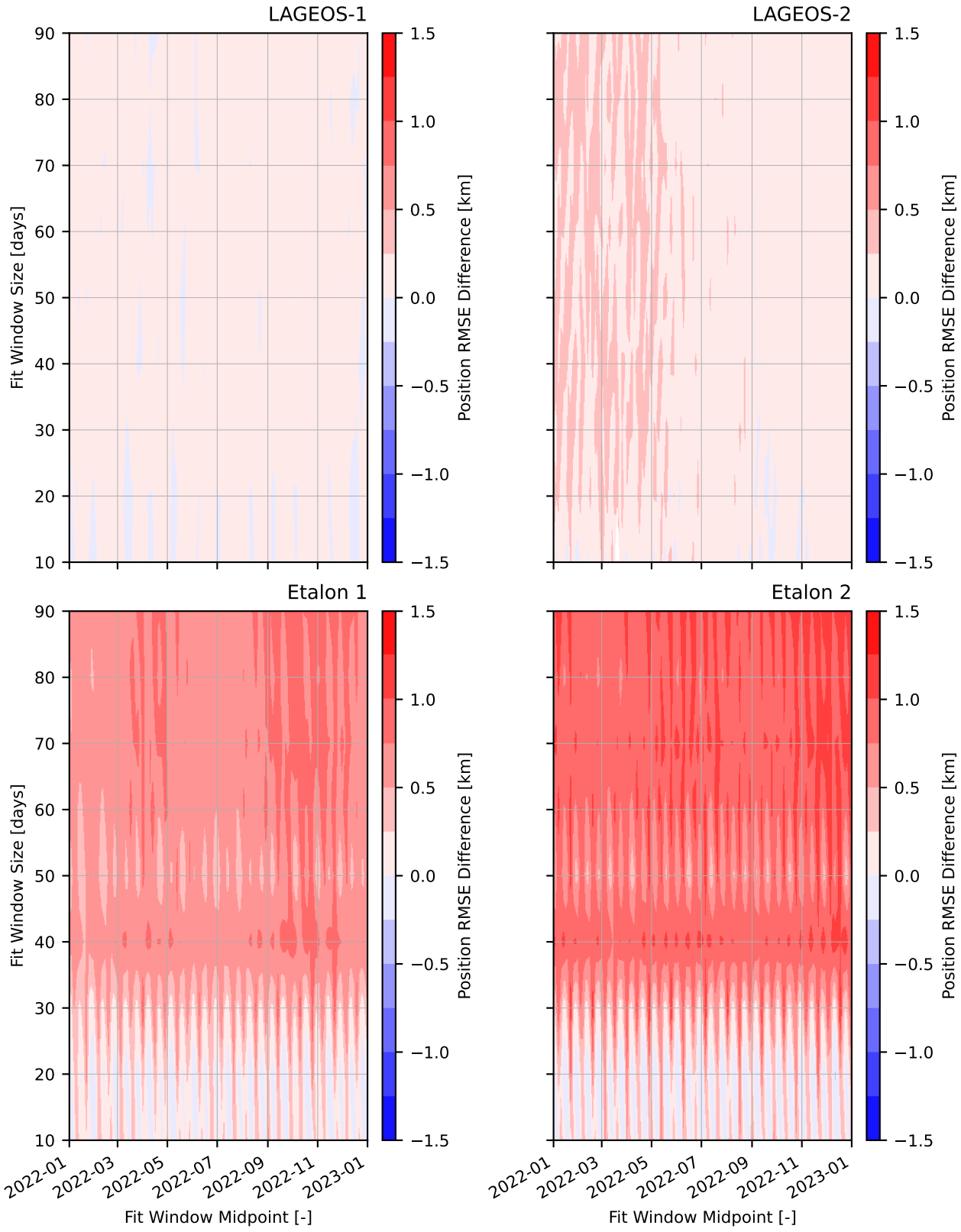


Figure 4.13: Difference between the TLE- and SLR-based position RMSE, during the 30 days post-fit for long-term biased fits of the calibration satellites. Positive values correspond to a larger TLE-based position RMSE.

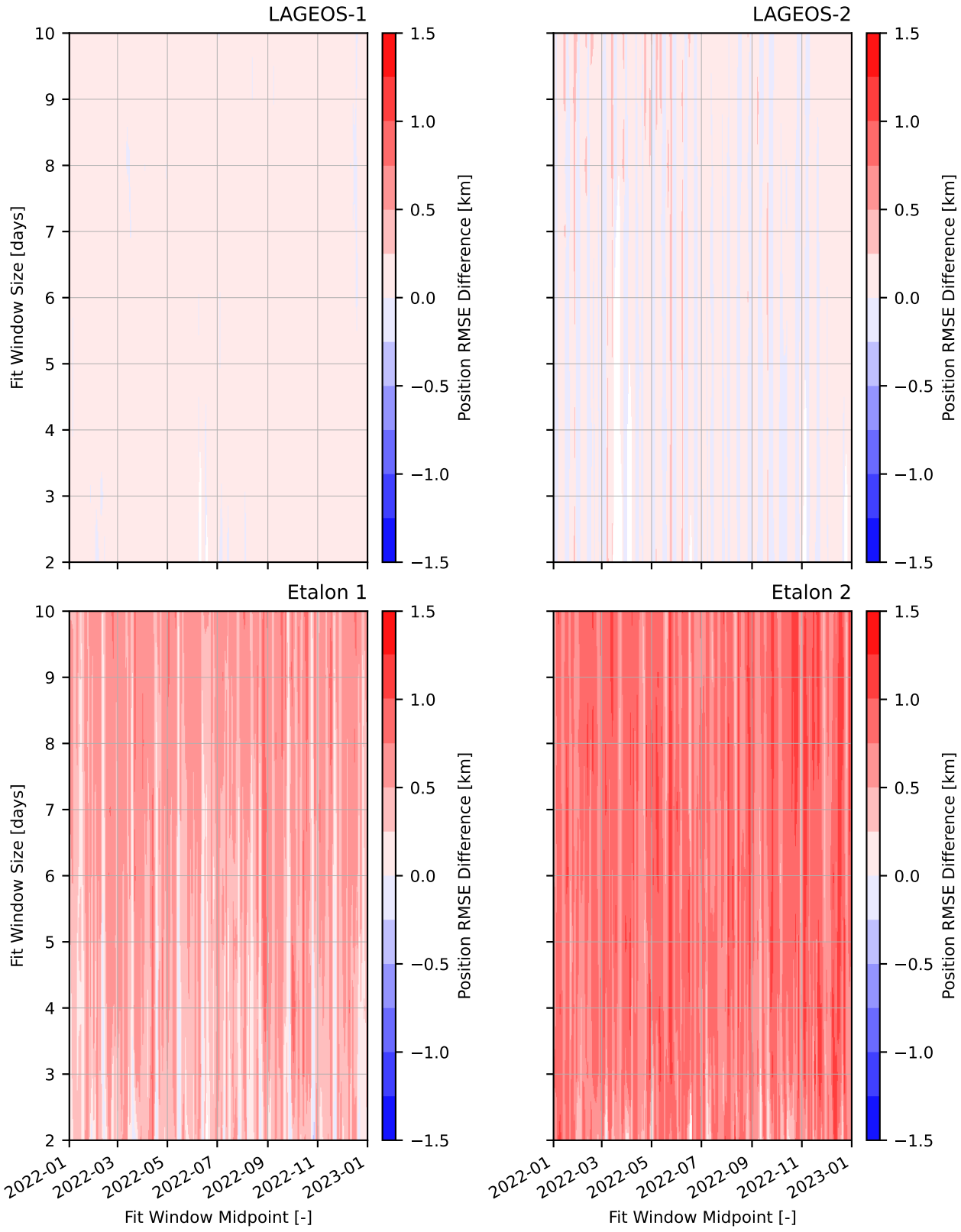


Figure 4.14: Difference between the TLE- and SLR-based position RMSE, during the 30 days post-fit for short-term debiased fits of the calibration satellites. Positive values correspond to a larger TLE-based position RMSE.

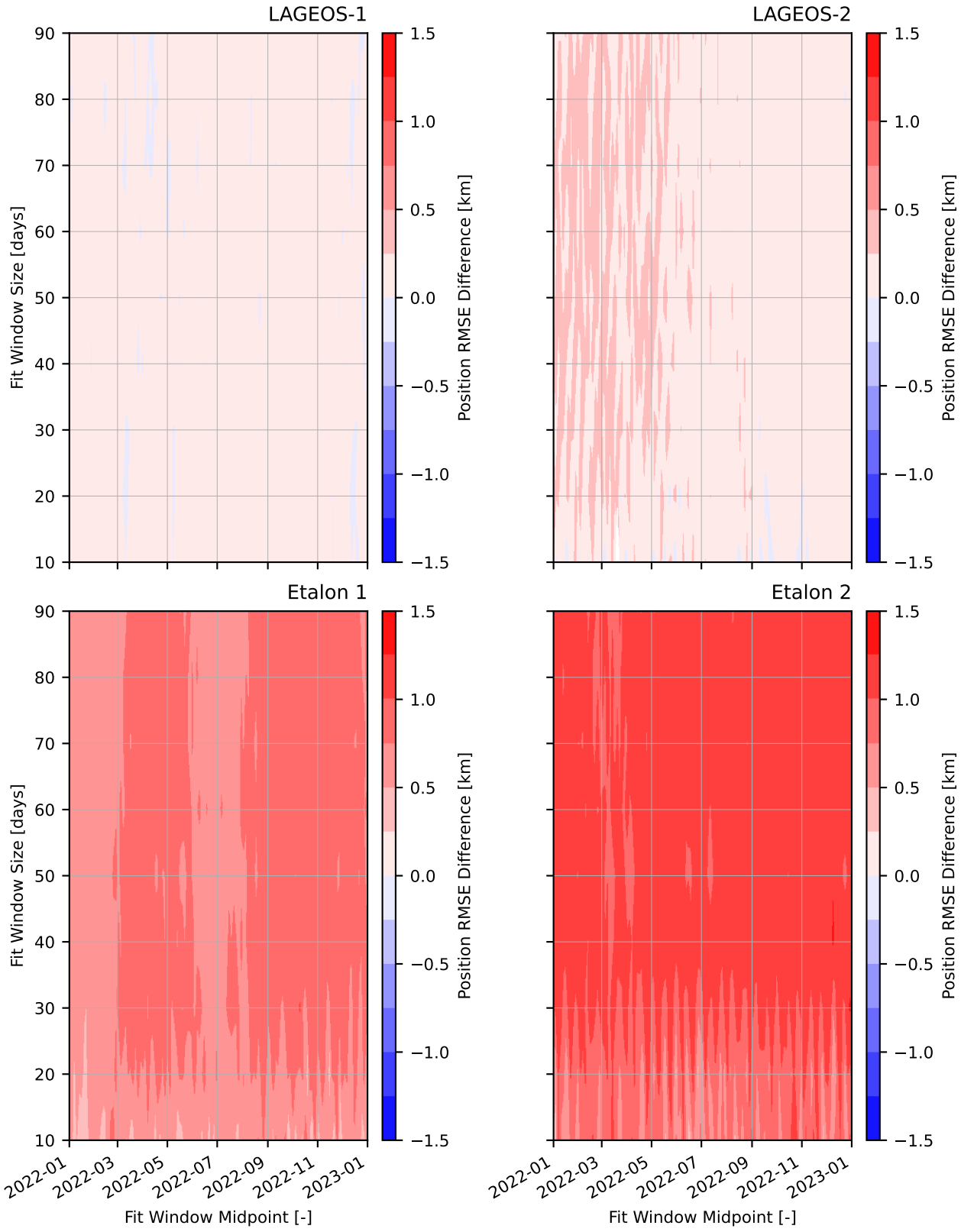


Figure 4.15: Difference between the TLE- and SLR-based position RMSE, during the 30 days post-fit for long-term debiased fits of the calibration satellites. Positive values correspond to a larger TLE-based position RMSE.

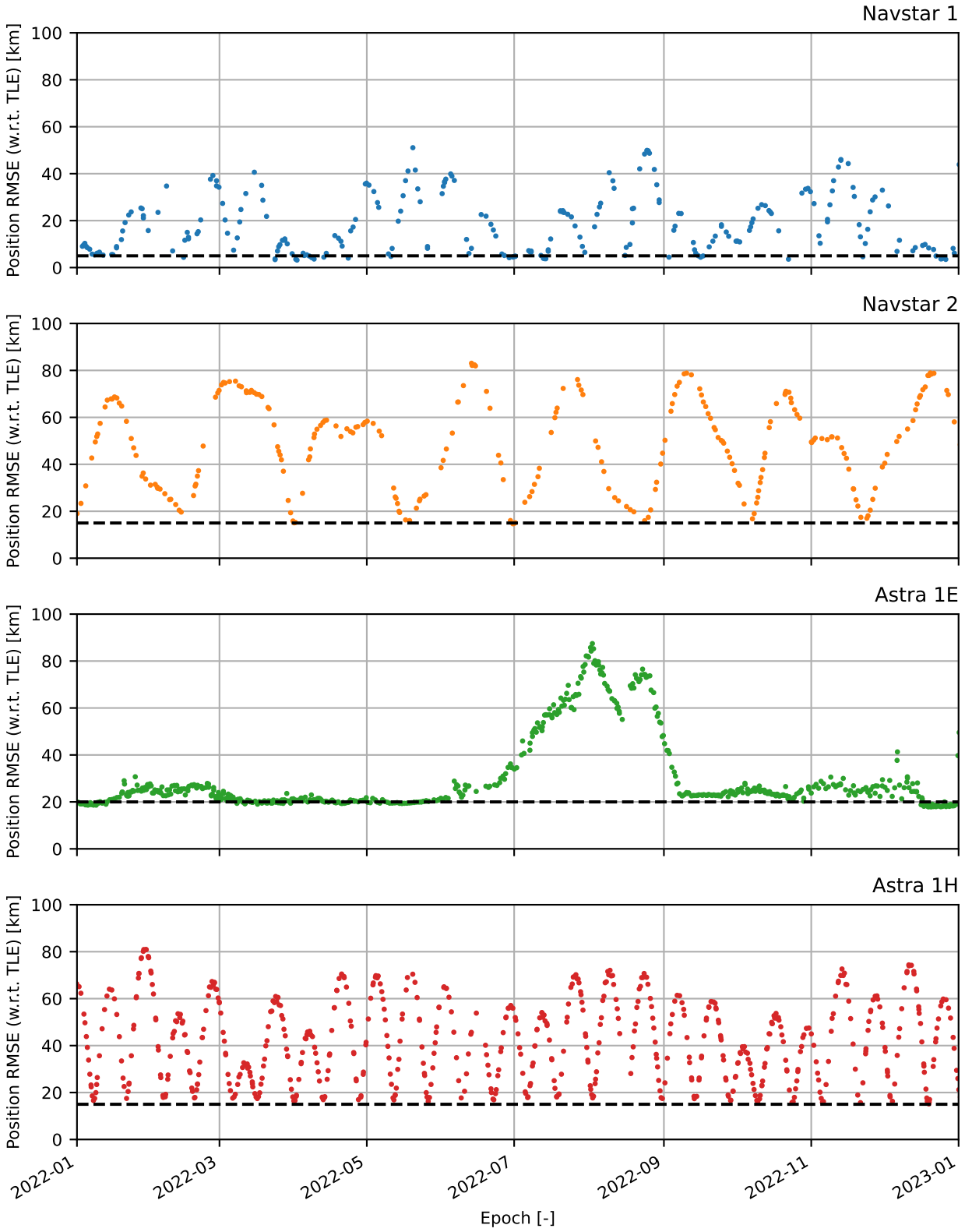


Figure 4.16: Position RMSE, with respect to TLEs, during 90 days post-epoch for test satellite TLEs. Periodic variations in position RMSE are highly visible due to varying bias in the TLEs. The dashed lines represent the established baselines for each satellite.

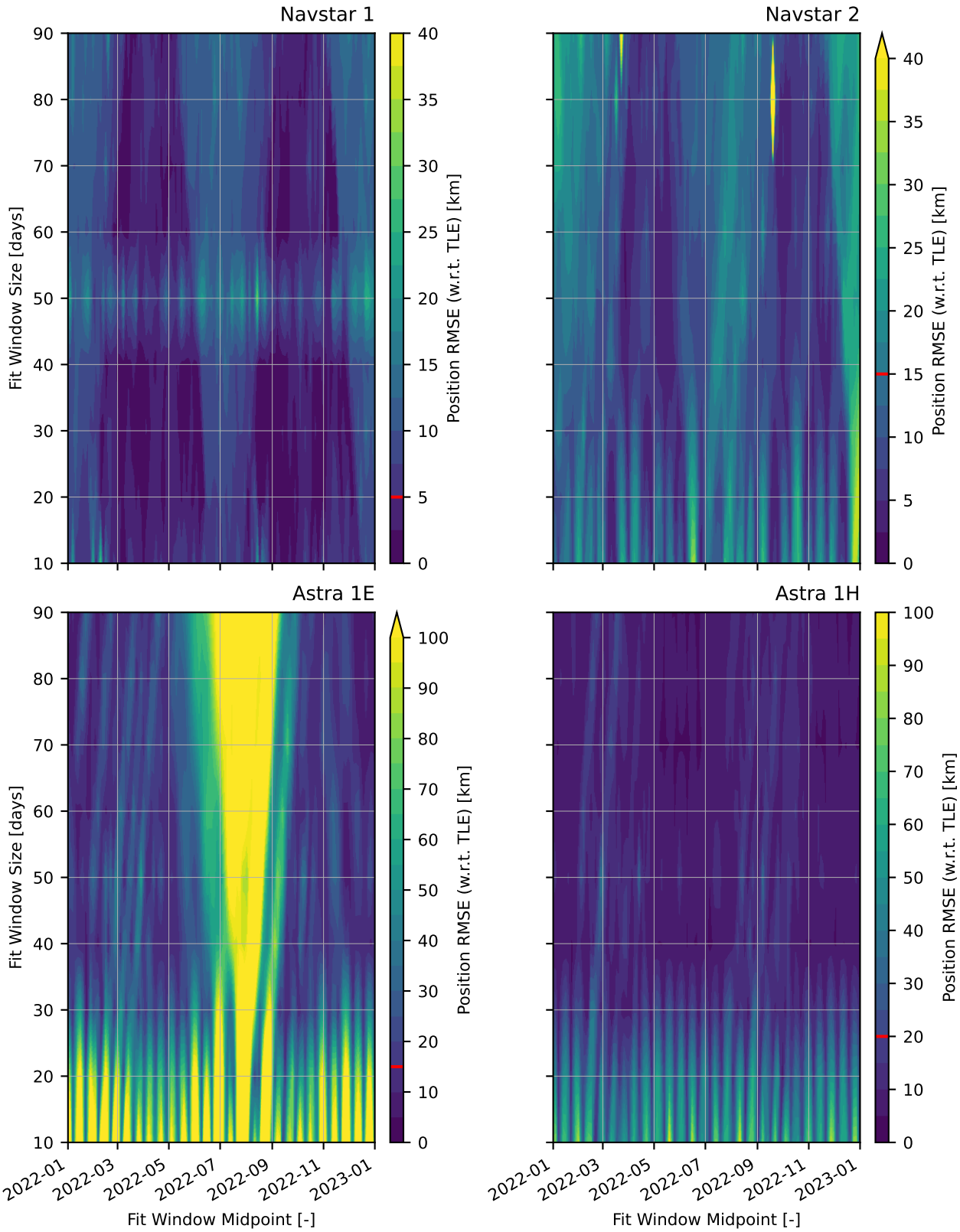


Figure 4.17: Position RMSE during the 90 days post-fit for long-term biased fits of the test satellites. The red marker in the colour bar indicates the RMSE baseline derived from TLEs.

The periodic variation in error throughout the year for short fit windows was highly apparent for Navstar 2, and Astra 1E and 1H. The fits on Navstar 1, on the other hand, did not show this variation as strongly, instead demonstrating a longer period variation throughout the year with slightly increased errors at two points in the year: November through February and June through August. Nevertheless, along with Astra 1H, a notable increase in periodic error was visible for 50-day windows. The increased TLE error for Astra 1E between July and September was highly apparent, as seen by very high errors for the fits during the time period. It was unexpected that Navstar 1 would not show oscillatory behaviour in the fits despite oscillations in TLE quality, and vice versa for Astra 1E, which showed oscillatory behaviour for short-term windows despite constant TLE-on-TLE error.

Distributions of the estimated SRP coefficients are presented in Figure 4.18. The majority of fits resulted in coefficients close to the initial guess of $3 \times 10^{-2}\,\mathrm{m}^2/\mathrm{kg}$, as expected due to the aforementioned low observability of the SRP coefficient. Nevertheless, additional peaks could be seen for three of the satellites at approximately $1.5 \times 10^{-2}\,\mathrm{m}^2/\mathrm{kg}$ for Navstar 1 and 2, and $2.5 \times 10^{-2}\,\mathrm{m}^2/\mathrm{kg}$ for Astra 1H. It is possible that these second peaks were closer to the true SRP coefficients of the satellites. One potential reason could be better observability of the coefficient for certain fit windows.

4.3 Pseudo-Orbit Determination for Bias Estimation

The TLE bias models presented in Chapter 3 were highly effective at reducing position error, both for individual pseudo-observed states and, subsequently, for TLE-based P-OD fits. Nonetheless, the analysis resulting in these models required high-accuracy reference ephemerides, in this case derived from SLR and GNSS pseudo-ranging. The concerns with this methodology, specifically issues with extrapolation and overfitting, cannot be addressed without enlarging the TLE error dataset to include a greater variety of orbits, critically in semi-major axis, inclination, and RAAN.

In Sections 3.1 and 3.2, it was shown that TLE bias can be suppressed with extended fit windows spanning multiple cycles of TLE bias. In Section 4.2, this was demonstrated for for satellites without high-accuracy ephemerides, suggesting that TLE-based P-OD can be applied successfully for a greater number of RSOs without bias models. It is proposed that TLE-based P-OD could be used to expand the TLE error dataset. P-OD with long-duration fit windows could be conducted on a large-scale on known passive RSOs, such as rocket bodies, decommissioned satellites, and other

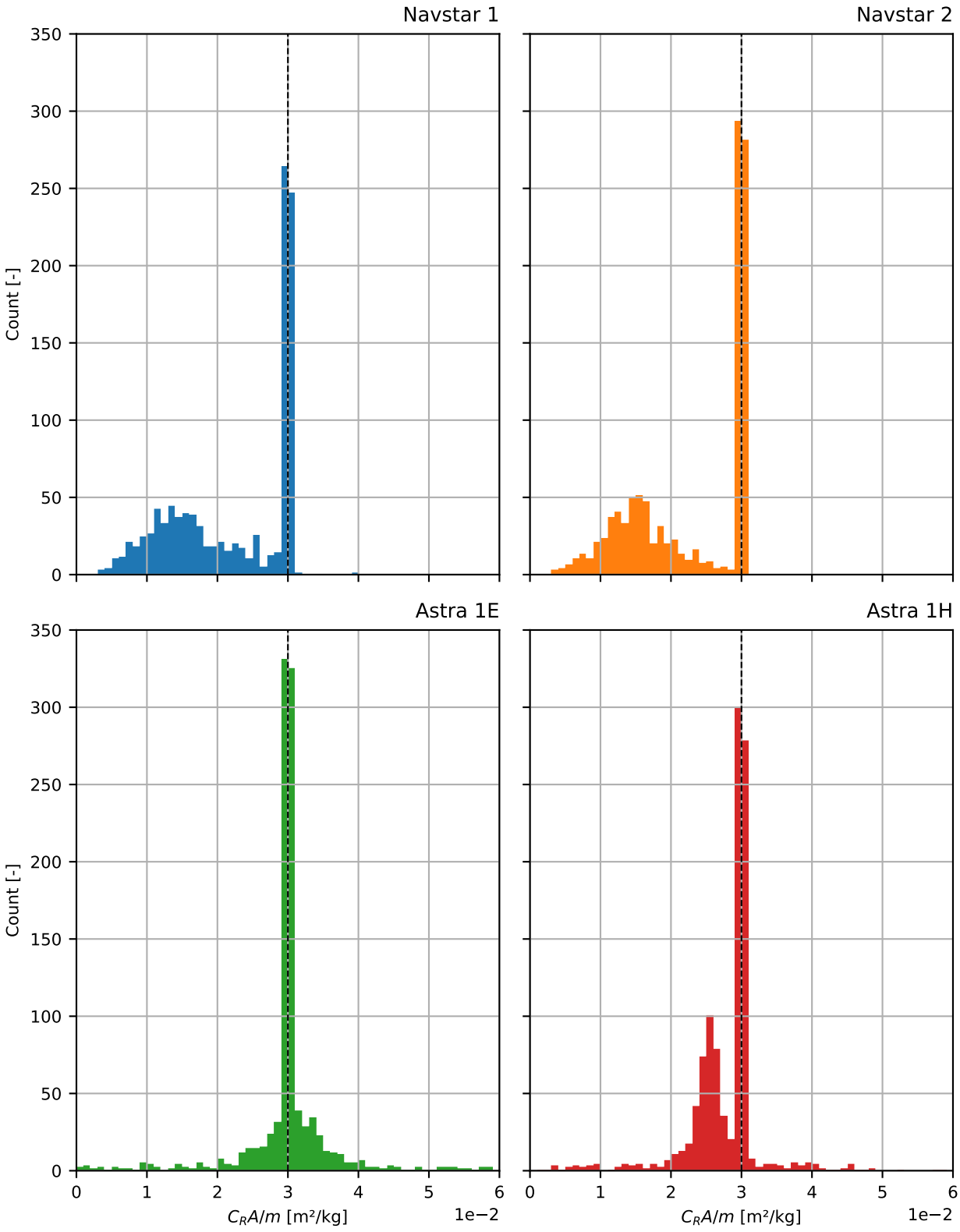


Figure 4.18: SRP coefficient distributions for the test satellites fits. Note that the x-axes have been cropped due to outliers.

debris, in a variety of orbital regimes to produce a large set of reference trajectories. The TLEs of the RSOs could be compared against their reference trajectories to estimate TLE errors, such as the along-track error which drives TLE uncertainty.

It is likely that this method for estimating TLE bias will have some limitations for TLE series with a long-term constant mean bias offset, for example, as seen for many of the GPS satellites in Section 3.6. Under this scenario, the P-OD fits will fail to capture the mean bias, as its period would be infinitely larger than the fit window. Nevertheless, oscillations about the mean would be captured, meaning that, at the very least, this method could be use to improve the consistency of the TLEs.

The proposed methodology was tested by estimating the RTN position and velocity errors for the calibration and test satellites, using 90-day fits as a reference solution in place of SLR orbit products. For this analysis, the fitted propagator and TLEs were sampled at a significantly finer temporal resolution than for the state estimation process itself: samples were taken every 60 minutes, instead of only 100 samples across the 90-day fit window (i.e. samples approximately every 1,310 minutes). This produced a much larger dataset and, importantly, improved the temporal resolution to reveal finer detail, particularly for short-period behaviours.

The results of aggregating the estimated RTN position and velocity errors are presented in Figures 4.19 to 4.22. Both LAGEOS-1 and -2 had several cases with poor fit quality, highly visible through outlying scatters where the estimated RTN errors were significantly larger. The fits for Etalon 1 and 2, on the other hand, did not appear to have any outlying results with all of the fits following the expected monthly sinusoidal variations throughout the year. For Navstar 2, and Astra 1E and 1H, a periodic variation about the origin was apparent, suggesting that the same lunisolar perturbation mismodelling seen for the calibration satellites was being captured by this method. There were large numbers of diverging fits for Navstar 1 and 2, and to a lesser extent for Astra 1E.

The state estimates produced from multiple TLE-based P-OD fits can be combined together to estimate the TLE bias at a given time without making any assumptions about the underlying behaviour. In this case, the estimated errors were filtered by applying a rolling median to the P-OD-derived state vectors. The median was chosen over the mean specifically due to it being more robust in the presence of extreme outliers. Nevertheless, alternative filtering techniques could be applied to fuse the P-OD results together. The filtered time-series can be used for further analysis, such as the

frequency analysis conducted in Section 3.2.1. In this case, the FFT analysis technique could not be applied without removing duplicate state vectors at a given time. The potential for the P-OD and filtering processes to introduce artifacts would need to be considered carefully due to their possible impacts on any downstream analysis.

The results of filtering the estimated position and velocity errors of the calibration and test satellites with a rolling median are presented in Figures 4.23 to 4.26. For the calibration satellites, the results of the bias estimation can be compared directly with Figures 3.7 and 3.8. The estimated biases were very similar to the true biases, both in terms of general structure and amplitude throughout the year, for all six of the RTN components. Importantly, the more varied behaviour of LAGEOS-2 was successfully captured, including the varying and decreasing amplitude throughout the year. For the test satellites, some interesting behaviours were highlighted, such as the sudden shifts in error for Navstar 1, suggesting sudden changes in TLE accuracy, and the large radial position and along-track velocity errors seen repeatedly for both Navstar satellites. Nevertheless, for Astra 1E and 1E, the trend continued of along-track position and radial velocity being the dominant bias components.

The results of fitting the individual time-based models to the estimated along-track position errors for the calibration satellites are presented in Table 4.3 and Figure 4.27. The resulting models were very similar to those produced in Section 3.3.3. More crucially, independent of whether the fitted individual time-based models accurately captured the behaviour, it can be seen that the along-track position bias variations for all of the satellites were clearly captured by the aggregated P-OD fits.

Table 4.3: Individual calibration satellite time-based models for the year 2022, using estimated error from 90.000-day biased P-OD fits.

Satellite	a_t [rad]	b_t [days]	c_t [days]	d_t [rad]
LAGEOS-1	1.440×10^{-5}	27.55	3.754	3.237×10^{-7}
LAGEOS-2	3.285×10^{-6}	28.89	1.833	-4.948×10^{-7}
Etalon 1	4.740×10^{-5}	27.51	−9.600	-4.101×10^{-7}
Etalon 2	6.658×10^{-5}	27.56	5.509	1.926×10^{-7}

The model parameters for LAGEOS-1, and Etalon 1 and 2 were very similar to those presented in Table 3.2, with amplitudes differing by only −13.5 %, 5.01 %, and −0.66 %, respectively; and periods by 0.013 %, −0.135 %, and 0.025 %, respectively. The phase for Etalon 1 was not comparable due to the difference in period. However, for LAGEOS-1 and Etalon 2, where the period was very similar

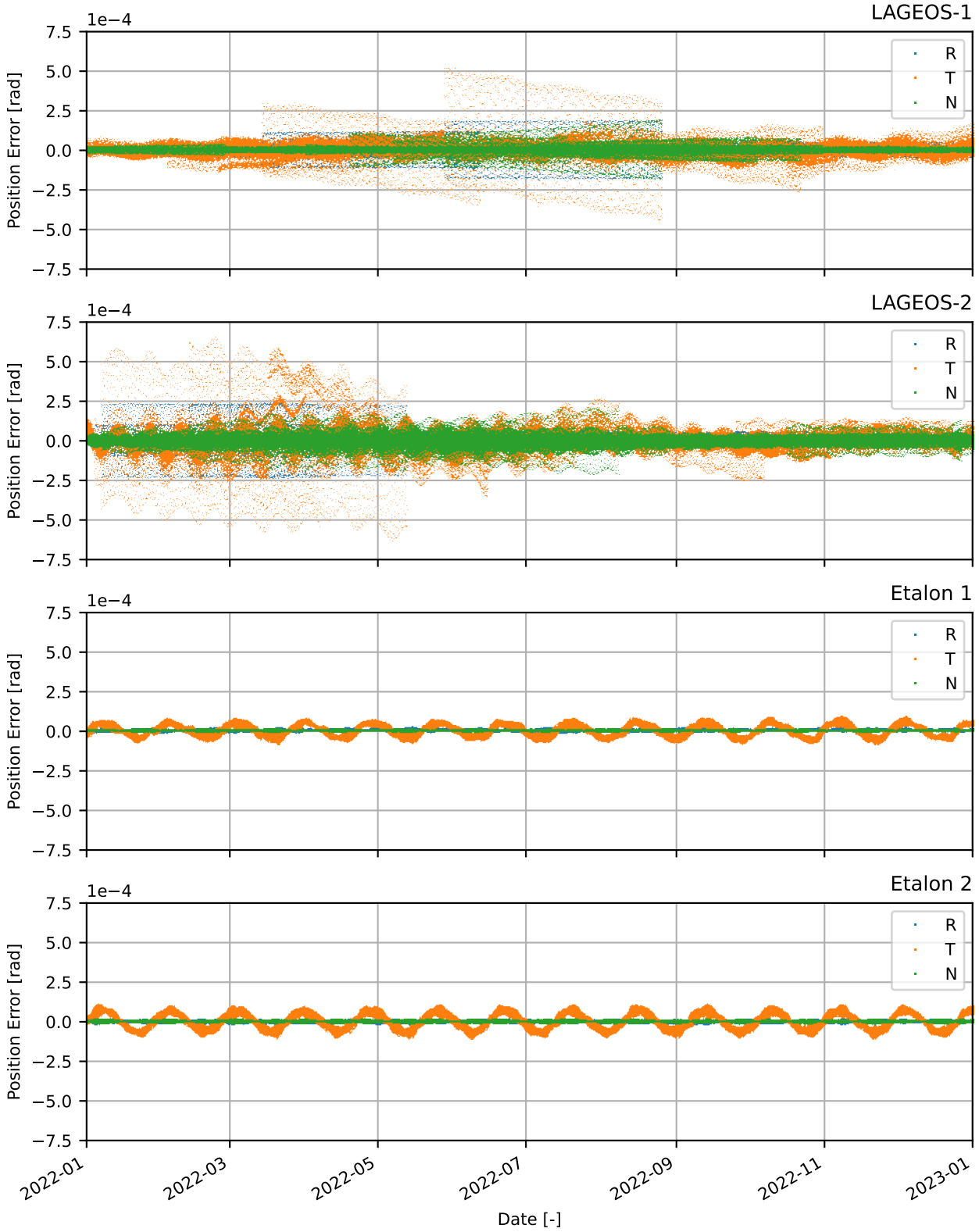


Figure 4.19: Angular RTN position errors of calibration satellite TLEs for the year 2022, estimated from with 90-day biased P-OD fits.

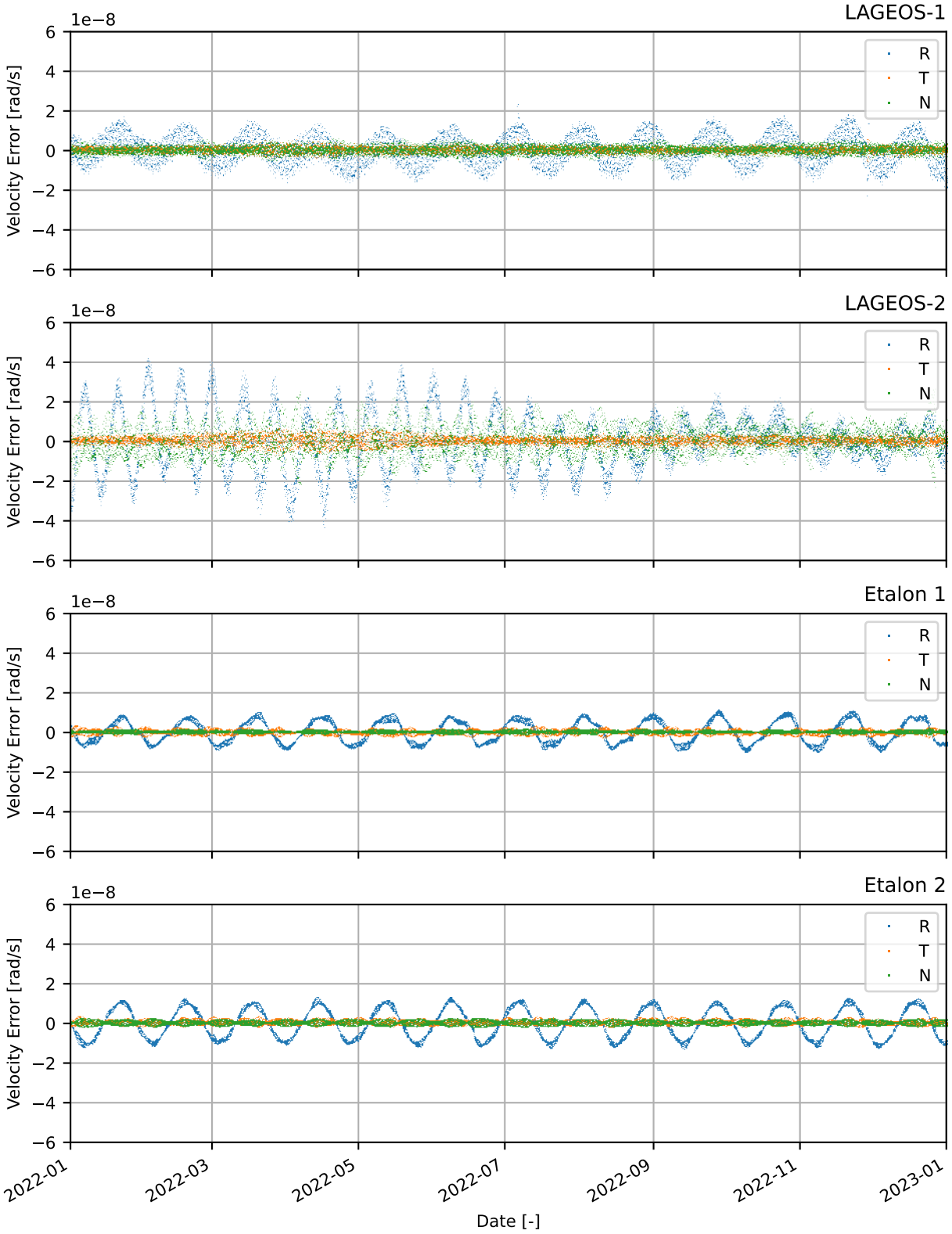


Figure 4.20: Angular RTN velocity errors of calibration satellite TLEs for the year 2022, estimated from 90-day biased P-OD fits.

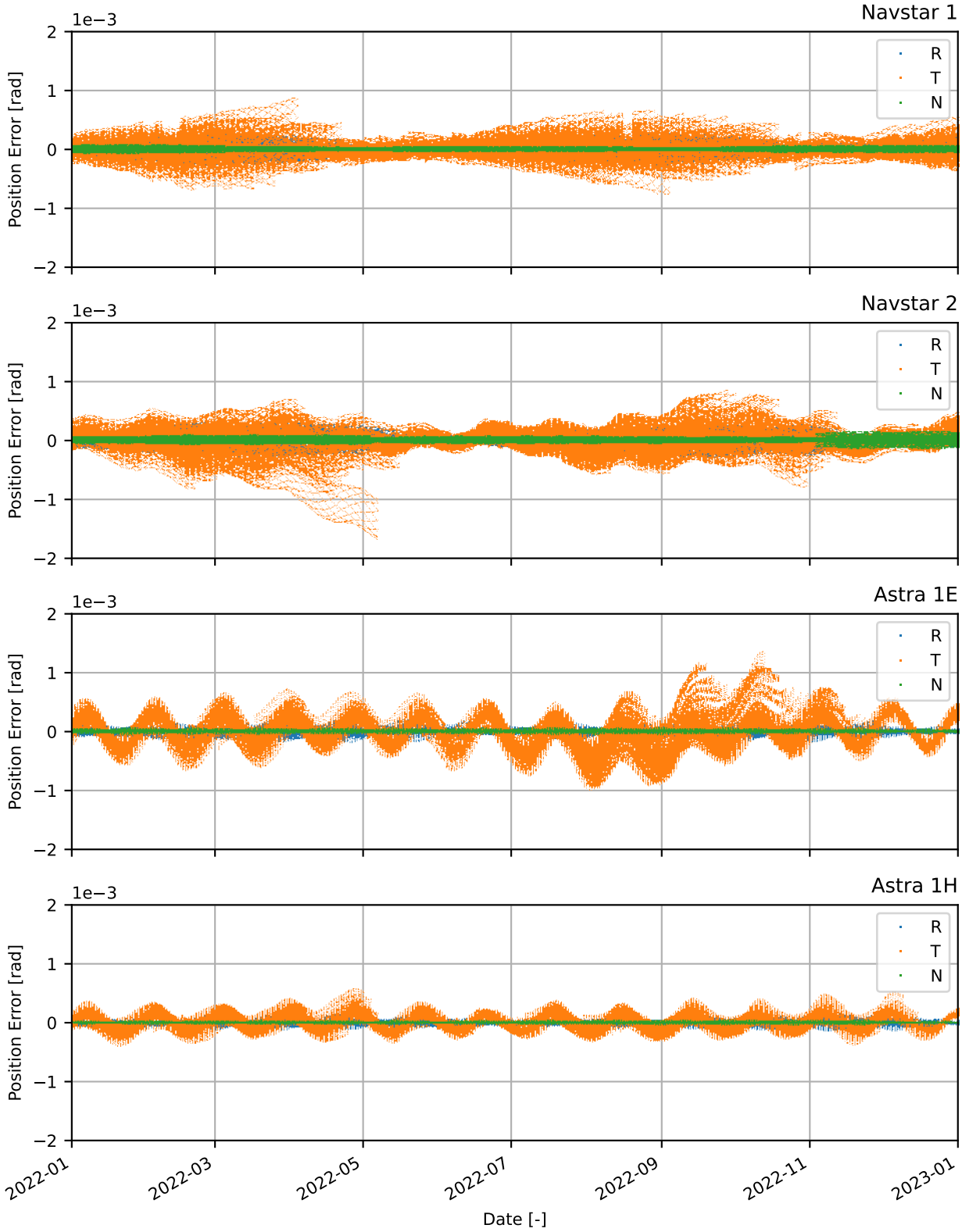


Figure 4.21: Angular RTN position errors of test satellite TLEs for the year 2022, estimated from 90-day biased P-OD fits.

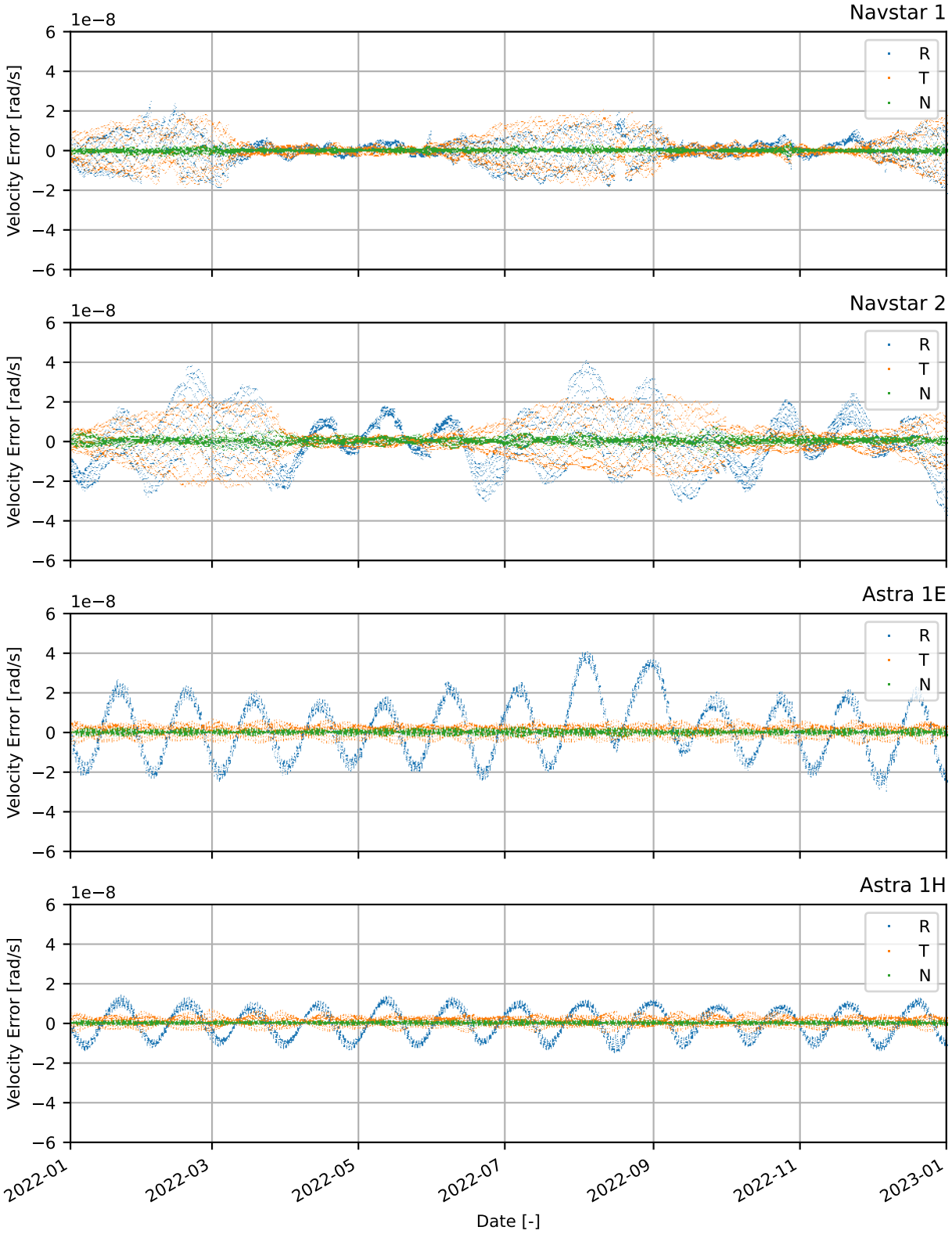


Figure 4.22: Angular RTN velocity errors of test satellite TLEs for the year 2022, estimated from 90-day biased P-OD fits.

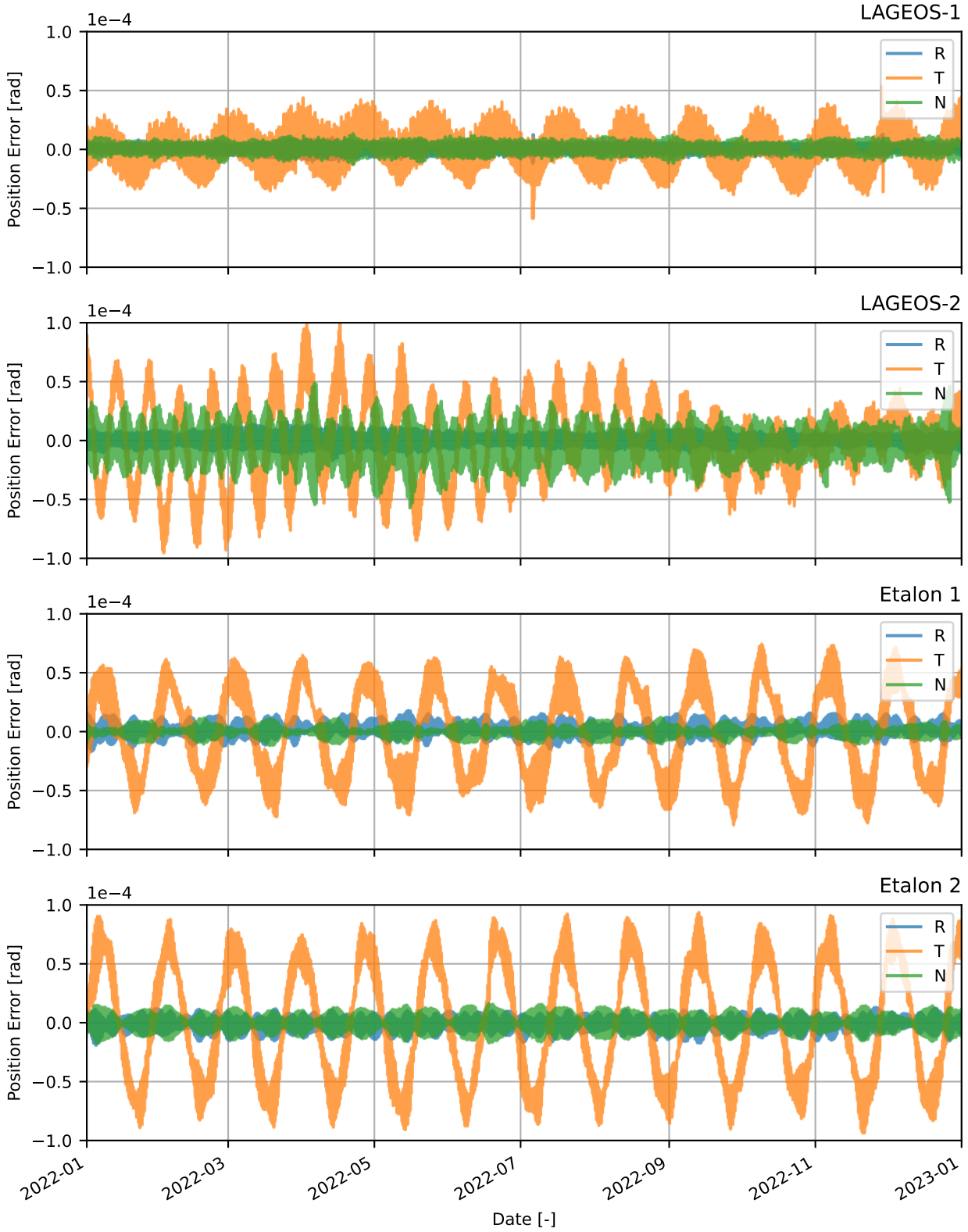


Figure 4.23: Angular RTN position errors of calibration satellite TLEs for the year 2022, using estimated error from 90-day biased P-OD fits filtered with an hourly rolling median.

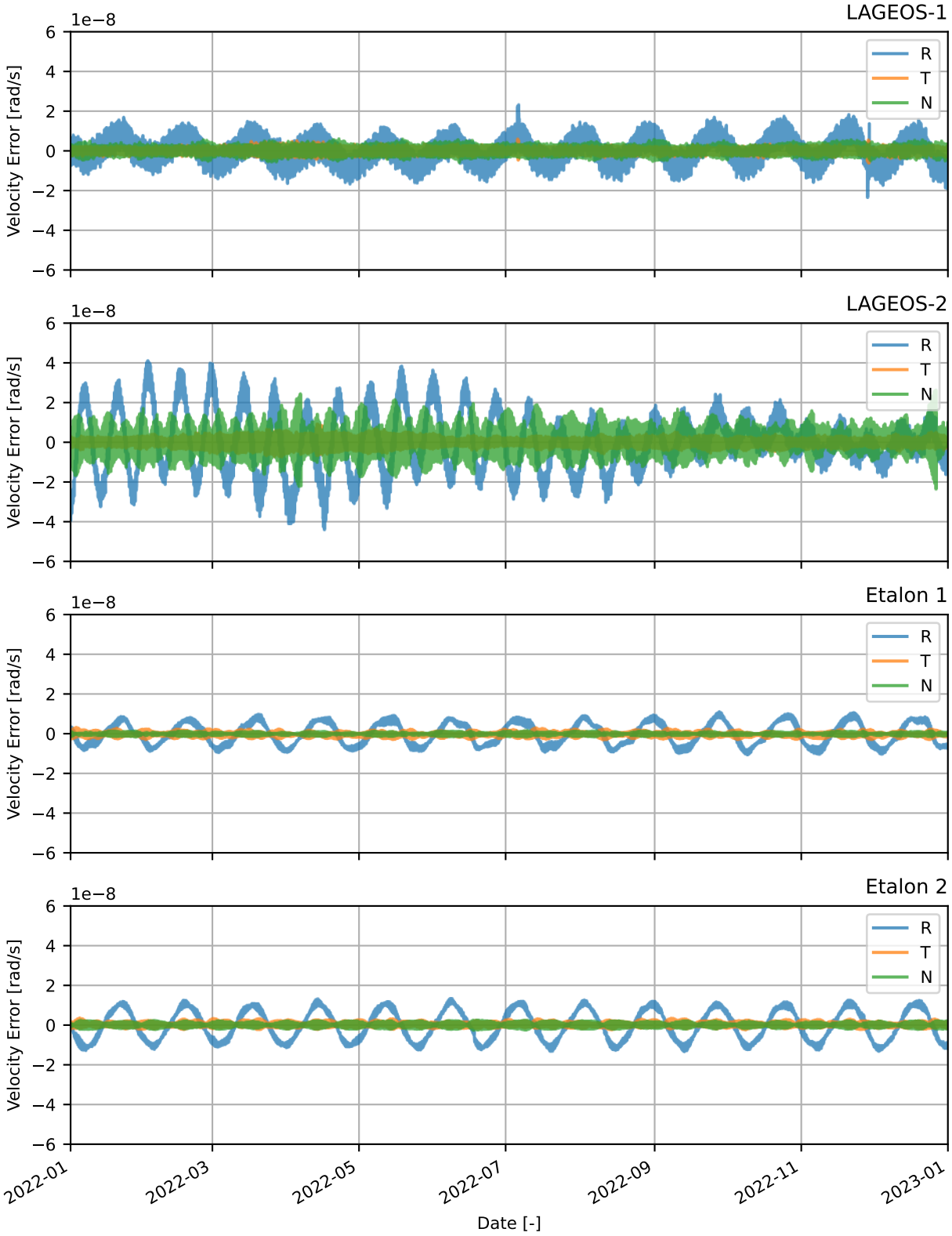


Figure 4.24: Angular RTN velocity errors of calibration satellite TLEs for the year 2022, using estimated error from 90-day biased P-OD fits filtered with an hourly rolling median.

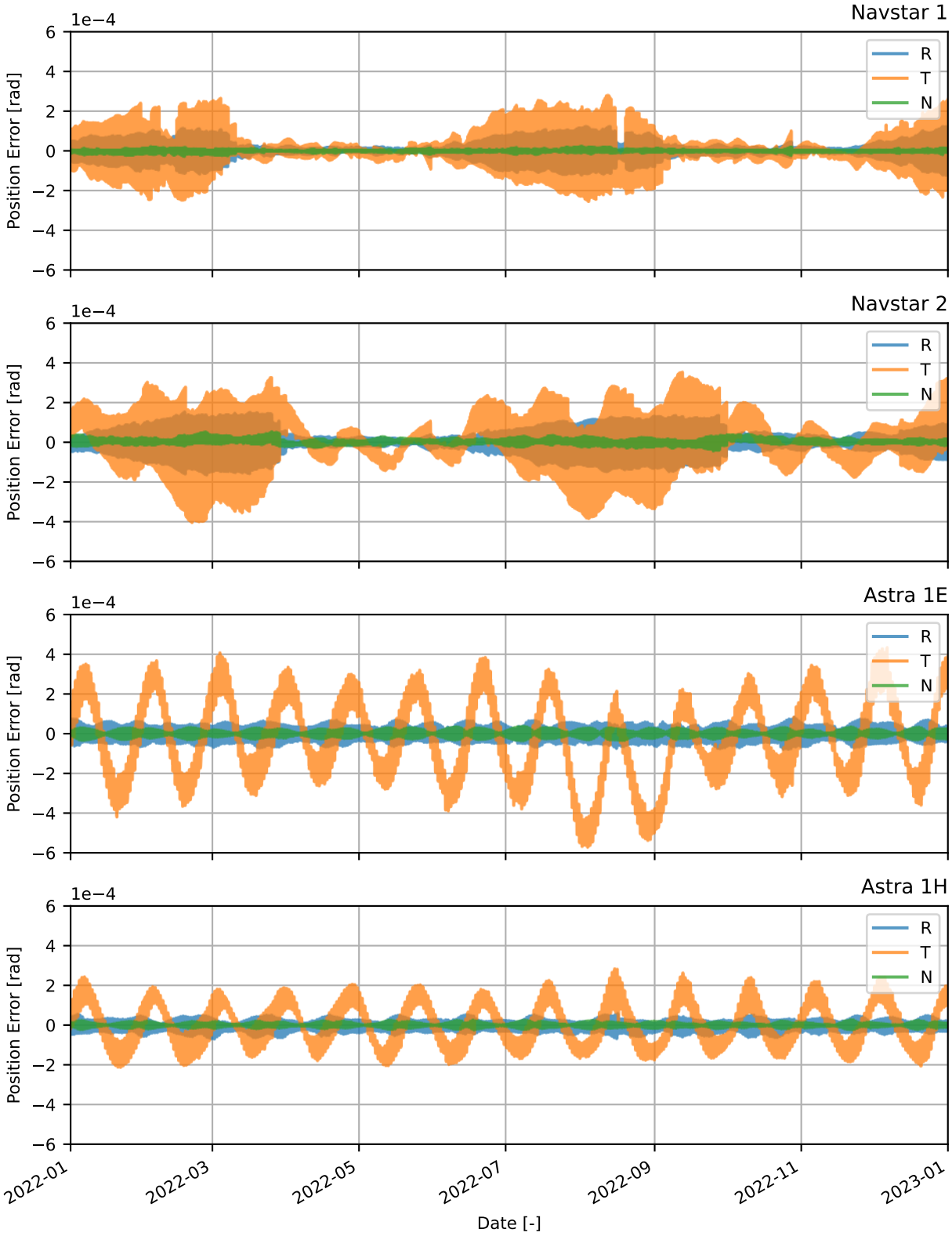


Figure 4.25: Angular RTN position errors of test satellite TLEs for the year 2022, using estimated error from 90-day biased P-OD fits filtered with an hourly rolling median.

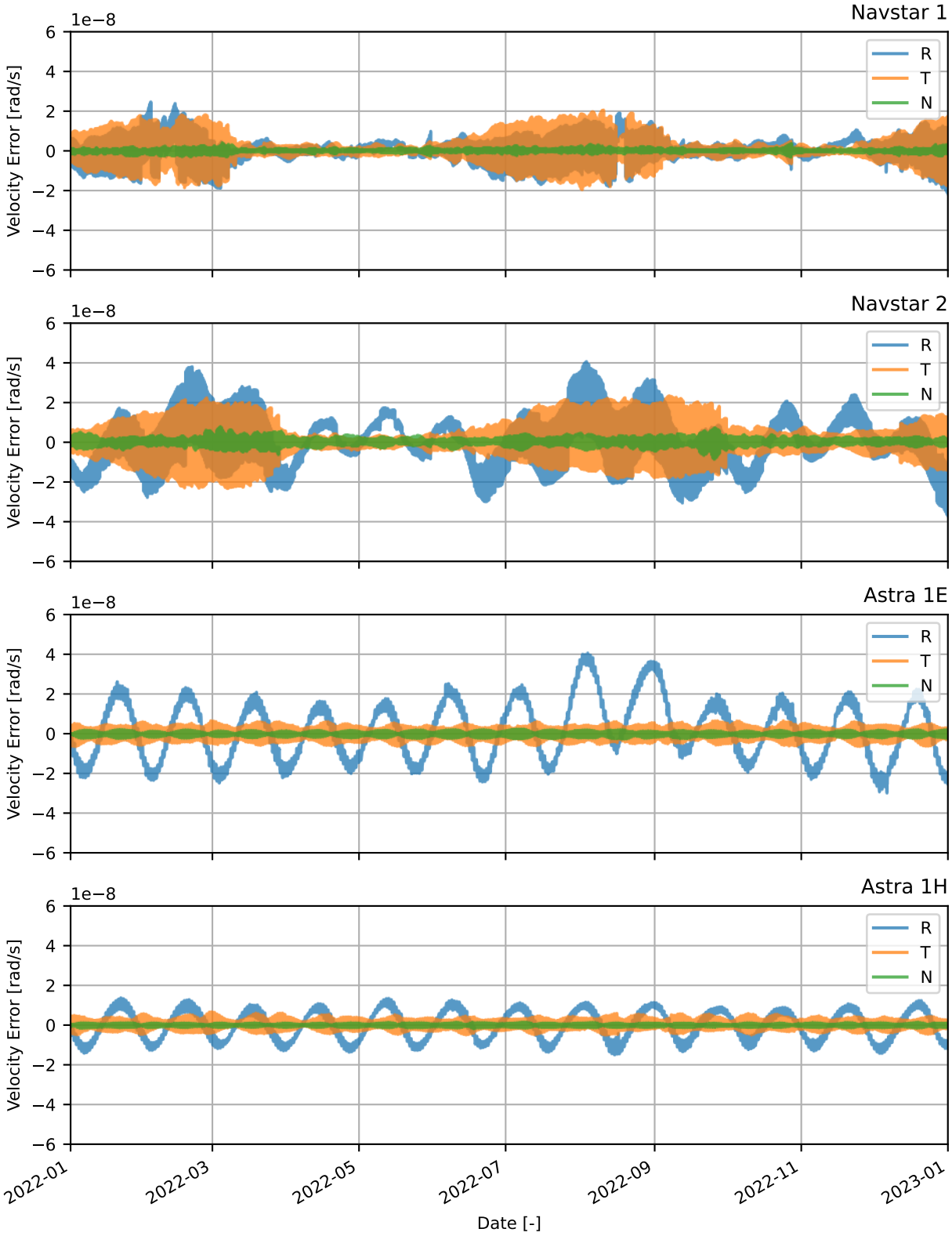


Figure 4.26: Angular RTN velocity errors of test satellite TLEs for the year 2022, using estimated error from 90-day biased P-OD fits filtered with an hourly rolling median.

to the fits in Table 3.2, the phases and zero-crossing points were very similar and close to the date of the Moon at apogee. The fit for LAGEOS-2 was very poor. This was expected, however, due to the same issues faced in Section 3.3. These results suggest that it is possible to use the results of TLE-based P-OD to estimate bias model parameters.

The results of fitting the individual time-based models to the estimated along-track position errors for test satellites are presented in Table 4.4 and Figure 4.28. Astra 1H had the best fitting model, followed by Astra 1E and Navstar 2. The large number of diverging fits for Navstar 1 prevented an effective fit, however this issue was not encountered for Navstar 2 nor Astra 1E which still contained sufficient periodic behaviour for the bias to be recovered.

Table 4.4: Individual test satellite time-based models for the year 2022, using estimated error from 90.00-day biased P-OD fits.

Satellite	a_t [rad]	b_t [days]	c_t [days]	d_t [rad]
Navstar 1	5.754×10^{-6}	27.77	12.60	1.170×10^{-6}
Navstar 2	6.484×10^{-5}	27.56	4.349	-5.196×10^{-6}
Astra 1E	2.580×10^{-4}	27.57	7.938	-1.453×10^{-5}
Astra 1H	1.353×10^{-4}	27.57	8.659	3.987×10^{-6}

The amplitudes of the bias models for Astra 1E and 1H were an order of magnitude higher than seen in the previously with a variety of MEO satellites. These amplitudes represented along-track position oscillations of approximately ±11 km and ±6 km, respectively. This suggests, as expected, that TLE biases grow significantly larger as altitude increases. The periods for Navstar 2, and Astra 1E and 1H were slightly higher than expected. The phases were slightly affected as a result, however these still placed the zero-crossing points near the expected date, in the vicinity of the Moon reaching apogee. It is expected that the accuracy of the estimated periods and phases would improve by using along-track position error estimates from a longer time period, such as the seven-year period used for the time- and Moon-based models in Section 3.3.

The results for Navstar 1 and 2, by virtue of these satellites being decommissioned GPS satellites, provided an interesting opportunity to compare the bias amplitude estimated with P-OD to that estimated with the RAAN-amplitude model from Section 3.6. The RAANs of the Navstar satellites were approximately 146.5° and 11.4°, respectively, at the start of the year 2022. The long-term ensemble time-based model presented in Table 3.6 predicted expected bias model amplitudes of

6.787×10^{-5} rad and 6.199×10^{-5} rad, respectively, for these orbits. The fit for Navstar 1 was very poor and not comparable to the expected amplitude; however, in the case of Navstar 2, the estimated amplitude was only 4.592 % higher than that expected from the RAAN-amplitude model. This further demonstrates how P-OD can be used for bias model estimation in the absence of higher-accuracy ephemerides.

The results of estimating the calibration and test satellites' along-track position biases showed an interesting property of aggregating multiple separate P-OD fits. An individual P-OD fit may not fully capture the true errors present in the TLEs; however, in this case, there were multiple overlapping windows throughout the entire year. This served to reduce the impact of any individual poor fit as there were multiple estimates of the TLE error for a given time. In the aggregate, the TLE errors were more accurately and more robustly estimated.

Frequency analysis was conducted on the filtered P-OD-derived along-track position error, using the same FFT technique as used previously in Section 3.2.1. In this case, the filtered P-OD-derived errors were used. The results of the FFTs are presented in Figures 4.29 and 4.30 for the calibration and test satellites, respectively. It should be noted that the datasets used to compute the FFTs were shorter than those used for with SLR-derived datasets, therefore it was expected that some of the longer-term periodic components would not be recovered and that some artifacts would be introduced.

For the calibration satellites, the strongest peaks of the FFTs were lower generally than those found in the FFTs conducted on the SLR-derived errors: for LAGEOS-1, the dominant peak at approximately one month was reduced from 1.574×10^{-5} rad to 9.490×10^{-6} rad; for Etalon 1, it was reduced from 4.270×10^{-5} rad to 3.277×10^{-5} rad; and, for Etalon 2, it was reduced from 6.281×10^{-5} rad to 4.350×10^{-5} rad. These represent an average reduction of 30 %; however, this ignores that there were multiple components in the vicinity which combined to provide similar overall amplitudes. This was seen by the peaks being more spread out in period, a feature which was particularly noticeable in the cases of Etalon 1 and 2.

For the test satellites, the results were more mixed than those for the calibration satellites. The highest amplitude components for both Navstar 1 and 2 occurred at their respective orbital periods; nevertheless, the former demonstrated no other significant periodic components, while the latter had a peak at approximately one month which was overshadowed by a peak at approximately three months.

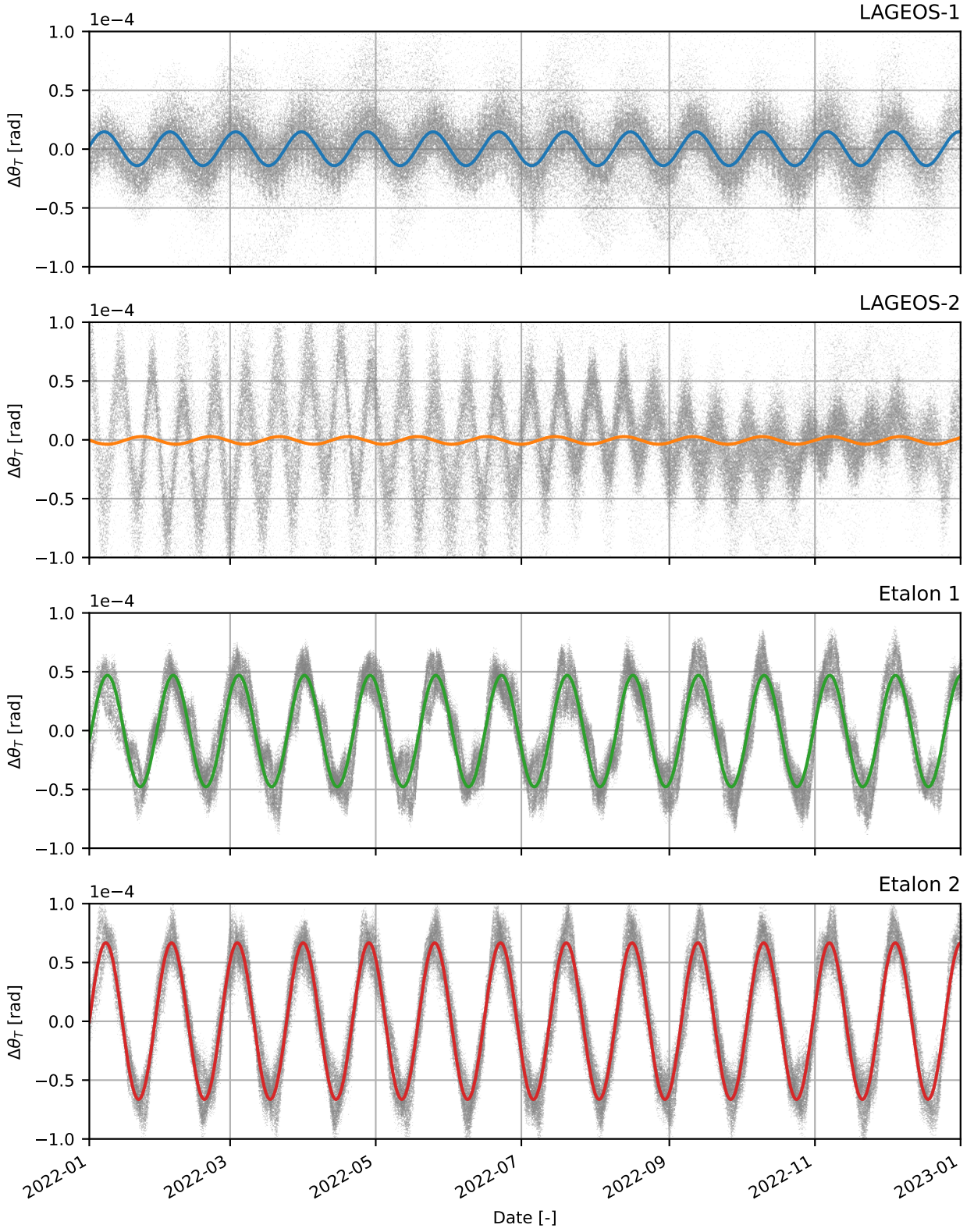


Figure 4.27: Time-based along-track position error models for the calibration satellites for the year 2022, using estimated error from 90-day biased P-OD fits. The along-track position error of the TLEs and the models are presented in grey and colour, respectively. Note that the y-axis has been cropped due to extreme outliers.

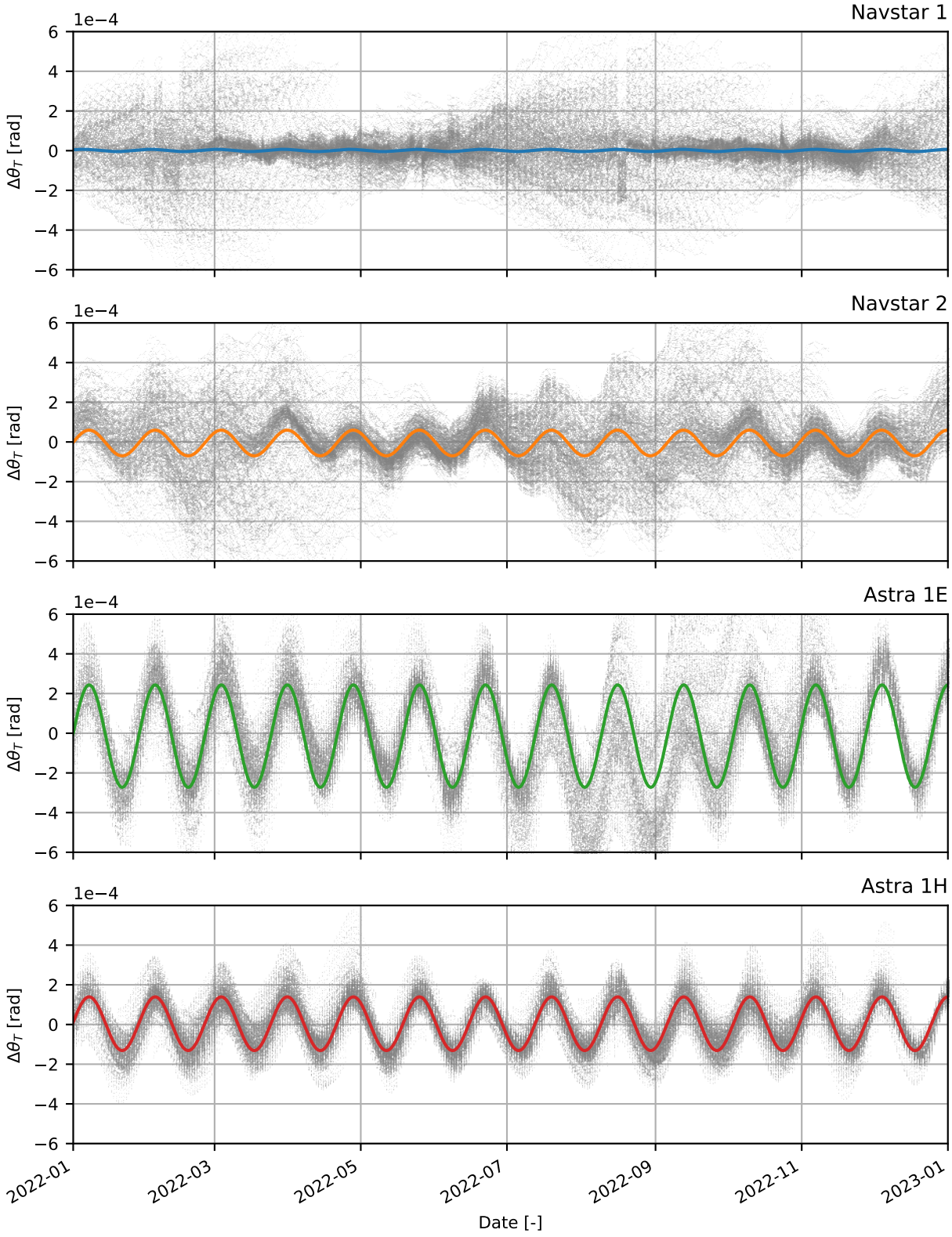


Figure 4.28: Time-based along-track position error models for the test satellites for the year 2022, using estimated error from 90-day biased P-OD fits. The along-track position error of the TLEs and the models are presented in grey and colour, respectively. Note that the y-axis has been cropped due to extreme outliers.

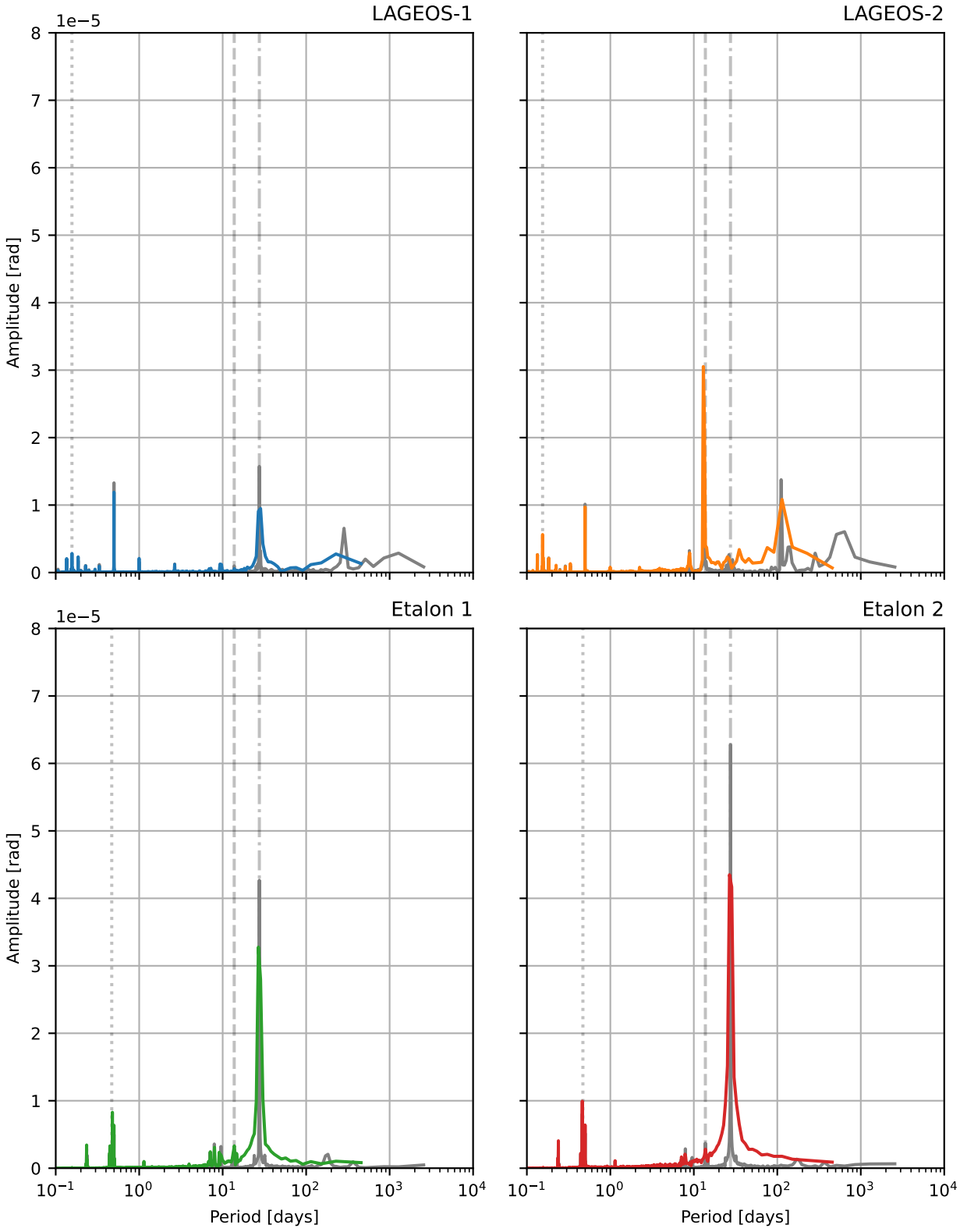


Figure 4.29: FFT analysis of the estimated along-track angular position errors of the calibration satellites for the year 2022. The FFTs of the SLR-derived errors, as presented in Figure 3.11, are represented in grey. The orbital period of each satellite, the half period of the Moon, and the Moon's orbital period are represented by the dotted, dashed, and dash-dotted lines respectively.

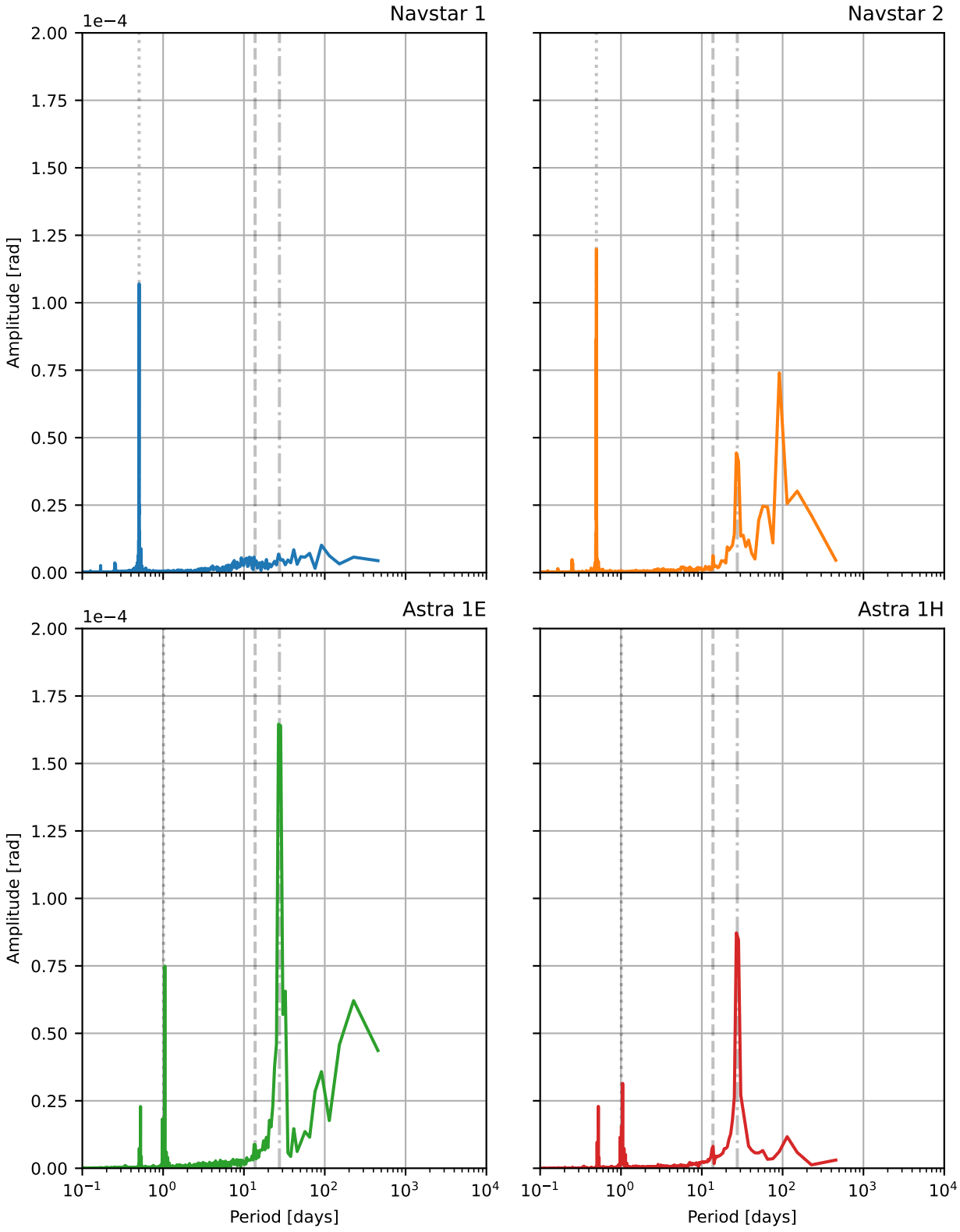


Figure 4.30: FFT analysis of the estimated along-track angular position errors of the test satellites for the year 2022. The orbital period of each satellite, the half period of the Moon, and the Moon's orbital period are represented by the dotted, dashed, and dash-dotted lines respectively.

For Astra 1E and 1H, the largest components for both occurred at approximately one day and one month, corresponding to their orbital periods and period of the Moon respectively. Astra 1E had an additional component at approximately 200 days, corresponding to the shift in bias seen during the summer of 2022.

Individual FFT-derived time-based models were generated for the calibration and test satellites, based on the filtered estimated along-track position errors from P-OD. Following the same methodology as in Section 3.7, the 20 largest periodic components were included in the models. The same cut-off of one day was used for the calibration and test satellites, except for Astra 1E and 1H where the cut-off was increased to two days. By doing so, it was ensured that the models for the GEO satellites would capture the the longer-term TLE bias variation, instead of capturing short-period errors.

The FFT-derived models for the calibration satellites are presented in Table 4.5 and Figure 4.31. For LAGEOS-1, and Etalon 1 and 2, dominant components were recovered with periods of 28.44 days and 26.77 days, respectively, against the 27.49-day period seen for the SLR-based models. In the case of LAGEOS-2, the dominant periodic component was captured with a period of 13.00 days, against the 13.05-day component found in the SLR-based model. Nevertheless, visual examination of Figure 4.31 reveals that all four models capture the main bias variation qualitatively.

The FFT-derived models for the test satellites are presented in Table 4.6 and Figure 4.32. Notably, in the cases of both Navstar 1 and 2, the largest periodic components did not occur approximately monthly, as expected, but with a period of 91.01 days. This is close to the size of the P-OD fit window. The models for both Astra 1E and 1H had dominant components with periods of 26.77 days, matching the results seen for Etalon 1 and 2. In the case of Astra 1E, it can be seen that the FFT-derived model captured the shift in along-track position bias that occurred between August and September.

The shorter timespan of the P-OD-derived along-track position errors (approximately one year against the seven years of SLR-derived errors in Chapter 3) introduced limitations with these FFT-derived models. The longer-period components, particularly important in the cases of LAGEOS 1 and 2, could not be captured by the frequency analysis. Furthermore, analysis of a longer time series could improve the capture of the dominant components, resulting in period estimates more closely matching those derived from SLR-derived errors.

Overall, bias modelling methods benefit from datasets which span longer time periods. For models using P-OD-derived estimates, in particular, longer timespan datasets have the additional benefit of reducing the influence of any given poor-quality P-OD fit. This mirrors the behaviour seen with P-OD fits, and how their accuracy can be improved by considering a larger, more diverse set of TLEs during the state estimation process. Future developments should consider extended timespans, on the order of multiple years, when creating P-OD-derived bias models.

Table 4.5: Individual calibration satellite FFT-derived time-based models for the year 2022, using estimated error from 90-day biased P-OD fits filtered with an hourly rolling median. The 20 largest periodic components with a period greater than one day were included, in addition to the constant offset. The largest amplitude component is highlighted in bold.

(a) LAGEOS-1.

a_t [rad]	b_t [days]	c_t [days]	d_t [rad]
9.490×10^{-6}	**2.844×10^{1}**	**1.343×10^{1}**	**-**
9.085×10^{-6}	2.677×10^{1}	9.243×10^{0}	-
4.241×10^{-6}	3.034×10^{1}	-1.575×10^{-1}	-
2.756×10^{-6}	2.275×10^{2}	1.654×10^{1}	-
2.401×10^{-6}	2.528×10^{1}	-4.838×10^{0}	-
2.393×10^{-6}	3.250×10^{1}	-1.491×10^{1}	-
1.590×10^{-6}	3.500×10^{1}	4.242×10^{0}	-
1.581×10^{-6}	2.395×10^{1}	4.728×10^{0}	-
1.554×10^{-6}	3.792×10^{1}	-1.245×10^{1}	-
1.431×10^{-6}	1.517×10^{2}	7.288×10^{1}	-
1.328×10^{-6}	4.550×10^{2}	5.730×10^{0}	-
1.284×10^{-6}	4.137×10^{1}	9.223×10^{0}	-
1.262×10^{-6}	9.287×10^{0}	1.160×10^{-2}	-
1.212×10^{-6}	2.661×10^{0}	9.715×10^{-1}	-
1.201×10^{-6}	9.682×10^{0}	1.059×10^{0}	-
1.172×10^{-6}	1.138×10^{2}	2.726×10^{1}	-
9.621×10^{-7}	2.275×10^{1}	-7.768×10^{0}	-
8.811×10^{-7}	4.550×10^{1}	-6.787×10^{0}	-
8.095×10^{-7}	1.978×10^{1}	-3.450×10^{-1}	-
7.335×10^{-7}	7.584×10^{1}	2.764×10^{1}	-
-	-	-	-7.403×10^{-8}

(b) LAGEOS-2.

a_t [rad]	b_t [days]	c_t [days]	d_t [rad]
3.053×10^{-5}	**1.300×10^{1}**	**-1.559×10^{0}**	**-**
2.296×10^{-5}	1.338×10^{1}	-3.572×10^{0}	-
1.084×10^{-5}	1.138×10^{2}	5.338×10^{1}	-
3.793×10^{-6}	1.379×10^{1}	5.677×10^{0}	-
3.756×10^{-6}	1.517×10^{2}	7.427×10^{1}	-
3.747×10^{-6}	1.422×10^{1}	-5.687×10^{-1}	-
3.699×10^{-6}	7.584×10^{1}	-1.178×10^{1}	-
3.405×10^{-6}	3.500×10^{1}	-7.374×10^{0}	-
3.003×10^{-6}	9.101×10^{1}	-3.775×10^{1}	-
2.904×10^{-6}	8.922×10^{0}	3.757×10^{0}	-
2.845×10^{-6}	2.275×10^{2}	-2.137×10^{1}	-
2.389×10^{-6}	8.751×10^{0}	-4.197×10^{0}	-
2.322×10^{-6}	2.528×10^{1}	-3.658×10^{0}	-
2.261×10^{-6}	1.468×10^{1}	-6.498×10^{0}	-
2.172×10^{-6}	1.517×10^{1}	1.981×10^{0}	-
2.068×10^{-6}	4.550×10^{1}	2.009×10^{1}	-
2.024×10^{-6}	3.792×10^{1}	1.479×10^{1}	-
1.926×10^{-6}	2.677×10^{1}	7.060×10^{0}	-
1.888×10^{-6}	1.264×10^{1}	3.683×10^{0}	-
1.884×10^{-6}	1.569×10^{1}	-4.810×10^{0}	-
-	-	-	-2.466×10^{-7}

(c) Etalon 1.

a_t [rad]	b_t [days]	c_t [days]	d_t [rad]
3.277×10^{-5}	**2.677×10^{1}**	**8.699×10^{0}**	**-**
2.797×10^{-5}	2.844×10^{1}	1.173×10^{1}	-
1.021×10^{-5}	3.034×10^{1}	-7.637×10^{-1}	-
9.968×10^{-6}	2.528×10^{1}	-5.556×10^{0}	-
5.108×10^{-6}	2.395×10^{1}	6.169×10^{0}	-
4.444×10^{-6}	2.275×10^{1}	-8.070×10^{0}	-
3.556×10^{-6}	3.250×10^{1}	-1.476×10^{1}	-
3.504×10^{-6}	2.167×10^{1}	1.650×10^{0}	-
3.316×10^{-6}	1.379×10^{1}	4.096×10^{-1}	-
3.184×10^{-6}	3.500×10^{1}	3.209×10^{0}	-
3.102×10^{-6}	7.983×10^{0}	9.860×10^{-1}	-
2.915×10^{-6}	2.068×10^{1}	-1.010×10^{1}	-
2.655×10^{-6}	1.978×10^{1}	-8.462×10^{-1}	-
2.505×10^{-6}	3.792×10^{1}	-1.178×10^{1}	-
2.440×10^{-6}	7.110×10^{0}	1.402×10^{0}	-
2.361×10^{-6}	9.101×10^{0}	4.189×10^{0}	-
2.354×10^{-6}	1.338×10^{1}	-2.696×10^{0}	-
2.263×10^{-6}	1.896×10^{1}	7.808×10^{0}	-
2.195×10^{-6}	1.468×10^{1}	-6.579×10^{0}	-
2.083×10^{-6}	4.137×10^{1}	1.066×10^{1}	-
-	-	-	-9.043×10^{-7}

(d) Etalon 2.

a_t [rad]	b_t [days]	c_t [days]	d_t [rad]
4.350×10^{-5}	**2.677×10^{1}**	**9.296×10^{0}**	**-**
4.168×10^{-5}	2.844×10^{1}	1.184×10^{1}	-
1.518×10^{-5}	2.528×10^{1}	-5.361×10^{0}	-
1.349×10^{-5}	3.034×10^{1}	-6.002×10^{-1}	-
9.746×10^{-6}	2.395×10^{1}	5.511×10^{0}	-
9.438×10^{-6}	3.250×10^{1}	-1.510×10^{1}	-
6.512×10^{-6}	3.500×10^{1}	3.851×10^{0}	-
6.374×10^{-6}	2.275×10^{1}	-7.785×10^{0}	-
5.119×10^{-6}	2.167×10^{1}	2.131×10^{0}	-
4.228×10^{-6}	2.068×10^{1}	-9.821×10^{0}	-
4.152×10^{-6}	3.792×10^{1}	-1.199×10^{1}	-
3.630×10^{-6}	4.137×10^{1}	1.079×10^{1}	-
3.556×10^{-6}	1.978×10^{1}	-4.281×10^{-1}	-
3.208×10^{-6}	1.896×10^{1}	8.047×10^{0}	-
2.824×10^{-6}	1.379×10^{1}	1.010×10^{0}	-
2.809×10^{-6}	5.056×10^{1}	2.096×10^{1}	-
2.785×10^{-6}	4.550×10^{1}	-7.751×10^{0}	-
2.723×10^{-6}	1.820×10^{1}	-2.479×10^{0}	-
2.517×10^{-6}	5.688×10^{1}	-2.665×10^{0}	-
2.459×10^{-6}	1.750×10^{1}	5.066×10^{0}	-
-	-	-	-9.786×10^{-8}

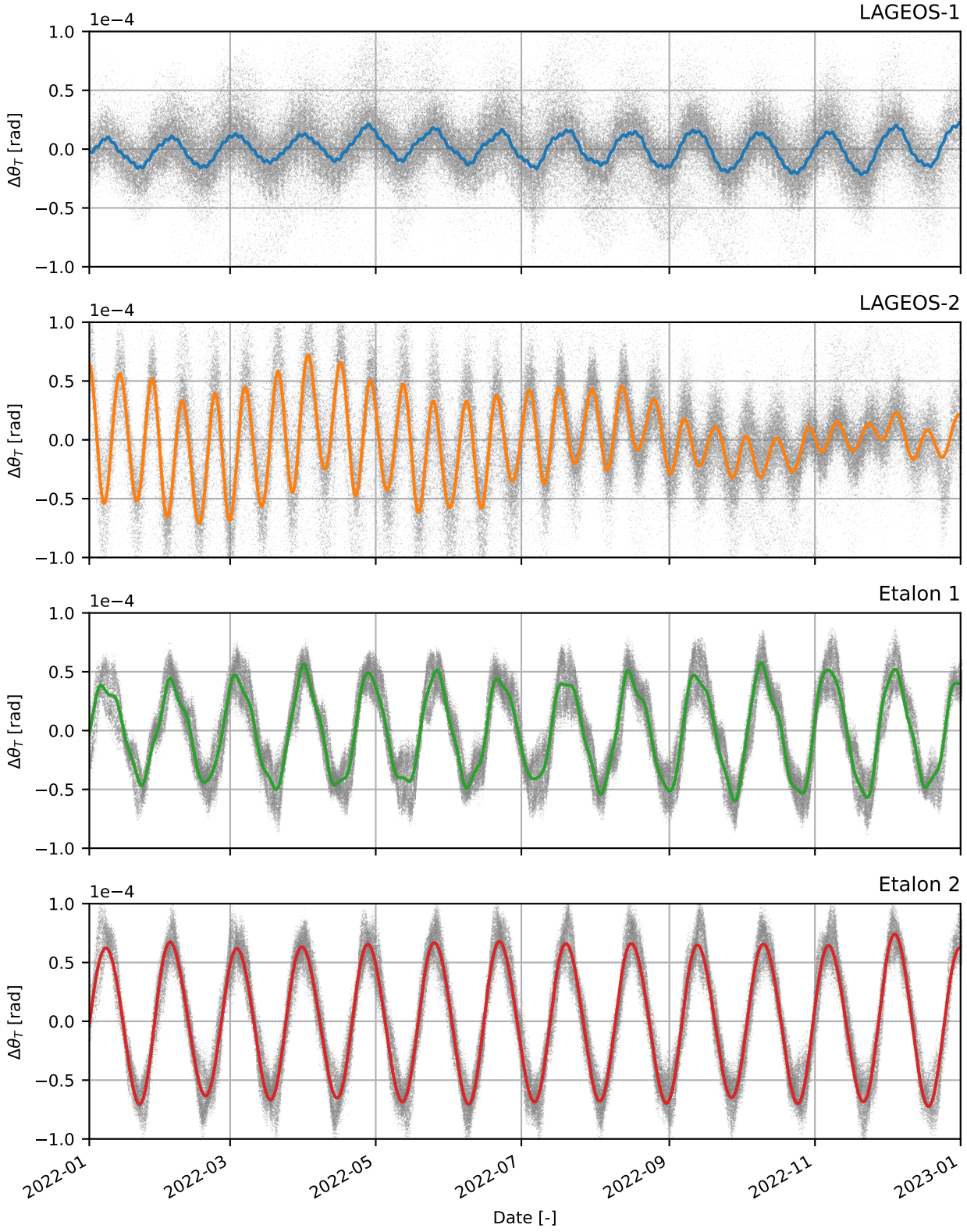


Figure 4.31: FFT-derived time-based along-track position error models for the calibration satellites for the year 2022, using estimated error from 90-day biased P-OD fits. The along-track position error of the TLEs and the models are presented in grey and colour, respectively. Note that the y-axis has been cropped due to extreme outliers.

Table 4.6: Individual test satellite FFT-derived time-based models for the year 2022, using estimated error from 90-day biased P-OD fits filtered with an hourly rolling median. The 20 largest periodic components with periods greater than one day, for Navstar 1 and 2, and two days, for Astra 1E and 1H, were included, in addition to the constant offset. The largest amplitude component is highlighted in bold.

(a) Navstar 1.

a_t [rad]	b_t [days]	c_t [days]	d_t [rad]
1.017×10^{-5}	**9.101×10^{1}**	**-2.567×10^{1}**	**-**
8.448×10^{-6}	4.137×10^{1}	9.504×10^{0}	-
7.133×10^{-6}	6.501×10^{1}	2.461×10^{1}	-
6.808×10^{-6}	2.677×10^{1}	1.069×10^{1}	-
6.258×10^{-6}	1.138×10^{2}	-2.344×10^{1}	-
5.908×10^{-6}	5.056×10^{1}	-1.835×10^{0}	-
5.794×10^{-6}	1.338×10^{1}	-5.001×10^{-1}	-
5.735×10^{-6}	2.275×10^{2}	-2.290×10^{1}	-
5.715×10^{-6}	1.167×10^{1}	2.395×10^{0}	-
5.692×10^{-6}	5.688×10^{1}	-2.389×10^{1}	-
5.519×10^{-6}	1.230×10^{1}	5.487×10^{0}	-
5.474×10^{-6}	9.287×10^{0}	-2.687×10^{0}	-
5.374×10^{-6}	1.083×10^{1}	-3.258×10^{0}	-
5.049×10^{-6}	1.034×10^{1}	4.814×10^{0}	-
4.837×10^{-6}	1.896×10^{1}	-5.649×10^{0}	-
4.786×10^{-6}	3.034×10^{1}	2.398×10^{0}	-
4.687×10^{-6}	3.500×10^{1}	-8.967×10^{0}	-
4.651×10^{-6}	2.844×10^{1}	1.168×10^{1}	-
4.490×10^{-6}	7.584×10^{0}	-2.507×10^{0}	-
4.470×10^{-6}	1.058×10^{1}	1.438×10^{0}	-
-	-	-	9.391×10^{-7}

(b) Navstar 2.

a_t [rad]	b_t [days]	c_t [days]	d_t [rad]
7.403×10^{-5}	**9.101×10^{1}**	**-2.308×10^{1}**	**-**
4.435×10^{-5}	2.677×10^{1}	8.364×10^{0}	-
4.129×10^{-5}	2.844×10^{1}	1.251×10^{1}	-
3.019×10^{-5}	1.517×10^{2}	-7.646×10^{-1}	-
2.557×10^{-5}	1.138×10^{2}	2.874×10^{1}	-
2.464×10^{-5}	5.688×10^{1}	8.543×10^{0}	-
2.435×10^{-5}	6.501×10^{1}	-1.772×10^{1}	-
2.113×10^{-5}	2.275×10^{2}	-1.080×10^{2}	-
1.929×10^{-5}	5.056×10^{1}	-2.397×10^{1}	-
1.429×10^{-5}	2.528×10^{1}	-6.882×10^{0}	-
1.385×10^{-5}	3.250×10^{1}	-1.096×10^{1}	-
1.354×10^{-5}	3.034×10^{1}	2.583×10^{0}	-
1.207×10^{-5}	3.792×10^{1}	-5.854×10^{0}	-
1.098×10^{-5}	7.584×10^{1}	2.148×10^{1}	-
1.011×10^{-5}	2.395×10^{1}	3.387×10^{0}	-
9.599×10^{-6}	3.500×10^{1}	8.530×10^{0}	-
9.517×10^{-6}	2.068×10^{1}	1.022×10^{1}	-
9.232×10^{-6}	2.275×10^{1}	-8.917×10^{0}	-
8.298×10^{-6}	2.167×10^{1}	2.975×10^{-1}	-
7.178×10^{-6}	4.137×10^{1}	1.587×10^{1}	-
-	-	-	-3.463×10^{-6}

(c) Astra 1E.

a_t [rad]	b_t [days]	c_t [days]	d_t [rad]
1.645×10^{-4}	**2.677×10^{1}**	**9.380×10^{0}**	**-**
1.640×10^{-4}	2.844×10^{1}	1.200×10^{1}	-
6.562×10^{-5}	3.250×10^{1}	-1.353×10^{1}	-
6.212×10^{-5}	2.275×10^{2}	4.965×10^{1}	-
5.700×10^{-5}	3.034×10^{1}	-4.451×10^{-1}	-
4.612×10^{-5}	2.528×10^{1}	-5.341×10^{0}	-
4.577×10^{-5}	1.517×10^{2}	-2.636×10^{0}	-
4.363×10^{-5}	4.550×10^{2}	1.499×10^{2}	-
3.774×10^{-5}	2.395×10^{1}	4.680×10^{0}	-
3.582×10^{-5}	9.101×10^{1}	-2.257×10^{1}	-
2.848×10^{-5}	7.584×10^{1}	3.147×10^{1}	-
2.314×10^{-5}	2.275×10^{1}	-7.029×10^{0}	-
1.781×10^{-5}	2.068×10^{1}	-9.232×10^{0}	-
1.766×10^{-5}	1.138×10^{2}	-2.866×10^{1}	-
1.527×10^{-5}	2.167×10^{1}	1.596×10^{0}	-
1.468×10^{-5}	4.137×10^{1}	1.491×10^{1}	-
1.361×10^{-5}	5.688×10^{1}	8.605×10^{0}	-
1.149×10^{-5}	6.501×10^{1}	-3.095×10^{1}	-
1.148×10^{-5}	1.896×10^{1}	6.945×10^{0}	-
1.020×10^{-5}	1.750×10^{1}	4.248×10^{0}	-
-	-	-	-2.974×10^{-5}

(d) Astra 1H.

a_t [rad]	b_t [days]	c_t [days]	d_t [rad]
8.722×10^{-5}	**2.677×10^{1}**	**9.466×10^{0}**	**-**
8.469×10^{-5}	2.844×10^{1}	1.191×10^{1}	-
2.718×10^{-5}	3.034×10^{1}	-2.769×10^{-1}	-
2.635×10^{-5}	2.528×10^{1}	-5.387×10^{0}	-
2.214×10^{-5}	3.250×10^{1}	-1.444×10^{1}	-
1.788×10^{-5}	2.395×10^{1}	5.732×10^{0}	-
1.524×10^{-5}	3.500×10^{1}	4.511×10^{0}	-
1.269×10^{-5}	2.275×10^{1}	-7.705×10^{0}	-
1.170×10^{-5}	1.138×10^{2}	-5.643×10^{1}	-
1.073×10^{-5}	2.167×10^{1}	2.266×10^{0}	-
8.233×10^{-6}	3.792×10^{1}	1.830×10^{0}	-
8.129×10^{-6}	1.379×10^{1}	-1.669×10^{0}	-
7.908×10^{-6}	2.068×10^{1}	-9.594×10^{0}	-
7.308×10^{-6}	1.978×10^{1}	-6.543×10^{-1}	-
7.279×10^{-6}	1.338×10^{1}	-4.625×10^{0}	-
7.254×10^{-6}	1.896×10^{1}	8.488×10^{0}	-
6.683×10^{-6}	4.137×10^{1}	1.354×10^{1}	-
6.567×10^{-6}	5.688×10^{1}	2.282×10^{0}	-
6.202×10^{-6}	9.101×10^{1}	-1.682×10^{1}	-
5.864×10^{-6}	1.517×10^{2}	2.599×10^{1}	-
-	-	-	2.391×10^{-6}

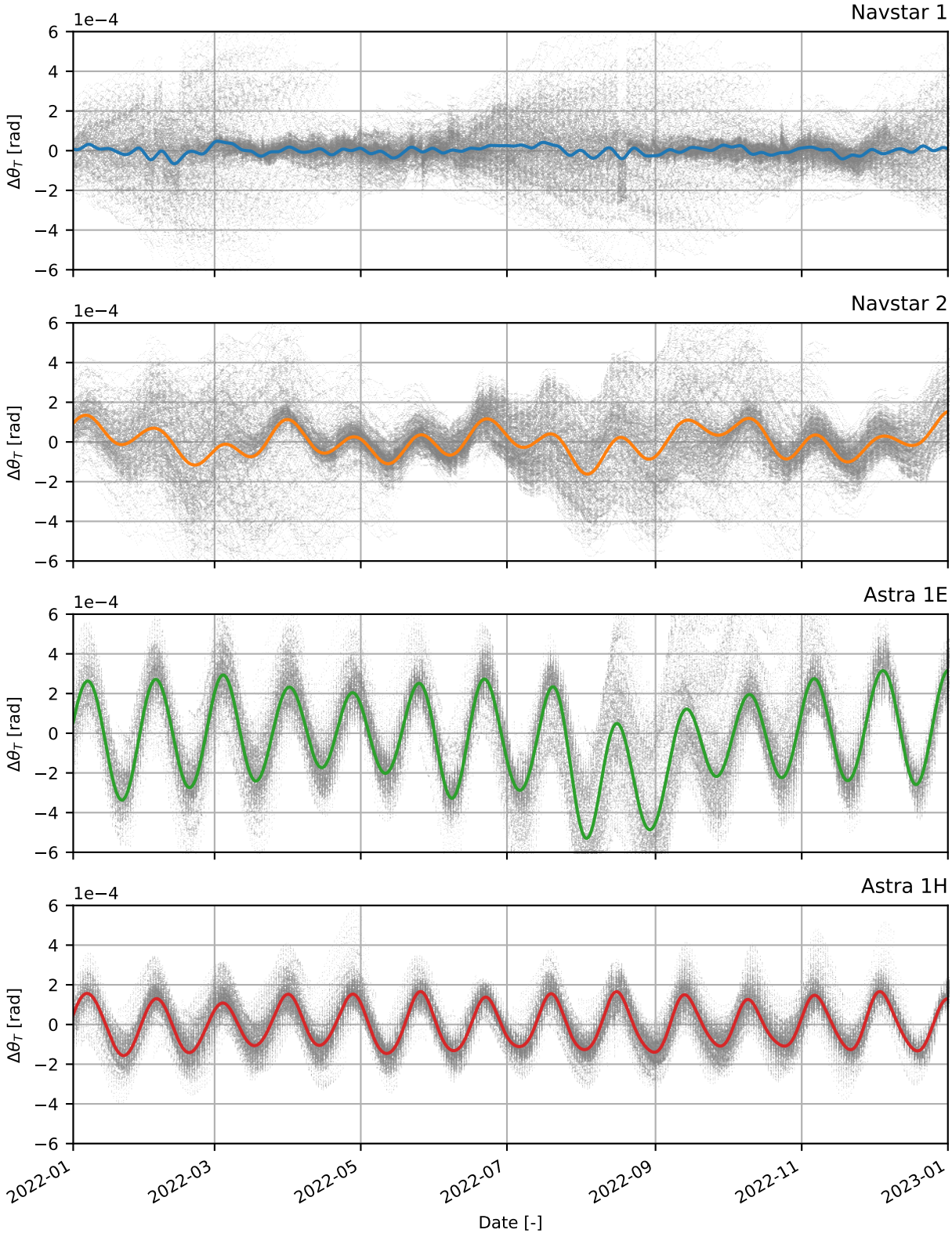


Figure 4.32: FFT-derived time-based along-track position error models for the test satellites for the year 2022, using estimated error from 90-day biased P-OD fits. The along-track position error of the TLEs and the models are presented in grey and colour, respectively. Note that the y-axis has been cropped due to extreme outliers.

Chapter 5

Conclusions

5.1 Summary

In Chapter 1, the motivation and objectives of the thesis were presented, emphasising the challenges faced by a variety of stakeholders due to growing congestion in key orbital regimes, and the demands and requirements this places on SSA. The various sources of RSO ephemerides were outlined, discussing their various advantages and disadvantages, including how TLEs from USSF remain the only publicly available, comprehensive source of RSO ephemerides. The current literature on quantification and improvement of TLE accuracy and uncertainty was introduced, underscoring key issues and questions which need to be addressed, some of which by this thesis. It was reiterated how ephemeris enhancement methods, such as TLE-based P-OD and TLE bias modelling, will continue to remain crucial for many SSA stakeholders, including smaller operators and academia, in the absence of the release of higher quality information, through formats such as Type 4 TLEs compatible with SGP4-XP.

In Chapter 2, the process for conducting P-OD with TLEs was introduced, as described Levit and Marshall [86], using batch least squares state estimation. The SGP4 (and SDP4) propagators were introduced to highlight the perturbations which are included and, importantly, the simplifications which are made by the analytical formulations. TLE sampling techniques were discussed, including forward, backward, and blended strategies, before presenting the batch least squares state estimation method and methods for evaluating the quality of state estimates. The chapter was concluded by specific

considerations for the implementation of the P-OD method, including physical model selection for the numerical propagator, THALASSA, and parameter selection for derivative estimates.

In Chapter 3, it was demonstrated that TLE-based P-OD continues to work with the newer, post-2013 'enhanced' TLEs by testing the method on several geodesy satellites with known, high-accuracy reference ephemerides. At the same time, it was shown that there are major periodic, temporal variations in P-OD fit accuracy that could be attributed to the accuracy of TLEs in a given fit window. These variations were critical as they resulted in P-OD fits which were less accurate for making long-term state predictions than simply using the TLEs and SGP4 directly. It was demonstrated that extending the duration of the fit windows, from the order of days to the order of months, significantly reduced the magnitude of these periodic variations. This ensured that the accuracy of post-fit state predictions were the same or better than simply using TLEs with SGP4. Subsequently, the error characteristics of the geodesy satellites' TLEs were investigated further. This identified the along-track position error and radial velocity error components as the most significant sources of error in their TLEs. Additionally, frequency analysis confirmed the presence of a dominant monthly variation in both error components, excluding LAGEOS-2, which could be attributed to mismodelling of the third-body perturbation from the Moon. Modelling of the along-track position bias was presented as a method for improving pseudo-observation quality prior to conducting P-OD. It was demonstrated that a single periodic oscillation with a period matching that of the Moon's orbit was sufficient to significantly reduce along-track position biases for several of the geodesy satellites. This resulted in an up to 80 % reduction in post-fit error for some P-OD cases. Bias modelling was extended to include multiple GNSS satellites, producing a large-scale bias model which could be applied to other objects in MEO. It was revealed by developing this large-scale bias model that the coplanarity between a satellite's orbit and the orbit of the Moon has significant influence on bias amplitude, further supporting the conclusion that the errors in deep space TLEs are driven primarily by mismodelling of the Moon's third-body perturbation. Finally, higher-order time-based bias models, derived from the frequency analysis, were presented which provided improved and more generalisable results at mitigating deep-space TLE bias.

In Chapter 4, the use of other TLEs as a reference solution was investigated for scenarios where alternative high-accuracy ephemerides are not available, due to this being the case for the overwhelming majority of the TLE catalogue. The relationship between error metrics derived from high-accuracy ephemerides and from TLEs was investigated. It was shown that errors relative to TLEs would need

to be significant to guarantee a certain level of error estimate accuracy. P-OD was conducted on two MEO and two near-GEO satellites and evaluated against TLEs to demonstrate that it can be used still to reveal behaviours such as the periodic oscillation in TLE quality. Importantly, it was demonstrated in this chapter that the results of long-term TLE-based P-OD can be used as a reference solution for developing bias models. By aggregating the results of multiple fits, the true bias can be recovered and modelled, using the same methods as presented in Chapter 3. This opens the door, potentially, to widespread bias modelling across multiple orbital regimes without requiring access to high-accuracy ephemerides, such as USSF's SP catalogue.

5.2 Discussion

The biases present in deep-space TLEs constitute the largest barrier to successfully extracting higher-accuracy, higher-precision state estimates of RSOs through P-OD. Methods that do not account for the influence of the biases are liable to produce misleading state estimates, where it may appear that accuracy has been improved but, where in fact, it has been degraded. The results presented in this thesis demonstrated this risk. Nonetheless, TLE-based P-OD can be a powerful tool when used correctly, keeping in mind the potential pitfalls which are introduced by TLE bias: it was demonstrated that the successful application of P-OD can result in an order of magnitude reduction in post-fit prediction error.

In the context of TLE-based P-OD, state estimation and bias modelling are complimentary to each other, as one can be used to improve the other and vice versa. For short-term P-OD fits, an accurate bias model results in a significant improvement in the consistency of the state estimates; meanwhile, long-term P-OD fits can be used as a substitute for high-accuracy reference ephemerides when creating bias models. It cannot be understated how the two components are tightly coupled, where the combination of both in a P-OD process can be greater than the sum of its parts.

Critically, it has been shown that the accuracy and precision of states from TLEs can be improved through careful application of both P-OD and bias modelling. This opens the possibility of using the TLE dataset for objectives outlined in Chapter 1, such as CA; manoeuvre detection; improved transparency of the near-Earth space environment; better safety and space sustainability; and mitigation of some of the negative effects of spacecraft on 'dark and quiet skies' for scientific research.

5.3 Key Contributions

The key contributions of the thesis were:

1. Demonstration of the continuing applicability of TLE-based P-OD techniques for improving state estimates of RSOs in the near-Earth environment;

2. Presentation of further evidence of widespread, systematic biases affecting deep space TLEs in MEO and GEO due to lunisolar perturbation mismodelling in SGP4;

3. Modelling of important biases present in TLEs with simple, explainable models that do not require large-scale ML models; and

4. Initial demonstration of long-term TLE-based P-OD being used to generate large-scale datasets for further investigation of TLE bias without requiring access to higher-accuracy ephemerides.

5.4 Future Work

In Chapter 3, it was shown that both the single-component time-based models and the Moon-based models were insufficient for accurately modelling the bias present in the TLEs for LAGEOS-1 and -2. At the same time, it was shown that multiple-component FFT-derived time-based models were more effective without requiring *a priori* assumptions. Future work should concentrate on the extension of the time-based models to include additional periodic components. The use of FFTs provides a generalisable method for bias model creation, under the assumption that high-accuracy reference ephemerides are available or, alternatively, P-OD-derived ephemerides, as demonstrated in Section 4.3.

The analysis of TLE bias should be extended and generalised for other orbital regimes. The logical next step is GEO where SGP4 continues to use the same deep space model as in MEO, albeit with some slight changes for low inclination, as seen in Section 2.1. GEO has similar dynamics to MEO where lunisolar and SRP perturbations can have significant influence on orbits. The results of P-OD in this orbital regime presented in Section 4.2 would suggest that the same mismodelling of the lunar third-body perturbation affects GEO TLEs. Bias modelling should be considered for LEO, however it is expected that TLE error behaviour will be different in this orbital regime. Lunisolar perturbations have

a reduced importance relative to other perturbations in LEO and, furthermore, they are not modelled by SGP4 for these orbits. In LEO, the main driver of error will be mismodelling of atmospheric drag which will require different techniques for analysis.

The main limitation of the large-scale bias model presented in Section 3.6 is the limited spatial sampling space. By using GNSS satellites, a large number of high-accuracy ephemerides are available to estimate the biases, however these are limited to a very specific set of orbits in a very narrow band of semi-major axis and inclination, and a limited set of RAANs. Furthermore, the orbits are near-circular, therefore the impact of eccentricity and angle of perigee is not considered. Future work should consider leveraging the bias model estimation without reference ephemerides, as presented in Section 4.3, as a method for greatly expanding the number of objects considered when modelling the bias. A large number of objects, known to be passive such as debris and decommissioned satellites, exist in a number of orbital regimes and could be used to expand the spatial sampling space.

Large-scale bias model estimation may also provide greater insight into the TLE generation pipeline. A question out of scope for this thesis was whether the analysed satellites, both geodesy and GNSS alike, had TLEs that were representative of the general TLE population. Due to these satellites being of particular interest to USSF and other stakeholders, the properties of their TLEs may vary slightly. For example, the spread in mean along-track position offset for GPS satellites does not match other GNSS constellations, despite the satellites and orbits being very similar. This prompts the question of whether these specific satellites and their TLEs are being treated differently by USSF. Additionally, it is unknown whether the TLE generation pipeline includes data from sources such as SLR or GNSS pseudo-ranging to improve the TLEs of these satellites.

The biases present in the TLEs may prevent effective use of sequential filters, such as the Kalman Filter (KF) and its derivatives. Many sequential filters, such as the KF, make certain statistical assumptions, including that observation errors have zero-mean, or in other words that they are unbiased, and that observation error noise is not correlated in time [139]. The systematic, time-varying biases present in TLEs, as identified in Chapter 3, break these assumptions, therefore effective bias modelling may be a requirement before the advantages of sequential filtering can be leveraged for TLE enhancement. There is further scope to consider bias-aware sequential filters [140, 141, 142, 143], where the filter estimates bias alongside state, however the use of such filters will require more detailed investigation.

References

[1] European Space Agency Space Debris Office, 'ESA's Annual Space Environment Report,' Darmstadt, Germany, GEN-DB-LOG-00288-OPS-SD, 19th Jul. 2024. Accessed: 10th Mar. 2025. [Online]. Available: https://www.sdo.esoc.esa.int/environment_report/Space_Environment_Report_latest.pdf.

[2] J. McDowell. 'Starlink Statistics,' Jonathan's Space Report, Accessed: 22nd Sep. 2025. [Online]. Available: https://planet4589.org/space/con/star/stats.html.

[3] Federal Communications Commission, 'In the Matter of Kuiper Systems, LLC Application for Authority to Deploy and Operate a Ka-band Non-Geostationary Satellite Orbit System,' Washington, D.C., United States of America, FCC-20-102A1, 29th Jul. 2020. Accessed: 18th Sep. 2025. [Online]. Available: https://docs.fcc.gov/public/attachments/FCC-20-102A1.pdf.

[4] G. Gillinger, 'Developing and testing China's Guowang constellation,' *The Space Review*, 16th Jun. 2025. Accessed: 18th Sep. 2025. [Online]. Available: https://www.thespacereview.com/article/5004/1.

[5] London Economics, UK Space Agency and Department for Science, Innovation and Technology, 'The economic impact on the UK of a disruption to GNSS,' Aug. 2023. Accessed: 5th Aug. 2025. [Online]. Available: https://www.gov.uk/government/publications/report-the-economic-impact-on-the-uk-of-a-disruption-to-gnss.

[6] International Astronomical Union Centre for the Protection of the Dark, Quiet Sky from Satellite Constellation Interference, G. I. G. Józsa, A. Williams, R. Green, I. Marsh, J. Antoniadis, D. Barbosa, J. Barentine, G. Blanc, A. Boley, B. Coelho, P. Cooper, S. Dalledonne, F. D. Vruno, J. Diamond, A. Dong, R. Drimmel, S. Eggl, N. Habeeb, J. Heim, C. Hofer, N. Hwang, M. Isidro, D. Koplow, J. Lowenthal, S. Lucatello, M. Lyubenova, R. Massey, M. Peel, M. Rawls, A. Saada, A. Sanchez, P. Sanhueza, W. Skidmore, B. Sorokin, P. Sreekumar, T. Stevenson, P. Tartari,

V. Tornatore, C. Walker, B. Winkel and Y. Yakushina, *Call to Protect the Dark and Quiet Sky from Harmful Interference by Satellite Constellations*, 13th Feb. 2025. Accessed: 22nd Aug. 2025. [Online]. Available: http://arxiv.org/abs/2412.08244.

[7] S. Nandakumar, S. Eggl, J. Tregloan-Reed, C. Adam, J. Anderson-Baldwin, M. T. Bannister, A. Battle, Z. Benkhaldoun, T. Campbell, J. P. Colque, G. Damke, I. Plauchu Frayn, M. Ghachoui, P. F. Guillen, A. E. Kaeouach, H. R. Krantz, M. Langbroek, N. Rattenbury, V. Reddy, R. Ridden-Harper, B. Young, E. Unda-Sanzana, A. M. Watson, C. E. Walker, J. C. Barentine, P. Benvenuti, F. Di Vruno, M. W. Peel, M. L. Rawls, C. Bassa, C. Flores-Quintana, P. García, S. Kim, P. Longa-Peña, E. Ortiz, Á. Otarola, M. Romero-Colmenares, P. Sanhueza, G. Siringo and M. Soto, 'The high optical brightness of the BlueWalker 3 satellite,' *Nature*, vol. 623, no. 7989, Nov. 2023. Accessed: 6th Aug. 2025. [Online]. Available: https://www.nature.com/articles/s41586-023-06672-7.

[8] European Space Agency Space Debris Office, 'ESA's Annual Space Environment Report,' Darmstadt, Germany, GEN-DB-LOG-00288-OPS-SD, 31st Mar. 2025. Accessed: 31st Jul. 2025. [Online]. Available: https://www.sdo.esoc.esa.int/environment_report/Space_Environment_Report_latest.pdf.

[9] D. J. Kessler and B. G. Cour-Palais, 'Collision frequency of artificial satellites: The creation of a debris belt,' *Journal of Geophysical Research: Space Physics*, vol. 83, A6 1978. Accessed: 11th Jul. 2025. [Online]. Available: https://onlinelibrary.wiley.com/doi/abs/10.1029/JA083iA06p02637.

[10] J. C. Liou and N. L. Johnson, 'Risks in Space from Orbiting Debris,' *Science*, vol. 311, no. 5759, 20th Jan. 2006. Accessed: 9th Sep. 2025. [Online]. Available: https://www.science.org/doi/10.1126/science.1121337.

[11] J. C. Liou and N. L. Johnson, 'Instability of the present LEO satellite populations,' *Advances in Space Research*, vol. 41, no. 7, 1st Jan. 2008. Accessed: 9th Sep. 2025. [Online]. Available: https://www.sciencedirect.com/science/article/pii/S0273117707004097.

[12] J. C. Liou, 'An active debris removal parametric study for LEO environment remediation,' *Advances in Space Research*, vol. 47, no. 11, 1st Jun. 2011. Accessed: 9th Sep. 2025. [Online]. Available: https://www.sciencedirect.com/science/article/pii/S0273117711000974.

[13] L. Anselmo and C. Pardini, ‘Analysis of the Consequences in Low Earth Orbit of the Collision between Cosmos 2251 and Iridium 33,’ presented at the 21st International Symposium on Space Flight Dynamics, Toulouse, France, Sep. 2009.

[14] T. Wang, ‘Analysis of Debris from the Collision of the Cosmos 2251 and the Iridium 33 Satellites,’ *Science & Global Security*, vol. 18, no. 2, 30th Jun. 2010. Accessed: 23rd Sep. 2025. [Online]. Available: https://doi.org/10.1080/08929882.2010.493078.

[15] R. Shepperd, ‘Subsequent Assessment of the Collision between Iridium 33 and COSMOS 2251,’ presented at the Advanced Maui Optical and Space Surveillance Technologies Conference, Maui, Hawaii, United States of America, Sep. 2023.

[16] N. L. Johnson, E. Stansbery, J. C. Liou, M. Horstman, C. Stokely and D. Whitlock, ‘The characteristics and consequences of the break-up of the Fengyun-1C spacecraft,’ *Acta Astronautica*, Touching Humanity - Space for Improving Quality of Life. Selected Proceedings of the 58th International Astronautical Federation Congress, Hyderabad, India, 24-28 September 2007, vol. 63, no. 1, 1st Jul. 2008. Accessed: 9th Sep. 2025. [Online]. Available: https://www.sciencedirect.com/science/article/pii/S0094576507003281.

[17] C. Stokely and M. Matney, ‘Haystack Radar Observations of Debris from the Fengyun-1C Antisatellite Test,’ *Orbital Debris Quarterly News*, vol. 12, no. 3, Jul. 2008. Accessed: 9th Sep. 2025. [Online]. Available: https://orbitaldebris.jsc.nasa.gov/quarterly-news/pdfs/ODQNv12i3.pdf.

[18] C. Pardini and L. Anselmo, ‘Assessment of the consequences of the Fengyun-1C breakup in low Earth orbit,’ *Advances in Space Research*, vol. 44, no. 5, 1st Sep. 2009. Accessed: 9th Sep. 2025. [Online]. Available: https://www.sciencedirect.com/science/article/pii/S0273117709002531.

[19] United States of America, United Kingdom of Great Britain and Northern Ireland and Union of Soviet Socialist Republics, *Treaty on principles governing the activities of States in the exploration and use of outer space, including the moon and other celestial bodies*, 1967. Accessed: 28th Jul. 2025. [Online]. Available: https://treaties.un.org/Pages/showDetails.aspx?objid=0800000280128cbd.

[20] Foreign, Commonwealth & Development Office and UK Space Agency, ‘Responsible space behaviours: the UK commits not to destructively test direct ascent anti-satellite missiles,’ 3rd Oct. 2022. Accessed: 10th Jul. 2025. [Online]. Available: https://www.gov.uk/govern

ment/news/responsible-space-behaviours-the-uk-commits-not-to-destructively-test-direct-ascent-anti-satellite-missiles.

[21] Inter-Agency Space Debris Coordination Committee, 'IADC Report on the Status of the Space Debris Environment,' IADC-23-01 Issue 3, Jan. 2025. Accessed: 22nd Aug. 2025. [Online]. Available: https://iadc-home.org/documents_public/file_down/id/5837.

[22] European Space Agency Space Debris Mitigation Working Group, *ESA Space Debris Mitigation Requirements*, 30th Oct. 2023. Accessed: 22nd Aug. 2025. [Online]. Available: https://sdup.esoc.esa.int/documents/download/ESSB-ST-U-007_Issue_1_30October2023.pdf.

[23] Federal Communications Commission, 'Space Innovation; Mitigation of Orbital Debris in the New Space Age,' F.R. 89, 9th Aug. 2024. Accessed: 22nd Aug. 2025. [Online]. Available: https://www.federalregister.gov/d/2024-17093.

[24] Inter-Agency Space Debris Coordination Committee, *IADC Space Debris Mitigation Guidelines*, version 4, Jan. 2025. Accessed: 7th Jul. 2025. [Online]. Available: https://www.iadc-home.org/documents_public/file_down/id/5836.

[25] D. McKnight, R. Witner, F. Letizia, S. Lemmens, L. Anselmo, C. Pardini, A. Rossi, C. Kunstadter, S. Kawamoto, V. Aslanov, J.-C. Dolado Perez, V. Ruch, H. Lewis, M. Nicolls, L. Jing, S. Dan, W. Dongfang, A. Baranov and D. Grishko, 'Identifying the 50 statistically-most-concerning derelict objects in LEO,' *Acta Astronautica*, vol. 181, 1st Apr. 2021. Accessed: 11th Jul. 2025. [Online]. Available: https://www.sciencedirect.com/science/article/pii/S0094576521000217.

[26] D. S. Mcknight, E. Dale, J. Cassady, S. Kawamoto, A. Rossi, A. Ratcliffe and D. Grishko, 'An Update of the Top 50 List,' presented at the 9th European Conference on Space Debris, 2025. Accessed: 28th Jul. 2025. [Online]. Available: https://conference.sdo.esoc.esa.int/proceedings/sdc9/paper/4.

[27] A. Gini, 'Don Kessler on Envisat and the Kessler Syndrome,' *Space Safety Magazine*, 25th Apr. 2012. Accessed: 11th Jul. 2025. [Online]. Available: https://www.spacesafetymagazine.com/space-debris/kessler-syndrome/don-kessler-envisat-kessler-syndrome/.

[28] European Space Agency, 'From active debris removal to in-orbit servicing: the legacy of e.Deorbit,' 26th Nov. 2018. Accessed: 19th Sep. 2025. [Online]. Available: https://blogs.esa.int/cleanspace/2018/11/26/from-active-debris-removal-to-in-orbit-servicing-the-legacy-of-e-deorbit/.

[29] European Space Agency, ‘ESA commissions world’s first space debris removal,’ 9th Dec. 2019. Accessed: 19th Sep. 2025. [Online]. Available: https://www.esa.int/Space_Safety/Clean_Space/ESA_commissions_world_s_first_space_debris_removal.

[30] N. T. Redd, ‘Bringing satellites back from the dead: Mission extension vehicles give defunct spacecraft a new lease on life - [News],’ *IEEE Spectrum*, vol. 57, no. 8, Aug. 2020. Accessed: 22nd Jul. 2025. [Online]. Available: https://ieeexplore.ieee.org/document/9150540.

[31] Northrop Grumman, ‘Northrop Grumman Achieves First-Ever Undocking Between Two Commercial Spacecraft in Geosynchronous Orbit,’ 9th Apr. 2025. Accessed: 22nd Jul. 2025. [Online]. Available: https://news.northropgrumman.com/satellites/Northrop-Grumman-Achieves-First-Ever-Undocking-Between-Two-Commercial-Spacecraft-in-Geosynchronous-Orbit.

[32] J. Amos, ‘Commercial satellites dock high above Earth,’ *BBC News*, 13th Apr. 2021. Accessed: 22nd Jul. 2025. [Online]. Available: https://www.bbc.com/news/science-environment-56731502.

[33] M. A. Skinner, D. Oltrogge, M. Strah, R. J. Rovetto, A. Lacroix, A. K. A. Kumar, K. Grattan, L. Francillout and I. Alonso, ‘Space traffic management terminology,’ *Journal of Space Safety Engineering*, vol. 9, no. 4, 1st Dec. 2022. Accessed: 12th Aug. 2025. [Online]. Available: https://www.sciencedirect.com/science/article/pii/S2468896722001069.

[34] M. J. Holzinger and M. K. Jah, ‘Challenges and Potential in Space Domain Awareness,’ *Journal of Guidance, Control, and Dynamics*, vol. 41, no. 1, 2018. Accessed: 23rd Sep. 2025. [Online]. Available: https://doi.org/10.2514/1.G003483.

[35] T. D. Hall, G. F. Duff and L. J. Maciel, ‘The Space Mission at Kwajalein,’ *Lincoln Laboratory Journal*, vol. 19, no. 2, 2012. Accessed: 27th Sep. 2025. [Online]. Available: https://www.ll.mit.edu/sites/default/files/page/doc/2018-05/19_2_3_Hall.pdf.

[36] B. Weeden, P. Cefola and J. Sankaran, ‘Global Space Situational Awareness Sensors,’ presented at the Advanced Maui Optical and Space Surveillance Technologies Conference, Maui, Hawaii, United States of America, Sep. 2010. Accessed: 28th Sep. 2025. [Online]. Available: https://amostech.com/TechnicalPapers/2010/Integrating_Diverse_Data/Weeden.pdf.

[37] G. Muntoni, G. Montisci, T. Pisanu, P. Andronico and G. Valente, ‘Crowded Space: A Review on Radar Measurements for Space Debris Monitoring and Tracking,’ *Applied Sciences*, vol. 11, no. 4, Jan. 2021. Accessed: 28th Sep. 2025. [Online]. Available: https://www.mdpi.com/2076-3417/11/4/1364.

[38] J. A. Haimerl and G. P. Fonder, ‘Space Fence System Overview,’ presented at the Advanced Maui Optical and Space Surveillance Technologies Conference, Maui, Hawaii, United States of America, Sep. 2015. Accessed: 23rd Sep. 2025. [Online]. Available: https://amostech.com/TechnicalPapers/2015/SSA/Haimerl.pdf.

[39] G. Fonder, M. Hughes, M. Dickson, M. Schoenfeld and J. Gardner, ‘Space Fence Radar Overview,’ in *2019 International Applied Computational Electromagnetics Society Symposium (ACES)*, Apr. 2019. Accessed: 23rd Sep. 2025. [Online]. Available: https://ieeexplore.ieee.org/abstract/document/8712890.

[40] T. Michal, J. P. Eglizeaud and J. Bouchard, ‘GRAVES: The new French System for Space Surveillance,’ presented at the 4th European Conference on Space Debris, Darmstadt, Germany, Aug. 2005. Accessed: 23rd Sep. 2025. [Online]. Available: https://conference.sdo.esoc.esa.int/proceedings/sdc4/paper/122/SDC4-paper122.pdf.

[41] A. Bloom, J. Wysack, J. D. Griesbach and A. Lawitzke, ‘Space and Ground-Based SDA Sensor Performance Comparisons,’ presented at the Advanced Maui Optical and Space Surveillance Technologies Conference, Maui, Hawaii, United States of America, Sep. 2022. Accessed: 28th Sep. 2025. [Online]. Available: https://amostech.com/TechnicalPapers/2022/Poster/Bloom.pdf.

[42] E. Kaygorodov, M. Hjelmstad Rattigan, M. I. Hallgarten La Casta and D. Amato, ‘Development and Operation of CICLOPS, the Compact Imperial College London Optical Sensor,’ presented at the 9th European Conference on Space Debris, Bonn, Germany, Apr. 2025. Accessed: 28th Sep. 2025. [Online]. Available: https://conference.sdo.esoc.esa.int/proceedings/sdc9/paper/283.

[43] K. Burke, ‘China’s Different Approach to Space Situational Awareness,’ China Aerospace Studies Institute, Dec. 2024. Accessed: 24th Sep. 2025. [Online]. Available: https://www.airuniversity.af.edu/Portals/10/CASI/documents/Research/Space/2024-12-02%20China’s%20Different%20Approach%20to%20Space%20Situational%20Awareness.pdf?ver=C9GMGVpQFfXWJWBtKeaIEA%3d%3d.

[44] J. Rowland, D. McKnight, B. P. Pino, B. Reihs and M. A. Stevenson, ‘A Worldwide Network of Radars for Space Domain Awareness in Low Earth Orbit,’ presented at the Advanced Maui Optical and Space Surveillance Technologies Conference, Maui, Hawaii, United States of America, Sep. 2021.

[45] L. Tantiparimongkol, X. Guo, P. Gao, M. Shen, H. Yu and Y. Zhao, 'Study and investigation on LeoLabs radar for space traffic management,' in *AOPC 2024: Astronomical Technologies and Instrumentation*, vol. 13505, SPIE, 13th Dec. 2024. Accessed: 23rd Sep. 2025. [Online]. Available: https://www.spiedigitallibrary.org/conference-proceedings-of-spie/13505/1350504/Study-and-investigation-on-LeoLabs-radar-for-space-traffic-management/10.1117/12.3046705.full.

[46] LeoLabs. 'Radars,' Accessed: 23rd Sep. 2025. [Online]. Available: https://leolabs.space/radars/.

[47] ExoAnalytic Solutions. 'Space Domain Awareness,' Accessed: 23rd Sep. 2025. [Online]. Available: https://exoanalytic.com/space-domain-awareness/.

[48] T. Hitchens, 'Space Force cell explores reorg to push commercial data to military,' *Breaking Defense*, 17th Sep. 2025. Accessed: 23rd Sep. 2025. [Online]. Available: https://breakingdefense.com/2025/09/space-force-reorganizing-to-add-commercial-space-monitoring-data-analysis-into-operations/.

[49] T. Hitchens, 'Beyond 'potpourri' of sensors: Saltzman pushes holistic approach to space domain awareness,' *Breaking Defense*, 18th Sep. 2025. Accessed: 23rd Sep. 2025. [Online]. Available: https://breakingdefense.com/2025/09/beyond-potpourri-of-sensors-saltzman-pushes-holistic-approach-to-space-domain-awareness/.

[50] M. R. Pearlman, C. E. Noll, E. C. Pavlis, F. G. Lemoine, L. Combrink, J. J. Degnan, G. Kirchner and U. Schreiber, 'The ILRS: approaching 20 years and planning for the future,' *Journal of Geodesy*, vol. 93, no. 11, 1st Nov. 2019. Accessed: 8th Apr. 2025. [Online]. Available: https://doi.org/10.1007/s00190-019-01241-1.

[51] K. Sośnica, D. Thaller, R. Dach, P. Steigenberger, G. Beutler, D. Arnold and A. Jäggi, 'Satellite laser ranging to GPS and GLONASS,' *Journal of Geodesy*, vol. 89, no. 7, 1st Jul. 2015. Accessed: 28th Sep. 2025. [Online]. Available: https://doi.org/10.1007/s00190-015-0810-8.

[52] K. Sośnica, L. Prange, K. Kaźmierski, G. Bury, M. Drożdżewski, R. Zajdel and T. Hadas, 'Validation of Galileo orbits using SLR with a focus on satellites launched into incorrect orbital planes,' *Journal of Geodesy*, vol. 92, no. 2, 1st Feb. 2018. Accessed: 30th Jul. 2025. [Online]. Available: https://doi.org/10.1007/s00190-017-1050-x.

[53] G. Bury, K. Sośnica and R. Zajdel, 'Multi-GNSS orbit determination using satellite laser ranging,' *Journal of Geodesy*, vol. 93, no. 12, Dec. 2019. Accessed: 8th Apr. 2025. [Online]. Available: http://link.springer.com/10.1007/s00190-018-1143-1.

[54] G. Bury, K. Sośnica, R. Zajdel, D. Strugarek and U. Hugentobler, 'Determination of precise Galileo orbits using combined GNSS and SLR observations,' *GPS Solutions*, vol. 25, no. 1, 31st Oct. 2020. Accessed: 30th Jul. 2025. [Online]. Available: https://doi.org/10.1007/s10291-020-01045-3.

[55] F. R. Hoots, P. W. Schumacher and R. A. Glover, 'History of Analytical Orbit Modeling in the US Space Surveillance System,' *Journal of Guidance, Control, and Dynamics*, vol. 27, no. 2, Mar. 2004. Accessed: 10th Feb. 2020. [Online]. Available: https://arc.aiaa.org/doi/10.2514/1.9161.

[56] United States Space Force, *Space Track*. Accessed: 27th Sep. 2025. [Online]. Available: https://www.space-track.org/.

[57] M. D. Hejduk, S. J. Casali, D. A. Cappellucci, N. L. Ericson and D. E. Snow, 'A catalogue-wide implementation of general perturbations orbit determination extrapolated from higher order orbital theory solutions,' presented at the AAS/AIAA Spaceflight Mechanics Meeting, Kauai, Hawaii, United States of America, Aug. 2013.

[58] D. Conkey and M. Zielinski, 'Assessing Performance Characteristics of the SGP4-XP Propagation Algorithm,' presented at the Advanced Maui Optical and Space Surveillance Technologies Conference, Maui, Hawaii, United States of America, Sep. 2022.

[59] C.-C. Chao and F. R. Hoots, *Applied Orbit Perturbation and Maintenance*, 2nd ed. El Segundo, California, United States of America: The Aerospace Press, 2018.

[60] T. Payne, F. Hoots, A. Butkus, Z. Slatton and D. Nguyen, 'Improvements to the SGP4 propagator (SGP4-XP),' presented at the Advanced Maui Optical and Space Surveillance Technologies Conference, Maui, Hawaii, United States of America, Sep. 2022.

[61] A. Holincheck and J. Cathell, 'Improved Orbital Predictions using Pseudo Observations - Maximizing the Utility of SGP4-XP,' presented at the Advanced Maui Optical and Space Surveillance Technologies Conference, Maui, Hawaii, United States of America, Sep. 2021.

[62] International Laser Ranging Service, *SLR Orbit Products*. Accessed: 27th Sep. 2025. [Online]. Available: https://cddis.nasa.gov/archive/slr/products/orbits/.

[63] D. Hampf, S. Bauer, M. Ploner, L. Heinzl, A. Kloth, E. Bennemann, D. Escobar, E. Cordelli and D. Tietze, 'Space Debris Laser Ranging: Moving from experiments to operation,' presented at

the 9th European Conference on Space Debris, Bonn, Germany, 2025. Accessed: 28th Jul. 2025. [Online]. Available: https://conference.sdo.esoc.esa.int/proceedings/sdc9/paper/39.

[64] M. A. Steindorfer, G. Kirchner, F. Koidl, P. Wang, B. Jilete and T. Flohrer, 'Daylight space debris laser ranging,' *Nature Communications*, vol. 11, no. 1, 4th Aug. 2020. Accessed: 30th Jul. 2025. [Online]. Available: https://www.nature.com/articles/s41467-020-17332-z.

[65] M. A. Steindorfer, P. Wang, F. Koidl and G. Kirchner, 'Space debris and satellite laser ranging combined using a megahertz system,' *Nature Communications*, vol. 16, no. 1, 10th Jan. 2025. Accessed: 30th Jul. 2025. [Online]. Available: https://www.nature.com/articles/s41467-024-55777-8.

[66] M. Brunet, A. Auriol, P. Agnieray and F. Nouel, 'DORIS precise orbit determination and localization system description and USOs performances,' in *Proceedings of the 1995 IEEE International Frequency Control Symposium (49th Annual Symposium)*, May 1995. Accessed: 2nd Apr. 2025. [Online]. Available: https://ieeexplore.ieee.org/document/483892/?arnumber=483892.

[67] Centre National d'Études Spatiales, 'DORIS for Beginners,' 10102016, 10th Oct. 2016. Accessed: 2nd Apr. 2025. [Online]. Available: https://ids-doris.org/documents/BC/WhatIsDORIS.pdf.

[68] International DORIS Service, *DORIS Orbit Products*. Accessed: 27th Sep. 2025. [Online]. Available: https://cddis.nasa.gov/archive/doris/products/orbits/.

[69] International GNSS Service, 'International GNSS Service: Terms of Reference,' 2019. Accessed: 1st Jul. 2025. [Online]. Available: https://files.igs.org/pub/resource/governance/IGS-Terms-of-Reference-2019.pdf.

[70] International GNSS Service, *GNSS Orbit Products*. Accessed: 27th Sep. 2025. [Online]. Available: https://cddis.nasa.gov/archive/gnss/products/.

[71] International GNSS Service. 'Antenna Committee,' Accessed: 27th Sep. 2025. [Online]. Available: https://igs.org/wg/antenna/.

[72] N. Bonnor, 'A Brief History of Global Navigation Satellite Systems,' *The Journal of Navigation*, vol. 65, no. 1, Jan. 2012. Accessed: 28th Sep. 2025. [Online]. Available: https://www.cambridge.org/core/journals/journal-of-navigation/article/brief-history-of-global-navigation-satellite-systems/F3B51AED21EAD7459CA7A09E4C37E765.

[73] 'GLONASS: The Once and Future GNSS,' *Inside GNSS*, 1st Jan. 2006. Accessed: 28th Sep. 2025. [Online]. Available: https://insidegnss.com/glonass-the-once-and-future-gnss/.

[74] R. B. Langley, 'Innovation: GPS, GLONASS and More,' *GPS World*, 1st Jun. 2010. Accessed: 28th Sep. 2025. [Online]. Available: https://www.gpsworld.com/innovation-gps-glonass-and-more/.

[75] United Nations Office for Outer Space Affairs, *The Interoperable Global Navigation Satellite Systems Space Service Volume*. Vienna, Austria: United Nations, Oct. 2018. Accessed: 28th Sep. 2025. [Online]. Available: https://www.un-ilibrary.org/outer-space/the-interoperable-global-navigation-satellite-systems-space-service-volume_5fce7904-en.

[76] T. A. Stansell, 'GNSS Interoperability,' in *Position, Navigation, and Timing Technologies in the 21st Century: Integrated Satellite Navigation, Sensor Systems, and Civil Applications*, Y. J. Morton, F. van Diggelen, J. J. Spilker Jr. and B. W. Parkinson, Eds., Wiley-IEEE Press, 2021. Accessed: 28th Sep. 2025. [Online]. Available: https://ieeexplore.ieee.org/document/9305068.

[77] European Space Agency, 'Galileo begins serving the globe,' 15th Dec. 2016. Accessed: 28th Sep. 2025. [Online]. Available: https://www.esa.int/Applications/Satellite_navigation/Galileo_begins_serving_the_globe.

[78] Y. Jiang, S. Zhang and H. Zhao, *BeiDou Navigation Satellite System: Maritime Applications*, 1st ed. Singapore: Springer Singapore, 22nd Mar. 2025, 260 pp. Accessed: 28th Sep. 2025. [Online]. Available: https://link.springer.com/book/10.1007/978-981-96-2192-7.

[79] P. Marks, 'China's satellite navigation plans threaten Galileo,' *New Scientist*, 8th Nov. 2006. Accessed: 28th Sep. 2025. [Online]. Available: https://www.newscientist.com/article/dn10472-chinas-satellite-navigation-plans-threaten-galileo/.

[80] D. Levin, 'Chinese Square Off With Europe in Space,' *The New York Times*, 23rd Mar. 2009. Accessed: 28th Sep. 2025. [Online]. Available: https://www.nytimes.com/2009/03/23/technology/23iht-galileo23.html.

[81] International Laser Ranging Service. 'ILRS Operational Station Identification Table,' Accessed: 1st Jul. 2025. [Online]. Available: https://ilrs.gsfc.nasa.gov/network/stations/active/.

[82] International DORIS Service. 'DORIS stations (Site Logs),' Accessed: 30th Jun. 2025. [Online]. Available: https://ids-doris.org/network-stations/sites.html.

[83] International GNSS Service. 'Network Resources,' Accessed: 1st Jul. 2025. [Online]. Available: https://igs.org/network-resources/.

[84] M. E. Fieger, ‘An Evaluation of Semianalytical Satellite Theory against Long Arcs of Real Data for Highly Eccentric Orbits,’ Master’s Thesis, Massachussetts Institute of Technology, Cambridge, Massachusetts, United States of America, Jan. 1987. Accessed: 18th Nov. 2021. [Online]. Available: https://apps.dtic.mil/sti/pdfs/ADA185825.pdf.

[85] T. Flohrer, H. Krag and H. Klinkrad, ‘Assessment and Categorization of TLE Orbit Errors for the US SSN Catalogue,’ presented at the Advanced Maui Optical and Space Surveillance Technologies Conference, Maui, Hawaii, United States of America, Sep. 2008.

[86] C. Levit and W. Marshall, ‘Improved orbit predictions using two-line elements,’ *Advances in Space Research*, vol. 47, no. 7, 1st Apr. 2011. Accessed: 28th Jan. 2020. [Online]. Available: http://www.sciencedirect.com/science/article/pii/S0273117710006964.

[87] J. C. Bennett, J. Sang, C. Smith and K. Zhang, ‘Improving low-Earth orbit predictions using two-line element data with bias correction,’ presented at the Advanced Maui Optical and Space Surveillance Technologies Conference, Maui, Hawaii, United States of America, Sep. 2012.

[88] D. A. Vallado, B. Bastida Virgili and T. Flohrer, ‘Improved SSA through orbit determination of Two-Line-Element sets,’ presented at the 6th European Conference on Space Debris, Darmstadt, Germany, Apr. 2013.

[89] D. L. Oltrogge and J. Ramrath, ‘Parametric Characterization of SGP4 Theory and TLE Positional Accuracy,’ presented at the Advanced Maui Optical and Space Surveillance Technologies Conference, Maui, Hawaii, United States of America, Sep. 2014.

[90] J. F. San-Juan, I. Pérez, M. San-Martín and E. P. Vergara, ‘Hybrid SGP4 orbit propagator,’ *Acta Astronautica*, vol. 137, 1st Aug. 2017. Accessed: 28th Nov. 2025. [Online]. Available: https://www.sciencedirect.com/science/article/pii/S0094576516311535.

[91] P. R. Winters, ‘Forecasting Sales by Exponentially Weighted Moving Averages,’ *Management Science*, vol. 6, no. 3, 1960. Accessed: 27th Jan. 2026. [Online]. Available: https://www.jstor.org/stable/2627346.

[92] J. Geul, E. Mooij and R. Noomen, ‘TLE uncertainty estimation using robust weighted differencing,’ *Advances in Space Research*, vol. 59, no. 10, 15th May 2017. Accessed: 31st Oct. 2023. [Online]. Available: https://www.sciencedirect.com/science/article/pii/S0273117717301515.

[93] D. Racelis and M. Joerger, ‘High-Integrity TLE Error Models for MEO and GEO Satellites,’ presented at the 2018 AIAA SPACE and Astronautics Forum and Exposition, Orlando, Florida, United States of America, 17th Sep. 2018.

[94] I. Pérez, M. San-Martín, R. López, E. P. Vergara, A. Wittig and J. F. San-Juan, 'Extending the hybrid methodology for orbit propagation by fitting techniques,' *Neurocomputing*, Recent Advancements in Hybrid Artificial Intelligence Systems, vol. 354, 18th Aug. 2019. Accessed: 28th Nov. 2025. [Online]. Available: https://www.sciencedirect.com/science/article/pii/S0925231219304618.

[95] T. J. Hastie, *Generalized Additive Models*. New York: Routledge, 19th Oct. 2017.

[96] J. H. Friedman, 'Multivariate Adaptive Regression Splines,' *The Annals of Statistics*, vol. 19, no. 1, Mar. 1991. Accessed: 29th Jan. 2026. [Online]. Available: https://projecteuclid.org/journals/annals-of-statistics/volume-19/issue-1/Multivariate-Adaptive-Regression-Splines/10.1214/aos/1176347963.full.

[97] D. Ly, R. Lucken and D. Giolito, 'Correcting TLEs at epoch: Application to the GPS constellation,' *Journal of Space Safety Engineering*, Space Debris: The State of Art, vol. 7, no. 3, 1st Sep. 2020. Accessed: 31st Oct. 2023. [Online]. Available: https://www.sciencedirect.com/science/article/pii/S2468896720300963.

[98] B. Li, Y. Zhang, J. Huang and J. Sang, 'Improved orbit predictions using two-line elements through error pattern mining and transferring,' *Acta Astronautica*, vol. 188, 1st Nov. 2021. Accessed: 7th Aug. 2025. [Online]. Available: https://www.sciencedirect.com/science/article/pii/S0094576521004045.

[99] J. Chen and C. Lin, 'Research on Enhanced Orbit Prediction Techniques Utilizing Multiple Sets of Two-Line Element,' *Aerospace*, vol. 10, no. 6, Jun. 2023. Accessed: 9th Jan. 2024. [Online]. Available: https://www.mdpi.com/2226-4310/10/6/532.

[100] H. Bizalion, A. Guillot, A. Petit and R. Lucken, 'Systematic TLE data improvement by neural network for most cataloged resident space objects,' *Advances in Space Research*, Space Environment Management and Space Sustainability, vol. 72, no. 7, 1st Oct. 2023. Accessed: 7th Aug. 2025. [Online]. Available: https://www.sciencedirect.com/science/article/pii/S0273117722005804.

[101] D. L. Oltrogge, G. Getz, D. Vallado, S. Alfano, R. Gist and S. Shogren, 'Using Spacebook and Cesium to promote and enhance flight safety,' presented at the 9th European Conference on Space Debris, Bonn, Germany, 2025. Accessed: 28th Jul. 2025. [Online]. Available: https://conference.sdo.esoc.esa.int/proceedings/sdc9/paper/212.

[102] M. I. Hallgarten La Casta and D. Amato, ‘Debiasing of two-line element sets for batch least squares pseudo-orbit determination in MEO and GEO,’ *Advances in Space Research*, vol. 75, no. 10, 15th May 2025. Accessed: 6th May 2025. [Online]. Available: https://www.sciencedirect.com/science/article/pii/S0273117725002856.

[103] M. I. Hallgarten La Casta and D. Amato, ‘Bias Correction of Two-line Element Sets in the MEO Regime,’ presented at the NATO DIANA International Workshop, London, United Kingdom, 4th Apr. 2025.

[104] M. I. Hallgarten La Casta and D. Amato, ‘Generalisable Bias Correction of Two-line Element Sets in the Medium Earth Orbit Regime,’ presented at the 9th European Conference on Space Debris, Bonn, Germany, Apr. 2025. Accessed: 28th Sep. 2025. [Online]. Available: https://conference.sdo.esoc.esa.int/proceedings/sdc9/paper/282.

[105] M. I. Hallgarten La Casta and D. Amato, ‘Revisiting Filtering of Two-line Element Sets for Higher Precision Ephemerides,’ presented at the 29th International Symposium on Space Flight Dynamics, ESA ESOC, Darmstadt, Germany, Apr. 2024. Accessed: 28th Sep. 2025. [Online]. Available: https://www.researchgate.net/publication/380784772_Revisiting_Filtering_of_Two-line_Element_Sets_for_Higher_Precision_Ephemerides.

[106] M. I. Hallgarten La Casta, D. Amato and M. Vasile, ‘Chebyhsev-based Polynomial Algebra Monte Carlo Propagation with Generalised Equinoctial Orbital Elements,’ presented at the 2nd International Stardust Conference, ESA ESTEC, Noordwijk, the Netherlands, 8th Nov. 2022.

[107] M. I. Hallgarten La Casta, D. Amato and M. Vasile, ‘Polynomial Algebra for Uncertainty Propagation in Generalised Equinoctial Orbital Elements,’ presented at the 73rd International Astronautical Congress, Paris, France, 19th Sep. 2022. Accessed: 28th Sep. 2025. [Online]. Available: https://www.researchgate.net/publication/365114606_Polynomial_Algebra_for_Uncertainty_Propagation_in_Generalised_Equinoctial_Orbital_Elements.

[108] M. I. Hallgarten La Casta, L. Sánchez Fernandez-Mellado, D. Amato and M. Vasile, ‘Non-linear set propagation with generalised equinoctial orbital elements,’ presented at the 5th International Workshop on Key Topics in Orbit Propagation Applied to Space Situational Awareness, Logroño, Spain, 23rd Jun. 2022.

[109] D. Vallado, P. Crawford, R. Hujsak and T. Kelso, ‘Revisiting Spacetrack Report #3,’ presented at the AIAA/AAS Astrodynamics Specialist Conference and Exhibit, Keystone, Colorado,

United States of America, 21st Aug. 2006. Accessed: 11th Oct. 2022. [Online]. Available: https://arc.aiaa.org/doi/10.2514/6.2006-6753.

[110] F. R. Hoots and R. L. Roehrich, 'Spacetrack Report No. 3: Models for Propagation of NORAD Element Sets,' United States Air Force, Peterson Air Force Base, Colorado, United States of America, Dec. 1980.

[111] I. A. Araya and D. Amato, 'Spectral analysis of US Space Catalog ephemerides for LAGEOS-1,' in *AIAA SCITECH 2022 Forum*, American Institute of Aeronautics and Astronautics. Accessed: 30th Sep. 2024. [Online]. Available: https://arc.aiaa.org/doi/abs/10.2514/6.2022-1772.

[112] J. D. Giorgini, *Private Communication*, 1st Dec. 2021.

[113] K. Levenberg, 'A Method for the Solution of Certain Non-Linear Problems in Least Squares,' *Quarterly of Applied Mathematics*, vol. 2, no. 2, 1944. Accessed: 16th Dec. 2024. [Online]. Available: https://www.jstor.org/stable/43633451.

[114] D. W. Marquardt, 'An Algorithm for Least-Squares Estimation of Nonlinear Parameters,' *Journal of the Society for Industrial and Applied Mathematics*, vol. 11, no. 2, 1963. Accessed: 16th Dec. 2024. [Online]. Available: https://www.jstor.org/stable/2098941.

[115] M. D. Hebden, 'An Algorithm for Minimization Using Exact Second Derivatives,' Atomic Energy Research Establishment, Harwell, United Kingdom, Mar. 1973. Accessed: 24th Sep. 2025. [Online]. Available: https://www.numerical.rl.ac.uk/media/reports/AERE_TP515.pdf.

[116] J. J. Moré, 'The Levenberg-Marquardt Algorithm: Implementation and Theory,' Argonne National Laboratory, Argonne, Illinois, United States of America, 1977. Accessed: 23rd Jun. 2025. [Online]. Available: https://digital.library.unt.edu/ark:/67531/metadc1448594/.

[117] J. J. Moré, B. S. Garbow and K. E. Hillstrom, 'User Guide for MINPACK-1,' Argonne National Laboratory, Argonne, Illinois, United States of America, ANL-80-74, Aug. 1980. Accessed: 24th Sep. 2025. [Online]. Available: https://cds.cern.ch/record/126569/files/CM-P00068642.pdf.

[118] A. Cano Sánchez, *Private Communication*, 8th Jan. 2024.

[119] M. Pearlman, D. Arnold, M. Davis, F. Barlier, R. Biancale, V. Vasiliev, I. Ciufolini, A. Paolozzi, E. C. Pavlis, K. Sośnica and M. Bloßfeld, 'Laser geodetic satellites: a high-accuracy scientific tool,' *Journal of Geodesy*, vol. 93, no. 11, 1st Nov. 2019. Accessed: 25th Jan. 2024. [Online]. Available: https://doi.org/10.1007/s00190-019-01228-y.

[120] D. Amato, A. J. Rosengren and C. Bombardelli, 'THALASSA: a fast orbit propagator for near-Earth and cislunar space,' in *2018 Space Flight Mechanics Meeting*, ser. AIAA SciTech Forum, American Institute of Aeronautics and Astronautics, 7th Jan. 2018. Accessed: 22nd Nov. 2021. [Online]. Available: https://arc.aiaa.org/doi/10.2514/6.2018-1970.

[121] G. Baù, H. Urrutxua and J. Pelaez, 'EDROMO: An accurate propagator for elliptical orbits in the perturbed two-body problem,' *Adv. Astronaut. Sci.*, vol. 152, 1st Jun. 2014.

[122] A. C. Hindmarsh, *ODEPACK, A Systematized Collection of ODE Solvers*, Livermore, California, United States of America, Aug. 1982. Accessed: 29th Oct. 2024. [Online]. Available: https://computing.llnl.gov/sites/default/files/ODEPACK_pub1_u88007.pdf.

[123] R. Biancale, G. Balmino, J.-M. Lemoine, J.-C. Marty, B. Moynot, F. Barlier, P. Exertier, O. Laurain, P. Gegout, P. Schwintzer, C. Reigber, A. Bode, R. König, F.-H. Massmann, J.-C. Raimondo, R. Schmidt and S. Yuan Zhu, 'A new global Earth's gravity field model from satellite orbit perturbations: GRIM5-S1,' *Geophysical Research Letters*, vol. 27, no. 22, 2000. Accessed: 16th Sep. 2024. [Online]. Available: https://onlinelibrary.wiley.com/doi/abs/10.1029/2000GL011721.

[124] W. M. Folkner, J. G. Williams, D. H. Boggs, R. S. Park and P. Kuchynka, 'The Planetary and Lunar Ephemerides DE430 and DE431,' Jet Propulsion Laboratory, 15th Feb. 2014. Accessed: 4th Oct. 2025. [Online]. Available: https://naif.jpl.nasa.gov/pub/naif/generic_kernels/spk/planets/de430_and_de431.pdf.

[125] J. Meeus, *Astronomical Algorithms*, 2nd ed. Willmann-Bell, 1998.

[126] D. A. Vallado, *Fundamentals of Astrodynamics and Applications*, 4th ed. Hawthorne, California, United States of America: Microcosm Press, 2013.

[127] L. Maisonobe, V. Pommier and P. Parraud, 'Orekit: an Open-source Library for Operational Flight Dynamics Applications,' presented at the 4th ICATT International Conference on Astrodynamics Tools and Techniques, Madrid, Spain, May 2010. Accessed: 2nd Apr. 2025. [Online]. Available: https://www.researchgate.net/publication/310250345_OREKIT_AN_OPEN_SOURCE_LIBRARY_FOR_OPERATIONAL_FLIGHT_DYNAMICS_APPLICATIONS.

[128] F. Biscani and D. Izzo, 'Revisiting high-order Taylor methods for astrodynamics and celestial mechanics,' *Monthly Notices of the Royal Astronomical Society*, vol. 504, no. 2, 21st Jun. 2021. Accessed: 13th Mar. 2026. [Online]. Available: https://doi.org/10.1093/mnras/stab1032.

[129] J. W. Cooley and J. W. Tukey, 'An Algorithm for the Machine Calculation of Complex Fourier Series,' *Mathematics of Computation*, vol. 19, no. 90, 1965. Accessed: 13th Sep. 2025. [Online]. Available: https://www.jstor.org/stable/2003354.

[130] A. A. Lidtke, D. J. Gondelach and R. Armellin, 'Optimising filtering of two-line element sets to increase re-entry prediction accuracy for GTO objects,' *Advances in Space Research*, vol. 63, no. 3, 1st Feb. 2019. Accessed: 28th Jan. 2020. [Online]. Available: http://www.sciencedirect.com/science/article/pii/S0273117718307877.

[131] A. Mukundan and H.-C. Wang, 'Simplified Approach to Detect Satellite Maneuvers Using TLE Data and Simplified Perturbation Model Utilizing Orbital Element Variation,' *Applied Sciences*, vol. 11, no. 21, Jan. 2021. Accessed: 28th Sep. 2025. [Online]. Available: https://www.mdpi.com/2076-3417/11/21/10181.

[132] J. Liu, L. Liu, J. Du and J. Sang, 'TLE outlier detection based on expectation maximization algorithm,' *Advances in Space Research*, vol. 68, no. 7, 1st Oct. 2021. Accessed: 18th Aug. 2021. [Online]. Available: https://www.sciencedirect.com/science/article/pii/S0273117721005688.

[133] H. Zhang, C. Zhao and Z. He, 'Two-Line Element Outlier and Space Event Detection Method Based on Multi-Strategy Genetic Algorithm,' *Applied Sciences*, vol. 14, no. 9, Jan. 2024. Accessed: 28th Sep. 2025. [Online]. Available: https://www.mdpi.com/2076-3417/14/9/3729.

[134] A. Dutt and V. Rokhlin, 'Fast Fourier Transforms for Nonequispaced Data,' *SIAM Journal on Scientific Computing*, vol. 14, no. 6, Nov. 1993. Accessed: 29th Aug. 2025. [Online]. Available: https://epubs.siam.org/doi/10.1137/0914081.

[135] N. R. Lomb, 'Least-squares frequency analysis of unequally spaced data,' *Astrophysics and Space Science*, vol. 39, no. 2, 1st Feb. 1976. Accessed: 22nd May 2025. [Online]. Available: https://doi.org/10.1007/BF00648343.

[136] J. D. Scargle, 'Studies in astronomical time series analysis. II. Statistical aspects of spectral analysis of unevenly spaced data.,' *The Astrophysical Journal*, vol. 263, 1st Dec. 1982. Accessed: 22nd May 2025. [Online]. Available: https://ui.adsabs.harvard.edu/abs/1982ApJ...263..835S.

[137] J. W. Tukey, *Exploratory Data Analysis*, 1st ed. Reading, Massachusetts, United States of America: Addison-Wesley Publishing Company, 1977.

[138] R. McGill, J. W. Tukey and W. A. Larsen, ‘Variations of Box Plots,’ *The American Statistician*, vol. 32, no. 1, 1st Feb. 1978. Accessed: 29th Sep. 2025. [Online]. Available: https://www.tandfonline.com/doi/abs/10.1080/00031305.1978.10479236.

[139] D. Simon, *Optimal State Estimation: Kalman, H Infinity, and Nonlinear Approaches*. Hoboken, New Jersey, United States of America: John Wiley & Sons, Incorporated, 2006.

[140] B. Friedland, ‘Treatment of bias in recursive filtering,’ *IEEE Transactions on Automatic Control*, vol. 14, no. 4, Aug. 1969. Accessed: 7th Sep. 2025. [Online]. Available: https://ieeexplore.ieee.org/document/1099223.

[141] D. P. Dee and A. M. Da Silva, ‘Data assimilation in the presence of forecast bias,’ *Quarterly Journal of the Royal Meteorological Society*, vol. 124, no. 545, 1998. Accessed: 7th Sep. 2025. [Online]. Available: https://onlinelibrary.wiley.com/doi/abs/10.1002/qj.49712454512.

[142] D. Haessig and B. Friedland, ‘Separate-bias estimation with reduced-order Kalman filters,’ *IEEE Transactions on Automatic Control*, vol. 43, no. 7, Jul. 1998. Accessed: 7th Sep. 2025. [Online]. Available: https://ieeexplore.ieee.org/document/701106.

[143] J.-P. Drécourt, H. Madsen and D. Rosbjerg, ‘Bias aware Kalman filters: Comparison and improvements,’ *Advances in Water Resources*, vol. 29, no. 5, 1st May 2006. Accessed: 7th Sep. 2025. [Online]. Available: https://www.sciencedirect.com/science/article/pii/S0309170805001818.

[144] R. Brandon. ‘Skyfield: High precision research-grade positions for planets and Earth satellites generator,’ Accessed: 28th Sep. 2025. [Online]. Available: https://ascl.net/1907.024.

Appendix A

Software

A.1 THALASSA

THALASSA [120] was developed as a stand-alone Command Line Interface (CLI) program. It was not designed to be used as a dependency by other programs. It had a number of limitations, both at compile- and run-time, which prevented smooth integration into other projects. It was decided, therefore, to modernise certain aspects of the program, resulting in a new release of THALASSA[1].

A refactor of the existing code was conducted to split THALASSA into a separate library and application. This preserved the original CLI functionality of THALASSA while laying the groundwork for THALASSA to be used as a library by other applications. During the refactor, several memory leaks were identified and removed from THALASSA. These memory leaks were not a concern previously as the memory was released after the propagation finished and the program exited.

THALASSA's existing build script, written for Make, was replaced with a full CMake implementation. This introduced additional features, including easier integration of the library into other projects as a CMake subproject, automatic compilation of additional language bindings, and automatic compiler parallelisation when using compatible build systems. Issues experienced previously with THALASSA's dependencies were streamlined by introducing CMake build scripts for the SOFA[2] and SPICE[3] libraries.

[1] Available at: https://github.com/maxhlc/thalassa (accessed 27/09/2025)
[2] Available at: https://github.com/maxhlc/sofa (accessed 27/09/2025)
[3] Available at: https://github.com/maxhlc/spice (accessed 27/09/2025)

Language bindings for THALASSA were created for several languages, including:

- C;
- C++;
- MATLAB; and
- Python.

The language bindings are categorised into three separate libraries: CTHALASSA, for C and C++; MTHALASSA, for MATLAB; and PyTHALASSA, for Python. All of the bindings are dependent on the bindings between C and Fortran, as illustrated in Figure A.1.

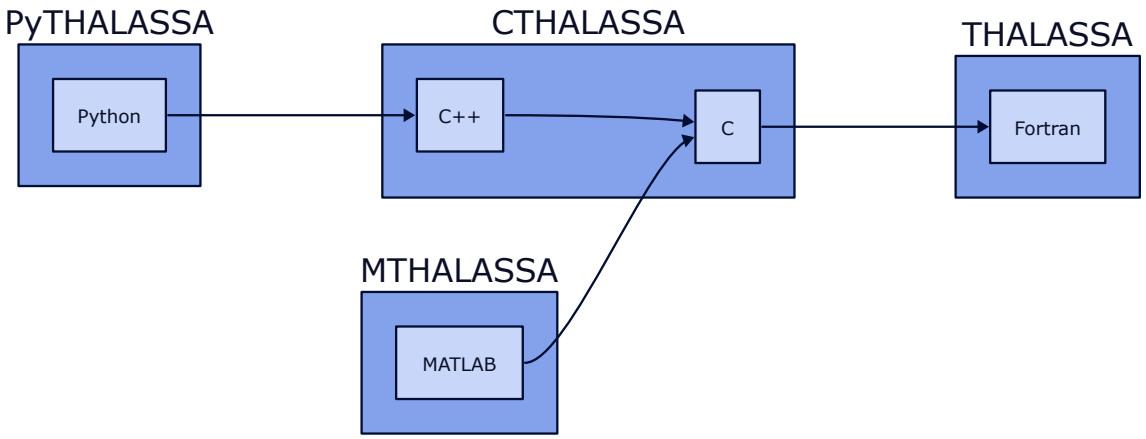


Figure A.1: THALASSA language binding dependencies.

The language bindings provide several improvements over stand-alone THALASSA, most notably basic thread-safety. The original stand-alone version of THALASSA was not thread-safe as it was not required for single propagations. In CTHALASSA, thread-safety is provided by forking the process prior to propagation. This provides a basic level of thread-safety by separating and isolating the memory of each propagation, enabling a single process to execute multiple propagations in parallel. However, it should be noted that this feature is available only for systems compliant with the Portable Operating System Interface (POSIX) standards, such as most distributions of Linux and MacOS. Some issues remain with SPICE, even when using this thread-safety mechanism, and it does not represent a full thread-safe implementation as some variables, such as the loaded settings and kernels, have to be shared between propagations.

It was found during testing of the TLE-based P-OD methods that propagations from THALASSA were not fitting well to either TLE pseudo-observations nor high-accuracy SLR-derived states. Following debugging, THALASSA's use of simplified transformations between Earth-Centred Inertial (ECI) and Earth-Centred, Earth-Fixed (ECEF) frames was identified as the source of error. Although THALASSA was using GCRF as its ECI frame, it was not considering nutation nor precession for its ECEF frame. A full International Terrestrial Reference Frame (ITRF) implementation was re-introduced to THALASSA, based on existing code which was left in one of THALASSA's stale development branches. The full reference frame transformation removed the source of error and ensured that THALASSA could be used for TLE-based P-OD moving forward.

A.2 BRENT

TLE-based P-OD was conducted using BRENT[4]. This software package was developed specifically for this thesis. It contains several submodules which can be used for a variety of tasks, such as orbit propagation, both analytical and numerical; batch least squares state estimation; and TLE bias modelling. Notable dependencies include THALASSA, Orekit, and Skyfield [120, 127, 144].

[4] Available at: https://github.com/maxhlc/brent (accessed 27/09/2025)